THE COMPOSITION OF THE LUNAR CRUST:
AN IN-DEPTH REMOTE SENSING VIEW

A DISSERTATION SUBMITTED TO THE GRADUATE DIVISION OF THE UNIVERSITY OF HAWAIʻI AT MĀNOA IN PARTIAL FULFILLMENT OF THE REQUIREMENTS FOR THE DEGREE OF

DOCTOR OF PHILOSOPHY

IN

GEOLOGY AND GEOPHYSICS

August 2016

By

Myriam Lemelin

Dissertation Committee:

Paul G. Lucey, Chairperson
G. Jeffrey Taylor
Jeffrey J. Gillis-Davis
Peter Englert
Karen Meech

Keywords: Moon; Remote sensing; Spectroscopy; Lunar crust; Central peak; Basin ring

ACKNOWLEDGEMENTS

Five years ago I was working at the Lunar and Planetary Institute with amazing colleagues such as Carolyn Eve, David Blair, Kirby Runyon, Stephanie Quintana and Sarah Crites. We were discussing our future on our way back home from work, stopping to see the alligators and armadillos on the way, and they asked me what I wanted do next. If I could do anything, what would it be? I wanted to do a PhD in Hawaii with Paul Lucey. I feel very privileged that it happened, as it has been such a marking moment in my life, both from a science and a personnel perspective. I want to thank many people who contributed in making this experience incredible.

I want to thank my advisor, Paul Lucey, for his endless creative ideas, his impressive knowledge and for allowing me to take part in many science meetings and conferences where I learned so much about various aspects of planetary sciences, and where I met numerous space enthusiast scientists.

I want to thank my dissertation committee members, Jeff Taylor, Jeff Gillis-Davis, Peter Englert, and Karen Meech for their suggestions and comments.

I want to thank my comprehensive exam committee members, Julia Hammer, Scott Rowland, Ed Scott, and Peter Isaacson. I especially enjoyed taking Julia Hammer's mineralogy class even if it sounded terrifying, I learned so much. I enjoyed taking Scott Rowland's class where we mapped lava flows and sampled active lava, it was a memorable first trip to Big Island. I thank Ed Scott for teaching me about asteroids and comets. I enjoyed it so much that I will soon embark on the OSIRIS-REx mission to asteroid Bennu.

I want to thank collaborators who helped with various aspects of the research presented herein: Greg Neumann, Erwan Mazarico, Ben Greenhagen, Katarina Miljković, Lisa Gaddis, Trent Hare, Mike Barker, Makiko Ohtake, Mark Wood, Jessica Norman, and Ashley Kakazu.

I thank Ethan Kasner, and Eric Pilger for their previous technical support, Vi Nakahara, Grace Furuya and Rena Lefevre for their help with the massive amount of administrative work involved.

This experience would not have been the same without the lunatic friends I made in Hawaii, Sarah Crites, Katie Robinson, David Trang, Laura Corley, Eugenie Song, Tanja Giebner, and Elizabeth Fisher. Thanks for the great discussions.

Thanks to my officemates and friends Caroline Caplan, Estelle Bonny, Melissa Adams, Andrea Gabrieli, David Frank, Tayro Acosta, Myriam Telus, and Elise Rumpf. You made every work day feels like just another day in paradise, besides the days I was hiding in my office.

Thanks to the GG peeps. You enriched the experience in so many ways, including teaching me precious things such as what a meme is and how to pronounce the word salmon.

Thanks to my friends in Canada for always being present, and to those who could visit me in paradise. Thanks to my family who was so supportive, truly tried to understand what I was doing, and made sure I was happy.

Last but not the least, thanks to my love Simon (and the fluffiest of all, Paco). It has been extremely difficult to leave home every time, but knowing that you were proud of me and that you were waiting for me to go on the next adventures made it bearable.

This work was supported by the financial help from the Hawaii Institute of Geophysics and Planetology, and from the Natural Sciences and Engineering Research Council of Canada (PGSD3 - 442668 - 2013).

ABSTRACT

In this dissertation, we investigate the composition of the lunar crust by conducting a quantitative and comprehensive analysis of the mineralogical composition of the central peak in 61 craters and the innermost ring of 18 impact basins, which expose material originating from various depths, using reflectance data acquired by the Kaguya Multiband Imager and Spectral Profiler in the visible and near infrared wavelengths. We also place constraints on the depth of origin of the material exposed by the innermost ring of impact basins using impact modeling code that tracks the fate of tracer particles in the target site.

We find that the central peaks in the Feldspathic Highlands Terrane are composed of anorthositic lithologies. The variability of their mafic assemblage suggests that some of them are sampling intrusions of mafic material into that crust, though no ultramafic material was detected that might suggest fully differentiated plutons. The central peaks in the South Pole-Aitken basin indicate mafic compositions at all depths, consistent with the presence of a large differentiated melt sheet that assimilated anorthositic crust and ultramafic mantle. The central peaks in the thorium rich Procellarum KREEP Terrane are composed of lithologies intermediate between the anorthositic material of the Feldspathic Highlands Terrane and the more mafic South Pole-Aitken Basin Terrane.

We find that the most abundant rock type is anorthosite on the innermost ring of most basins, consistent with our impact modeling results suggesting that the innermost rings are dominated by crustal material. Models indicate that most basins excavate mantle material and should expose a small proportion of such on their innermost ring. However, we do not detect ultramafic lithologies, thus mantle exposures should be present at the subpixel scale, or intermixed with crustal component.

We also produced various datasets that are now available to the lunar community, such as maps of olivine, low- and high-calcium pyroxene, plagioclase, iron and optical maturity parameter at 62 meters per pixel (available from the USGS Astropedia website), and maps of the normal albedo measured by the Lunar Orbiter Laser Altimeter at 3 and 1 km per pixel (available on the Planetary Data System website).

TABLE OF CONTENTS

LIST OF TABLES

LIST OF FIGURES

LIST OF ABBREVIATIONS

Abbreviation/Variable	Definition
CPX	clinopyroxene
D_o	depth of origin
D_{tr}	transient crater diameter
DTM	digital terrain model
FHT	Feldspathic Highlands Terrane
GRAIL	Gravity Recovery And Interior Laboratory
GRS	Gamma-Ray Spectrometer
KREEP	rich in potassium (K), rare earth elements, and phosphorus
LEND	Lunar Exploration Neutron Detector
LKFM	compositional group similar to the Low-potassium (K) Fra Mauro basalts
LOLA	Lunar Orbiter Laser Altimeter
LRO	Lunar Reconnaissance Orbiter
LROC	Lunar Reconnaissance Orbiter Camera
LSCC	Lunar Soil Characterization Consortium
Mg#	molar MgO/(MgO+FeO)
MI	Multiband Imager
NA	normal albedo
NAC	narrow angle camera
NIR	near infrared
nm	nanometers
OL	olivine

OMAT	optical maturity parameter
OPX	orthopyroxene
P	proximity to the crust/mantle boundary parameter
PAN	“purest anorthosite” containing ≤2 wt.% mafic minerals
PKT	Procellarum KREEP Terrane
PLG	plagioclase
ppd	pixels per degree
RDR	reduced data record
SP	Spectral Profiler
SPA	South Pole-Aitken basin
SPAT	South Pole-Aitken Terrane
T	crustal thickness
TDT	terrestrial dynamical time
μ	microns
USGS	United Stated Geological Survey
UV	ultraviolet
VIS	visible
wt.%	weight percent

CHAPTER 1

INTRODUCTION

1.1 Our closest celestial neighbor

The Moon, Earth's ~4.5 billion year old companion, has been through an eventful history. Due to the absence of plate tectonics and atmosphere, the scars created during our solar system's violent past and volcanic eruptions are still visible on its surface, a surface which currently records interactions with solar wind, galactic cosmic rays, and meteorites. Thus, the Moon represents an ideal laboratory to study a variety of processes occurring in our solar system. In this dissertation, we are specifically interested in learning about the composition of the lunar crust, as it holds the key to better understand global magma oceans, and, by the study of its bulk compositions, the formation of the Moon itself. Four research Chapters are presented herein, and some concepts necessary to understand the Chapters as a whole are presented first, such as the formation of the primary lunar crust, its subsequent modification by impacts and the formation of the three main geochemical terranes.

1.2 The formation of the primary crust

It is currently thought that the Moon formed when Theia, an impactor approximately the size of Mars, impacted into our proto Earth. The debris left over from the impact accreted in Earth's orbit to form the Moon [*Hartmann and Davis*, 1975]. Analysis of rock fragments originating from the primary crust and brought back during the Apollo missions, revealed the presence of abundant anorthosite (rock with ≥ 90 wt.% plagioclase). Forming a thick layer of anorthosite requires igneous activity on a global scale: a magma ocean [*Wood*, 1970]. In its early days, the Moon was likely covered by a vast global magma ocean, which then fractionally crystallized [*Elkins-Tanton et al*., 2011]. Magnesium-rich olivine crystallized first and sank, leaving a magma ocean increasingly rich in iron and aluminum. Pyroxene, the next mineral to crystallize, also sank, and increased the aluminum content of the magma ocean. Plagioclase began to crystallize after ~80% of the magma ocean had crystallized. As it was less dense than the remaining magma, it floated to form an anorthositic crust. Ilmenite-rich cumulates containing

high concentrations of incompatible radioactive elements crystallized from the last liquids between the top of the mantle and the bottom of the crust. The result of this crystallization sequence, low density magnesium-rich minerals at the bottom grading to high density iron-rich minerals and even denser ilmenite and radioactive elements on top of the mantle, was a gravitationally unstable pile. It is hypothesized that an overturn occurred; the ilmenite-rich layer and the underlying iron-rich cumulates sank, while the magnesium-rich early cumulates buoyantly rose to the base of the crust [*Hess and Parmentier*, 1994; 1995]. In light of global remotely sensed data, however, the Moon can no longer be viewed as a simple stratified structure, so a better understanding of its composition is key to understanding the limits of the concepts of its formation [*Jolliff*, 2000].

1.3 The evolution of the primary crust: cratering history and geochemical terranes

The Moon went through a period of intense bombardment early in its history, ending about 3.8 billion years ago, which considerably reworked its primary crust. The ~2500 km diameter South Pole-Aitken basin is likely one of the first impacts to form, although its age has not been determined and is of high scientific interest [*National Research Council*, 2007; 2011]. Such a huge impact likely redistributed considerable amounts of crustal, and probably mantle material across the surface [*Petro and Pieters*, 2008]. The energy released by the impact was so large that it also could have created a ~50 km deep melt sheet, which then differentiated [*Morrison,* 1998]. Subsequent impacts were smaller, but some of them were large enough to create impact basins: structures larger than ~150 km in diameter that contain one or multiple concentric rings which consist in material uplifted from great depths. The impacts that led to their formation also ejected and redistributed considerable amounts of crustal, and potentially mantle, material on top of the crust. Some estimates suggest that the veneer of ejecta from the entire population of lunar basins, the megaregolith, consist in approximately the top kilometer of material now on the surface of the Moon, maybe more [*Petro and Pieters*, 2008]. The population of impactors decreased in size and abundance with time, and the smaller impactors formed smaller impact features. Craters with diameter between ~15 and 150 km, uplift material originating from approximately one tenth of the crater diameter to form central peaks, kilometer high mountains that lie in the center of these craters [*Melosh*, 1989].

Because of their distinct geochemistry and petrologic history, three major geochemical terranes have been defined, the Feldspathic Highlands Terrane (FHT), the Procellarum KREEP Terrane (PKT), and the South Pole-Aitken Terrane (SPAT) [*Jolliff et al*., 2000]. The FHT is largest of the three main geochemical terranes. It occupies most of the far side of the Moon, and a portion of the near side. Its composition is anorthositic, which means that it predominantly consists in plagioclase and exhibits a low iron content (~4 wt.% FeO). The FHT is the terrane that most likely contains remnants of the primary lunar crust. The PKT occupies ~16% of the Moon's surface. It is located on the near side, and is characterized by high thorium concentrations, generally exceeding 3.5 ppm, as well as potassium (K), Rare Earth Elements, and Phosphorus (KREEP). It has largely been flooded by mare basalts. The SPAT consists of the South Pole-Aitken basin, a ~2500 km diameter impact basin that spans from the South Pole to Aitken crater (16.8°S). It consist in a mafic (rich in magnesium and iron) anomaly (7-14 wt.% FeO) that likely represents a differentiated melt pool of mixed crustal and mantle material.

When considering all the impacts and volcanic events that happened since the crystallization of the magma ocean, it is clear that the lunar crust has been considerably reworked to hundreds if not thousands meters deep, and that the key to understand its composition is the subsurface. Two options are then available: (1) analyze the composition of samples that lie on the lunar surface but that were once buried at great depths, such as some of the samples brought back from the Apollo missions, and (2) use remote sensing datasets to analyze the composition of central peaks and basin rings which also expose at the surface material that originates at greater depths, underneath the megaregolith. In this dissertation, we rely on the latter option, and use the former option to provide ground-truth data to spectroscopic models.

1.4 The composition of the lunar crust interpreted by the study of lunar samples

Shortly after the return of the first lunar samples, the crust of the Moon was proposed to be of anorthositic composition [*Wood et al*., 1970] based on fragments of anorthosite found in the mare soil samples of Apollo 11. Based on Apollo rock samples that were likely excavated by lunar basins and therefore coming from deep within the lunar crust, *Ryder and Wood* [1977] later proposed that the anorthositic crust might become more mafic with depth. They analyzed impact melts from the Serenitatis (Apollo 17) and Imbrium (Apollo 15) impact events to infer the composition of the deep crust, assuming that a significant fraction of impact melts are derived

from the deepest portion of the target and form deposits of melt rocks on or near the rim of large basins. The matrices of the fragment-laden melt boulders from both the Serenitatis and the Imbrium impact events were found to be noritic in character (richer in pyroxene than anorthosite). *Ryder and Wood* [1977] noted that the Imbrium compositions are more mafic (*i.e.,* have a higher Mg number, molar MgO/(MgO+FeO) and higher abundance of pyroxene), and also exhibit a lower abundance of KREEP component than the Serenitatis compositions. They reasoned that, since the Imbrium basin is larger than the Serenitatis basin, the Imbrium even must have melted material from greater depths than the Serenitatis event.

Studies of Apollo rock samples provide critical clues regarding the stratigraphy of the lunar crust, but despite the enduring power of sample analysis, they do have some important limitations: the Apollo samples represent only the equatorial near side region. In addition, the impact basin samples studied by *Ryder and Wood* [1977] originate from, or near, the PKT and so may not be representative of the deep crust elsewhere. In fact, it has been hypothesized that all of the thorium-rich impact-melt breccias, such as those studied analyzed by *Ryder and Wood* [1977], might come from a single event, the Imbrium impact [*Haskins et al*., 1998].

1.5 The composition of the lunar crust interpreted by the study of impacts features

Remote sensing observations of central peaks and basin rings provide a view that extends compositional information far from the Apollo missions zone, and at a wide range of depths. Remote sensing studies of central peak mineralogy was pioneered by *Pieters* [1982], first in a study of Copernicus crater, and subsequently of multiple central peaks [*Pieters*, 1986] using near infrared reflectance spectra from Earth-based telescopes. Since then, many studies have used this approach, using remote sensing data acquired from the lunar orbiting spacecraft [*e.g*., *Tompkins and Pieters*, 1999; *Cahill et al*., 2009; *Ohtake et al*. 2009; *Yamamoto et al.,* 2010; *Song et al*., 2013; *Donaldson Hanna et al*., 2014]. These studies have benefited from new remote sensing data acquired in the visible and near infrared by the multiple lunar missions from 1994 to present (*e.g*., Clementine, Chandrayaan-1, Kaguya, and Lunar Reconnaissance Orbiter) and have used a variety of techniques. These studies provided important clues regarding the composition of the lunar crust, but did not reach a consensus regarding its composition with depth, potentially for many reasons. Indeed, since the first global study by *Tompkins and Pieters* [1999], significant improvements in data and analytical methodologies have occurred in terms of spectral imaging,

geochemistry, and global crustal thickness [*e.g.*, *Lucey*, 2004; *Wieczorek et al*., 2013], in the recognition of the three major geologic terranes, and in a redefinition of the depth of origin of the material exposed by central peaks, from the proximity to the surface to proximity to the mantle, a reference less influenced by impacts [*Cahill et al*., 2009].

The rings of impact basins also expose material originating from various depths within the lunar crust, and can therefore be used to study its composition with depth. However, the depth of origin of the material exposed was not heretofore well constrained. Thus, studies related to the mineralogy of lunar impact basins could not relate the compositional observations with depths in the crust. Compositional observations have been mostly conducted via global surveys to identify exposures spectrally dominated by a mineral [*Hawke et al.*, 1991; 2003; *Nakamura et al*. 2012; *Yamamoto et al*., 2010; 2012; *Donaldson Hanna et al*., 2014]. *Cheek et al*. [2013] provided the first extensive survey of the plagioclase abundance in an impact basin, which revealed the utter dominance of nearly pure anorthosite in the innermost ring of Orientale basin.

In Chapter Two, we re-examine the hypothesis postulated by *Ryder and Wood* [1977] that the crust becomes more mafic with depth; we analyze the composition of crater central peaks by using recent remote sensing data and combining the best practices of previous studies. Radiative transfer equations describe the scattering of light interacting with surfaces, which allows to model reflectance spectra of various mineral mixtures. Modeled reflectance spectra of known composition are then compared to remote sensing spectra, which allows quantitative estimates of mineral abundances of remotely sensed surfaces. Here, we compute the mineralogy for 34 central peaks using visible and near-infrared data from the Kaguya Multiband Imager, *Hapke* radiative transfer modeling [*e.g*., *Hapke*, 1981; 1993; 2001], validated with spectra of lunar soils with well-known modal mineralogy, and recent crustal thickness models from the Gravity Recovery and Interior Laboratory (GRAIL) data to examine the variation in composition with depth.

In Chapter Three, we conduct a quantitative and comprehensive analysis of the mineralogical composition of the innermost ring of 13 lunar impact basins in the equatorial region, using data and methods similar to Chapter Two to derive the mineralogical composition. We use a newly developed hydrocode, which allows to simulate the evolution of the lunar surface in response to impacts [*e.g*., *Amsden et al*., 1980; *Melosh et al*., 1992; *Ivanov et al*., 1997; *Collins et al*., 2002], to place constraints on the depth of origin of the material exposed by the

innermost ring, and to relate the observed compositions with their depth of origin in the crust. We also develop a general depth estimation for the innermost ring of basins.

In Chapter Four, we derive the first mineral and iron maps of the polar regions, and use them to analyze the composition of 27 additional central peaks, and five additional basins. Due to the Moon's spin axis nearly perpendicular to the ecliptic, the topographic depressions in the polar region are poorly illuminated, making it challenging to use visible and near infrared data reflected by the Sun to derive mineralogical compositions. We tackle this problem by combining visible and near infrared reflectance data measured by the Kaguya Spectral Profiler during the polar summers with active measurements acquired by the Lunar Orbiter Laser Altimeter (LOLA) at 1064 nm. The reflectance measured by the Kaguya Spectral Profiler during the polar summers still contains regions with low illumination, but the reflectance measured by LOLA does not. Indeed, the LOLA reflectance experiment is unique among optical measurements of the Moon in that it actively measures the reflectance of the Moon at a constant phase angle of nearly zero degrees, independent of latitude or solar illumination from a global nadir viewing perspective [*Smith et al*., 2010]. However, as LOLA measures the reflectance of the lunar surface at only one wavelength (1064 nm), it cannot be used alone to derive mineralogical abundances. Thus, combining the reflectance measurements from both the Kaguya Spectral Profiler and LOLA allow us to derive precise mineralogical abundances, and in turn analyze the composition of central peaks and basin rings in the polar region.

In Chapter Five, we present a new calibration for the data acquired by LOLA, and produce equatorial and polar maps of its reflectance data at 1064 nm. We use these maps to investigate and confirm a newly discovered dependence of reflectance with latitude [*Hemmingway et al*., 2015].

Chapters Two and Five have been published in the Journal of Geophysical Research (Planets) and Icarus. Chapters Three and Four will be submitted shortly. Many datasets derived in these Chapters are available to the public, such as the composition of the central peaks in the equatorial region, as well as global maps of olivine, low- and high-calcium pyroxene, plagioclase, FeO and optical maturity parameter (OMAT) at ~62 m per pixel, available from the United States Geological Survey's Astropedia website (Chapters Two and Three). Equatorial and polar maps of the calibrated reflectance from the Lunar Orbiter Laser Altimeter presented in Chapter Five at respectively 3 and 1 km per pixel are available on the Planetary Data System.

CHAPTER 2

LUNAR CENTRAL PEAK MINERALOGY AND IRON CONTENT USING THE KAGUYA MULTIBAND IMAGER: REASSESSMENT OF THE COMPOSITIONAL STRUCTURE OF THE LUNAR CRUST

Published as: Lemelin, M., P. G. Lucey, E. Song, and G. J. Taylor (2015), Lunar central peak mineralogy and iron content using the Kaguya Multiband Imager: Reassessment of the compositional structure of the lunar crust, Journal of Geophysical Research-Planets, 120, 869–887, doi:10.1002/2014JE004778.

Abstract— Ryder and Wood [1977] suggested that the lunar crust becomes more mafic with depth because the impact melts associated with the large Imbrium and Serenitatis basins are more mafic than the surface composition of the Moon. In this study, we re-examine the hypothesis that the crust becomes more mafic with depth; we analyze the composition of crater central peaks by using recent remote sensing data and combining the best practices of previous studies. We compute the mineralogy for 34 central peaks using (1) nine-band visible and near-infrared data from the Kaguya Multiband Imager, (2) an improved version of Hapke's radiative transfer model validated with spectra of lunar soils with well-known modal mineralogy, and (3) new crustal thickness models from the Gravity Recovery and Interior Laboratory data to examine the variation in composition with depth. We find that there is no increase in mafic mineral abundances with proximity to the crust/mantle boundary or with depth from the current lunar surface and, therefore, that the crust does not become more mafic with depth. We find that anorthosite with very low mafic abundance ("purest anorthosite" or PAN) is a minority constituent in these peaks, and there is no clear evidence of a distinct PAN-rich layer in the middle crust as previously proposed. The composition of most of the central peaks we analyze is more mafic than classically defined anorthosites with an average noritic anorthosite composition similar to that of the lunar surface.

2.1. Introduction

An anorthositic crust was proposed shortly after the return of lunar samples [*Wood et al*., 1970]. Based on Apollo rock samples that were potentially excavated by lunar basins and therefore coming from deep within the lunar crust, *Ryder and Wood* [1977] proposed that the crust might become more mafic with depth. They analyzed impact melts from the Serenitatis (Apollo 17) and Imbrium (Apollo 15) impacts to infer the composition of the deep crust, assuming that a significant fraction of impact melts are derived from the deepest portion of the target and form deposits of melt rocks on or near the rim of large craters. The matrices of the fragment-laden melt boulders from the Serenitatis impact event were found to be noritic in character, corresponding to a variety of low-K Fra Mauro (LKFM) basalt, as defined by *Reid et al*. [1972]. The matrices of the fragment-laden black-and-white rocks (samples 15445 and 15455) from the Imbrium impact event were also found to be of LKFM basalt composition. The Imbrium compositions differ slightly from the Serenitatis boulders in that they are more mafic, have a higher Mg number (molar MgO/(MgO+FeO)), and have a lower KREEP component. *Ryder and Wood* [1977] suggested that since the Imbrium impact event was larger than the Serenitatis event, the Imbrium event melted material from a greater depth than the Serenitatis event. Therefore, they suggested that the content of mafic minerals and Mg number tend to increase with depth, but that the KREEP component exists in a zone of intermediate depth in the crust. To reconcile the heat-flow measurements and crustal thickness model of the time as well as the sample compositions, they suggested that the lunar crust consists of 3 layers: from top to bottom, (1) a ~18 km thick "anorthositic gabbro" layer (composed of generally anorthositic compositions), (2) a ~18 km thick LKFM layer (composed of KREEP norites, norites and some olivine-rich rocks), and (3) a ~24 km thick mafic layer (composed of troctolites and spinel-troctolites, some dunites and norites). They also concluded that the Serenitatis and Imbrium events did not excavate mantle material because nearly all clasts are plagioclase-bearing rocks, whose seismic properties are incompatible with those of the mantle. The only ultramafic clast was found in Serenitatis sample 72417 (a dunite clast). These characteristics suggest that the deep crust is more mafic than the composition of the average anorthositic surface material in the highlands. However, in a study of impact melt and clasts of the Mistastin impact crater, *McCormick et al*. [1989] demonstrated that the clast population in an impact melt appears to be mostly derived from material relatively far from the zone of impact melting, and is related to the

path the melt follows (radially outward from the point of impact). In that perspective, the failure to find ultramafic clasts in the Serenitatis samples does not exclude the possibility that this impact event excavated mantle material.

Studies of Apollo rock samples provide critical clues regarding the stratigraphy of the lunar crust, but despite the enduring power of sample analysis, they do have some important limitations: the Apollo samples represent only the lunar near side region near the equator, and the original location of the samples must be inferred. In addition, the impact basin samples studied by *Ryder and Wood* [1977] originate from, or near, the anomalous Procellarum KREEP Terrane and so may not be representative of the deep lunar crust elsewhere.

Remote sensing observations provide a view that extends compositional information far from the Apollo missions zone. Remote sensing of central peaks in particular, as pioneered by *Pieters* [1982], provides a unique three-dimensional view of the lunar crust since central peaks expose rocks from across the Moon and over a range of depths. Remote sensing studies of central peak mineralogy brought new insights regarding the composition of the lunar crust. However, existing studies are equivocal with respect to a crust that becomes more mafic with depth; some support the notion [*e.g.*, *Pieters*, 1982; *Pieters*, 1986; *Tompkins and Pieters*, 1999; *Ohtake et al*. 2009; *Donaldson Hanna et al*., 2014], and others do not [*e.g.*, *Cahill et al*., 2009; *Song et al*., 2013]. Since the first global study by *Tompkins and Pieters* [1999], significant improvements in data and analytical methodologies have occurred: (1) in terms of spectral imaging, geochemistry, and global crustal thickness [*e.g*., *Lucey*, 2004; *Wieczorek et al*., 2013], (2) in the recognition of the three major geologic terranes, the South Pole-Aitken Terrane (SPAT), the Feldspathic Highlands Terrane (FHT), and the Procellarum KREEP Terrane (PKT) [*Jolliff et al*., 2000], and (3) in a redefinition of depth from the proximity to the surface (where redistribution of material by basins was common), to proximity to the mantle, a reference much less influenced by basins [*Cahill et al*., 2009].

In this study, we re-examine the hypothesis that the crust becomes more mafic with depth by exploiting both new data, and the best of the prior methodologies for analysis of central peaks. We compute the mineralogy for 34 central peaks using: (1) nine band visible and near-infrared data from the Kaguya Multiband Imager (MI) which enables reduced uncertainties in radiative transfer analysis, (2) an improved version of Hapke's radiative transfer model validated with spectra of lunar soil with well-known modal mineralogy [*Taylor et al*., 2001; 2010; *Lucey et*

al., 2014], and (3) new crustal thickness models derived from the Gravity Recovery and Interior Laboratory (GRAIL) data [*Wieczorek et al*., 2013] to examine the variation in composition both with depth below the current lunar surface, and with proximity to the lunar mantle that may better reflect the original position of the material exposed in the central peaks.

2.2. Background

Remote sensing studies beginning with *Pieters* [1982] have used central peaks as a probe into the lunar surface in order to better understand the crustal composition with depth [*e.g.*, *Tompkins and Pieters*, 1999; *Wieczorek and Zuber*, 2001; *Cahill et al*., 2009; *Ohtake et al*., 2009; *Song et al*., 2013; *Donaldson Hanna et al*., 2014]. In the first global analysis, enabled by data from the Clementine satellite, *Tompkins and Pieters* [1999] used spectral parameters to estimate the composition of 109 central peaks. They suggested a bulk plagioclase content of ~81 % for the whole crust (~82 % for the upper crust and ~75 % for the lower crust), with local compositions on peaks ranging from nearly pure anorthosite (>85 % plagioclase) in the central peaks of craters outside major basins (which they interpreted to be representative of the upper crust), towards more mafic (noritic) and more heterogeneous compositions found in the central peaks of craters within major basins (which they interpreted to be representative of the lower crust). They interpreted some of this heterogeneity to be evidence for mafic plutons in both highlands and basins, and found that the lower crust is more compositionally diverse than the highlands, with a greater range of rock types and more diversity within each central peak, which is consistent with the results of *Pieters* [1986]. *Wieczorek and Zuber* [2001] extended the work of *Tompkins and Pieters* [1999] by refining the depth of origin of the 109 central peaks, but keeping the same mineral abundance estimations. Because of their updated depth of origin for the 109 central peaks, *Wieczorek and Zuber* [2001] estimate of crustal composition with depth differed slightly from that of *Tompkins and Pieters* [1999], although they also concluded that the crust becomes more mafic with depth. They found that the upper crust contains nearly pure anorthosite, and intermediate lithologies (*i.e.*, anorthositic norites, anorthositic gabbro-norites, anorthositic gabbros, and anorthositic troctolites), and found that the lower crust is composed of norites and gabbro-norites. Although they specified that the composition of the lower crust should be considered less robust than the composition of the upper crust because of the 109 peaks studied, only 18 were considered as having excavated lower crustal material. These were

confined to the Procellarum KREEP Terrane (PKT) and the South Pole-Aitken basin (SPA). *Cahill et al.* [2009] used quantitative radiative transfer modeling to estimate peak compositions, and defined a new concept for the depth of origin of central peaks. They found that central peaks having anorthositic mineralogy (>60 vol% plagioclase) are seen throughout the crustal column, and are almost all confined to the Feldspathic Highlands Terrane (FHT). They also found that the peaks with dominantly mafic mineralogy are mostly confined to the SPA and in the PKT. The results from *Cahill et al*. [2009] are inconsistent with the idea that the crust globally becomes more mafic with depth, but rather support a dominantly anorthositic crustal column with intrusions of more plagioclase-rich magnesian and ferroan anorthositic rocks at depth in the crust. Other recent studies [*Ohtake et al*., 2009; *Donaldson Hanna et al*., 2014] focused their search on the detection and characterization of purest anorthosite (PAN, plagioclase ≥98 %). *Ohtake et al*. [2009] identified PAN in 13 central peaks as well as 16 wall exposures and 10 ejecta deposits, and proposed that either a global layer of PAN may exist within the upper crust, ranging from 3 km to 30 km in depth, or that PAN may exist as large patches within the upper crust. *Donaldson Hanna et al*. [2014] also detected PAN in many central peaks where the most recent GRAIL crustal thickness model indicates a 9-63 km thick crust, and concluded that the primary anorthositic crust must have been at least 30 km thick. Overall, these studies suggest that the crust becomes more mafic with depth, with potentially a layer of PAN in the upper crust, although findings from *Cahill et al*. [2009] do not support this hypothesis.

2.3. Data and Methods

2.3.1 Multiband Imager UVVIS/NIR data

The Kaguya Multiband Imager acquired data in 9 UVVIS (415, 750, 900, 950, 1001 nm) and NIR (1000, 1050, 1250, 1550 nm) spectral bands. The instrument provides a spatial resolution of ~20 m in the UVVIS, and ~60 m in the NIR at the nominal altitude of 100 km [*Haruyama et al*., 2008; *Ohtake et al*., 2009]. Recently, the Kaguya team released a version of their high spatial resolution data corrected for the shading effects of topography (using the geometric calibration presented in *Ohtake et al*. [2008]), drastically reducing the error associated with mineral and elemental mapping algorithms using reflectance data [*Lucey*, 1998; *Robinson and Jolliff*, 2002], and enabling the detection of PAN in previously poorly illuminated areas.

Figure 2.1 shows, as an example, the central peak of Jackson Crater as seen by the Multiband Imager at 1001 nm, in (a) uncorrected radiance data (2B2 level, available online via the SELENE data archive at http://l2db.selene.darts.isas.jaxa.jp/index.html.en), and (b) reflectance data corrected for the shading effects of topography (MAP level, available online via the USGS Astropedia website at http://astrogeology.usgs.gov/search). The reflectance data corrected for the shading effects of topography corresponds to the MAP processing level. In this processing level, the reflectance images have been converted to mosaics, by matching overlapping areas in the original images, and projected into a simple cylindrical projection. In this study we use this newly corrected reflectance data (MAP level), and downsample the UVVIS data (20 m) to the same spatial resolution as the NIR data (60 m per pixel). We also correct systematic differences between the UVVIS and NIR data using methods described in the Supplemental Material.

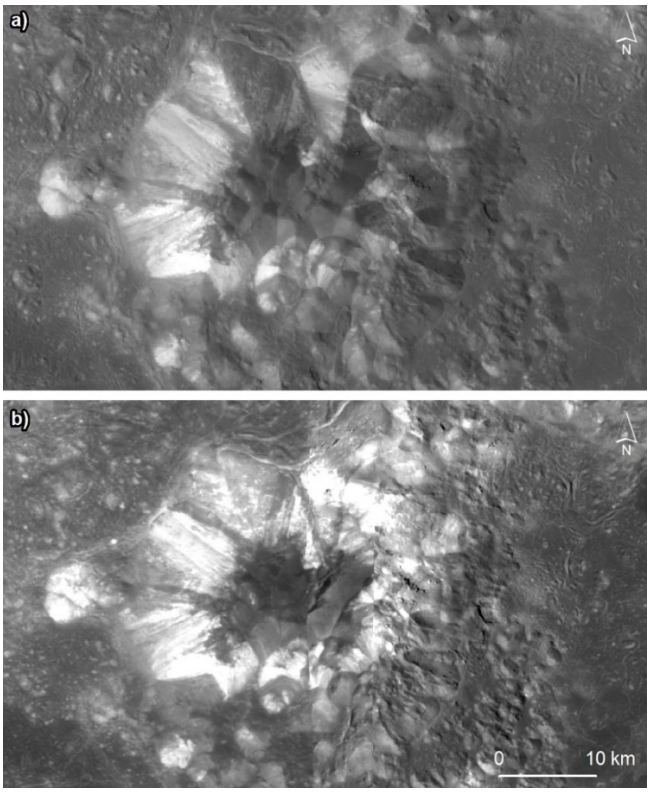

Figure 2.1. Central peak of Jackson Crater (22.4°N, 196.9°E) as seen by the Multiband Imager at 1001 nm, at ~20 m spatial resolution. a) 2B2 level product (uncorrected radiance), b) Map level product (reflectance corrected for the shading effects of topography). The highly anorthositic base of the central peak is easily apparent in the corrected data, while largely obscured in the uncorrected radiance image.

The correction for the shading effects of topography performed by the Kaguya team have provided the most accurate results for latitudes between ±50º (details can be found in the Supplemental Material, here shown in Appendix A). Therefore, we constrain our analysis to central peaks previously analyzed by *Cahill et al*. [2009] within this range of latitudes. This yields 34 central peaks (Table 2.1): 17 are located in the Feldspathic Highlands Terrane (FHT), 6 are located in the Procellarum KREEP Terrane (PKT), and 11 are located in the South Pole-Aitken basin (SPA) (Figure 2.2).

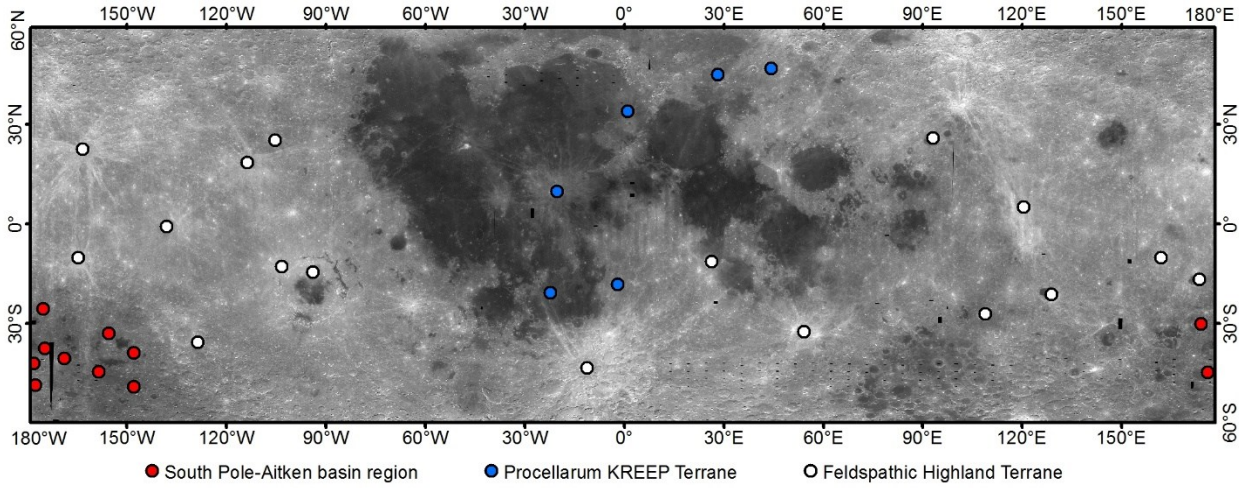

Figure 2.2. Location of the 34 crater central peaks analyzed in the Feldspathic Highlands Terrane (white), in the Procellarum KREEP Terrane (blue), and in the South Pole-Aitken basin (red). The background image is a 750 nm reflectance Multiband Imager global mosaic.

2.3.2 Hapke radiative transfer model

Radiative transfer equations describe the scattering of light interacting with surfaces, which allows to model reflectance spectra of mineral mixtures, varying grain sizes, chemistry, and space weathering effects. Modeling reflectance spectra of various mineral mixtures and comparing these to remote sensing spectra then allows retrieving quantitative mineral abundances of remote surfaces. In our study we use *Hapke*'s radiative transfer equations [*e.g.*, *Hapke*, 1981; 1993; 2001] and the approach described in *Lucey et al*. [2014]. To derive compositions from peak locations, we compute a spectrum library of mineral mixtures of plagioclase, orthopyroxene, clinopyroxene and olivine, then compare the central peak spectra

with the library to arrive at an estimated composition. The endmembers are all crystalline, including plagioclase. If shocked plagioclase is present, this would tend to reduce the amount of plagioclase reported. However, the tight constraints we place on iron abundance greatly mitigates this potential uncertainty. The spectrum library does not contain ilmenite, which is a minor phase in lunar highland rocks [*Papike et al*., 1991], as *Lucey* [2004] showed that in abundances less than 15 wt%, the presence of ilmenite does not affect the relative abundance estimation of the minerals present in a soil. The relative abundances of the mafic minerals are computed at 10 % abundance intervals, as it represents the typical error in mafic mineral abundances reported by *Lucey* [2004]. The relative abundance of plagioclase is computed at 1 % abundance intervals, as *Cheek et al.* [2013] found that changes in plagioclase content of 1 % are detectable. This yields a total of 6,601 different compositions. We use a fixed molar MgO/(MgO+FeO) (Mg#) of 65 (representative of the more magnesian of the ferroan anorthosites), and a grain size of 17 μm [*Pieters et al*., 1993; *Lucey*, 2006], to produce this library. We use the optical constants of *Lucey* [1998], which have been refined and validated using the Lunar Soil Characterization Consortium (LSCC) data by *Lucey et al*. [2014], in order to better represent the lunar soil and lower the error on the mineral abundance estimations. The error in mineral abundance between our model and the LSCC data at the MI spectral bands is ~8 wt% using refined and validated optical constants [*Lucey et al*., 2014] (Fig. 2.3), compared to ~25 wt% using the *Lucey* [1998] optical constants. We also compute these 6,601 mixtures at seven different amounts of nanophase iron (including the optical effects of nanophase iron of two sizes, *Lucey and Riner* [2011]) leading to a total of 46,207 modeled spectra. Nanophase iron includes: (1) optically small nanophase iron ("submicroscopic iron") which is responsible for the observed reddening of the lunar soil [*Hapke*, 2001; *Noble et al*., 2007; *Lucey and Noble*, 2008], and (2) larger nanophase iron ("Britt-Pieters particles" which is responsible for the observed darkening [*Britt and Pieters*, 1994; *Lucey and Riner*, 2011]. We built a second spectral library having the same compositions, but use a grain size of 200 μm for plagioclase only (as done by *Ohtake et al*. [2009]) because of the very strong plagioclase absorption bands found in PAN, for a total of 92,414 spectra.

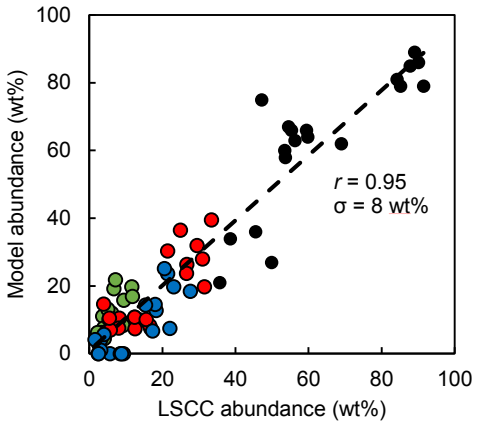

Figure 2.3. Error in mineral abundance between our model, at the Multiband Imager wavelengths using refined and validated optical constants [*Lucey et al*., 2014], and the mineral abundances measured by the Lunar Soil Characterization Consortium (LSCC). Olivine is shown is green, orthopyroxene in red, clinopyroxene in blue, and plagioclase in black. The correlation (*r*) between the two datasets is 95 % and the error (σ) in mineral abundance estimation is 8 wt%.

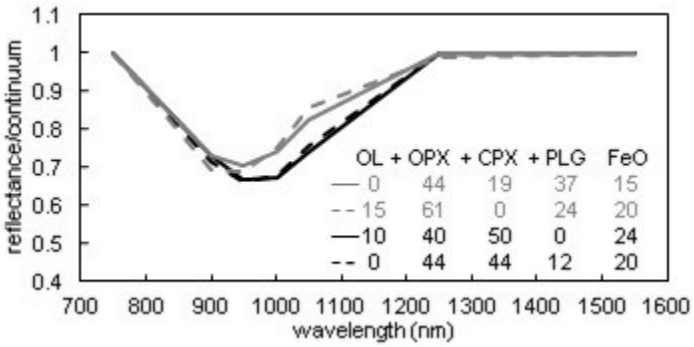

Figure 2.4. Examples of continuum removed modeled reflectance spectra that have similar shape at the Multiband Imager spectral sampling, but very distinct mineralogical composition and distinct FeO abundances. The solid and dashed line of each color show similar spectral shape, but distinct composition. These similar spectra can be distinguished with their distinct FeO content.

To assign a mineralogical composition to an MI pixel spectrum, we remove a continuum (straight line tangential to the reflectance spectrum at 750 and 1550 nm) from the library spectra and from the given MI pixel spectrum, and find the closest spectral match (using an evenly weighted average of the correlation between library and the unknown spectrum and the sum of the absolute difference in reflectance between the library and the given pixel spectrum). However, because reflectance spectra of different compositions can be similar in shape at the relatively coarse MI spectral sampling (Fig. 2.4), we use the abundance of FeO as a constraint.

We compute the FeO abundance consistent with the stoichiometric abundance of each mineral mixture in the spectral library, and we compute the FeO abundance corresponding to each pixel using an updated FeO algorithm described below. Only the library spectra that have a stoichiometric iron abundance within ±2 wt% of the FeO content of a given pixel are compared. The new FeO abundance mapping algorithm (Eq. 2.1-2.3, where x_{0Fe}=0.04 and y_{0Fe}=1.39), has a RMSE of 1 wt% FeO, and is a refinement of the work by *Otake et al*. [2012] (details can be found in the Appendix A). Once we obtain the closest spectral match in the library, we refine the abundance further using a gradient descent algorithm. We iteratively and sequentially vary the abundance of the minerals and space weathering products using the best library fit as the starting point, until the fit no longer improves, or 1000 iterations are reached. The process yields quantitative, validated (Fig. 2.3) and physically plausible mineral abundances (using the abundance of iron as a constraint) for every pixel analyzed in each of the 34 central peaks we study. Figure 2.5 shows an example of the result for Jackson crater: a map of plagioclase, olivine, orthopyroxene, clinopyroxene and iron abundances, as well as ternary diagrams showing the composition of each pixel for that central peak.

$$\text{FeO (wt\%)} = (1.0708 * \theta_{Fe2}) - 0.3986 \quad (2.1)$$

$$\theta_{Fe2} = 0.0656e^{(3.6681*\theta Fe1)} \quad (2.2)$$

$$\theta_{Fe1} = -\arctan(((R_{950}/R_{750})-y_{0Fe})/(R_{750}- x_{0Fe})) \quad (2.3)$$

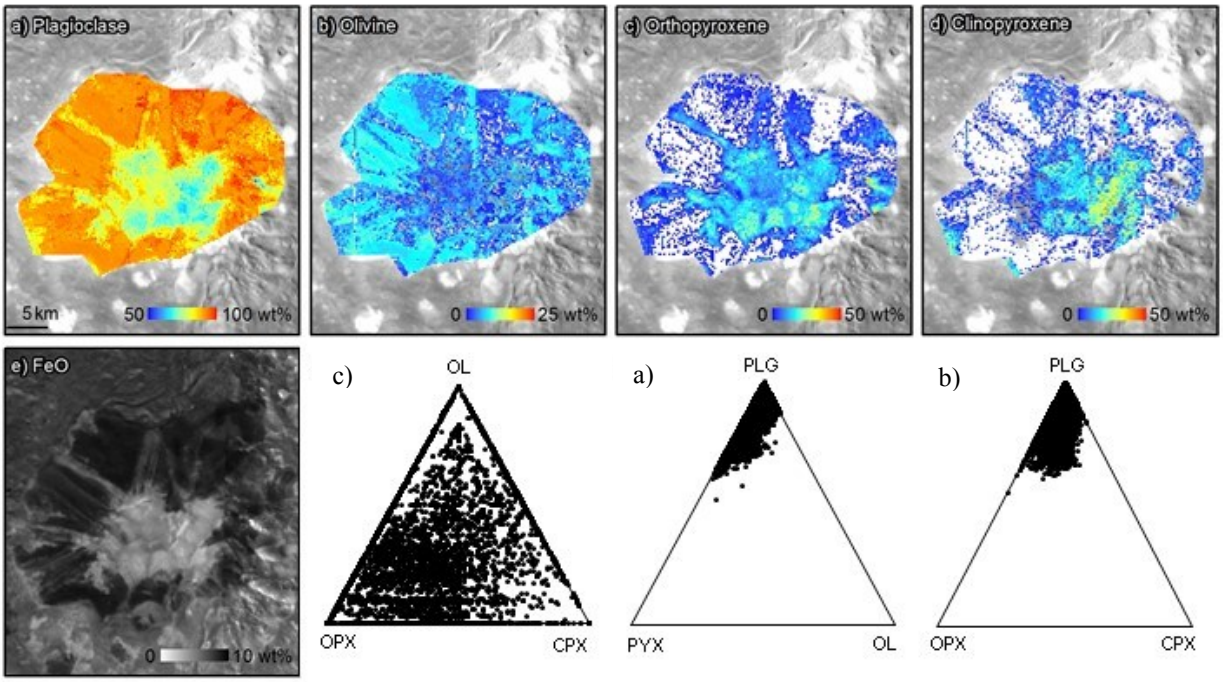

Figure 2.5. Example of the mineral mapping result for Jackson crater. a) plagioclase, b) olivine, c) orthopyroxene, d) clinopyroxene and e) iron abundance, as well as ternary diagrams (f-h) showing the composition of each pixel for that central peak. Note the changes in color scale in a-d.

The methodology used to assess the formal error in the mineral abundance using data from the LSCC gives an uncertainty of 8 wt%. However, in plagioclase-rich mixtures such as frequently encountered on the Moon, mafic minerals can be detected at much lower levels [*Cheek et al*., 2013]. To estimate the error in determining abundances and relative abundances of mafic minerals in plagioclase-rich mixtures, we compute spectral mixtures, add noise representative of the MI dataset, and use our algorithm to retrieve the abundances and relative abundances of mafic minerals from the computed mixtures. The test cases all have equal proportion of olivine, orthopyroxene, and clinopyroxene, and plagioclase abundances of 50, 60, 70, 80, 90, 95, and 98 wt%. For each of the 7 computed mixtures, we produce 300 test cases with 1 % random noise added. We then exercise our algorithm on the 2,100 test cases to derive statistics on mineral abundance error. This is the same procedure used by *Lucey* [2004] to estimate error in Clementine-based mineral maps. The choice of addition of 1% noise is based on

an analysis of the noise in the MI data; we select two 1ºx1º homogeneous areas, one in the mare (22-23°S, 267-268°E) and one in the highlands (7-8°S, 259-260°E) and in both cases, we compute the difference between the reflectance at 900 and 950 nm. We find that the standard deviation of the difference is 0.85 % in both cases. To be conservative, we add 1 % noise to each computed test spectrum. The results are shown in Figure 2.6, where the error in absolute and relative abundances of mafic minerals are given as a function of plagioclase content. The error in relative mafic mineral abundance is most relevant to the ability to distinguish various type of anorthosites or anorthositic rocks. Even in the most plagioclase rich examples, 30 % error is found which is sufficient to determine if an anorthositic assemblage is noritic, gabbroic, or troctolitic, in other words, if the mafic assemblage is dominated by orthopyroxene, clinopyroxene, or olivine.

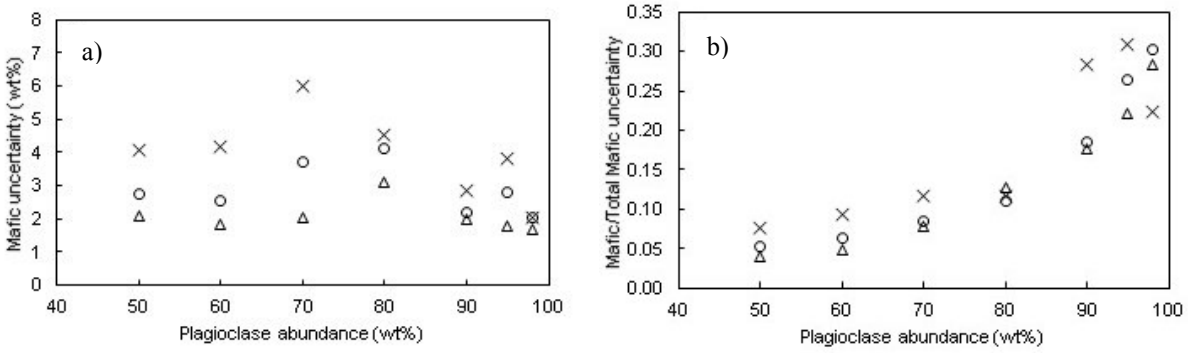

Figure 2.6. Error in mafic mineral abundance modeling between 50 to 98 wt% plagioclase when the mafics are present in equal proportion (0.33). A 1% random noise in reflectance has been added 300 times to each modeled spectra of predefined composition, and the best spectral match (mineral abundance) has been retrieved. (a) mafic mineral abundance uncertainty (standard deviation, wt%), (b) mafic mineral abundance uncertainty over the total abundance of mafics (standard deviation, wt%). Triangles represent olivine, "o" represent orthopyroxene, and "x" represent clinopyroxene.

2.3.3 Depth estimates

Excepting *Cahill et al*. [2009], prior work investigating the relationship between peak composition and depth of origin of material have used the depth of excavation as the principal depth variable. However, the many observed lunar basins have greatly redistributed lunar

material since the formation of the lunar crust [*Petro and Pieters*, 2008], so using the actual lunar surface as a reference may obscure depth relationships established at the time of origin of the lunar crust. For example, in a portion of the crust thinned by basins, especially SPA, a shallow depth of origin for a central peak from a relatively small crater obscures the fact that the material was once at great depth. For this reason, *Cahill et al*. [2009] reasoned that the proximity to the lunar mantle is a more reliable indicator of the original location of the material exposed in a central peak. Therefore, we compute the proximity to the crust-mantle boundary (*P*) parameter of *Cahill et al*. [2009] (Eq. 2.4) for each crater we analyze. *P* is calculated from:

$$P = T - D_{exc} \tag{2.4}$$

T is the crustal thickness model (Model 1) using data from GRAIL (accessed online at http://www.ipgp.fr/~wieczor/GRAILCrustalThicknessArchive/GRAILCrustalThicknessArchive.html), and D_{exc} is the depth of origin of the material exposed by the central peak (D_{exc} = 0.1D) from *Melosh* [1989]. Using this parameter, we then compare the abundance and the average abundance of plagioclase and mafic minerals derived from Hapke radiative transfer modeling, versus the proximity to the crust/mantle boundary for each of the 34 central peaks, as well as the more traditional depth of excavation relative to the lunar surface.

2.4. Results

2.4.1 Mineral abundances

Mineral abundances follow a unimodal distribution within most of the central peaks we analyze. Figure 2.7 shows the normalized histograms of plagioclase abundance versus the proximity to the crust/mantle boundary (*P*) for each of the central peaks in the FHT (Fig. 2.7a), in SPA and in the PKT (Fig. 2.7b). To obtain the normalized histograms, we divide each histogram by its maximum value, which enables to better compare the distribution shapes and standard deviations. We find that only one central peak has a bimodal distribution of plagioclase; the central peak of Jackson has a global maximum of 92 wt% plagioclase, and a local maximum of 98 wt% plagioclase (Fig. 2.7a, *P* = 46 km). Since the abundance of plagioclase of most central peaks follow a unimodal distribution we chose to continue the analysis by using the average

mineral abundance values. We find that the average mineral content for the 34 central peaks we analyze range between 42 and 95 wt% plagioclase, 1 and 11 wt% olivine, 1 and 22 wt% clinopyroxene, and between 1 and 40 wt% orthopyroxene (Table 2.1). We also find that these central peaks have excavated material located between 4 km below the crust/mantle boundary (*i.e.*, within the mantle) up to 49 km above the crust mantle boundary (Table 2.1). It should be noted that impact melt has likely been identified on some of the central peaks we analyze (Tycho, Aristillus, Copernicus and Jackson) by recent studies [*Dhingra and Pieters*, 2012; *Kuriyama et al*., 2012; *Dhingra, D. et al*., 2014; *Dhingra, R.D. et al*., 2014]. However, since the proportion of impact melt covering these central peaks is small (3.1 % on average), it does not have a significant impact on the average central peak compositions reported here (see Section 2.5).

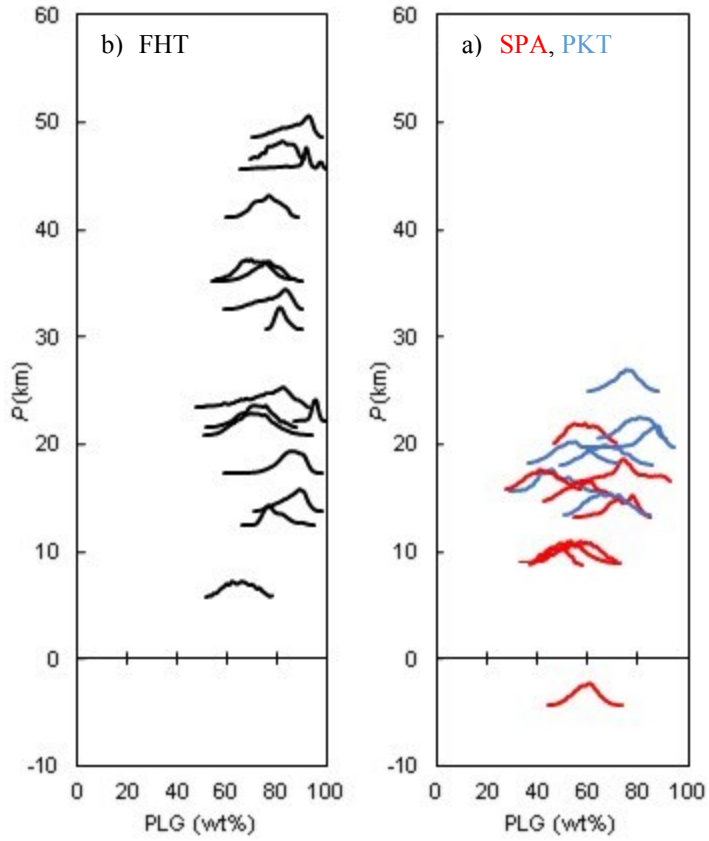

Figure 2.7. Normalized histograms of plagioclase (PLG) abundance (wt%) in the central peaks we analyze versus the proximity to the crust/mantle boundary (*P*) in (a) the Feldspathic Highlands Terrane (FHT), (b) the South Pole Aitken (SPA) basin and the Procellarum KREEP Terrane (PKT).

Table 2.1. Average abundance of plagioclase (PLG), olivine (OL), orthopyroxene (OPX), clinopyroxene (CPX), and iron (FeO) (± 1σ) of craters analyzed in this study, estimated proximity to the crust-mantle boundary (*P*), crustal thickness (*T*), depth of origin $(D)_{exc}$, and detection of purest anorthosite (*).

Crater	Lat (deg)	Long (deg)	PLG (wt%)	OL (wt%)	OPX (wt%)	CPX (wt%)	FeO (wt%)	*P* *(km)*	*T* *(km)*	D_{exc} *(km)*
Feldspathic Highlands Terrane (FHT)										
Aitken*	-16.8	173.4	93 ± 3	3 ± 2	2 ± 3	2 ± 2	4 ± 1	27	40	14
Berkner	25.2	254.8	82 ± 2	4 ± 2	10 ± 5	4 ± 4	7 ± 0	31	39	9
Crookes	-10.3	195.5	81 ± 6	2 ± 3	7 ± 4	10 ± 5	5 ± 1	46	51	5
Jackson*	22.4	196.9	88 ± 8	5 ± 4	5 ± 6	2 ± 4	3 ± 2	46	53	7
Joliot	25.8	93.1	79 ± 5	4 ± 2	9 ± 6	8 ± 5	7 ± 1	12	29	16
Keeler*	-10.2	161.9	95 ± 2	3 ± 2	1 ± 1	1 ± 1	3 ± 0	22	38	16
King	5.0	120.5	75 ± 6	3 ± 3	11 ± 4	10 ± 5	5 ± 1	35	43	8
Langmuir*	-35.7	231.6	79 ± 6	3 ± 2	11 ± 4	7 ± 4	6 ± 1	32	42	9
Lowell	-12.9	256.9	76 ± 5	3 ± 3	12 ± 4	9 ± 4	6 ± 1	41	48	7
Maunder	-14.6	266.2	62 ± 7	3 ± 3	15 ± 6	16 ± 5	9 ± 1	5	11	6
Ohm	18.4	246.5	71 ± 6	3 ± 3	10 ± 3	15 ± 5	7 ± 1	35	42	6
Scaliger	-27.1	108.9	75 ± 11	6 ± 5	10 ± 6	9 ± 8	7 ± 2	23	32	8
Stevinus	-32.5	54.2	72 ± 6	2 ± 3	18 ± 5	8 ± 4	7 ± 1	22	29	7
Theophilus*	-11.4	26.4	86 ± 5	4 ± 3	3 ± 3	7 ± 4	4 ± 1	14	25	11
Tsiolkovsky*	-21.2	128.9	85 ± 5	5 ± 4	5 ± 4	6 ± 4	5 ± 1	17	36	19
Tycho*	-43.4	348.9	71 ± 8	3 ± 4	15 ± 9	11 ± 7	6 ± 2	21	31	10
Vavilov*	-0.8	222.1	87 ± 6	2 ± 2	6 ± 4	4 ± 3	4 ± 1	49	58	10
Minimum			*62*	*2*	*1*	*1*	*3*	*5*	*11*	*5*
Maximum			*95*	*6*	*18*	*16*	*9*	*49*	*58*	*19*
Average			*80*	*3*	*9*	*8*	*6*	*28*	*38*	*10*
South Pole-Aitken basin (SPA)										
Alder	-48.6	182.6	57 ± 7	3 ± 4	32 ± 9	9 ± 5	11 ± 1	9	17	8
Birkeland	-30.2	173.9	46 ± 6	2 ± 3	38 ± 6	14 ± 5	13 ± 1	16	24	8
Borman	-38.8	212.3	73 ± 6	3 ± 2	18 ± 7	6 ± 4	8 ± 1	13	18	5
Davisson	-37.5	185.4	52 ± 6	2 ± 3	29 ± 5	16 ± 4	12 ± 1	9	18	9
Dryden	-33.0	204.8	59 ± 6	2 ± 3	28 ± 6	11 ± 4	10 ± 1	20	25	5
Finsen	-42.0	182.1	53 ± 6	1 ± 2	35 ± 7	11 ± 5	11 ± 1	9	16	7
Grissom M	-49.1	212.3	58 ± 7	5 ± 4	28 ± 6	9 ± 5	11 ± 1	15	18	4
Maksutov	-40.5	191.3	47 ± 6	3 ± 3	40 ± 6	10 ± 6	13 ± 1	8	17	8
Orlov	-25.7	185.0	76 ± 7	4 ± 2	13 ± 7	7 ± 4	8 ± 1	17	25	8
Von Karman	-44.8	175.9	59 ± 5	5 ± 3	23 ± 5	13 ± 5	11 ± 1	-4	14	18
White	-44.6	201.7	42 ± 6	3 ± 4	33 ± 7	22 ± 6	14 ± 1	16	20	4
Minimum			*42*	*1*	*13*	*6*	*8*	*-4*	*14*	*4*
Maximum			*76*	*5*	*40*	*22*	*14*	*20*	*25*	*18*
Average			*57*	*3*	*29*	*12*	*11*	*11*	*19*	*8*

Procellarum KREEP Terrane (PKT)										
Aristillus	33.9	1.2	54 ± 7	2 ± 3	29 ± 7	15 ± 6	11 ± 1	18	24	6
Arzachel	-18.2	358.1	75 ± 5	3 ± 3	12 ± 4	9 ± 5	7 ± 1	25	34	10
Atlas	46.7	44.4	79 ± 6	4 ± 5	10 ± 6	7 ± 5	6 ± 1	20	29	9
Bullialdus	-20.7	337.8	68 ± 7	3 ± 3	22 ± 7	7 ± 4	8 ± 1	13	19	6
Burg	45.0	28.2	67 ± 7	3 ± 3	18 ± 6	12 ± 5	8 ± 1	18	22	4
Copernicus	9.7	339.9	85 ± 4	11 ± 4	1 ± 2	4 ± 3	5 ± 2	20	29	9
Minimum			*54*	*2*	*1*	*4*	*5*	*13*	*19*	*4*
Maximum			*85*	*11*	*29*	*15*	*11*	*25*	*34*	*10*
Average			*71*	*4*	*15*	*9*	*8*	*19*	*26*	*7*
All terranes										
Minimum			*42*	*1*	*1*	*1*	*3*	*-4*	*11*	*4*
Maximum			*95*	*11*	*40*	*22*	*14*	*49*	*58*	*19*
Average			*71*	*3*	*16*	*9*	*8*	*21*	*30*	*9*

Although we derive the mineral abundance in each pixel of each central peak, we use the average mineral abundances of each central peak to derive its average rock type based on the rock classification diagrams of *Stöffler et al*. [1980] (Fig. 2.8). Even if we find that the central peaks contain multiple lithologies (*e.g.*, Fig. 2.11), they are generally dominated by a single lithology as suggested by the small variation in the plagioclase content in most cases (Fig. 2.7). Hence, we use the average rock type of each central peak to represent its dominant lithology. We find that central peaks from the FHT (white circles in Fig. 2.8a) are composed of anorthosites, noritic/gabbroic anorthosites, and anorthositic norites/gabbros. The central peaks from the PKT (blue circles in Fig. 2.8a) are composed of noritic/gabbroic anorthosites, anorthositic norites/gabbros, norites/gabbros, and troctolitic anorthosite. The central peaks from SPA (red circles in Fig. 2.8a) are composed of anorthositic norites/gabbros, and norites/gabbros.

Figure 2.9 shows the average plagioclase content of each central peak analyzed relative to their proximity (*P*) to the crust/mantle boundary. If all the central peaks are treated together (Fig. 2.9a), there appears to be a weak decrease in average plagioclase content with increasing proximity to the crust/mantle boundary (*i.e.*, an increase in mafic character with depth), although the correlation (*r*) is only 0.56 between these parameters. We compute the *p*-value to determine if this correlation is statistically significant, the null hypothesis (H_0) being that there is a decrease in average plagioclase content with increasing proximity to the crust/mantle boundary. We find that the *p*-value is equal to 0.001, which is lower than the *p*-value for a 95% confidence interval (0.05), and therefore, the null hypothesis has to be rejected (*i.e.*, the correlation is not statistically

significant). Even this weak (and not statistically significant) correlation disappears when we separate the data by terrane [*Jolliff et al*., 2000]. Craters located in SPA (Fig. 2.9b), in the PKT (Fig. 2.9c) and in the FHT (Fig. 2.9d) have average central peak plagioclase contents varying from 42 to 76 wt%, 54 to 85 wt%, and 71 to 95 wt% (excluding Maunder) respectively, and a correlation of 0.09, 0.38 and 0.27 respectively, between their average plagioclase content and their proximity to the crust/mantle boundary. We find that when central peaks from the major terranes are treated separately, SPA, the PKT and the FHT have similar average plagioclase content within each terrane (average plagioclase content of 57 wt%, 71 wt% and 80 wt% respectively) and no significant correlation of mafic content character with depth. Note that Von Karman has exposed mantle material according to our method, yet shows no particular enhancement in mafic character.

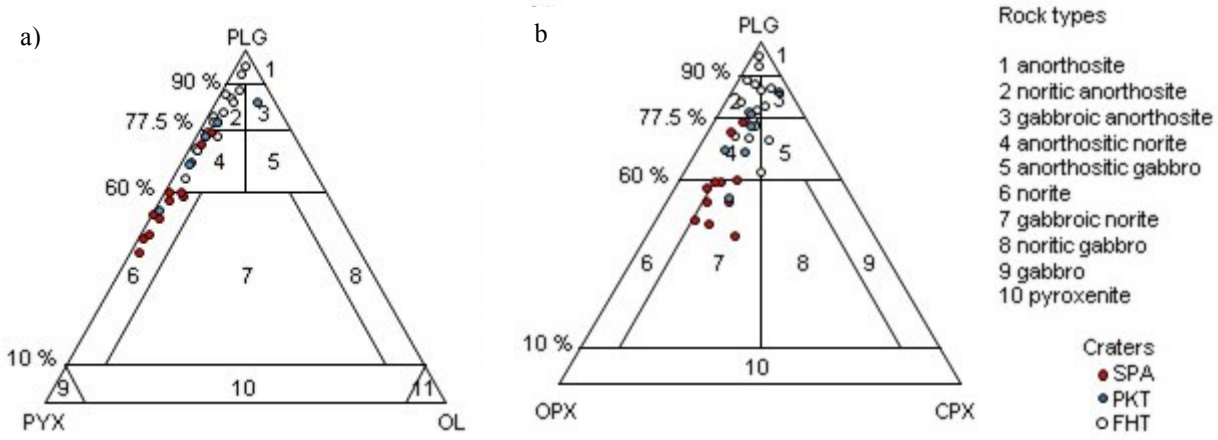

Figure 2.8. Average mineral abundance for the central peaks analyzed on rock classification diagrams of *Stöffler et al*. [1980].

For completeness, Figure 2.10 shows the average plagioclase content of each central peak analyzed relative to the depth of excavation of the material exposed by the central peak (D_{exc}), which can be used to compare our results with results from previous studies and references our central peak composition relative to the current surface. We do not find any statistically significant correlation between these two parameters, neither by looking at all terranes together (Fig. 2.10a) (*p*-value is equal to 0.01, which is lower than the *p*-value for a 95% confidence interval (0.05)), nor by looking at each terrane individually (Fig. 2.10b-d). Moreover, craters in the FHT and in SPA have both excavated material ~16-20 km below the surface, but show

different plagioclase contents; the crater in SPA has an average plagioclase content of 59 wt%, whereas the three craters in the FHT with the same depth of excavation have an average plagioclase content ranging between 79 to 95 wt%.

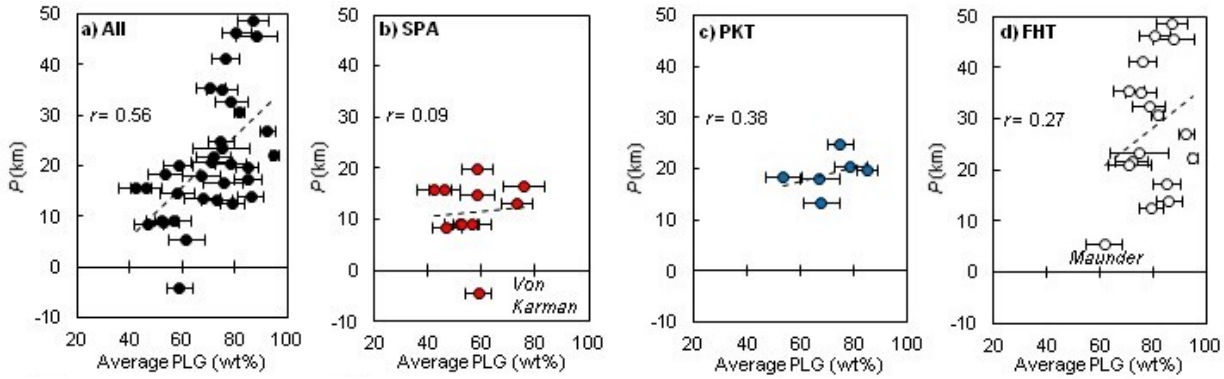

Figure 2.9. Average plagioclase (PLG) content (wt%) of the central peaks analyzed versus their proximity (*P*) to the crust mantle/boundary (km) for (a) all terranes, (b) craters within the South Pole-Aitken basin, (c) craters within the Procellarum KREEP Terrane, and (d) craters within the Feldspathic Highlands Terrane only. The variation in plagioclase content for each central peak is shown using ± 1σ.

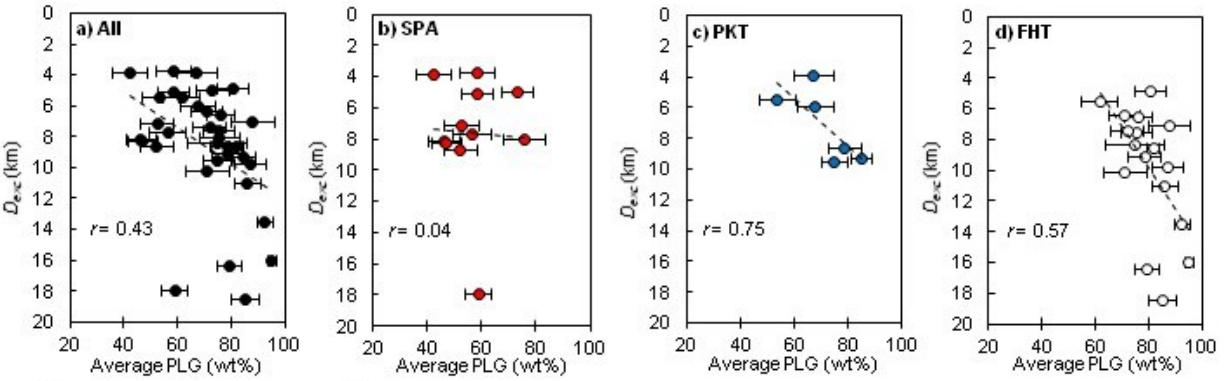

Figure 2.10. Average plagioclase (PLG) content (wt%) of the central peaks analyzed referenced to the current lunar surface ($D_{exc} = 0$) using the depth of excavation of the material exposed by the central peak (D_{exc}) (km). (a) all terranes, (b) craters within the South Pole-Aitken basin, (c) craters within the Procellarum KREEP Terrane, and (d) craters within the Feldspathic Highlands Terrane only. The variation in plagioclase content for each central peak is shown using ± 1σ.

2.4.2 Exposures of purest anorthosite

Ohtake et al. [2009] have argued that the detection of purest anorthosite (PAN, ≥98 wt% plagioclase) in the deposits of all craters larger than 30 km indicates the presence of a middle crust layer of this material. To test this hypothesis, we identify the central peaks in which we detect ≥98 wt% plagioclase (*i.e.*, "purest anorthosite", or PAN) in some pixels although the average plagioclase abundance for the entire central peak is lower, derive their proximity to the crust/mantle boundary as well as their depth of excavation relative to the actual lunar surface, and compare our results with those from *Ohtake et al*. [2009].

Based on our radiative transfer modeling, we find exposures of PAN within eight central peaks: Aitken, Jackson, Keeler, Langmuir, Theophilus, Tsiolkovsky, Tycho and Vavilov (Fig. 2.11). These central peaks are all located in the FHT, and have a wide range of depths of excavation and proximity to the crust/mantle boundary (Table 2.2). Although we find local exposures of PAN in eight central peaks, the average composition of most of the central peaks is more mafic than anorthosite, which by definition contains ≥90 wt% plagioclase and ≤10 wt% mafic minerals (Fig. 2.8). Indeed, only the central peaks of Aitken and Keeler (Fig. 2.11a, 2.11c) have an anorthosite composition, by the definition of *Stöffler et al*. [1980], with an average plagioclase abundance of 93 and 95 wt% respectively. The other central peaks analyzed contain on average >10 wt% of mafic minerals (Table 2.1). Moreover, only tens of pixels in Aitken, Jackson and Keeler are identified as PAN, versus even fewer pixels for the other central peaks (Fig. 2.11).

Ohtake et al. [2009] reported exposures of PAN in 13 central peaks using the Multiband Imager data (Table 2.2). We measure the proximity to the crust/mantle boundary for these craters, except for the 3 basin-related central peaks (*i.e.*, Orientale Inner Rook North, Orientale Inner Rook Massif, and Schrödinger) because the calculation for the maximum depth of excavation [*Melosh*, 1989] used to derive the crust/mantle boundary parameter is not applicable to multi-ringed impact basins. We find that the detections of PAN of *Ohtake et al*. [2009] also have a wide range of depths of excavation and proximity to the crust/mantle boundary (Table 2.2).

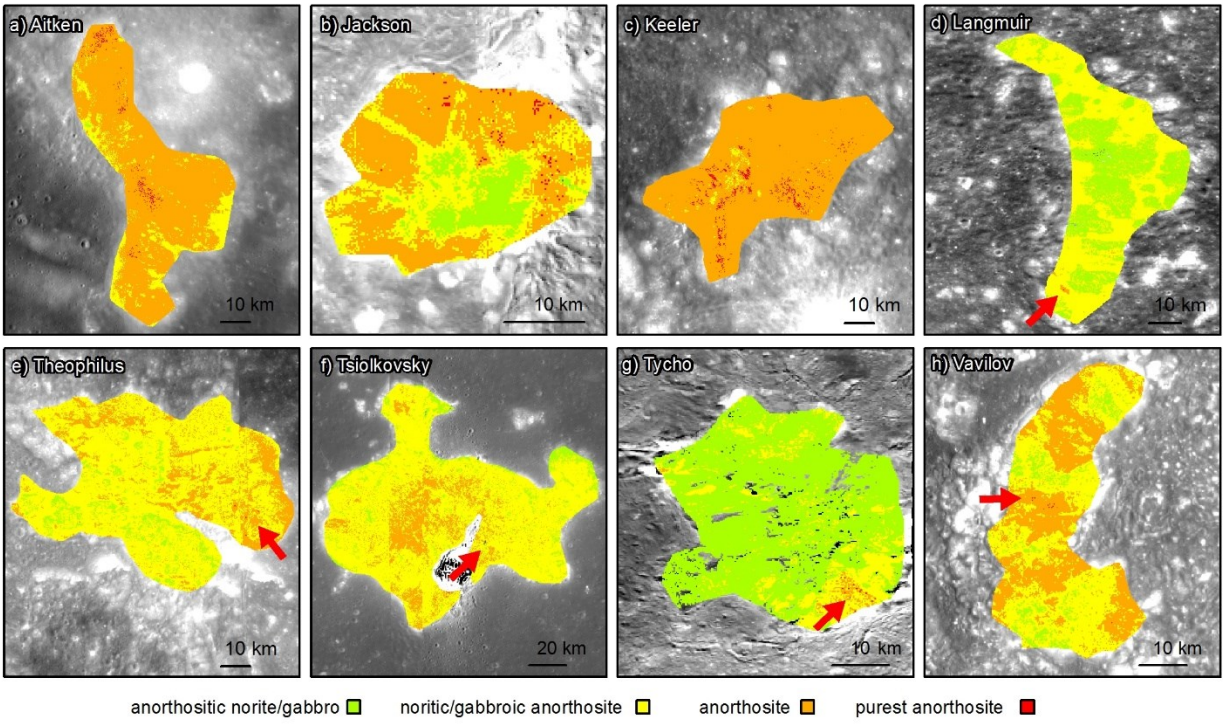

Figure 2.11. Maps of rock types for the eight central peaks in which we detect purest anorthosite. The red arrows are pointing to the few pixels in which we detect purest anorthosite.

The study of *Ohtake et al*. [2009] and this study show very similar results in the detection of PAN (Table 2.2). Our sample includes six craters where *Ohtake et al*. [2009] reported PAN in their central peak. Four of these central peaks showed maximum plagioclase abundances ≥98 wt% (Jackson, Tsiolkovsky, Tycho and Vavilov). In the other two cases (Atlas and King), maximum plagioclase abundances were only slightly lower (93 and 97 wt% respectively). Overall, both studies (*Ohtake et al*. [2009] and this study) have detected PAN with similar ranges of depths of excavation and proximity to the crust/mantle boundary (Table 2.2, Fig. 2.12).

Table 2.2. Craters where purest anorthosite (PAN) has been detected in the central peak by this study, or by *Ohtake et al*. [2009], or by both studies, along with the proximity to the crust-mantle boundary parameter (P), the depth of excavation (D_{exc}), and the crustal thickness (T) from GRAIL at these sites.

Crater name	Latitude (deg)	Longitude (deg)	PAN (this study)	PAN (*Ohtake et al*. [2009])	P (km)	D_{exc} (km)	T (km)
Aitken	-16.8	173.4	Yes	-	27	14	40
Atlas	47.0	44.4	No	Yes	20	9	29
Jackson	22.4	196.9	Yes	Yes	46	7	53
Kant	-11.0	20.0	-	Yes	46	3	49
Keeler	-10.2	161.9	Yes	-	22	16	38
King	5.0	120.5	No	Yes	36	8	44
Langmuir	-35.7	231.6	Yes	-	33	9	42
O'Day	-31.0	157.0	-	Yes	31	7	38
Inner Rook N.[a]	-10.0	264.0	-	Yes	-	-	-
Inner Rook m.[b]	-21.0	274.0	-	Yes	-	-	-
Petavius	-25.0	60.4	-	Yes	12	19	31
Pythagoras	64.0	297.0	-	Yes	21	13	34
Schrödinger	-73.0	138.0	-	Yes	-	-	-
Theophilus	-11.4	26.4	Yes	-	14	11	25
Tsiolkovsky	-21.2	128.9	Yes	Yes	17	19	36
Tycho	-43.4	348.9	Yes	Yes	21	10	31
Vavilov	-0.8	222.1	Yes	Yes	49	10	58

[a] Inner Rook N. stands for Orientale Inner Rook North
[b] Inner Rook m. stands for Orientale Inner Rook massif

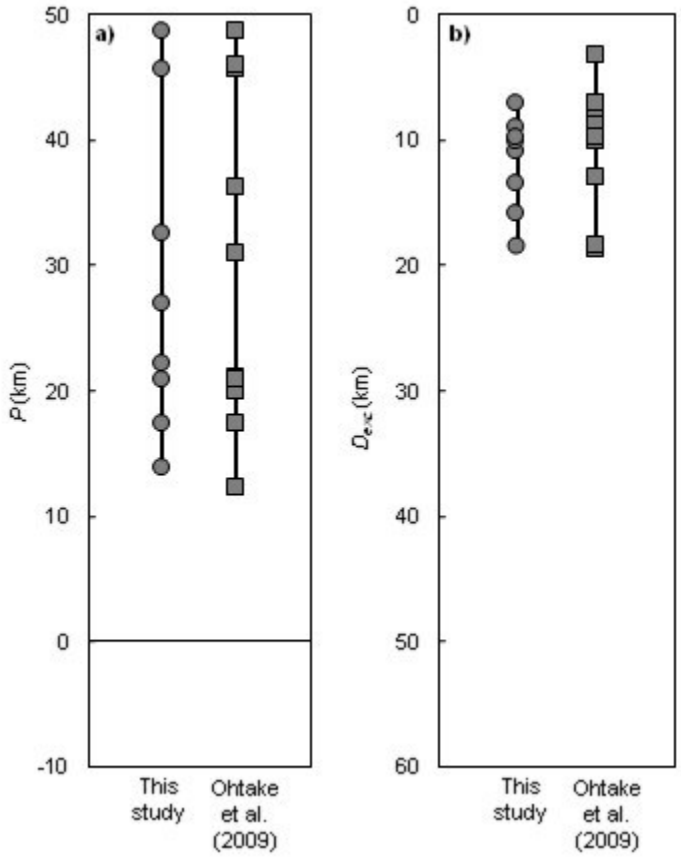

Figure 2.12. Central peaks in which purest anorthosite was detected by this study and by *Ohtake et al*. [2009], a) relative to their proximity (*P*) to the crust/mantle boundary, and b) relative to the current lunar surface ($D_{exc} = 0$) using the depth of origin of the material exposed by the central peak (D_{exc}).

2.4.2 The Mafic Mineral Assemblages of Central Peaks

For the majority of the craters we analyze, orthopyroxene is the most abundant mafic mineral, followed by clinopyroxene, and olivine (Fig. 2.13, Table 2.1). This is especially the case for craters in SPA and in the PKT. The FHT is more diverse in mafic character, as shown by the scatter of data in figures 2.13 and 2.14.

There are two craters with central peaks having mafic assemblages dominated by olivine: Keeler and Copernicus. Keeler (FHT) has 67 % olivine relative to the total abundance of mafics (Figs. 2.13- 2.15), though it only contains on average 5 wt% mafics (3 wt% olivine, 1 wt% orthopyroxene, and 1 wt% clinopyroxene). As shown in figure 2.6a, for a mixture of 95 wt%

plagioclase and 3 mafic minerals, the error is 2 wt% on olivine, and 3 wt% on both pyroxenes. Therefore, olivine might not be the dominant mafic constituent in Keeler. Copernicus (PKT) also has much more olivine/mafics (73 %) than the other craters (Figs. 2.13-2.15), and contains on average 16 wt% mafics (11 wt% olivine, 1 wt% orthopyroxene, and 4 wt% clinopyroxene). Von Karman, the only crater having excavated mantle material based on our estimates (~4 km below the crust/mantle boundary), has similar abundance of mafic mineral as the craters having excavated crustal material. Its mafic assemblage is dominated by orthopyroxene (orthopyroxene/mafics 56 %), and lesser amounts of clinopyroxene (clinopyroxene/mafics 34 %), and olivine (olivine/mafics 11 %). Overall, we do not find any significant correlation between the mafic mineral assemblages and the proximity to the crust/mantle boundary. Therefore, we conclude that orthopyroxene is the dominant mafic mineral through the entire crustal column, followed by clinopyroxene and olivine (Copernicus being the exception), and we conclude that the FHT is more diverse in mafic minerals than SPA and the PKT.

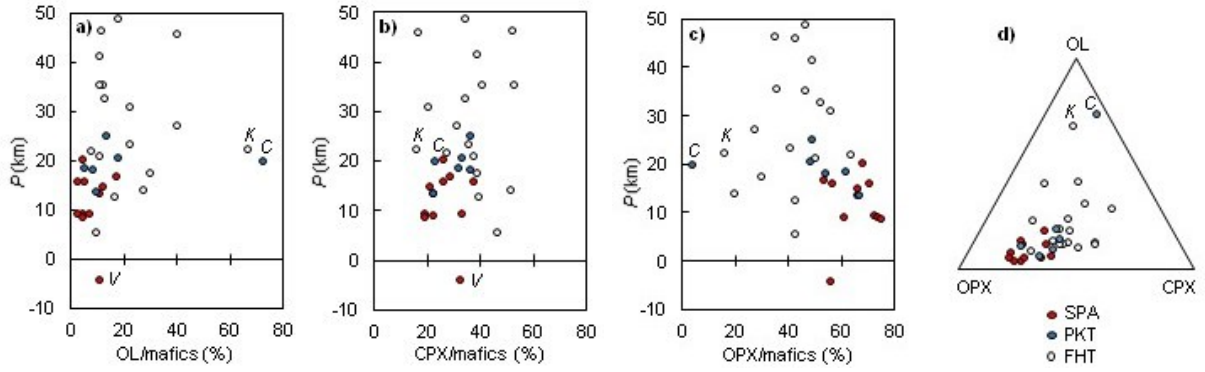

Figure 2.13. Average abundance of (a) olivine/mafics, (b) clinopyroxene/mafics, (c) orthopyroxene/mafics versus the promitity to the crust/mantle boundar parameter (*P*) for the 34 central peaks analyzed (*K*=Keeler, *C*=Copernicus, *V*=Von Karman), and (d) ternary diagram showing the relative average abundance of each mafic mineral in these craters. The craters from South Pole Aitken basin are shown in red, from the Procellarum KREEP Terrane in blue, and from the Feldspathic Highlands Terrane in white.

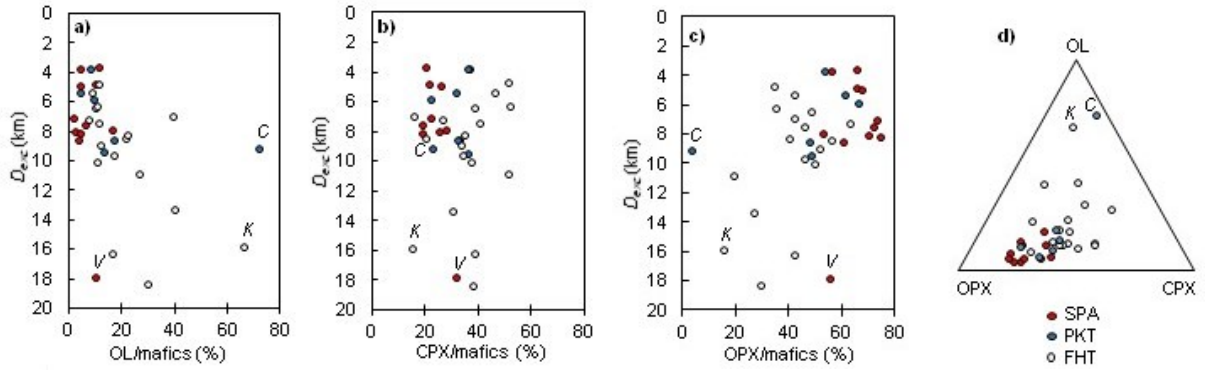

Figure 2.14. Average abundance of (a) olivine/mafics, (b) clinopyroxene/mafics, (c) orthopyroxene/mafics versus the depth of excavation (D_{exc}) for the 34 central peaks analyzed (*K*=Keeler, *C*=Copernicus, *V*=Von Karman), and (d) ternary diagram showing the relative average abundance of each mafic mineral in these craters. The craters from South Pole Aitken basin are shown in red, from the Procellarum KREEP Terrane in blue, and from the Feldspathic Highlands Terrane in white.

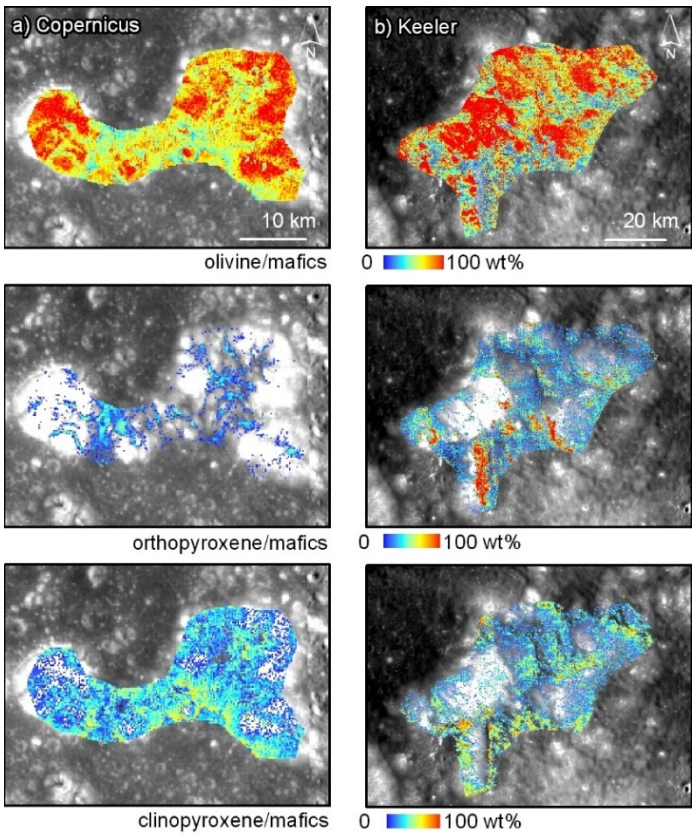

Figure 2.15. Map of olivine, orthopyroxene, and clinopyroxene abundance over the total abundance of mafic minerals for (a) Copernicus and (b) Keeler.

2.5. Discussion

Our results suggest that the lunar crust does not become more mafic with depth. When the central peaks from all terranes are treated together, we measure a correlation (r) of 0.56 between the average abundance of plagioclase of each central peak and their proximity to the crust/mantle boundary, and a correlation (r) of 0.43 between the average abundance of plagioclase of each central peak and their depth of origin relative to the current lunar surface. These weak correlations are due to the systematically more mafic character of the central peaks we analyze in SPA (42 to 76 wt% plagioclase) and the PKT (54 to 85 wt% plagioclase) that on average are closer to the crust-mantle boundary compared to the central peaks in the FHT (71 to 95 wt% plagioclase). When the three terranes are treated separately, the correlation coefficients are even lower. Within the FHT, the central peaks span the entire crustal column and do not show a correlation with either proximity to the mantle ($r = 0.27$) or depth of origin ($r = 0.57$). Moreover, we have computed the p-value for these correlations (H_0 = there is a decrease in plagioclase content with increasing depth in the crust) and found that none of them are statistically significant within a 95 % confidence interval. This leads us to reject the null hypothesis (H_0) and therefore we conclude that the lunar crust does not become more mafic with depth. We find small exposures (a few pixels) of PAN in only eight of the 34 central peaks we analyze. The low abundance and the low occurrence of PAN we measure relative to other lithologies seems to rule out PAN as the dominant rock type in the crust. These few exposures, and those of *Ohtake et al*. [2009], are found throughout the crustal column, confined to the FHT, which suggests that the PAN does not occur as a middle crustal layer, but rather as small regional occurrences. These observations stand in stark contrast to the utter dominance of PAN in the inner Rook ring of Orientale basin [*Cheek et al*., 2013], which shows that the distribution of anorthosite is highly variable.

Most of the central peaks we analyze in the FHT have an average composition that is more mafic than anorthosite as defined by *Stöffler et al*. [1980]. Only two central peaks, in Aitken and Keeler craters, have an average composition within the anorthosite field, whereas the other 15 central peaks contain on average >10 wt% of a mafic component, and show variability in their abundance of mafic over total abundance of mafic minerals. From our analysis, the crust in the FHT is composed entirely of material with the composition of the "anorthositic gabbro" layer suggested by *Ryder and Wood* [1977], containing noritic and gabbroic anorthosites,

anorthosites, and occasionally PAN. This composition is consistent with either a mafic anorthosite crust [*Warren*, 1985] or mafic intrusions into a plagioclase matrix [*Cahill et al*., 2009]. Recent studies of lunar meteorites suggest that the latter might be a more plausible scenario [*Gross et al*., 2014; *Nagaoka et al*., 2014]. Indeed, *Gross et al*. [2014] found that lunar anorthosites are more similar (chemically and in mineralogical abundance) to terrestrial massif anorthosites than to anorthosites predicted in a lunar magma ocean. They suggest that the lunar crust included more complex crustal processes such as "massif-like" anorthosite bodies. Similarly, *Nagaoka et al*. [2014] found a large chemical variation in Mg number (nearly 60 to more than 80) of each mafic mineral coexisting in PAN clasts in feldspathic lunar meteorites and in Apollo samples, implying that the PAN underwent complex formation processes and were most likely not derived from simple flotation of plagioclase on top of a magma ocean. Therefore, we support the suggestion of *Cahill et al*. [2009] that the magma ocean produced a more or less mafic anorthosite crust and that subsequent mafic intrusions have been emplaced into it.

The central peaks in SPA and the PKT have a distinct character compared to the central peaks in the FHT. Even at the same depth within the crust, measured from the surface or the crust mantle boundary, most of the central peaks in SPA and in the PKT are more noritic than the central peaks in the FHT and contain less olivine in their mafic assemblage (Fig. 2.13). Most of the central peaks in SPA have a gabbroic norite composition, and few have an anorthositic norite composition. The central peaks in the PKT have a more variable composition, ranging between gabbroic norite to gabbroic anorthosite, and contain less abundant mafic minerals than the central peaks in SPA. The central peak of Copernicus (PKT) and Keeler (FHT) are distinct outliers with olivine dominating their mafic mineral assemblage (Table 2.1, Figs. 2.13-2.15). Given the recent crustal thickness estimates from GRAIL [*Wieczorek et al*., 2013], impact crater modeling [*Melosh et al*., 2013], and melt sheet formation and evolution in large basins [*Vaughan et al*., 2013], we suggest that the central peaks in SPA and in the PKT are composed of a mixture of crustal material and an olivine-poor mantle component. Central peaks of craters that may sample possible melt bodies associated with large lunar basins (such as Orientale, SPA, mare Imbrium, or mare Serenitatis) might also have excavated material from large-scale igneous differentiation of the melt sheet created following the impact that created the basins [*Vaughan et al*., 2013], although this idea is disputed by *Spudis et al*. [2014]. Also, recent crustal thickness estimates and impact crater modeling support the hypothesis that some lunar basins might have excavated

mantle material. The analysis of GRAIL data has shown that the crust is thinner (between 34-45 km, *Wieczorek et al*. [2013]) than previously thought, supporting the fact that basins such as Serenitatis and Imbrium could have excavated mantle material [*Miljkovic et al*., 2014] rather than lower crustal material, as proposed by *Ryder and Wood* [1977].

Using high spatial resolution imagery, recent studies have potentially identified the presence of impact melt on some central peaks and have suggested that it might modify the "pristine" character of the central peak, which would in turn have an impact on the interpretation of the lunar composition with depth [*Dhingra and Pieters*, 2012; *Kuriyama et al*., 2012; *Dhingra, D. et al*., 2014; *Dhingra, R.D. et al*., 2014]. Impact melt has likely been identified, in increased proportion of the melt area over the total central peak area, on the central peak of Tycho (1.5 %), Aristillus (1.8 %), Copernicus (2.4 %), and Jackson (6.8 %) [*Dhingra, R.D. et al*., 2014]. However, since the proportion of impact melt is small for these craters, and perhaps smaller or even absent [*e.g*., Theophilus, *Dhingra, R.D. et al.,* 2014] for the rest of the craters we analyze, it does not have a significant impact on the average central peak compositions reported here.

2.6. Conclusion

Topographically corrected and high-resolution data from the Multiband Imager coupled with Hapke radiative transfer model have been used to measure the mineral abundances from 34 crater central peaks located within 50º latitude of the equator, with examples in all three lunar terranes: the Feldspathic Highlands Terrane (FHT), the Procellarum KREEP terrane (PKT) and the South Pole-Aitken basin terrane (SPAT). Modeled crustal thickness from GRAIL [*Wieczorek et al*., 2013] and depth of excavation estimates [*Melosh*, 1989] have been used to derive the proximity to the crust/mantle boundary of the material excavated by these central peaks. We find that there is no statistically significant increase in mafic mineral abundances with proximity to the crust/mantle boundary, or with depth from the current lunar surface, and therefore that the crust does not become more mafic with depth. What little correlation exists is due to the systematically closer crust/mantle boundary location and more mafic character of the central peaks in SPAT and in the PKT compared to the central peaks in the FHT. Indeed, craters from the FHT span the entire crustal column and do not become more mafic with depth. We find exposures of purest anorthosites (PAN) largely consistent with the analysis of *Ohtake et al*.

[2009], but also find that PAN is a minority constituent and there is no clear evidence of a distinct PAN-rich layer. The average composition of the central peaks we analyze (except Aitken and Keeler) is more mafic than anorthosites (central peaks have on average <90 wt% plagioclase). Our results show that orthopyroxene is the dominant mafic component throughout the entire crustal column, followed by lesser amount of clinopyroxene, and olivine. Olivine is the dominant mafic component only in the central peak of Copernicus (PKT). Because of the scarcity of extremely anorthositic lithologies, we suggest that the FHT is a remnant of a primary crust that was a relatively mafic anorthosite, as suggested by *Warren* [1985]. The variability of the mafic assemblage in the FHT relative to the other terranes suggests that at least some of the central peaks in the FHT may be sampling subsequent intrusion of mafic material into that crust, though no ultramafic material was detected that might suggest fully differentiated plutons. The PKT and SPAT impact events probably incorporated an orthopyroxene-rich and olivine-poor mantle component in their melts. Central peaks in SPAT and in some regions of the PKT might also expose material derived from the differentiation of large-scale melt sheets associated with basin formation events.

CHAPTER 3

MINERALOGY AND CONSTRAINTS ON THE DEPTH OF ORIGIN OF IMPACT BASIN RINGS USING THE KAGUYA MULTIBAND IMAGER: REASSESSMENT OF THE COMPOSITIONAL STRUCTURE OF THE LUNAR CRUST

In Preparation for publication as: Lemelin, M., P. G. Lucey, K. Miljković, L. R. Gaddis, M. Ohtake (2016), Mineralogy and constraints on the depth of origin of impact basin rings using the Kaguya Multiband Imager: Reassessment of the compositional structure of the lunar crust.

Abstract—The rings of impact basins expose material originating from various depths within the lunar crust, and can therefore be used to study its composition with depth. However, the depth of origin of the material exposed is not well constrained. In this study, we conduct a quantitative and thorough analysis of the mineralogical composition of the innermost ring of 13 lunar impact basins, and use iSALE-2D hydrocode model to place constraints on the depth of origin of the material exposed by the innermost ring. We find that the most abundant rock type on the innermost ring of most basins is anorthosite, with Orientale having the highest proportion of nearly pure anorthosite. Impact modeling suggests that the basins' innermost ring expose material originating from two mean depths: a shallow component from $0.06D_{tr,}$ and a deep component from $0.16D_{tr}$ (where D_{tr} is the transient crater diameter). The deep component originates from the mantle in 10 of the basins we study, but the shallow component largely dominates the ring material. We find that average abundance of high-calcium pyroxene over the total abundance of mafic minerals generally increases with the proportion of crustal material exposed on the innermost ring, and the average abundance of olivine over the total abundance of mafic minerals decreases with the proportion of mantle material, suggesting a crustal origin for these constituents. The average abundance of low-calcium pyroxene generally increases with the proportion of mantle material, suggesting a mantle origin.

3.1. Introduction

Impact features such as complex craters and impact basins excavate material from various depths in the lunar crust and expose it on their central peak and peak rings. As these impact features are found at all longitudes and latitudes across the Moon, central peak and peak rings can be used to better understand the composition of the lunar crust at a wide range of depths across the Moon.

The mineralogy of central peaks has been extensively studied using a variety of instruments and techniques of increasing spatial and spectral resolution [*e.g.*, *Pieters*, 1982; *Pieters*, 1986; *Tompkins and Pieters*, 1999; *Cahill et al*., 2009; *Ohtake et al*. 2009; *Song et al*., 2013; *Donaldson Hanna et al*., 2014; *Lemelin et al*., 2015]. Most studies suggest that the central peaks found in the Feldspathic Highlands Terrane (FHT) are dominated by anorthosite, and anorthositic lithologies, whereas the central peaks found in the Procellarum KREEP Terrane (PKT) and in the South Pole-Aitken (SPA) Terrane are more compositionally diverse, and are composed of anorthositic, noritic and gabbro-noritic lithologies.

Most studies related to the mineralogy of lunar impact basins conducted global surveys and found exposures spectrally dominated by plagioclase, low-calcium pyroxene, or olivine [*Hawke et al.*, 1991; 2003; *Nakamura et al*. 2012; *Yamamoto et al*., 2010; 2012; *Cheek et al.*, 2013; *Donaldson Hanna et al*., 2014]. *Hawke et al.* [2003] reported that major portions of the inner rings of Grimaldi, Humorum, Crisium, Orientale [*Spudis et al*. 1984; *Hawke et al.*, 1991; 2003], and Nectaris are composed of exposures spectrally dominated by plagioclase. *Yamamoto et al*. [2012] identified such spectra in and around 18 impact basins, and *Donaldson Hanna et al*. [2014] in craters in association with the inner and sometimes outer rings of 17 impact basins. *Cheek et al*. [2013] provided the first extensive survey of plagioclase abundance in an impact basin, Orientale, which revealed the utter dominance of nearly pure anorthosite in the inner rook ring (the innermost ring). In other studies, exposures spectrally dominated by low-calcium pyroxene or olivine were identified in concentric regions around impact basins, suggesting potential excavation of mantle material [*e.g.*, *Nakamura et al*. 2012; *Yamamoto et al*., 2010]. Of the basin studies, only *Cheek et al*. [2013] quantified the abundance of the mineral present.

The widespread abundance of nearly pure anorthosite (likely containing <5 wt.% mafic minerals) on the innermost ring of many impact basins, stands in contrast with the more mafic average composition (on average 5-38 wt.% mafic minerals) of central peaks of the FHT

[*Lemelin et al.,* 2015]. A potential explanation for this difference might be that impact craters and impact basins expose material originating from different depths into the crust, and therefore reveal different aspects of the crustal stratigraphy. To confirm this hypothesis, better constraints have to be placed on the depth of origin of the material exposed by the basins' innermost ring. Indeed, while the depth of origin of the material exposed by central peaks is well accepted (~0.10D_{tr}, where D_{tr} is the transient crater diameter, *Melosh* [1989]), the depth of origin of the material exposed by basin rings is not. Some estimates range from about <0.03 D_{tr} [*Sharpton*, 2014] to ~0.10 D_{tr} [*Baker and Head,* 2015]. Another potential hypothesis is that while the basins' innermost ring contain abundant exposures of nearly pure anorthosite, the rings also contain more mafic exposures, and thus have an average composition corresponding to anorthositic lithologies, similar to central peaks. To confirm this hypothesis, all immature exposures (*i.e*., that have not been extensively influenced by space weathering) on the basins' innermost ring have to be studied, as done by *Cheek et al.* [2013] for Orientale. Indeed, while pure anorthosites have been reported in association with many basin rings, only at Orientale is it known that anorthosites are the dominant rock type on the innermost ring.

In this study, we (1) conduct a quantitative and comprehensive analysis of the mineralogical composition of the innermost ring of 13 lunar impact basins, (2) place constraints on the depth of origin of the material exposed by the basins' innermost ring, using hydrocode modeling, and (3) compare the composition of the basins' innermost ring to the composition of central peaks studies by *Lemelin et al*. [2015] and others. We analyze the composition of the innermost rings (rather than other rings) in order to compare our results to results from previous studies [*e.g*., *Hawke et al*., 2003; *Cheek et al*., 2013], and focus our analysis on the 13 basins where exposures spectrally dominated by olivine and/or plagioclase have been reported [e.g., *Yamamoto et al*., 2010; 2012].

3.2. Background

3.2.1 Mineralogical composition of central peaks

Beginning with *Pieters* [1982; 1986], remote sensing studies have used central peaks as probes into the lunar surface [*e.g.*, *Tompkins and Pieters*, 1999; *Wieczorek and Zuber*, 2001; *Cahill et al*., 2009; *Ohtake et al*., 2009; *Song et al*., 2013; *Donaldson Hanna et al*., 2014;

Lemelin et al., 2015]. In the first global analysis, *Tompkins and Pieters* [1999] used Clementine data and spectral parameters to estimate the composition of 109 central peaks. They found that the central peaks in the highland craters basins (which they characterized as coming from the upper crust) are mainly composed of anorthosites, whereas the central peaks within major basins (which they characterized as coming from the upper crust) are composed of somewhat more mafic anorthosites. They also found that central peaks within major basins are more compositionally diverse than the other central peaks, consistent with the results of *Pieters* [1986].

Wieczorek and Zuber [2001] refined the depth of origin of the 109 central peaks studied by *Tompkins and Pieters* [1999] using a geophysically derived dual-layered crustal thickness model. Using the mineral abundance estimates of *Tompkins and Pieters* [1999], they found that the upper crust (91 central peaks) contains nearly pure anorthosite, and anorthositic lithologies, and the lower crust (18 central peaks) is composed of norites and gabbro-norites. These 18 more mafic central peaks were confined to the Procellarum KREEP Terrane (PKT) and the South Pole-Aitken basin (SPA).

Cahill et al. [2009] built upon the previous work by using radiative transfer modeling and Clementine UVVIS/NIR data to quantify the composition of 55 central peaks, and by defining a new concept for the depth of origin of central peaks relative to the crust-mantle boundary (the pre-impact crustal thickness minus the depth of origin of the material exposed by central peaks) rather than from the top of the crust which has been intensively reworked. They found central peaks with anorthositic mineralogy throughout the crustal column, and mostly confined to the FHT.

Lemelin et al. [2015] used a quantitative radiative transfer approach similar to that of *Cahill et al.* [2009], with the better calibrated Kaguya Multiband Imager UVVIS/NIR data to estimate the composition of 34 central peaks. They also calculated the depth of origin of central peaks relative to the crust-mantle boundary using crustal thickness model from the Gravity Recovery And Interior Laboratory (GRAIL) instrument. They found that central peaks with anorthositic mineralogy are mostly confined to the FHT, whereas the central peaks from the PKT and SPA are composed of anorthositic mineralogy and norites or gabbros. They identified low-calcium pyroxene as the dominant mafic component in these peaks, followed by lesser amounts of high-calcium pyroxene, and olivine.

Other studies focused their search on the detection of exposures spectrally dominated by plagioclase (purest anorthosite, or PAN), or high-calcium pyroxene [*Ohtake et al*., 2009; *Donaldson Hanna et al*., 2014; *Yamamoto et al*., 2015]. *Ohtake et al*. [2009] identified PAN in 13 central peaks as well as 16 wall exposures and 10 ejecta deposits, and proposed that either a global layer of PAN exists within the upper crust (from 3 km to 30 km in depth), or that PAN exists as large patches within the upper crust. *Donaldson Hanna et al*. [2014] also detected PAN in many central peaks where the crust is 9-63 km thick. *Lemelin et al.* [2015] identified exposures with ≥98 wt% plagioclase (also spectrally dominated by plagioclase) in 8 of the 17 central peaks they studied in the FHT, 14 to 49 km away from the crust/mantle boundary, consistent with other studies. These exposures were limited to only very few pixels. *Yamamoto et al*. [2015] found exposures dominated by high-calcium pyroxene on the ejecta, rim and floor of complex craters, which originates from shallower depth than the material exposed by the central peaks, and concluded that a layer rich in high-calcium pyroxene might be present above a layer of pure anorthosite.

3.2.2 Mineralogical composition of basins

3.2.2.1 Exposures spectrally dominated by plagioclase

Many remote sensing studies of impact basin composition have focused their search on identifying exposures spectrally dominated by plagioclase [*Spudis et al*. 1984; *Hawke et al.*, 1991; 2003, *Yamamoto et al*., 2012; *Cheek et al*., 2013; *Donaldson Hanna et al.,* 2014]. Using telescopic near-infrared spectra, *Spudis et al*. [1984] and *Hawke et al.* [1991] identified exposures spectrally dominated by plagioclase (often referred to as "pure anothosite") on the rings of Orientale, and *Hawke et al.* [2003] reported that major portions of the inner rings of Grimaldi, Humorum, Crisium, Orientale, and Nectaris are also composed of such exposures.

Yamamoto et al. [2012] searched through the ~70 million near-infrared reflectance spectra acquired by the Kaguya Spectral Profiler to identify spectra dominated by plagioclase (characteristic absorption band minimum between 1.20 and 1.35 μm). They identified 564 such spectra, with most of these located in and around the following basins: Australe, Birkhoff, Coulomb-Sarton, Crisium, Dirichlet-Jackson, Freundlich-Sharonov, Hertzsprung,

Humboldtianum, Humorum, Korolev, Lorentz, Mendeleev, Mendel-Rydberg, Moscoviense, Nectaris, Orientale, Schiller-Zucchius, and Serenitatis (Fig. 3.1).

Similarly, *Donaldson Hanna et al.* [2014] looked through Chandrayaan-1 Moon Mineralogy Mapper near-infrared reflectance data to identify spectra dominated by plagioclase based on the integrated band depth of the 1.25 μm absorption band. They identified plagioclase-rich spectra in craters in association with the inner and sometimes outer rings of large impact basins such as Crisium, Hertzsprung, Humboldtianum, Humorum, Imbrium, Mendel-Rydberg, Nectaris, Orientale, Schrödinger, Serenitatis, Smythii, and South Pole-Aitken basin. They also identified exposures spectrally dominated by plagioclase in association with smaller basins such as Birkhoff, Freundlich-Sharonov, Korolev, Lorentz, and Mendeleev basin.

Unlike previous studies, *Cheek et al.* [2013] conducted an extensive and quantitative regional mineral survey of an impact basin. Focussing on the rings of Orientale basin because of the anorthosite detected [*Spudis et al*., 1984; *Hawke et al*., 1991; *Hawke et al*., 2003], they identified all the spectra with strong absorption features in the non-mare material of Orientale, using data from the Moon Mineralogy Mapper near-infrared spectrometer, and classified them in terms of plagioclase abundances (Class A: 99-100 vol%, Class B: 96-98 vol%, and Class C: ≤95 vol%), based their relative plagioclase and pyroxene absorption band depths near 1.25 μm and 1 μm respectively. In Class A the plagioclase absorption band dominates, in Class B the plagioclase and pyroxene absorption bands are approximately equal in strength, and in Class C the pyroxene absorption band dominates. They found that crystalline anorthosite with >95 vol% plagioclase (Class A and B) is concentrated in the inner most ring of Orientale, with most of the pixels likely contain up to 99-100 vol% plagioclase (Class A).

3.2.2.2 Exposures spectrally dominated by low-calcium pyroxene

Nakamura et al. [2012] also used Kaguya Spectral Profiler data to identify low-calcium pyroxene-dominated spectra (where the band minimum in continuum removed reflectance data is found at a shorter wavelength than 0.925 μm), as the lunar upper mantle would be predominantly composed of low-calcium pyroxene if the lunar magma ocean experienced significant fractional crystallization before the beginning of plagioclase floatation. They found high concentrations of low-calcium pyroxene around SPA, Imbrium and the potential Procellarum basins. *Lucey et al.* [2014] used Kaguya Spectral Profiler and radiative transfer modeling to identify the composition

of the mega-regolith, via the study of 4506 small (<1 km diameter) immature craters. They found noritic anorthosites containing exclusively very low calcium pyroxene within the Feldspathic Highlands Terrane, which suggests that large impact basin events excavated low calcium pyroxene from the mantle and redistributed it through the mega-regolith.

3.2.2.3 Exposures spectrally dominated by olivine

Yamamoto et al. [2010] also searched through the ~70 million reflectance spectra acquired by the Kaguya Spectral Profiler to identify olivine-dominated spectra (*i.e*., spectra that have an absorption minima at 1.050 ±0.030 μm, and absorption bands at 0.85 and 1.25 μm), as olivine is a candidate constituent of the lunar mantle. They identified only 245 olivine-dominated spectra, which they grouped into 34 olivine-rich sites that are mostly located on the nearside, in concentric regions around the following lunar impact basins: Australe, Crisium, Humboldtianum, Humorum, Imbrium, Moscoviense, Nectaris, Schrödinger, and Sereninatis (Figure 3.1). They suggest that these large impact events excavated mantle material or magnesium-rich plutons in the lower crust.

3.2.3 Impact basin formation and excavation depth

While the depth of origin of the material exposed by central peaks is well accepted, there is no consensus regarding the depth of origin of the material exposed by basin rings and thus, it is actually difficult to compare the composition of central peaks and basin rings with respect to their depth of origin. Here we review the main hypotheses describing the ring formation and their potential depth of origin.

Lunar impact basins can be divided in two categories based on their morphology and ring formation process: the peak ring basins (~150-300 km in diameter) and the multi-ring basins (>~300 km in diameter). Peak ring basins (*e.g*., Shrödinger) have a single ring located within their main topographic rim, and multi-ring basins (*e.g.,* Orientale) have multiple ring-like features which can be found within and/or beyond the main topographic rim [*Spudis*, 1993]. In this study we use the term “innermost ring” to refer to both the peak ring in peak-ring basins, and the innermost ring in multi-ring basins. There are several hypotheses (or models) describing the innermost ring formation in multi-ring basins [*e.g.*, *Baldwin*, 1972; *Hodges and Wilhelms*, 1978; *Melosh and McKinnon*, 1978; *Head*, 2010]. Recent modeling of the Orientale impact event by

Johnson et al. [2015] suggests that the innermost ring formed by gravitational collapse of the central uplift during the crater formation process, as in peak ring basins, followed by an inward collapse.

As our understanding of the formation of basin rings is still evolving, there is no well accepted relationship that can be used to derive the depth of origin of the material exposed on the basins' innermost ring. Current estimates range from about $\leq 0.03D_{tr}$ [*Sharpton*, 2014] to $0.10D_{tr}$ [*Baker and Head*, 2015], where D_{tr} is the transient crater diameter which equals the diameter of the excavation cavity [*Grieve et al*., 1981]. *Sharpton* [2014] measured the volume of ejecta deposits near lunar crater rims using high resolution images from the Narrow Angle Camera (NAC) onboard the Lunar Reconnaissance Orbiter, NAC stereo Digital Terrain Model (DTM), and subsets of the Global Lunar DTM 100 m topographic model. He found that the ejecta is ~3–4 times thinner than previously thought, and so should be the volume of material ejected, and the depth of excavation. *Baker and Head* [2015] analyzed the mineralogy of the peak ring in 10 peak ring basins using Moon Mineralogy Mapper near-infrared reflectance data and spectral parameters following those of *Cheek et al.* [2013]. As they did not observe strong evidence of (ultramafic) mantle material being exposed in these rings, they concluded that peak ring material originates from the crust, near (or shallower than) the maximum depth of excavation of 0.10-0.15*D* [*Melosh*, 1989]. Thus, as the depth of origin of the material exposed by basin rings varies widely according to different studies, we use hydrocode modeling to place constraints on the depth of origin of the material exposed by the basins' innermost ring.

3.3. Data

We use multispectral reflectance data from the Kaguya Multiband Imager for compositional analysis, as well as crustal thickness estimates from the Gravity Recovery and Interior Laboratory (GRAIL) to locate the depth of origin of the material exposed by the basins' innermost ring with respect to the crust/mantle boundary.

The Kaguya Multiband Imager acquired data in nine spectral bands (415, 750, 900, 950, 1001, 1000, 1050, 1250, 1550 nm). The instrument provides a spatial resolution of ~20 m per pixel for the first five spectral bands (415-1001 nm), and ~62 m per pixel for the last four (1000 to 1550 nm) at the nominal altitude of 100 km [*Haruyama et al*., 2008; *Ohtake et al*., 2008]. In this study we use reflectance data corrected for the shading effects of topography (MAP level

02), which reduces the error associated with topographic shading in mineral abundance estimations. In this processing level, the reflectance images have been converted to mosaics, and projected into a simple cylindrical projection. We downsampled the data in the 9 spectral bands to the same spatial resolution (~62 m per pixel), and corrected the systematic differences in reflectance between the first five spectral bands (UVVIS data) and the last four (NIR data), as they were acquired by two different sensors, using equation S1 in *Lemelin et al*. [2015].

The GRAIL crustal thickness data has a spatial resolution of 4 pixels per degree, and is expressed using spherical harmonic expansions with degrees up to 310, and a mean planetary radius of 1737.151 km. The data is available online, at the GRAIL Crustal Thickness Archive website (http://www.ipgp.fr/~wieczor/GRAILCrustalThicknessArchive/GRAILCrustalThicknessArchive.html), and details about this dataset can be found in *Wieczorek et al.* [2013].

3.4. Method

To derive the composition of the basins' innermost ring, we first compute maps of olivine, low-calcium pyroxene, high-calcium pyroxene, and plagioclase at ~62 m per pixel using reflectance data from the Kaguya Multiband Imager and Hapke's radiative transfer equations [*e.g.*, *Hapke* 1981, 1993, 2001]. We constrain our analysis to data within ±50° in latitude as the Multiband Imager data has been better calibrated within this latitude range [*Lemelin et al*., 2015]. We then define the area that corresponds to the innermost rings using the location (diameter) of the rings of *Neumann et al*. [2015] (based on GRAIL Bouguer gravity anomaly data) and the USGS geologic maps [*Fortezzo and Hare*, 2013]. We use the optical maturity parameter (OMAT) of *Lucey et al*. [2000] to identify the pixels that have been the least affected by space weathering on the ring and analyze their composition. Finally, we use iSALE-2D hydrocode model to place constraints on the depth of origin of the material exposed by the basins' innermost ring. The 13 basins we study are: Crisium, Freundlich-Sharonov, Hertzsprung, Humorum, Imbrium, Korolev, Lorentz, Mendeleev, Mendel-Rydberg, Moscoviense, Nectaris, Orientale, and Serenitatis (Fig. 3.1, Table 3.1).

3.4.1 Global map product

We determined the abundance of olivine, low-calcium pyroxene, high-calcium pyroxene and plagioclase at ~62 m per pixel using the Kaguya Multiband Imager reflectance data within

±50° in latitude and Hapke's radiative transfer equations [*e.g.*, *Hapke* 1981, 1993, 2001]. The abundance determination approach follows *Lemlin et al.* [2015]: (1) we constructed a lookup table of modeled spectra using Hapke's radiative transfer equations, (2) compared each pixel spectrum to the lookup table of spectra that contain within ±2 wt.% iron of that pixel, and (3) assigned the mineral abundance of the best spectral match to that pixel. The resulting mineral maps can be seen in Figure 3.2, as well as the equatorial map of FeO (Fig. 3.3). To avoid bias in mineral abundances in this study, we confined our analysis to the least mature surfaces on the basins' innermost ring; we analyzed only the pixels with OMAT >0.2, leaving ≥1% of the ring material for study. Thus, we also produced an equatorial map of OMAT using the Multiband Imager data (Fig. 3.3). The specifics of each step are as follows.

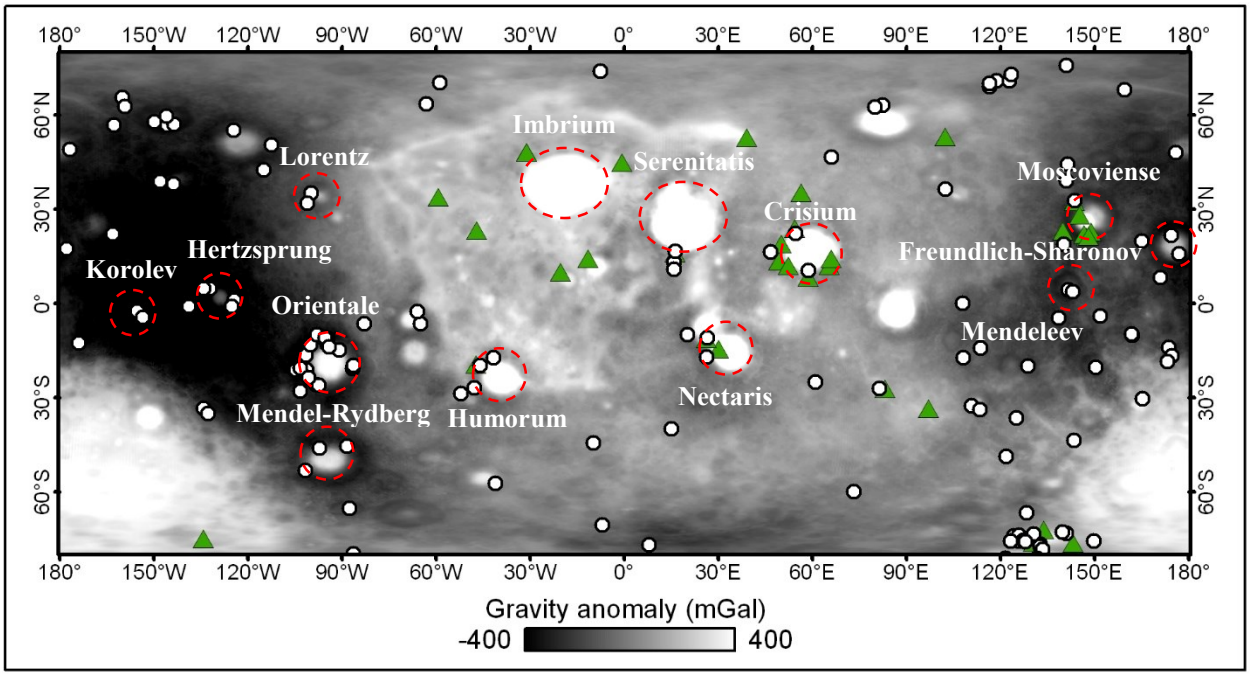

Figure 3.1. Impact basins in this study (red stars), location of the pure anorthosite detections from *Yamamoto et al.* [2012] (white circles), and location of the olivine detections from *Yamamoto et al.* [2010] (green triangles). The basemap is the GRAIL bouguer gravity anomaly.

To determine the mineral abundances, we constructed a spectral lookup table of the reflectance spectra of 6601 mixtures of olivine, low-calcium pyroxene, high-calcium pyroxene and plagioclase, at 7 amounts (0.5 to 10 wt.%) of small nanophase iron (submicroscopic iron) and large nanophase iron ("Britt-Pieters particles"), an Mg# (molar Mg/Mg+Fe) of 65

(representative of the more magnesian of the ferroan anorthosites), and a grain size of 17μm [*Pieters et al*., 1993; *Lucey*, 2006]. We constructed a second lookup table using a grain size of 200 μm for plagioclase to account for the corresponding band depth observed for purest anorthosite in the Multiband Imager data by *Ohtake et al.* [2009], for a total of 92,414 spectra. The relative abundances of the mafic minerals (olivine, low-calcium pyroxene and high-calcium pyroxene) are computed at 10% abundance intervals, representative of the typical error in mafic mineral abundances [*Lucey*, 2004], whereas the relative abundance of plagioclase to mafic minerals is computed at 1% abundance intervals, as *Cheek et al*. [2013] found that changes in plagioclase content of 1% are detectable. We used the optical constants of Lucey [1998], refined and validated using the Lunar Soil Characterization Consortium (LSCC) data by Lucey et al. [2014], to build our spectral lookup table. These optical constants yield an error of ~8 wt.% in mineral abundance estimation at the Multiband Imager wavelengths as shown by *Lucey at al*. [2014]. We also computed global maps of FeO using Multiband Imager reflectance data at 750 and 950 nm and the algorithm of *Lemelin et al.* [2015]. Then, for each pixel, we compared the model spectra that contain ±2 wt% FeO of the mapped FeO, and assigned the composition to the best spectral match, in terms of correlation and absolute difference in continuum removed reflectance.

In this study, we confined our analysis to the least mature surfaces on the basins' innermost ring. We produced an equatorial map of the optical maturity parameter (OMAT) using Multiband Imager reflectance data and the algorithm of *Lucey et al.* [2000] (Fig. 3.3). Since the OMAT algorithm has been derived using reflectance data from Clementine, which has been calibrated differently than Multiband Imager data, the algorithm cannot be directly used with Multiband Imager data. To use the OMAT algorithm, we scaled the Multiband Imager dataset to Clementine. We first computed the regression coefficients to be applied to the Multiband Imager data at 750 (*r750*) and 950 (*r950*) nm in order to match the reflectance of Clementine at these bands ($r750_{corr}$, $r950_{corr}$) (Eqs. 3.1-3.2), by minimizing the difference in histograms of the global distribution of Clementine-derived OMAT and Multiband Imager-derived OMAT.

$$r750_{corr} = (r750 \cdot 1.51) + 0.020 \quad (3.1)$$

$$r950_{corr} = (r950 \cdot 1.38) + 0.022 \quad (3.2)$$

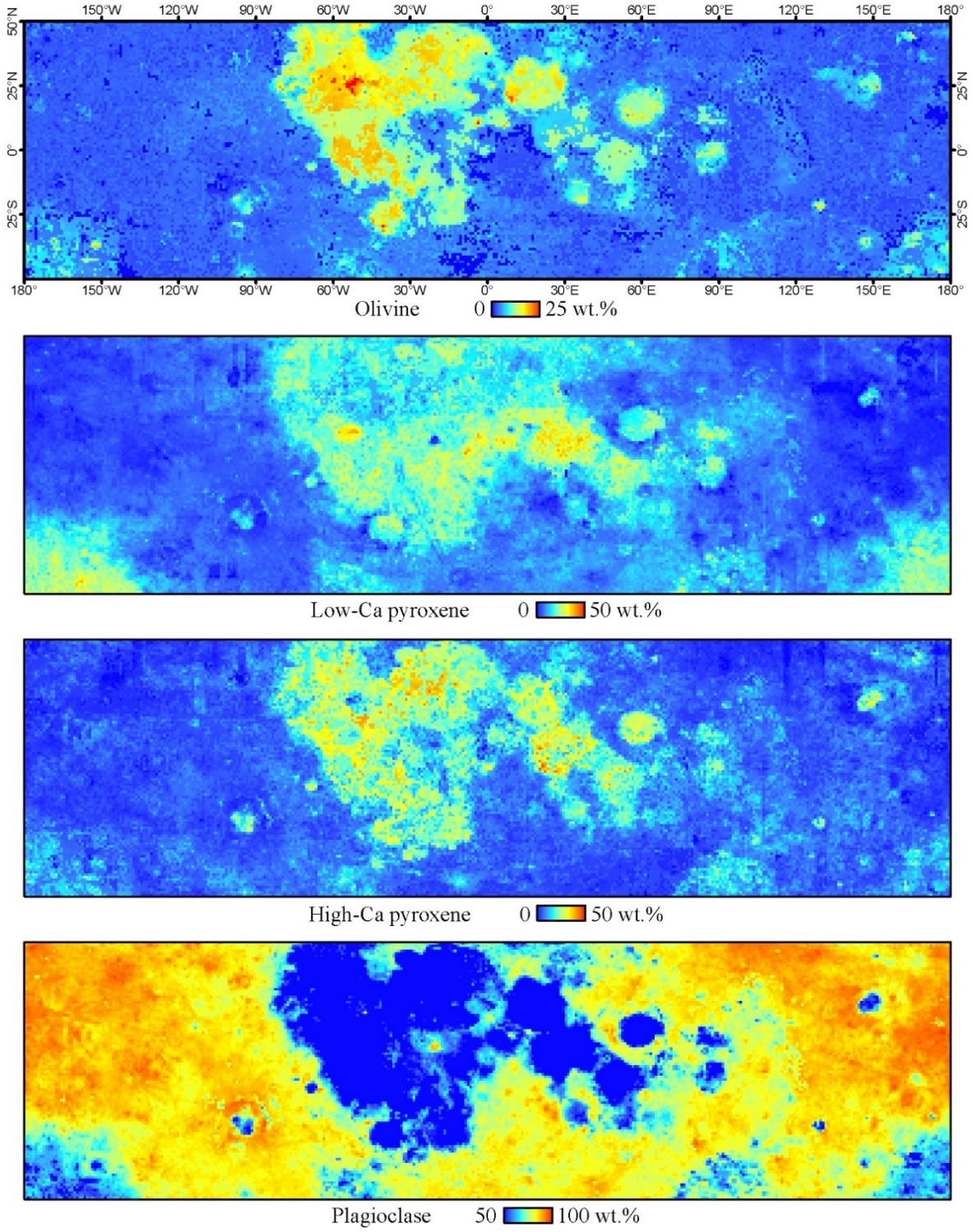

Figure 3.2. Abundance of the main lunar minerals within ±50° latitude, using the Multiband Imager reflectance data and the radiative transfer modeling method presented herein. The mineral abundances are shown here at 1 pixel per degree. Maps at 32 pixels per degree are shown in Appendix B. Maps at 512 pixels per degree were used in the basin ring analysis.

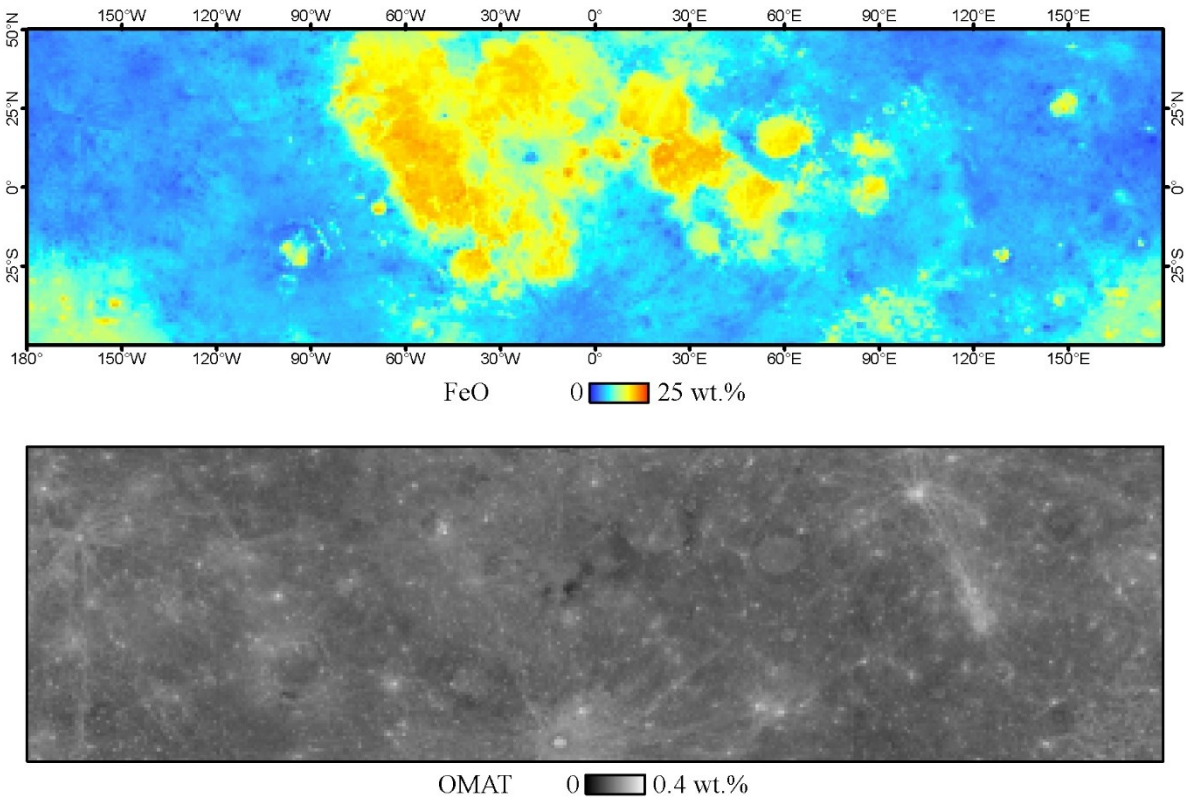

Figure 3.3. Abundance of iron (FeO) and Optical Maturity Parameter (OMAT) within ±50° latitude, derived using the Multiband Imager reflectance data. The FeO algorithm is from *Lemelin et al*. [2015]. The OMAT algorithm is from *Lucey* [2000] and uses scaled Multiband Imager reflectance data (Eqs. 3.1-3.1). The maps are shown at 1 pixel per degree. Maps at 32 pixels per degree are shown in Appendix B. Maps at 512 pixels per degree were used in the basin ring analysis.

3.4.2 Identification of the innermost ring

Identifying the innermost ring of basins poses challenge, as lunar impact basins are degraded and the assignment of location of inner rings varies according to different sources [*e.g*., *Spudis,* 1993; *Fortezzo and Hare*, 2013; *Neumann et al*., 2015]. Recently, *Neumann et al*. [2015] used GRAIL Bouguer gravity anomaly to identify and provide new and objective criterion for the location (diameter) of basins' innermost ring. They found that basins larger than ~200 km in diameter have a positive Bouguer anomaly within their innermost ring, and a negative anomaly extending outwards. The Bouguer anomaly corresponds to the gravity signature measured by GRAIL, once the contribution from topography has been removed. To define the area of the

inner most rings in this study, we used both the location (diameter) of the rings identified by *Neumann et al*. [2015] and the USGS geologic maps [*Fortezzo and Hare*, 2013]. We first use the location of the innermost ring of *Neumann et al*. [2015] to define the ring, and then we use the USGS geologic maps to define the area that corresponds to the ring material, termed "circumbasin materials" or "basin materials" in the USGS geologic maps. Two exceptions are Mendel-Rydberg and Serenitatis basins. *Neumann et al.* [2015] suggest a "probable" innermost ring diameter of 325 km for Mendel-Rydberg, but there are no "circumbasin materials" or "basin materials" identified by the USGS at that diameter, nor can we see distinct topographic features in the Lunar Orbiter Laser Altimeter (LOLA) dataset. The USGS identifies "basin massif material" collocated with distinct topographic features in the LOLA dataset at a diameter of ~420 km, which is what we use to define the polygon that corresponds to the innermost ring material of Mendel-Rydberg. *Neumann et al.* [2015] suggest a "possible" innermost ring diameter of 416 km for Serenitatis, but there is also no "circumbasin materials" or "basin materials", nor topographic feature at that location. The USGS identifies "circumbasin materials" collocated with topographic features at a diameter of ~620 km, the diameter of a ring proposed by *Spudis* [1993]. Thus, we use a diameter of 620 km for the innermost ring of Serenitatis.

3.4.3 Depth of origin of the innermost ring

There is no generally accepted rule of thumb for the depth of origin of the material exposed on the basins' innermost ring and previous estimates have not employed hydrocode modeling. Our approach is to use hydrocode to model the depth of origin of the material exposed by the innermost ring of the 13 basins we study. We then use these modeled observations to derive equations that can be used to approximate the depth of origin of the material exposed on the innermost ring of other lunar basins.

3.4.3.1 Depth of origin of the material exposed by the basins' innermost ring in this study

Hydrocode models allow computing the evolution of the lunar surface in response to impacts. In our case, we use iSALE-2D [*e.g*., *Melosh et al*., 1992; *Ivanov et al*., 1997; *Collins et al*., 2002], a multi-material, multi-rheology shock physics hydrocode based on the SALE hydrocode (Simplified Arbitrary Lagrangian Eulerian) of *Amsden et al*. [1980], to determine the origin of tracer particles from the crust, mantle and impactor that are present at the position of

the innermost ring at the end of the modeling run. It has been widely used to model the formation of lunar impact basins [*e.g.*, *Miljković et al.*, 2013; *Miljković et al.*, 2015] as it allows us to follow the displacement of the material affected by large impacts. Here we take the approach of *Miljković et al.* [2015] to model the formation of the 13 impact basins in this study; we model impacts using a dunite impactor traveling at 17 km/s and impacting vertically into the target, and observe the basin configuration two hours after the impact. A velocity of 17 km/s represents the average vertical component of the velocity vector at moderately oblique impact angles (40-70º) assuming that the mean asteroid impact speed during the basin-formation epoch was 20.9 km/s [*Miljković et al.,* 2015]. We run simulations for pre-impact crustal thickness of 30, 45, 60 and 90 km covering the current range of crustal thicknesses determined by the GRAIL mission. Important details of model impacts including depths and diameters are strongly affected by the target temperature, so "cold", "intermediate" and "hot" target temperature profiles were modeled as described in *Miljković et al.* [2015]. These parameters represent the state of the crust when most impact basins were formed [≥3.80 Ga, *Wilhelms*, 1987], based on lunar thermal evolution models of *Laneuville et al.* [2013]. A cold temperature profile and thick crust are representative of impacts occurring on the far side of the Moon, the intermediate temperature profile and crustal thickness are representative of impacts occurring on the near side of the Moon outside of the Procellarum KREEP region, and the hot temperature profile and thin crust are representative of impacts occurring in the Procellarum KREEP region [*Miljković et al.*, 2015]. We follow the material displacement using a cell size (or tracer particle size) of 1.5 by 1.5 km. In table 3.1 we report the model parameters that produced the basin configuration that are the most similar to what can be observed using GRAIL data, in terms of transient crater diameter and crustal thickness. The spatial sampling of the models (1.5 by 1.5 km per tracer particle) does not allow the direct detection of the rings, so we use the diameter of the innermost ring reported in Section 3.4.2 to locate the ring in the model output. We analyze the tracer particles located in a 10 km by 10 km bounding box centered on the location of the innermost ring (Table 3.1). We calculate the mean depth of origin of the tracers that originate from the crust and from the mantle within that bounding box, and calculate their proportion as well as the proportion of impactor material, when present. As an example, figure 3.4 shows the output of the iSALE-2D model that best represent the Orientale impact basin, two hours after the impact. Figure 3.5 shows the depth of origin of the tracer particles found at the location of Orientale's innermost ring.

Table 3.1. Input and output parameters used in iSALE-2D hydrocode model. Inputs include the impactor size, the target thermal profile, and the pre-impact crustal thickness (H). Outputs include the transient crater diameter (D_{tr}), the mean depth of origin (D_o) and the relative percentage (%) of the crustal (c), mantle (m) and impactor (i) components found in the 10 by10 km bounding box centered on the diameter of the innermost ring.

Basin	Model inputs				Model outputs					
	Impactor size	Thermal profile[a]	H (km)	Ring diameter[b] (km)	D_{tr}	D_o c (km)	D_o m (km)	% c	% m	% i
Crisium	60	Intermediate	30	505	348	18	44	73	27	0
Freundlich-Sharonov	45	Cold	45	318	314	32	52	78	16	6
Hertzsprung	45	Cold	45	256	314	32	55	84	16	0
Humorum	45	Intermediate	30	441	274	14	41	63	37	0
Imbrium	90	Hot	30	676	499	18	100	34	53	13
Korolev	30	Cold	45	206	225	32	0	96	0	4
Lorentz	30	Cold	30	173	219	26	0	97	0	3
Mendel-Rydberg	45	Cold	30	420	301	15	0	83	0	17
Mendeleev	30	Cold	45	144	225	37	0	100	0	0
Moscoviense	45	Cold	30	192	301	17	45	84	12	4
Nectaris	60	Intermediate	30	440	348	24	39	78	21	1
Orientale	60	Intermediate	30	481	348	20	39	70	30	0
Serenitatis	90	Hot	30	620	499	22	101	36	50	14

[a] See *Miljković et al*., [2013; 2015; 2016] for details on thermal profiles.
[b] See section 4.2 for identification of the innermost ring.

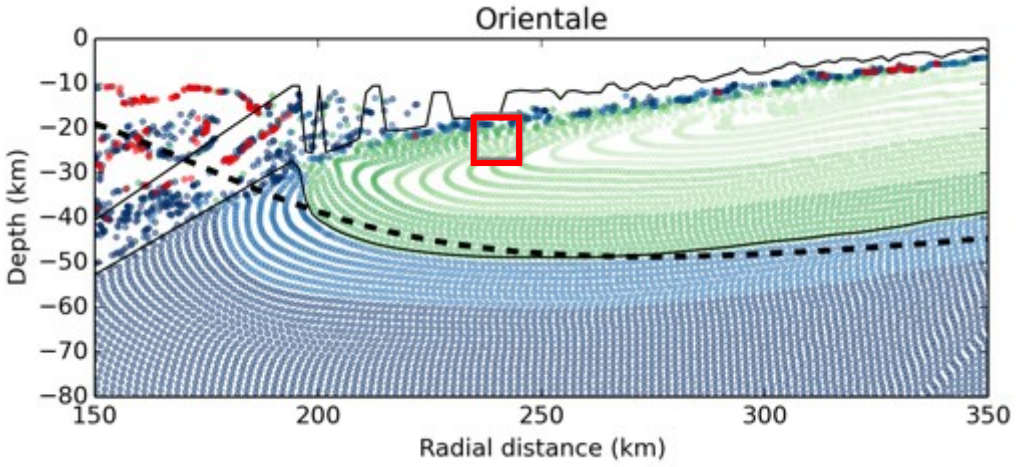

Figure 3.4. Configuration of an Orientale-like impact basin two hours after the impact, as seen by iSALE-2D. The green points represent crustal tracer particles, the blue points represent mantle tracer particles and the red points represent impactor tracer particles. The tracer particles

are originally set to 1.5 km apart. The dashed black line represent the crust/mantle boundary measured by GRAIL, and the thin black line represents the crust/mantle boundary modeled by iSALE-2D. These lines are likely to be reconciled following relaxation of the basin. The red square is a 10 by 10 km bounding box centered on the diameter of Orientale's innermost ring.

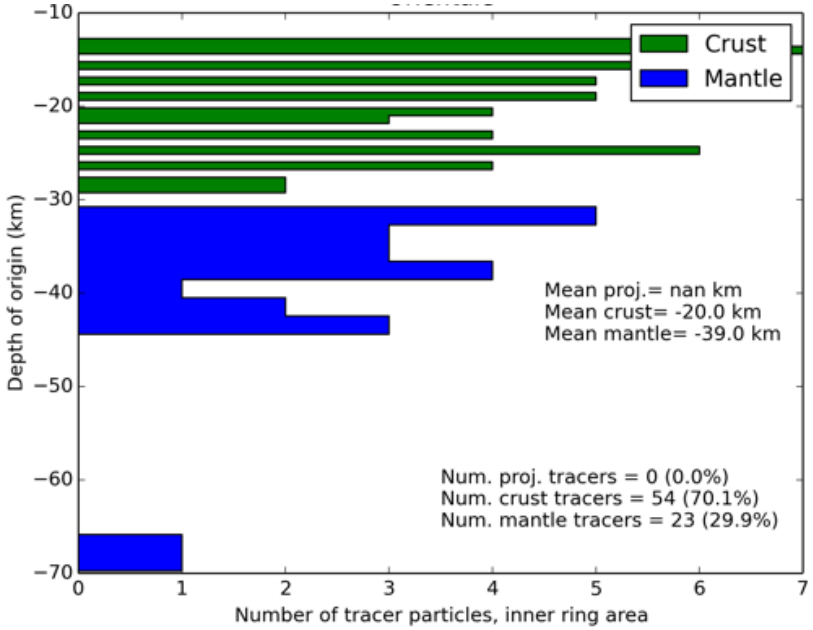

Figure 3.5. Depth of origin of the tracer particles of an Orientale-like impact basin as seen by iSALE-2D two hours after the impact. The tracer particles shown here are located in the 10 by 10 km bounding box centered at the location of Orientale's inner most ring. The tracer particles in that bounding box originate from various depth; the tracer particles originating from the crust originate on average from ~20 km deep, and the tracer particles originating from the mantle originate on average from ~39 km deep.

3.4.3.2 The general depth of origin of the material exposed by the basins' innermost ring

Our iSALE-2D simulations suggest that the innermost ring of 9 basins expose material originating from both the crust and the mantle. This allowed us to use the mean depth of origin of their crustal (shallow) and mantle (deep) components, as well as their relative proportions to derive equations that could be applied to other lunar basins (Fig. 3.6). Using these 9 basins as a guide, we find that the shallow component originates on average from $0.06\pm0.01D_{tr,}$ and that the deep component originates on average from $0.16\pm0.01D_{tr}$. These equations yield a standard error

in depth of origin of ±8 km and ±14 km respectively for the shallow and deep component. The percentage of shallow and deep component present on the innermost ring can be approximated using the transient crater diameter as -0.20±0.04D_{tr}+140 for the shallow component, and as 0.15±0.04D_{tr}-23for the dep component, with a standard error of ±10% in both cases. The equation for the percentage of deep component suggests that there is no contribution from the deep component in impacts smaller than ~150-200 km in diameter. Interestingly, this is also the transitional diameter between complex craters and peak ring basins [*Melosh*, 1989]. The equation for the percentage of shallow component suggests that the shallow component makes up the major proportion of the innermost ring material for basins smaller than ~460 km in transient diameter (*i.e.*, most lunar basins). Our modeling also suggests that material from the impactor can be mixed with the innermost ring material, although that proportion is very small (~0.01D_{tr}) and is not present in all our simulations. Our simulations show that basins that do not excavate mantle material still expose material originating from various depths in the crust. Therefore, the depth of origin of a "shallow" component can be calculated using the equation derived for the crustal component (0.06±0.01D_{tr}), and the depth of origin of a "deep" component can be calculated using the equation derived for the mantle component (0.16±0.01D_{tr}).

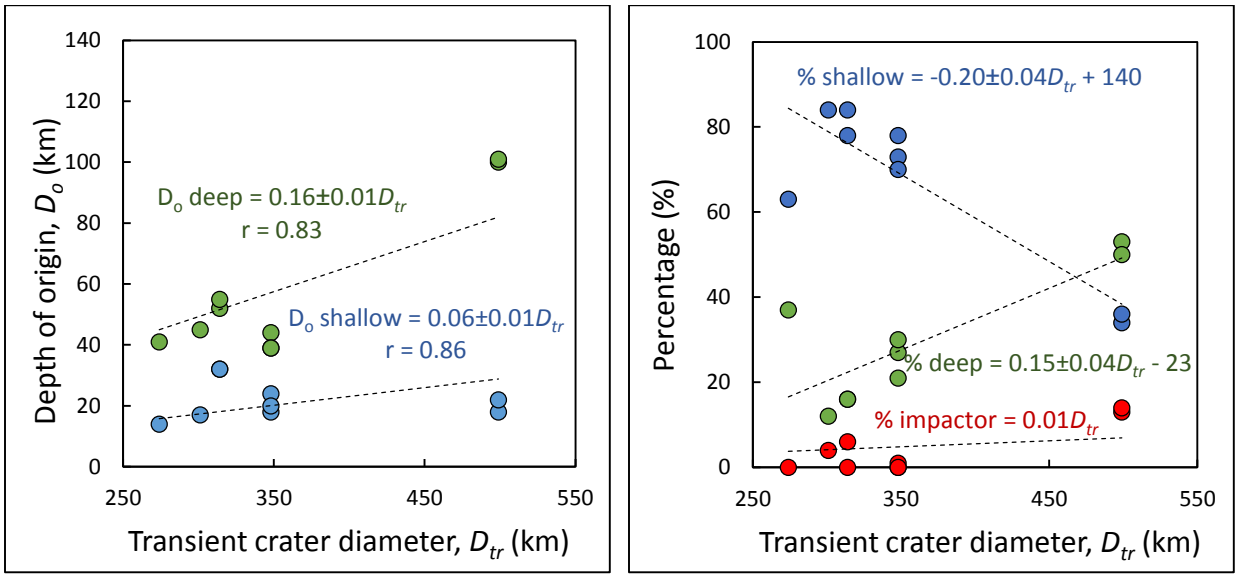

Figure 3.6. Mean depth of origin of the shallow (blue) and deep (green) material exposed by the basins' innermost ring and the percentage of shallow (blue), deep (green) and impactor (red) component exposed, from the analysis of a 10 km by 10 km region centered at the location of the innermost ring of 9 basins in iSALE-2D.

3.5. Results

We computed the abundance of olivine, low-calcium pyroxene, high-calcium pyroxene, and plagioclase using reflectance data from the Kaguya Multiband Imager for every immature pixel on the innermost ring of 13 impact basins. As this led to a considerable amount of data, here we report the modal mineral abundance for each basin (the ternary diagrams for each basin can be found in Appendix C). We then compute the rock type for each pixel, and report the proportion of each rock type found on each basin ring, including the abundance of pure anorthosite and potential mantle constituents. Finally we relate these compositions with depth.

3.5.1 Mineral abundances

We computed the modal plagioclase content as well as the modal abundance of each mafic mineral (olivine, low-calcium pyroxene, and high-calcium pyroxene) over the total abundance of mafic minerals for the immature pixels (OMAT >0.2) on each of the basin's innermost ring (Table 3.2). We find that the innermost ring of most of the basins have an anorthositic compositions with modal plagioclase content ≥77.5 wt.%, except for the more mafic Imbrium and Serenitatis basins. For 8 basins, high-calcium pyroxene is the most abundant mafic mineral, whereas for the other 5 basins, the most abundant mafic mineral is low-calcium pyroxene. Most of the basins that expose material the furthest away from the crust/mantle boundary (the shallow component is ≥13 km away from the crust/mantle boundary) contain more high-calcium pyroxene. Then, approximately half of the basins that expose material closer to the crust/mantle boundary (the shallow component is <13 km away from the crust/mantle boundary), contains more high-calcium pyroxene (Mendeleev, Nectaris, and Lorentz) and the other half contains more low-calcium pyroxene (Crisium, Imbrium, Orientale, and Serenitatis). iSALE-2D modeling suggests that 2 of the 3 basins that contain more high-calcium pyroxene excavated only crustal material (Mendeleev and Lorentz), whereas the third one (Nectaris) contains more crustal component (78%) than the 4 basins that are dominated by low-calcium pyroxene (<73%). This seems to indicate a crustal origin for most of the high-calcium pyroxene, and a mantle origin for most of the low-calcium pyroxene. Mendel-Rydberg does not follow that pattern: it is dominated by low-calcium pyroxene, and iSALE-2D modeling suggests that its innermost ring exposes material originating only from the crust (83%) and the impactor (17%). However, figure 3.7

shows that mantle material has been excavated by Mendel-Rydberg and has been deposited from the center of the basin to beyond the position of the innermost ring. Therefore it is likely that its innermost ring contains mantle material but we did not capture it in the 10x10 km bounding box. Thus, for the rest of the analysis, we consider that the innermost ring of Mendel-Rydberg contains mantle material. Olivine is usually the least abundant mafic mineral, and is present in basins exposing material from many depths, whether exposing mantle or not.

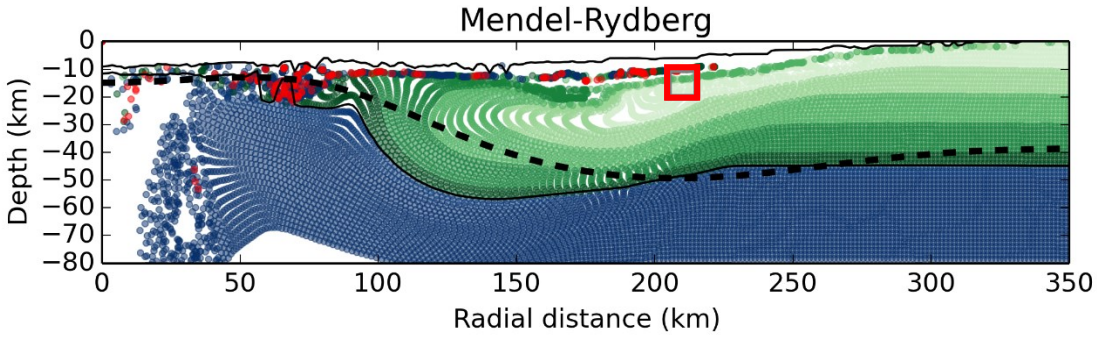

Figure 3.7. Configuration of a Mendel-Rydberg-like impact basin two hours after the impact, as seen by iSALE-2D. The green points represent crustal tracer particles, the blue points represent mantle tracer particles and the red points represent impactor tracer particles. The tracer particles are originally set to 1.5 km apart. The dashed black line represent the crust/mantle boundary measured by GRAIL, and the thin black line represents the crust/mantle boundary modeled by iSALE-2D. These lines are likely to be reconciled following relaxation of the basin. The red square is a 10 by 10 km bounding box centered on the diameter of Mendel-Rydberg's innermost ring (diameter of 420 km, Table 3.2).

Table 3.2. The 13 impact basins analyzed in this study, from the furthest away from the crust/mantle boundary (P), to the closest. The depth of origin (D_o) and the proximity to the crust/mantle boundary (P) of the shallow component, as well as the proportion of shallow component (% shallow) on the innermost ring are from iSALE modeling herein. The modal mineral abundances are calculated using the immature pixels (OMAT >0.2) on each basin ring. The proportion of immature pixels (% of OMAT >0.2) is shown for each basin.

	D_o (km)	P (km)	% shallow	Modal PLG (wt.%)	Modal OL/mafics (%)	Modal OPX/mafics (%)	Modal CPX/mafics (%)	% of PLG >98 wt.%	% of OMAT >0.2
Humorum	14	16	63	83	31	27	43	0.27	3
Mendel-Rydb.	15	15	83	82	12	53	35	0.16	10
Korolev	32	13	96	92	23	31	46	0.22	19
Hertzsprung	32	13	84	92	21	34	45	2.71	28
Moscoviense	17	13	84	90	34	20	46	1.46	3
Freundlich-S	32	13	78	94	24	30	46	2.80	53
Crisium	18	12	73	85	17	43	40	0.30	6
Imbrium	18	12	34	73	21	40	39	0.02	23
Orientale	20	10	70	90	17	48	35	2.91	68
Mendeleev	37	8	100	92	31	21	48	0.12	14
Serenitatis	22	8	36	67	13	50	37	0.00	6
Nectaris	24	6	78	88	24	28	48	0.05	6
Lorentz	26	4	97	89	30	24	46	0.18	2

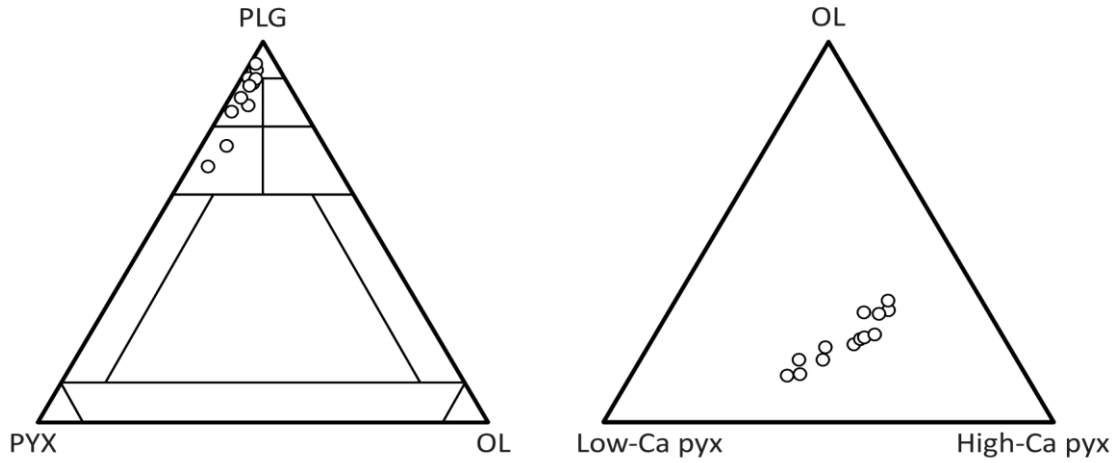

Figure 3.8. Ternary diagrams presenting the modal mineralogical composition of each basin's inner most ring. Ternary diagrams for each basin can be found in Appendix C.

3.5.2 Rock types

We computed the rock type for each immature pixel, based on the mineral abundances obtained by radiative transfer modeling, and rock type nomenclature of *Stöffler et al.* [1980], and determined the percentage of each rock type present on each ring. We find that anorthositic rock types (which contain ≥77.5 wt.% plagioclase) are the dominant types in 11 basins: all basins except for Imbrium and Serenitatis basins. These two basins expose the least amount of crustal component on their innermost ring (34 and 36%, Table 3.2). Anorthosite in the strict definition (which contains ≥90 wt.% plagioclase) is the major constituent on the innermost ring of 9 basins. Noritic or gabbroic anorthosite (N/G An, plagioclase 77.5-90 wt.%) is the major constituent on the innermost ring of Mendel-Rydberg, and is slightly more abundant than anorthosite on the innermost ring of Crisium (45 % versus ~41 %). Anorthositic norite or gabbro (An N/G, 60-77.5 wt% plagioclase) is the most abundant rock type on the innermost ring of Imbrium and Serenitatis basins, and is present in the same abundance (~57 %).

Rock types that contain <60 wt% plagioclase (norites or gabbros, and olivine norites or gabbros) are less abundant, and inspection of the mineral maps (Figs. 3.9-3.10) suggest that the innermost ring area for the basins containing these rock types might include some mare basalt component. We do not find ultramafic lithologies (rock types that contain <10 wt% plagioclase) such as pyroxenite, peridotites, or dunites.

Table 3.3. Percentage of rock types present in the immature pixels on the innermost ring of the 13 impact basins analyzed in this study. Rock types were computed for each pixel based on the mineral abundances obtained via radiative transfer modeling, and follow the nomenclature of *Stöffler et al*. [1980]. The basins are listed based on the proportion of crustal component on their innermost as suggested by iSALE-2D, from the most to the least.

	Anorthosite		Noritic/ Gabbroic anorth.	Troctolitic Anorth.	Anorth. Norite/ Gabbro	Anorth. Troctololite	Norite/ Gabbro	Olivine Norite/ Gabbro
	≥90wt% plg	>98wt% plg						
Mendeleev	92	0.1	7	1	0	0	0	0
Lorentz[a]	60	0.2	31	4	5	0	0	0
Korolev	85	0.2	15	0	0	0	0	0
Mendel-Rydberg	9	0.2	66	1	23	0	0	0
Moscoviense	78	1.5	12	3	4	0	1	1
Hertzsprung	77	2.7	21	0	2	0	0	0
Freundlich-Sharon.	98	2.8	2	0	0	0	0	0
Nectaris	52	0.1	41	2	5	0	0	0
Crisium	41	0.3	45	3	8	0	2	0
Orientale[a]	66	2.9	31	0	3	0	0	0
Humorum	36	0.3	32	7	20	1	1	3
Imbrium	5	0.0	25	4	57	1	4	5
Serenitatis	0	0.0	18	1	57	0	17	7

[a] Artifacts present in the multiband imager data led to vertical striping of alternating anorthosite and noritic/gabbroic anorthosite. Orientale's innermost ring is dominated by anorthosite outside these striped region. It is difficult to establish the true composition for Lorentz as the vertical striping of alternating anorthosite and noritic/gabbroic anorthosite is almost ubiquitous in the ring region (see Fig. 3.9).

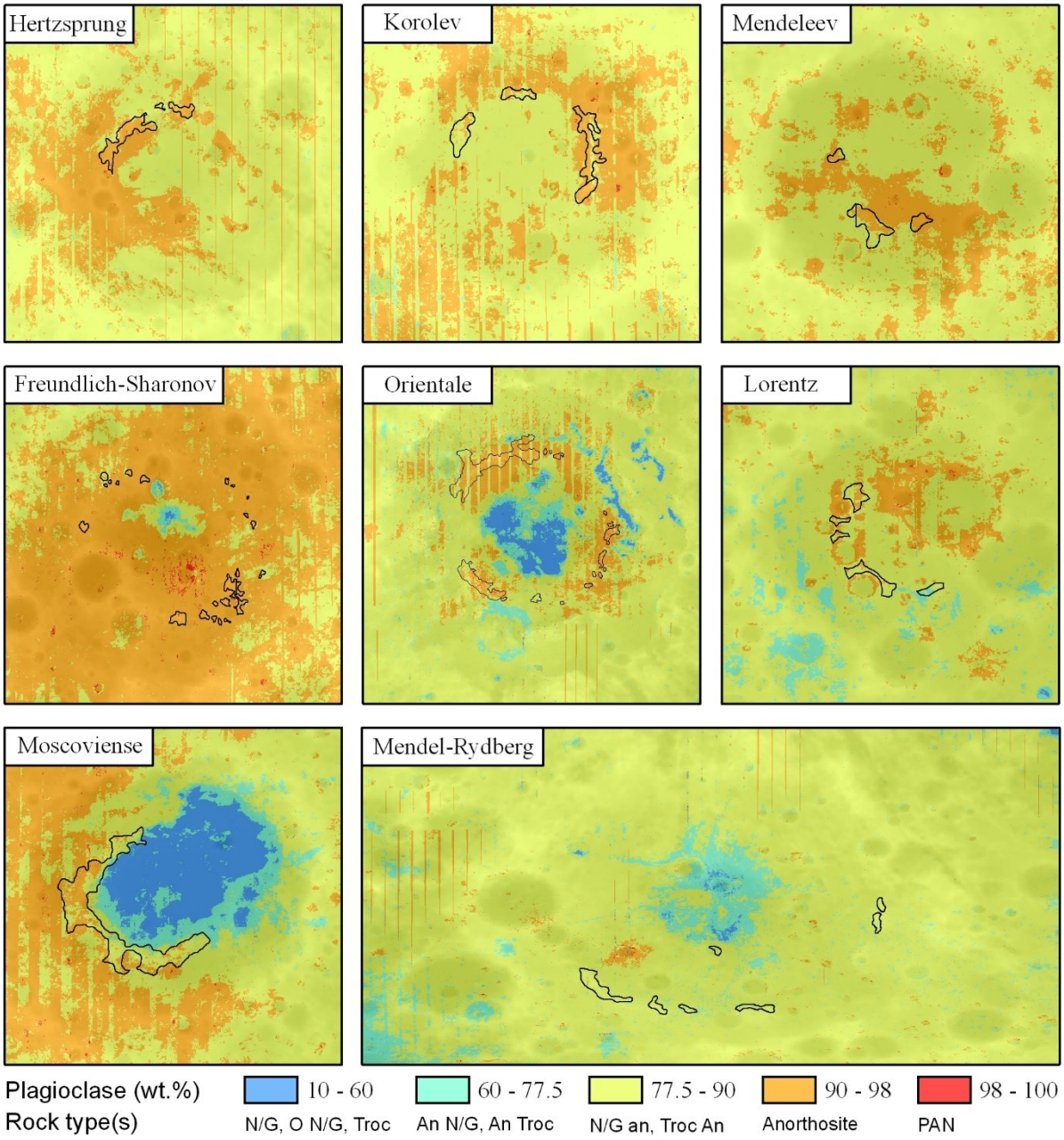

Figure 3.9. Plagioclase content for the basins located on the lunar far side. The black outlines represent the location of the innermost ring material. The rock types associated with each plagioclase content are from *Stöffler et al.* [1980]: norite/gabbro (N/G), olivine norite/gabbro (O N/G), troctolite (Troc), anorthositic norite/gabbro (An N/G), anorthositic troctolite (An troc), noritic/gabbroic anorthosite (N/G An), troctolitic anorthosite (Troc An), anorthosite, and purest anorthosite (PAN).

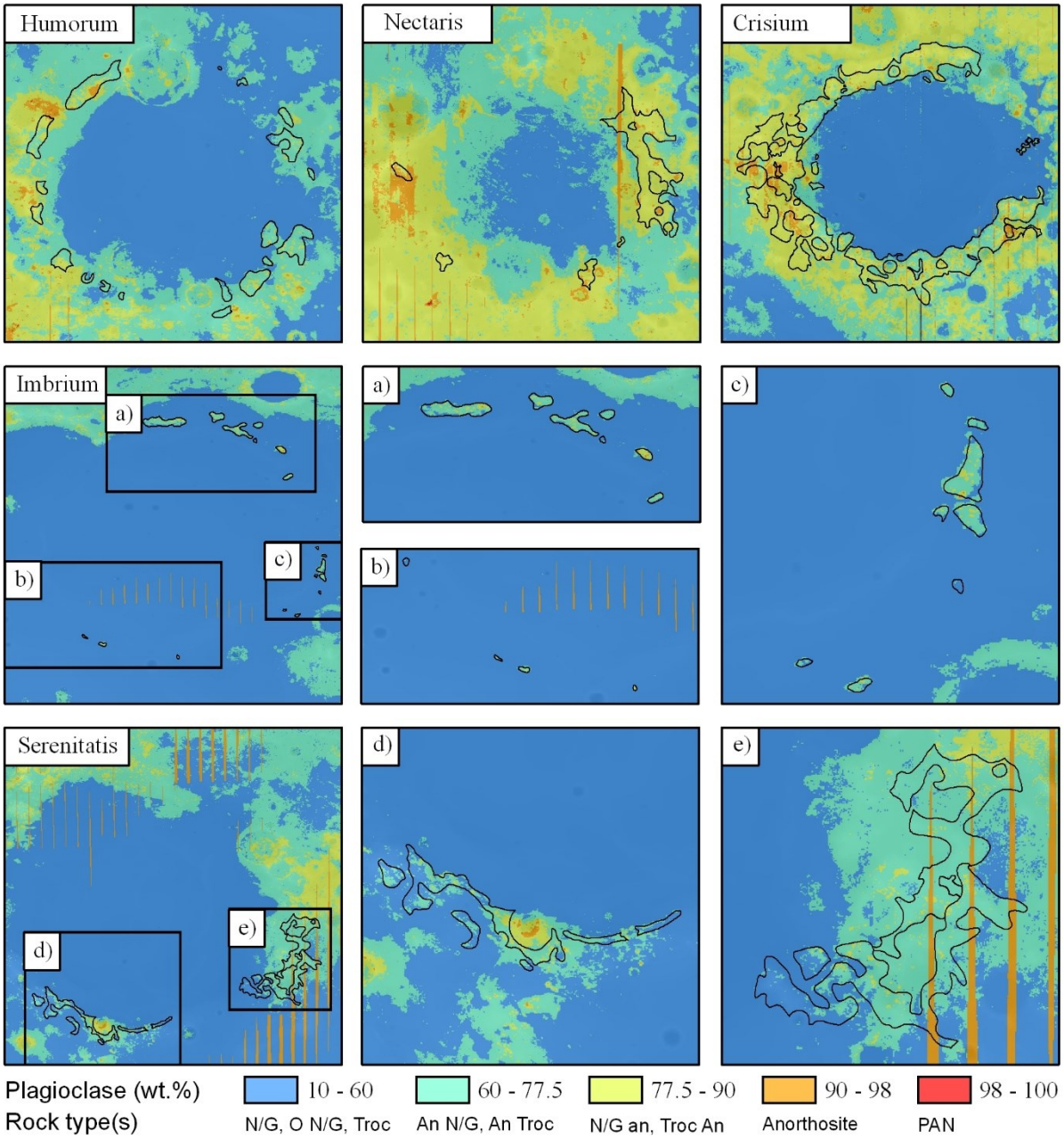

Figure 3.10. Plagioclase content for the basins located on the lunar near side. The black outlines represent the location of the innermost ring material. The rock types associated with each plagioclase content are from *Stöffler et al.* [1980]: norite/gabbro (N/G), olivine norite/gabbro (O N/G), troctolite (Troc), anorthositic norite/gabbro (An N/G), anorthositic troctolite (An troc), noritic/gabbroic anorthosite (N/G An), troctolitic anorthosite (Troc An), anorthosite, and purest anorthosite (PAN).

3.5.2.1 Exposures of purest anorthosite

Cheek et al. [2013] reported an utter dominance of anorthosite on the innermost ring of Orientale based on the ubiquitous presence of a strong plagioclase absorption band at 1.25 μm in the Moon Mineralogy Mapper data and weaker or absent pyroxene bands. Based on radiative transfer modeling of spectral mixtures of pyroxene and plagioclase at the Moon Mineralogy Mapper wavelengths, they concluded that anorthosite is nearly pure, with >95 wt.% plagioclase in most areas, and even up to 99-100 wt.%. Based on the radiative transfer modeling presented herein, using spectral mixtures of olivine, pyroxene and plagioclase at the Multiband Imager wavelengths, we also find that anorthosite is the dominant mineral on the innermost ring of Orientale (Table 3.3). The immature pixels composed of anorthosite (≥90 wt% plagioclase) on Orientale's innermost ring contain on average 94 wt% plagioclase (Figure 3.11), and ~3% of these pixels contain >98 wt% plagioclase. Of all the basins we study, the innermost ring of Orientale contains the highest proportion of pixels with >98 wt% plagioclase, followed by Hertzsprung and Freundlich-Sharonov (also ~3%), and Moscoviense (~2%) (Table 3.3). These four basins are located in the Feldspathic Highlands Terrane, on the far side of the Moon.

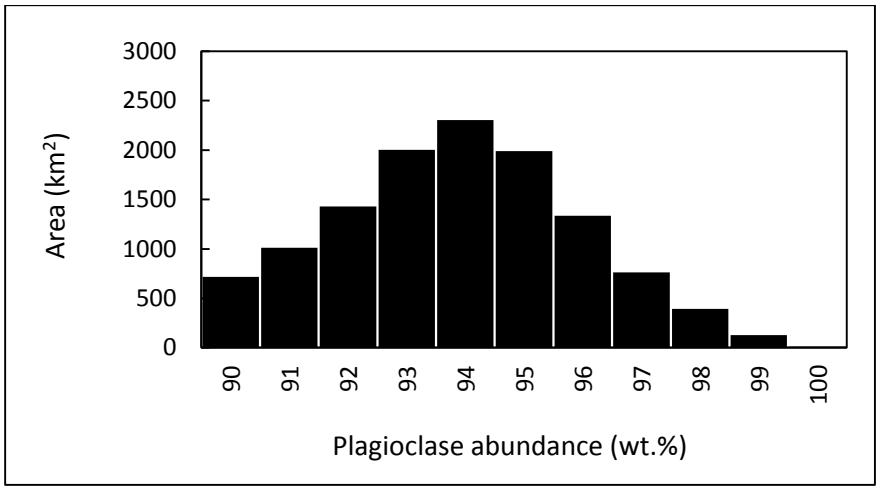

Figure 3.11. Plagioclase abundance for the immature pixels that are composed of anorthosite (≥90 wt% plagioclase) on Orientale's innermost ring, based on the radiative transfer model presented herein.

3.5.2.2 Exposures of mantle material

Exposures spectrally dominated by olivine were detected by *Yamamoto et al*. [2010] in concentric regions around Moscoviense, Humorum, Nectaris, Crisium, Imbrium and Serenitatis. They suggested that these exposures can be attributed to either the excavation of mantle material, or to magnesium-rich plutons in the Moon's lower crust. We find that olivine is found in both olivine norite/gabbro and troctolitic anorthosite on the innermost ring of Moscoviense, Humorum, Imbrium, and Serenitatis. Olivine is mostly found in troctolitic anorthosite on the innermost ring of Nectaris, and Crisium. Troctolitic anorthosites can correspond to mixture of crustal anorthositic material and mantle dunite, or originate from magnesium-rich pluton in the Moon's lower crust [*Hess*, 1994]. Our iSALE-2D modeling suggest that these 6 basins have excavated mantle material, thus the olivine exposures reported by *Yamamoto et al.* [2010] can indeed correspond to mantle material. However, we find that the innermost ring of Mendeleev and Lorentz also contain some troctolitic anorthosites (1-4 % or the ring material), even though iSALE-2D modeling suggests that their innermost ring does not contain mantle material. Therefore we cannot rule out magnesium-rich plutons in the Moon's lower crust as a source for the olivine exposures reported.

3.5.3 Depth of origin and relative proportion of material exposed by the basins' innermost ring

Of the 13 basins we study, iSale modeling suggests that the innermost ring of 10 basins expose mantle material (including Mendel-Rydberg), and the innermost ring of 3 basins expose only crustal material (Mendeleev, Lorentz, and Korolev). Figure 3.12a shows the modal plagioclase content of each ring versus the proximity to the crust/mantle boundary of the crustal component (blue), the mantle component (green) and depth of origin of corresponding to their weighted proportion ("x") 2 hours after the impact. The modal plagioclase content of the central peaks studied by *Lemelin et al.* [2015] is also shown. The modal plagioclase content of the shallow component of the basins' innermost ring corresponds to the modal plagioclase of the central peaks at similar depths. This suggests that the innermost ring material we observed with the Multiband Imager data is dominated by the shallow component, more than what iSALE-2D modeling suggests 2 hours after the impact (shown by the weighted proportion), which can

potentially be explained by the fact that we do not resolve the ring material at the resolution of the model. Figure 3.12b shows the modal plagioclase content of each peak and each ring versus the proximity to the crust/mantle boundary of its crustal component, color coded by geochemical terrane. The central peaks and basins have similar composition within each geochemical terrane. The basins and central peaks in the Feldspathic Highlands Terrane are generally the most anorthositic, and central peaks in the South Pole-Aitken basin the least.

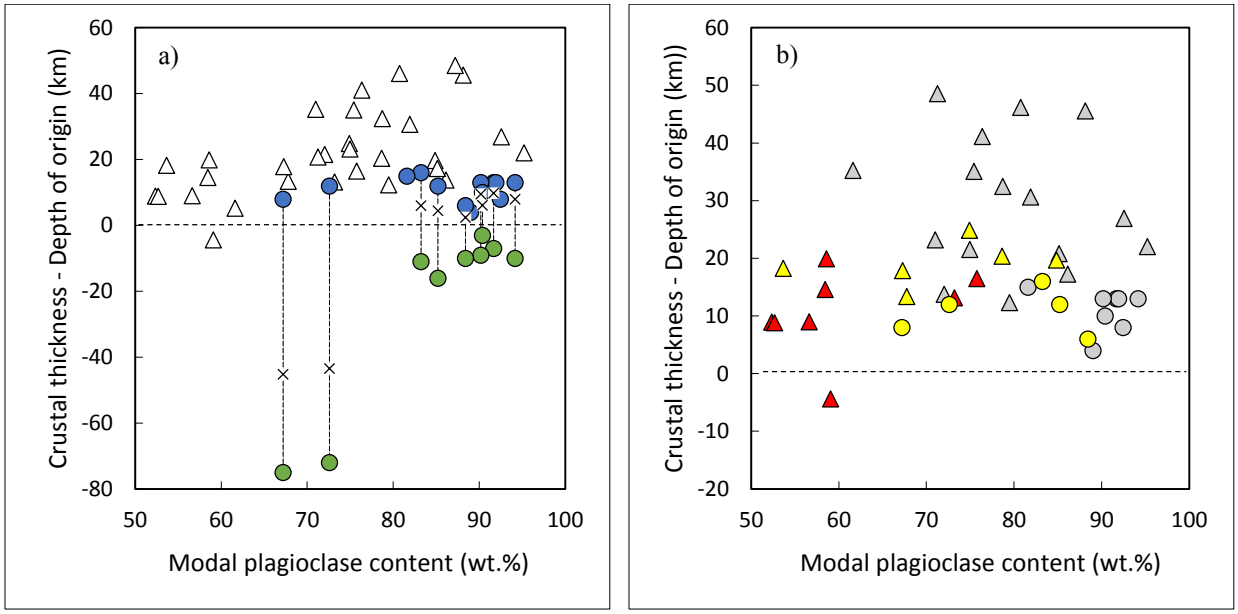

Figure 3.12. Modal plagioclase content of the basin's innermost ring in this study (circles) and the central peaks studied by *Lemelin et al*. [2015] (triangles), versus their proximity to the crust mantle boundary (dashed line). (a) The modal plagioclase content of each basin (circles) is shown at the location of the crustal (blue), mantle (green) component, and their weighted proportion ("x") from iSALE. (b) The modal plagioclase content of the basin rings and central peaks versus their proximity to the crust/mantle boundary, in the Feldspathic Highlands Terrane (gray), the Procellarum KREEP Terrane (yellow) and the South Pole Aitken basin (red). The depth of origin of the shallow component is used for the basins.

Figure 3.13 shows the modal mineral content of each basin ring (excluding Mendel-Rydberg) versus their proportion of crustal or mantle component, according to iSALE modeling. Figure 3.13a shows the modal plagioclase content versus their proportion of crustal component, and Figure 3.13b shows the modal high-calcium pyroxene content over the total abundance of mafic minerals versus their proportion of crustal component. Figure 3.13c and 3.13d show the modal content of low-calcium pyroxene and olivine over the total abundance of mafic minerals versus their proportion of mantle component. As expected, the modal abundance of plagioclase increases with the proportion of crustal material exposed on the innermost ring. The modal abundance of high-calcium pyroxene over the total abundance of mafic minerals also slightly increases with the proportion of crustal material exposed on the innermost ring. Moreover, the innermost ring of 3 basins that excavated only crustal material have modal plagioclase abundances between 89 and 92 wt.% and their dominant mafic component is high-calcium pyroxene which suggests a crustal origin for in high-calcium pyroxene as proposed by *Yamamoto et al*. [2015]. The modal abundance of low-calcium pyroxene over the total abundance of mafic minerals generally increases with the proportion of mantle material exposed on the innermost ring which supports a mantle origin for low-calcium pyroxene as proposed by *Nakamura et al*. [2012]. The abundance of olivine over the total abundance of mafic minerals generally decreases with increasing proportion of mantle component exposed, suggesting that it originates from the crust, potentially from magnesium-rich plutons in the Moon's lower crust.

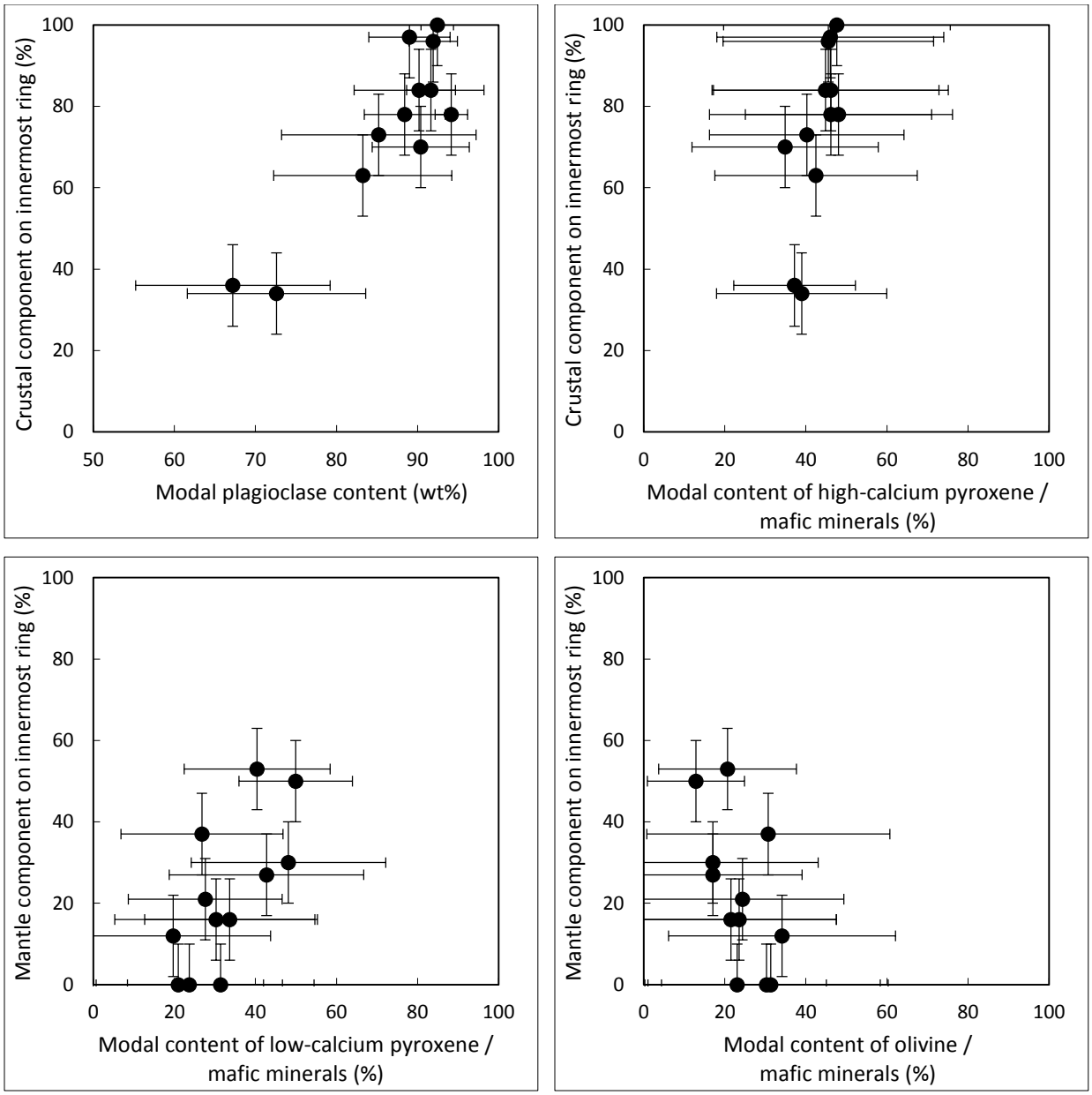

Figure 3.13. Modal mineral content versus the proportion of crustal or mantle component exposed on the basins' innermost ring according to iSALE modeling (Section 3.4.3.2). (a) Modal plagioclase content versus the proportion of crustal component. (b) Modal content of high-calcium pyroxene over the total content of mafic minerals versus the proportion of crustal component. (c) Modal content of low-calcium pyroxene and (d) modal content of olivine over the total content of mafic minerals versus the proportion of mantle component. The variation in mineral content for each basin ring is shown using ±1σ. The variation in the proportion of crustal or mantle component on the ring is shown using ±10% (error defined in Section 3.4.3.2).

3.6. Conclusion

In this study, we conducted a quantitative and comprehensive analysis of the mineralogical composition of the innermost ring of 13 lunar impact basins, placed constraints on the depth of origin of the material exposed by the basins' innermost ring, using iSALE-2D hydrocode modeling, and compared the composition of the basins' innermost ring to the composition of central peaks previously studied.

We find that the innermost ring of basins in the Feldspathic Highland Terrane have a modal plagioclase content between ~82-94 wt.% (corresponding to anorthositic compositions). The most abundant rock type is anorthosite (≥90 wt.% plagioclase) on the innermost ring of most basins, consistent with *Hawke et al.* [2003]. Orientale has the most abundant proportion of nearly pure anorthosite (with >98 wt.% plagioclase), slightly more than Hertzsprung and Freundlich-Sharonov. We do not find ultramafic lithologies such as pyroxenite, peridotites, or dunites, indicating that there are no exposures of pure mantle material at the scale of the resolution of the Multiband Imager data. We detect olivine on the innermost ring of basins where *Yamamoto et al*. [2010] also detected olivine. The olivine is found in both olivine norite/gabbro and troctolitic anorthosite, which can correspond to mixture of crustal anorthositic material and mantle dunite, or originate from magnesium-rich plutons in the Moon's lower crust [*Hess*, 1994].

iSALE-2D modeling suggests that basins expose material originating from various depths. Of the basins we studied, 10 excavated mantle material and expose some constituents on their innermost ring. Using these iSALE-2D observations, we derived equations that can be used to approximate the depth of origin of the material exposed on the innermost ring of other basins: a shallow component originates on average from $0.06\pm0.01D_{tr,}$ and a deep component originates on average from $0.16\pm0.01D_{tr}$. We also derived equations that can be used to approximate the proportion of shallow ($-0.20\pm0.04D_{tr}+140$) and deep component ($0.15\pm0.04D_{tr}-23$) present on the innermost ring. These equations imply that for basins smaller than ~460 km in diameters, the shallow component is the most abundant. This also implies that there is no contribution from the deep component in impacts smaller than ~150 km in diameter, *i.e*., in complex craters.

We compare the relative proportions of mafic minerals to the proportions of shallow and deep components present on the innermost rings to identify their source region. We find that the modal content of olivine over the total content of mafic minerals generally decreases with increasing proportion of mantle component, suggesting that it originates from the crust,

potentially from magnesium-rich plutons in the Moon's lower crust. The modal content of high-calcium pyroxene over the total content of mafic minerals generally increases with the proportion of crustal material exposed, also suggesting a crustal origin as proposed by *Yamamoto et al*. [2015]. The modal content of low-calcium pyroxene over the total content of mafic minerals generally increases with the proportion of mantle material exposed which supports a mantle origin [*Nakamura et al*., 2012]. This is also consistent with the detection of noritic anorthosite in small craters (< 1km in diameter) in the Feldspathic Highlands Terrane by *Lucey et al.* [2014]. These small craters sample megaregolith and require an orthopyroxenite mantle to explain their composition.

Finally we compared the composition of the basins' innermost ring to the composition of central peaks previously studied. We found that the modal composition of the innermost rings is consistent with the modal composition of the central peaks studied by *Lemelin et al.* [2015] at similar depths. The basin rings and central peaks in the Feldspathic Highlands Terrane are generally the most anorthositic, and central peaks in the South Pole-Aitken basin the least, which confirms the different geochemical evolution of the three main geochemical terranes. The basin rings and central peaks in the Feldspathic Highlands Terrane, which span through the entire crustal column, have modal plagioclase content ranging between ~60-95 wt.%. There appears to be no relationship between their modal compositions and their depth of origin in the crust. This suggests that the crust is dominantly anorthositic and heterogeneous, including intrusions of more mafic material as suggested by *Cahill et al*. [2009].

CHAPTER 4

MINERALOGY AND IRON CONTENT OF CENTRAL PEAK AND BASIN RINGS IN THE LUNAR POLAR REGIONS USING THE KAGUYA SPECTRAL PROFILER

In preparation for publication as: Lemelin, M., P. G. Lucey, and D. Trang (2015), Mineralogy and iron content of central peak and basin rings in the lunar polar regions using the Kaguya Spectral Profiler.

Abstract— Due to the low axial tilt of the Moon with respect to the ecliptic, major portions of craters walls and floors in the polar regions are often in shadow, making it difficult for instruments using the Sun as the illumination source to acquire high quality data in these regions. Thus, most mineralogical maps derived from visible and near infrared reflectance data have been constrained to within ~50° or 70°in latitude. In this study, we take a novel approach and use strong signal and well calibrated reflectance acquired by two different instruments, the Kaguya Spectra Profiler and the Lunar Orbiter Laser Altimeter, in order to derive the first high resolution FeO and mineralogic maps of the polar regions. The map of iron derived from these two datasets is in agreement with the abundance of iron measured by the Lunar Prospector Gamma-Ray spectrometer up to ~80° in latitude. We use the mineral maps to study the composition of 27 central peaks and 5 basin rings in the polar regions, and relate their composition to their depth of origin in the lunar crust. We find that the central peaks and basin rings in Feldspathic Highlands Terrane are mostly anorthositic in composition, whereas the central peaks and basin rings in the South Pole-Aikten are noritic and gabbroic at all depths, suggesting that they are sampling a potentially differentiated melt sheet of noritic composition. Low-calcium pyroxene is the most abundant mafic mineral present on all the central peaks originating from all depths, which supports a crustal origin.

4.1. Introduction

The mineralogical composition of the lunar surface derived using reflectance data in the visible and near infrared, requires strong signal and well calibrated reflectance. The calibrated reflectance can in turn be used to compute the abundance of FeO of a given spectra to unambiguously define its composition based on its spectral shape and chemistry. Due to the poor illumination conditions in the polar regions, strong signal and well calibrated reflectance data is scarce, and no sole instrument can meet these two critical requirements on the Moon. Thus, mineralogic maps have been constrained to within ~50° [*e.g.*, *Lemelin et al*., 2015] or ~70° of the equator [*e.g.*, *Lucey*, 2004; *Crites and Lucey*, 2015]. The mineralogy of the polar regions, which corresponds to more than 16 million km^2 poleward of 50° in latitude, or ~44% of the lunar surface, is almost entirely unknown. A few studies have provided limited compositional analysis where strong absorption bands were present in order to identify the minerals present based on their spectral shape. These studies were constrained to either individual detections of lithologies dominated by one or two minerals [*Yamamoto et al*., 2010; 2012; *Haruyama et al.,* 2013; *Kramer et al.,* 2013]. A few studies analyzed the composition of central peaks up to ~70° [*e.g.*, *Cahill et al.,* 2009; *Ohtake et al*., 2009]. Deriving mineral maps in the polar regions would be beneficial in that it would allow to study more thoroughly the composition of central peaks and basins rings and in turn further our understanding of the composition of the lunar crust with depth. It would also be beneficial for future lunar missions aiming to visit these polar regions (*e.g*., Resource Prospector), as knowledge of the mineralogy will likely influence the choice of landing sites and help designing mission activities (*e.g*., sample material, and/or primary crustal material). For example, a mission to determine the age of the South Pole Aitken basin, the oldest lunar basin located in the south polar region, is one of the highest lunar science priorities [*National Research Council*, 2007; 2011].

In this study, we take a novel approach and use strong signal and well calibrated reflectance acquired by two different instruments, the Kaguya Spectra Profiler and the Lunar Orbiter Laser Altimeter, in order to derive the first high resolution FeO and mineralogic maps of the polar regions. The Spectral Profiler acquired reflectance spectra of the surface between 500 and 2600 nm with a ~500 meters footprint [*Matsunaga et al*., 2001; *Haruyama et al*., 2008]. The profiler conducted continuous global spectral observations of the Moon in the visible to near infrared region in 2007-2009. Thus, for most of the polar region, hyperspectral data has been

acquired at least once when the surface was illuminated in a given area, especially during the polar summers. However, some crater walls facing the poles had low illumination (low signal to noise ratio), making mineralogical interpretation difficult. The Lunar Orbiter Laser Altimeter (LOLA) has also been acquiring global observations of the Moon since 2009, and has the advantage of being an active sensor; it sends a laser pulse towards the Moon at 1064 nm, and measures the energy backscattered from the surface regardless of the Sun's illumination conditions. It provides high signal to noise ratio even on pole facing slopes (*i.e*., it is not influenced by topography), and has been thoroughly calibrated and gridded into polar maps of ~1 km per pixel by *Lemelin et al*. [2016] (Chapter Five). We use reflectance ratio from the Spectral Profiler and calibrated reflectance data from the Lunar Orbiter Laser Altimeter to derive the first polar high resolution maps of FeO. We then use the reflectance data from the Spectral Profiler and Hapke radiative transfer model to compute the abundance of olivine, low-calcium pyroxene, high-calcium pyroxene and plagioclase, using iron as a constraint. We then use these mineral maps to analyze the composition of 27 central peaks and 5 basin rings in the polar region, nearly doubling the central peak (34) and basin ring (13) population studied in the previous Chapters, in order to refine our understanding of the composition of the lunar crust with depth. As the mineral abundance are derived using different datasets than the mineral abundances from the previous Chapters, they consist in an independent dataset to study composition of the lunar crust.

4.2 Background

Lemelin et al. [2015] found that the 34 central peaks they studied in the equatorial region are generally dominated by a single lithology as suggested by their small variation in plagioclase content, and that they found the dominant lithology is different in each of the lunar geochemical terranes [*Jolliff et al*., 2000], from the more anorthositic in the Feldspathic Highlands Terrane (FHT), to the more mafic in the South Pole Aitken Basin (SPA), and intermediate compositions in the Procellarum KREEP Terrane (PKT). They found that the most abundant mafic mineral is pyroxene, typically low-calcium pyroxene, in most of the central peaks. Olivine is usually much less abundant besides in the central peak of Copernicus and Keeler. Using the average plagioclase and mafic minerals present on each peak to define the dominant rock type, they found that central peaks in the FHT are composed of anorthosites, noritic or gabbroic anorthosites, and anorthositic norites or gabbros, the central peaks in the PKT are composed of

noritic or gabbroic anorthosites, anorthositic norites or gabbros, norites or gabbros, and troctolitic anorthosite, and the central peaks in SPA are composed of anorthositic norites or gabbros, and norites or gabbros. They also identified exposures of nearly pure anorthosite (with plagioclase ≥98 wt.%) on the central peaks of craters excavating various depths into the crust, from 14 to 49 km away from the crust-mantle boundary. They found that anorthosite with very low mafic abundance is a minority constituent in these peaks, which stands in contrast with the dominance of nearly pure anorthosite on the innermost ring of Orientale by *Cheek et al*. [2013].

In Chapter Three, we conducted a quantitative and comprehensive analysis of the mineralogical composition of the innermost ring of 13 lunar impact basins, including Orientale, to investigate the consistency between the composition of the central peaks and the composition of basin rings. We found that the most abundant rock type on the innermost ring of most basins is anorthosite, Orientale having the most abundant proportion of nearly pure anorthosite, followed by noritic or gabbroic anorthosite, and anorthositic norite or gabbro on the innermost ring of Serenitatis and Imbrium. We also found that the average composition of the basin rings is generally anorthositic but sometimes more mafic than anorthosite, as strictly defined in the lunar nomenclature with >90% plagioclase, similar to that of the central peaks in the corresponding geochemical terrane and at corresponding depths in the crust. Unlike the depth of origin of the material exposed on the central peak of craters less than 150 km in diameter, there has been no consensus regarding the depth of origin of material exposed in basin rings. To that end, we refined the depth of origin of the material exposed on the basins' innermost ring using a Laplacian impact model (iSALE-2D hydrocode) which allowed us to compare the material exposed by central peaks and by basin rings according to their depth of origin in the crust for the first time. It revealed that most of the basins we studied must have excavated mantle material and likely expose a small proportion of such on their innermost ring. We also found that the most abundant mineral on the innermost ring is either low-calcium or high-calcium pyroxene, but never olivine. High-calcium pyroxene is usually the most abundant mafic mineral on the innermost rings that contain the most abundant proportion of crustal material. The abundance of high-calcium pyroxene increases with increasing proportion of mantle material on the rings, whereas the abundance of olivine decreases, leading us to suggest a mantle source for the low-calcium pyroxene, and magnesium-rich intrusions in the lower crust as the source for olivine.

None of the central peaks studied by *Lemelin et al.* [2015] in the Feldspathic Highlands Terrane sampled these intrusions as they did not contain abundant olivine.

Due to the lack of strong signal and well calibrated reflectance data in the polar regions, mineralogical analysis have been previously constrained to either isolated detection of lithologies dominated by one or two minerals with strong absorption bands [*Yamamoto et al*., 2010; 2012; *Kramer et al.,* 2013], or to specific portions of craters such as the upper walls of Shackleton [*Haruyama et al.,* 2013], and central peaks up to ~70° in latitude [*e.g.*, *Cahill et al.,* 2009; *Ohtake et al*., 2009]. *Yamamoto et al*. [2012] identified spectra dominated by plagioclase on fresh craters or the slopes of peaks associated with large impact basins, five of those in the polar region: Birkhoff, Humboldtianum, Schiller-Zucchius, Schrödinger, and Amundsen-Ganswindt. *Ohtake et al*. [2009] detected spectra dominated by plagioclase associated with four impact features in the polar region: Anaxagoras, Fechner T, Pythagoras and Schrödinger, and *Haruyama et al.,* [2013] detected high 1050 nm reflectance and the diagnostic 1250 nm spectral absorption of nearly pure anorthosite on the upper walls of Shackleton. *Yamamoto et al*. [2010] detected spectra dominated by olivine in the polar craters Compton, Humboldtianum, Zeemand, and Schrödinger basin. *Kramer et al.* [2013] confirmed the presence of large areas of anorthite-rich material, low-calcium pyroxene material (a noritic unit), and olivine-rich material (troctolite or dunite), although the precise modal mineralogy was not determined. They suggest that Schrödinger excavated ~20 km into a noritic lunar crust. Thus, exposures of nearly pure lithologies have been reported in specific locations associated with impact craters and basin, but most of them were not quantified and no coverage map has been provided.

4.3 Data and Method

In this study, we use reflectance data from the Spectral Profiler and from the Lunar Orbiter laser Altimeter, as well as Hapke radiative transfer equations to derive the first high resolution maps of FeO and of the main lunar minerals, poleward of 50° in latitude. We compute the mineral abundance for each Spectral Profiler data point acquired during the north and south polar summer with strong signal, constraining the mineral abundances based on their local FeO content, and gridded the resulting mineral abundance points into maps. We then use these maps to analyze the composition of the central peak in 27 craters and the innermost ring of 5 basins located poleward of 50°, nearly doubling the number of central peaks and basin rings analyzed in

the previous Chapters. We selected these craters and basins that have a prominent central peak or ring, discernable in the Lunar Orbiter laser Altimeter topographic data. Figure 4.1 shows the location of the 27 complex craters and 5 basins we studied.

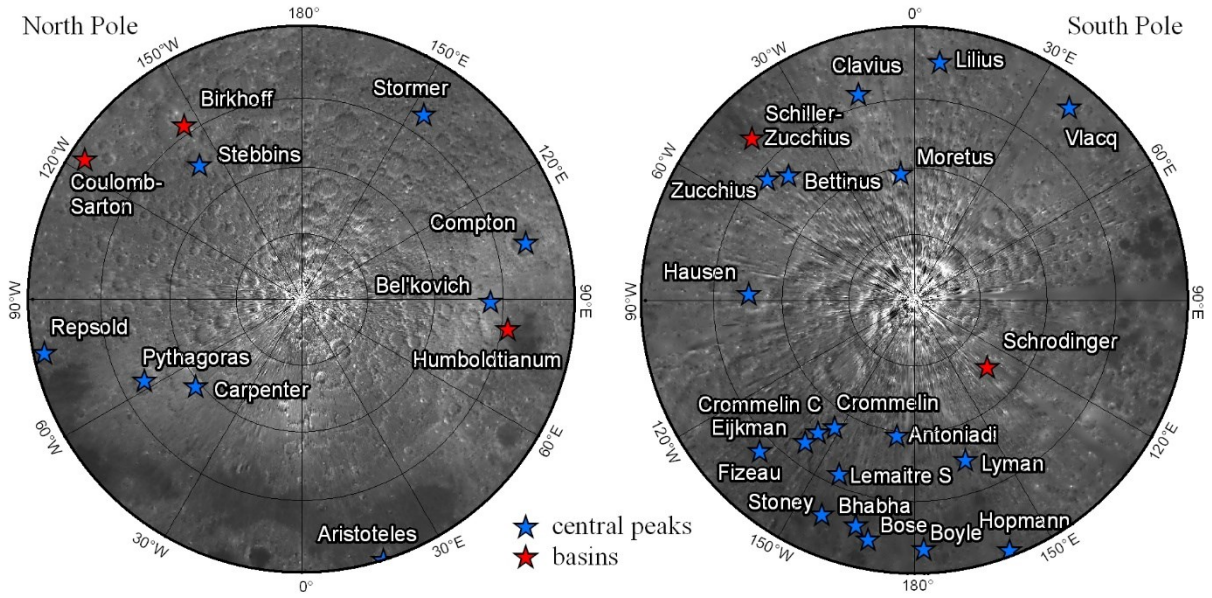

Figure 4.1. Location of the 27 central peaks (blue stars) and 5 basin rings (red stars) analyzed in this study poleward of 50° latitude. The background is the reflectance measured by the Spectral Profiler at 955.4 nm, scaled from 0 to 0.4 black to white, using orbits 2000-2700 in the north polar region, and orbits 4124-4998 in the south polar region.

4.3.1 Spectral Profiler UVVIS/NIR data

The Kaguya Spectral Profiler is a spot spectrometer which conducted continuous spectral observations of the Moon in the visible to near infrared region (500-2600 nm) between 2007 and 2009, yielding global coverage in the form of longitudinal strips of spectra covering all longitudes [*Matsunaga et al*., 2001; *Haruyama et al*., 2008]. It obtained three spectra per second below the spacecraft, which at the 1600 meter per second velocity of the Kaguya spacecraft gave a ~500 m spacing between each spectrum. In this study, we use Spectral Profiler data level 2B1, which contains radiometrically calibrated radiance data converted to diffuse reflectance data (http://pds-imaging.jpl.nasa.gov/documentation/LISM-SPICE_Format_en_V01.3.pdf). We then apply the photometric function of *Yokota et al*. [2011] to correct the diffuse reflectance data for the observational geometry in the 500 to 1600 nm wavelength range, and obtain the reflectance

at a standard viewing geometry of $i = 30°$, $e = 0°$, and $\alpha = 30°$. *Yamamoto et al.* [2011] compared the reflectance at the Apollo 16 landing site acquired during four different observation periods at six month interval and concluded that the photometric function of *Yokota et al*. [2011] yields an error (standard deviation) of ~1% in reflectance. Unlike the Multiband Imager data presented in the previous Chapters, the current photometric correction does not include the effect of local topography, but instead assumes a flat lunar surface. Areas that are locally tilted away from the sun will have lower apparent reflectance, while areas tilted toward the sun will have higher apparent reflectance. As this can affect the mineralogical composition derived herein, we minimize the shadowed areas by selecting the data that has been acquired during the south polar and the north polar summer, when the viewing geometry was optimal (low incidence angle) by analyzing data points that have a reflectance value greater than 0.05 at 746.8 nm (the approximate reflectance value of the darkest maria). Also, we only kept the spectral match that are within the Spectral Profiler error (1% reflectance) in each spectral band (described in section 4.3.2). The northern summer occurred approximately during orbits 2000-2999 and orbits 6000-6999, whereas the southern summer occurred approximately during orbits 4000-4999. In this study, we use 677 orbits (between 2000-2700) to map the north polar region, and 467 orbits (between 4124-4998) to map the south polar region.

4.3.2 Polar mineral maps

Quantitative assessment of the mineralogical composition of the lunar surface using visible and near infrared wavelengths, is obtained by comparing reflectance spectra to modeled spectra of known composition, and assigning the composition of the best spectral match. Radiative transfer equations, which describe the scattering of light interacting with surfaces, allow to model reflectance spectra of mineral mixtures, for various grain sizes, chemistry, and space weathering effects. As similar spectra can have different compositions, iron abundance can be used as a constraint to mitigate uncertainties. In this study we use *Hapke*'s radiative transfer equations [*e.g.*, *Hapke*, 1981; 1993; 2001] and the approach described in *Lemelin et al*. [2015] to derive compositions from the 1144 orbits that have optimal lighting conditions in the polar regions. We use *Hapke*'s radiative transfer equations to compute a spectral library corresponding to mixtures of olivine, low-calcium pyroxene, high-calcium pyroxene and plagioclase, at the 109 Spectral Profiler wavelengths between 746.8 and 1555.5 nm. We compare each data point of the

1144 orbits against the spectral library and assign the composition to the best spectral match, using FeO as a constraint. We then grid the mineral abundances into polar maps. Further details concerning each step are presented below and the resulting polar mineral maps can be seen in Figure 4.9-4.12.

The spectral library used herein contains the same mineral mixtures as derived by *Lemelin et al.* [2015] for the Multiband Imager wavelengths; it contains relative abundances of the mafic minerals at 10 % intervals, and a relative abundance of plagioclase at 1 % intervals, for a total of 6,601 different compositions. The exposure of the lunar surface to space leads to important modifications of its physical properties, *i.e.*, space weathering, which leads to important modifications in the spectral quantities measured. A vapor coating is deposited on soil grains by solar wind sputtering and micrometeorite impact vaporization, and metallic iron particles smaller than the wavelength are reduced and implanted in this coating by the selective loss of oxygen that occurs during vapor deposition [*Hapke*, 2001]. These physical changes lead to spectral darkening, reddening and subdued absorption bands characteristic of each mineral, and need to be accounted for in quantitative mineral analysis. Optically small nanophase iron ("submicroscopic iron") is responsible for the observed reddening of the lunar soil [*Hapke*, 2001; *Noble et al*., 2007; *Lucey and Noble*, 2008], and larger nanophase iron ("Britt-Pieters particles") is responsible for the observed darkening [*Britt and Pieters*, 1994; *Lucey and Riner*, 2011]. Here we compute the mineral mixtures at seven different amounts of submicroscopic and nanophase iron, between 0.5 and 10 wt.% [*Lucey and Riner,* 2011], for a total of 46,207 modeled spectra. We fix the molar MgO/(MgO+FeO) (Mg#) at 65 (representative of the more magnesian of the ferroan anorthosites), and a grain size of 17 μm for all minerals [*Pieters et al*., 1993; *Lucey*, 2006], and both 17 μm and 200 μm for plagioclase to match the band depth observed in the Multiband Imager data [*Ohtake et al*., 2009], for a total of 92,414 modeled spectra. We use the optical constants of *Lucey* [1998] and adjust them so that they provide the best agreement between the mineral abundances measured by the Lunar Soil Characterization Consortium for 19 lunar soil samples of 10-20 μm in particle size [*Taylor et al*., 2001] and our model at the Spectra Profiler wavelengths. *Lucey et al.* [2014] showed that there is a poor correlation of the model and measured mineralogy (25 wt.% error) when using the optical constants of *Lucey* [1998] as is. Olivine is overestimated and the modeled spectra do not match the trend of band minimum versus the ratio of low-calcium pyroxene to the total abundance of pyroxene. As done by *Lucey*

et al. [2014] for the Multiband Imager wavelengths, we perform a grid search, changing the intensity of the imaginary index spectrum for olivine and plagioclase, and changing the position of the imaginary index spectrum minimum for the pyroxenes. We find that increasing the intensity of the imaginary index spectrum for olivine by a factor of 5, that of plagioclase by a factor of 1.7, and shifting the position of the imaginary index spectrum minimum for low-Ca pyroxene by 15 nm to shorter wavelengths, and by 55 nm to longer wavelengths for high-Ca pyroxene provide the best agreement between the LSCC and the modeled mineral abundances. These modified optical constants yield an error (RMSE) of 9 wt.% in mineral abundance at the Spectra Profiler wavelengths (Fig. 4.2).

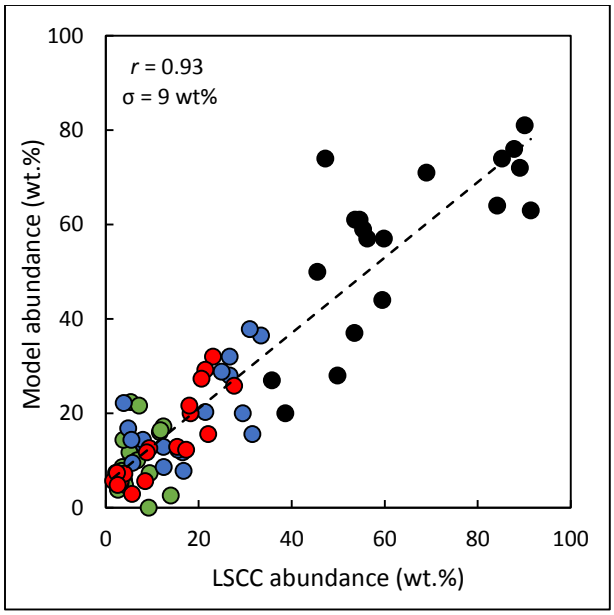

Figure 4.2. Error in mineral abundance between our model and the mineral abundances measured by the Lunar Soil Characterization Consortium (LSCC). The model uses refined optical constants of *Lucey* [1998] to minimize the difference in mineral abundances between our model and the LSCC data. The comparison uses the Spectral Profiler wavelengths between 746.8 and 1555.5 nm. Olivine is shown is green, low-calcium pyroxene in blue, high-calcium pyroxene in red, and plagioclase in black. The correlation (r) between the two data sets is 93%, and the root mean squared error in mineral abundance estimation is 9 wt.%.

To assign a mineralogical composition to a Spectral Profiler spectrum, we remove a continuum (a straight line tangential to the reflectance spectrum at 746.8 and 1555.5 nm) from the library spectra and from the given Spectral Profiler spectrum, and find the closest spectral match (in terms of highest correlation and lowest difference in reflectance between the library and the unknown spectrum). However, because reflectance spectra of different compositions can be similar in shape, we use the abundance of FeO as a constraint. We compute the FeO abundance consistent with the stoichiometric abundance of each mineral mixture in the spectral library, and we compute the FeO abundance corresponding to each spectrum using the algorithm described below (section 4.3.3). Only the library spectra that have ±2 wt% of the FeO content of a given spectrum are compared. After a mineralogical abundance is assigned to a data point, we only keep the compositions that result in spectral match within the Spectral Profiler error (1% reflectance), *i.e*., the spectral matches that have an overall difference in continuum removed reflectance of 1.09 (over the 109 spectral bands) between the Spectral Profiler spectrum and the closest match from the spectral library. We then use these points to produce polar mineral maps at a spatial resolution of 1 km per pixel using the GMT software (version 5.1.1) as done by [*Lemelin et al*., 2016] with the Lunar Orbiter Laser Altimeter data, and described in section (4.3.3).

4.3.3 FeO algorithm and polar map

Lucey et al. [1995] introduced a method for the determination of the iron content of the lunar surface using the reflectance in the visible wavelength (VIS, 750 nm) and the ratio of reflectances in the near infrared over visible wavelengths (NIR, 950 and VIS, 750 nm). They noted trends related to iron content and optical maturity (the optical effects of space weathering) on a plot of the NIR/VIS ratio versus the VIS reflectance for returned lunar samples, and defined an angular parameter using the samples location in that plot. They used the relationship between the iron content of the samples and the spectral parameter to provide a transformation from remotely sensed spectral information to iron content, normalizing the effects of space weathering. *Lucey et al*. [2000] presented this method using reflectance data from the Clementine mission in the equatorial region. Such method requires calibrated reflectance data, which is not available in the polar regions and thus, iron abundances using the reflectance in the visible and near infrared wavelengths have been generally limited to ~50-70°.

To derive the FeO algorithm using the approach of *Lucey et al*. [2000], we combine reflectance measurements acquired by both the Spectral Profiler and the Lunar Orbiter Laser Altimeter (LOLA). We use the reflectance measured by the Spectral Profile at 955.4 and 752.8 nm to derive the reflectance ratio, as the shading effects of topography cancel out in such ratio, and use the calibrated reflectance measured by LOLA at 1064 nm, as it provides calibrated reflectance measurements that are not affected by topography. We use the abundance of FeO measured by the Lunar Prospector Gamma-Ray Spectrometer [*Lawrence et al*., 2002] to validate the Feo abundances derived herein. The reflectance measurements provided by the Spectral Profiler and by LOLA have been acquired at different phase angles, and must be reconciled. The Spectral Profiler reflectance measurements have been calibrated to a standard viewing geometry of $i = 30°$, $e = 0°$, and $\alpha = 30°$, whereas LOLA reflectance measurements have viewing geometry of $i = e = \alpha = 0°$. Since the Moon is not a Lambert surface (an ideal surface that reflect light equally in all directions), its reflectance at $\alpha = 0°$ is greater than its reflectance at $\alpha = 30°$. Thus, 1064 nm LOLA data must be scaled to the Spectral Profiler reflectance data at 1064 nm before it can be used in the algorithm. We first derive an FeO algorithm using reflectance data from the Spectral Profiler in the equatorial region, and then scale the 1064 nm LOLA data to the Spectral Profiler reflectance data in the same equatorial region, far from any bias that could be introduced from topography. We then use that scale factor to derive the abundance of FeO in the polar regions using the reflectance ratio for the Spectral Profiler, and the reflectance data from LOLA.

We first we produce 1 pixel per degree equatorial mosaics of the Spectral Profiler reflectance ratio (955.4 nm over 752.8 nm), and reflectance at 1064 nm (averaging the reflectance at 1059.7 nm and 1067.8 nm) using 467 orbits between orbits 4124 and 4998. We also produce a 1 pixel per degree equatorial mosaic of the FeO abundance measured by the Lunar Prospector Gamma-Ray Spectrometer [*Lawrence et al*., 2002]. We extract the data within 10° of the equator to derive the following equations. We first plot the Spectral Profiler reflectance at 1064 nm (Eq. 4.1) versus the ratio of the reflectance at 955.4 and 752.8 nm and the optimized origin of *Lemelin et al.* [2015] (x_{0Fe}=0.04 and y_{0Fe}=1.39) to derive θ_{Fe1} (Fig. 4.3a, Eq. 4.2). We then use an exponential curve to fit θ_{Fe1} (Fig. 4.3b, Eq. 4.3), and a linear curve to fit θ_{Fe2} (Fig. 4.3c, Eq. 4.4). The abundance of FeO obtained using Spectral Profiler data and the equations herein (Eq. 4.1-4.4) are in agreement with the abundance of FeO measured by the Lunar Prospector Gamma-Ray Spectrometer (Fig. 4.3d, $r = 0.96$).

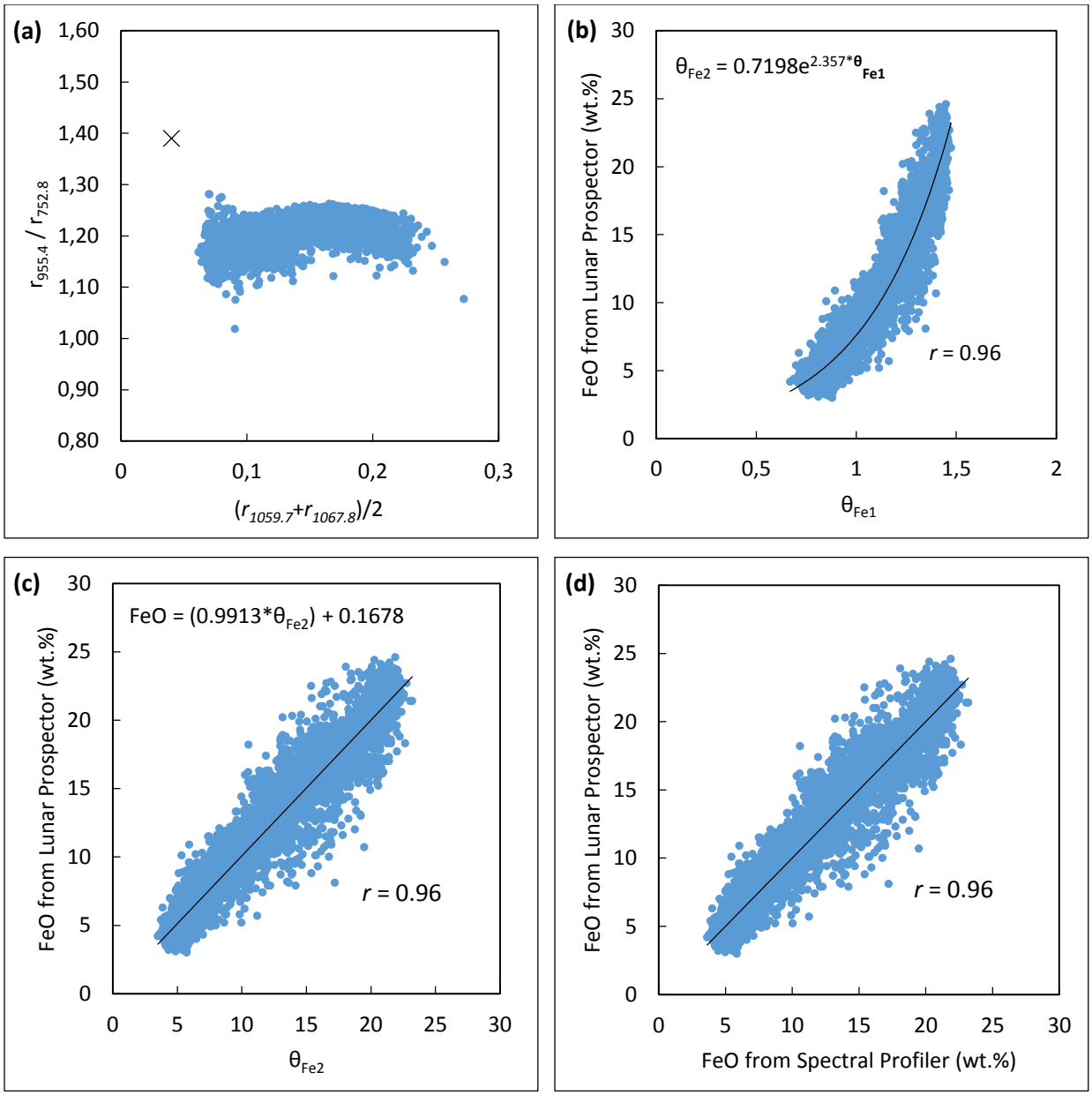

Figure 4.3. FeO algorithm using the Spectral Profiler reflectance data (blue), calibrated against the FeO abundance measured by the Lunar Prospector Gamma-Ray Spectrometer data [*Lawrence et al*., 2002]. a) reflectance data in reflectance versus ratio space, including the optimized origin ('x') of *Lemelin et al*. [2015]. b) regression between the θ_{Fe1} and Lunar Prospector FeO. c) regression between the θ_{Fe2} and Lunar Prospector FeO. d) correlation between the Spectral Profiler FeO and the Lunar Prospector FeO.

$$r_{1064(SP)} = \left(r_{1060(SP)} + r_{1068(SP)}\right)/2 \quad (4.1)$$

$$\theta_{Fe1} = -arctan\left\{\frac{[(r_{955.4}/r_{752.8}) - y_{0Fe}]}{(r_{1064} - x_{0Fe})}\right\} \quad (4.2)$$

$$\theta_{Fe2} = 0.7198e^{(2.357 \cdot \theta_{Fe1})} \quad (4.3)$$

$$FeO\ (wt.\%) = (0.9913 \cdot \theta_{Fe2}) + 0.1678 \quad (4.4)$$

We then scale the 1064 nm LOLA data to the Spectral Profiler 1064 nm reflectance. To find the appropriate scaling factor, we created a 1 pixel per degree equatorial mosaic of the Lunar Orbiter Laser Altimeter reflectance at 1064 nm, and used the 1 pixel per degree equatorial mosaic of the reflectance measured by the Spectral Profiler at 1064 nm (Eq. 4.1). We computed their respective histogram using data within 50° latitude, far from bias that could be introduced due to topography in the Spectral profiler data, and perform a histogram matching, varying the gain until a minimal difference between the two histograms is reached. That gain can then be applied to the Lunar Orbiter Laser Altimeter reflectance data in the polar region (Eq. 4.5), which can in turn be used in the FeO algorithm, replacing the Spectral Profiler reflectance data (Eq. 4.1).

$$r_{1064(LOLA\ corrected)} = r_{1064\ (LOLA)} \cdot 0.56 \quad (4.5)$$

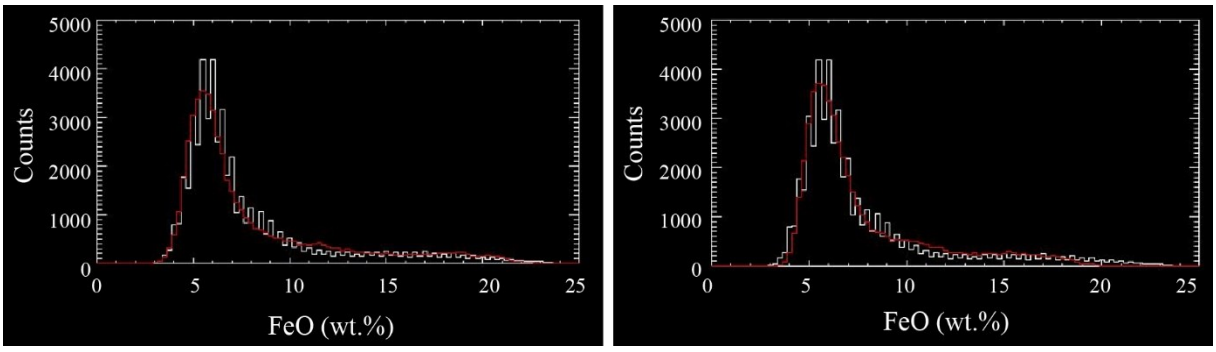

Figure 4.4. Histogram of FeO abundances measured by the Lunar Prospector Gamma-Ray Spectrometer (white line), and derived from the Kaguya Spectral Profiler data (red line) at 1 pixel per degree. Left: using only Spectral Profiler data, right: using Spectral Profiler and LOLA data.

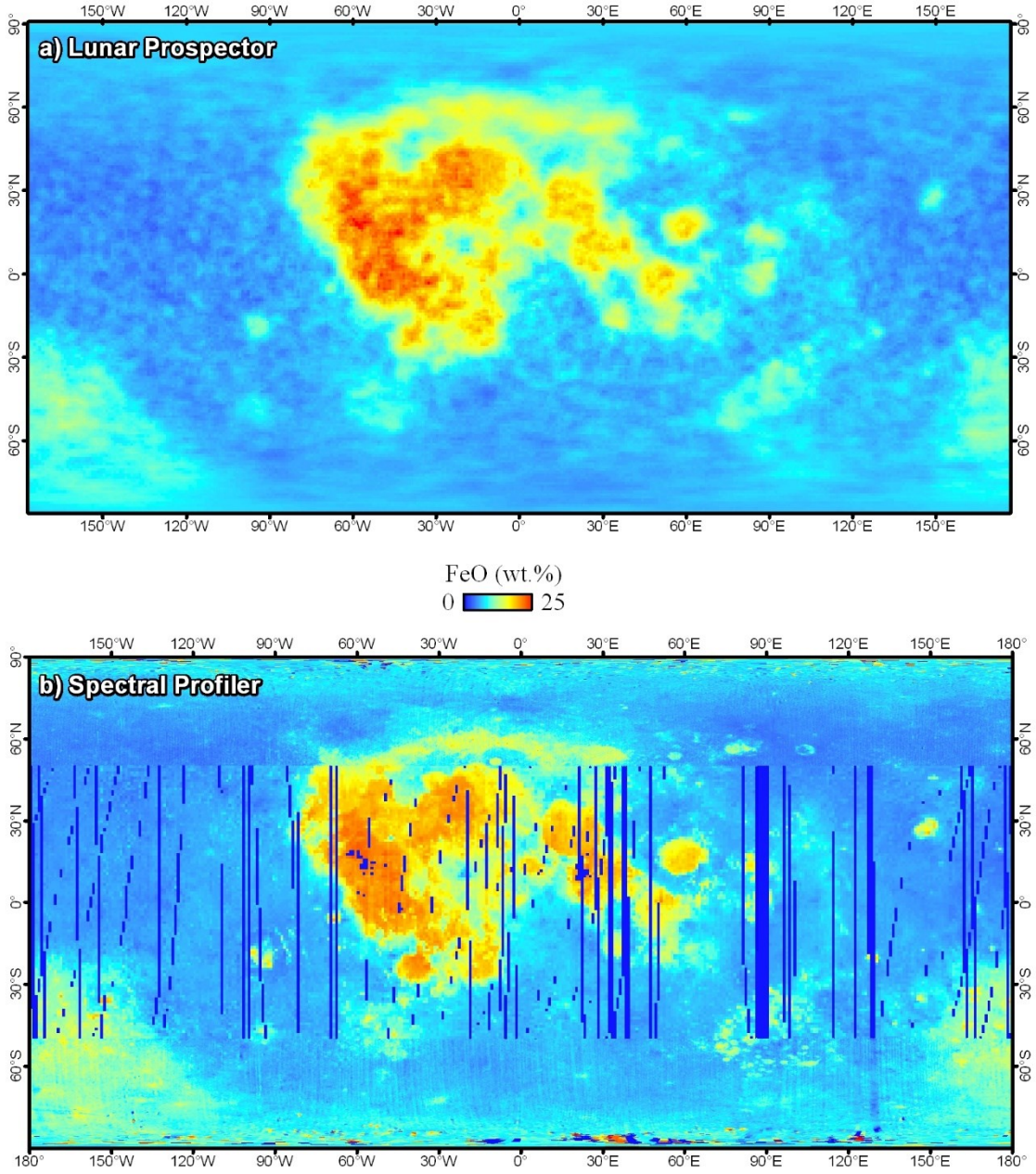

Figure 4.5. Global maps of FeO (a) measured by the Lunar Prospector Gamma-Ray Spectrometer [*Lawrence et al*., 2002], and (b) derived from the Kaguya Spectral Profiler data using the reflectance from orbits 4124 to 4998. The FeO data poleward of 50° in latitude uses Spectral Profiler and LOLA data (Eqs. 4.2-4.5), whereas the equatorial data uses Spectral Profiler data only (Eqs. 4.1-4.4). The maps are shown at 1 pixel per degree.

The Lunar Orbiter Laser Altimeter reflectance data in the polar region has been gridded at a spatial resolution of 1 km per pixel using the GMT software (version 5.1.1) and its "surface" function, an adjustable tension continuous curvature spline function (tension of 0.1, search radius of 5°), to interpolate the data [*Lemelin et al*., 2016]. Here we use the same software and function to produce polar mosaics of the Spectral Profiler reflectance ratio (955.4/752.8 nm) also at 1 km per pixel. We then compute the polar maps of FeO using these mosaics and the equations herein (Eqs. 4.2-4.5, Fig. 4.3). We use the polar maps of FeO as a constraint in our mineral mapping algorithm.

Figure 4.6 shows the resulting polar maps of FeO, and their notable artifacts: (1) minor artifacts parallel to lines of longitude are discernible and are caused by the orbits tracks being interpolated; (2) other artifacts are discernible poleward of ~85° in latitude, namely anomalous FeO values near the South Pole, which are caused by remaining artifacts in the Spectral Profiler reflectance ratio (Fig. 4.7). Inspection of Figure 4.6 also suggests that there is an increase in the abundance of FeO with latitude. We investigate if this increase was also measured by the Lunar Prospector Gamma-Ray Spectrometer. We calculate the average FeO abundance for all longitudes in 1° latitude bins, as measured by the Gamma-Ray Spectrometer and by the Spectral Profiler. Figure 4.8 shows the average FeO abundance versus latitude for each polar region; this increase in FeO with latitude is present in the Spectral Profiler data, but is absent in the Gamma-Ray Spectrometer data. Since the average FeO derived from the Spectral Profiler data is within ±2 wt.% FeO of the Gamma-Ray Spectrometer values at latitudes ≤80° (Fig. X), this artifact should not influence the composition of the central peaks and basin rings derived herein; the central peaks and basin rings are located at latitudes ≤80° and we defined their composition based on the most similar library spectrum within ±2 wt.% FeO of a pixel. Thus, we still investigate the cause of this artifact.

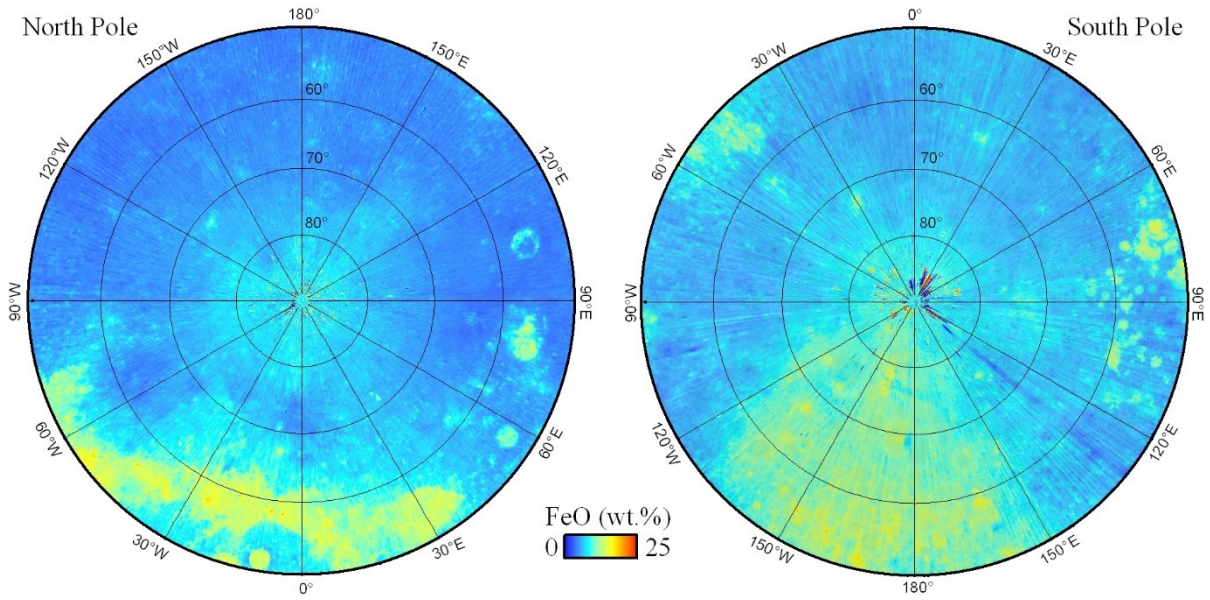

Figure 4.6. Polar maps of FeO abundance derived from the Spectral Profiler data at 1 km per pixel.

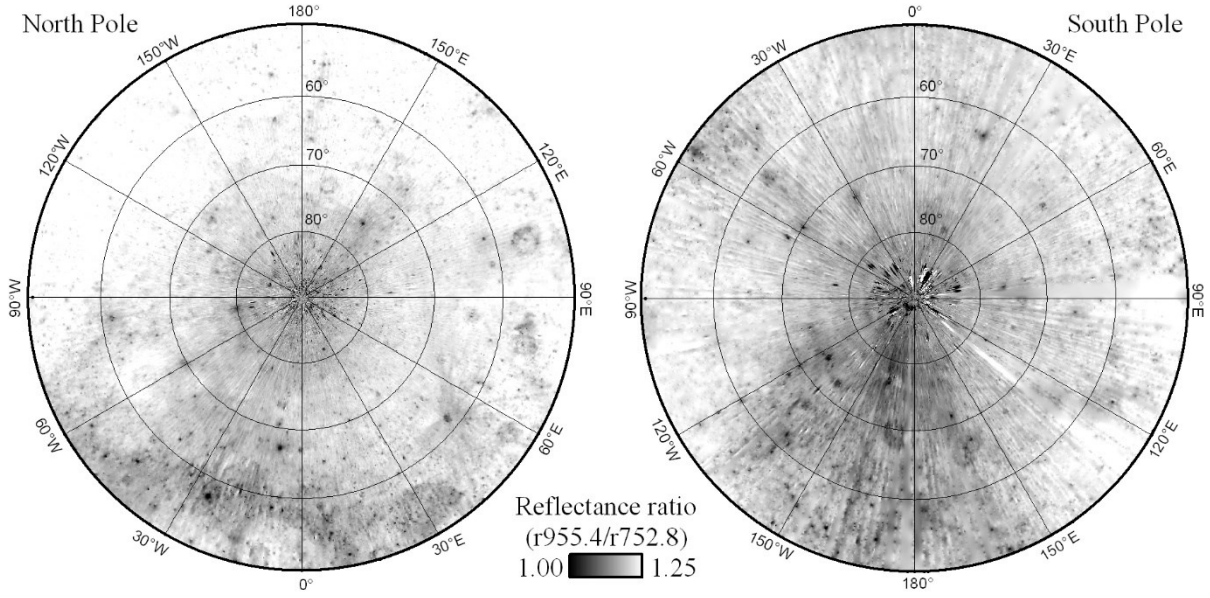

Figure 4.7. Polar maps of the reflectance ratio from the Spectral Profiler data at 1 km per pixel.

Figure 4.8 shows the average FeO abundance versus latitude for each polar region; this increase in FeO with latitude is present in the Spectral Profiler data, but is absent in the Gamma-Ray Spectrometer data, so we investigate the cause of this artifact. Based on equations 4.2-4.5, a decrease in 1064 nm reflectance is linked to an increase in FeO, and a decrease in the reflectance ratio ($r_{955.4}/r_{752.8}$) is due to a decrease in optical maturity. *Hemingway et al*. [2015] found there is a general increase in reflectance with latitude on the Moon, and *Lemelin et al*. [2016] confirmed this increase in the Lunar Orbiter Laser Altimeter reflectance data, which cannot explain the observed increase in FeO with latitude. On the other hand, we observe a decrease in the Spectral Profiler reflectance ratio (Fig. 4.7) with latitude, which was also noted by *Yokota et al*. [2011]. They concluded that highlands in the polar regions have bluer spectra than highlands at lower latitudes, due to the lower degree of space weathering in the polar regions. This indicates that close to the poles, our algorithm does not entirely suppress the effects of maturity, *i.e.*, it interprets an increase in iron where there is a decrease in maturity.

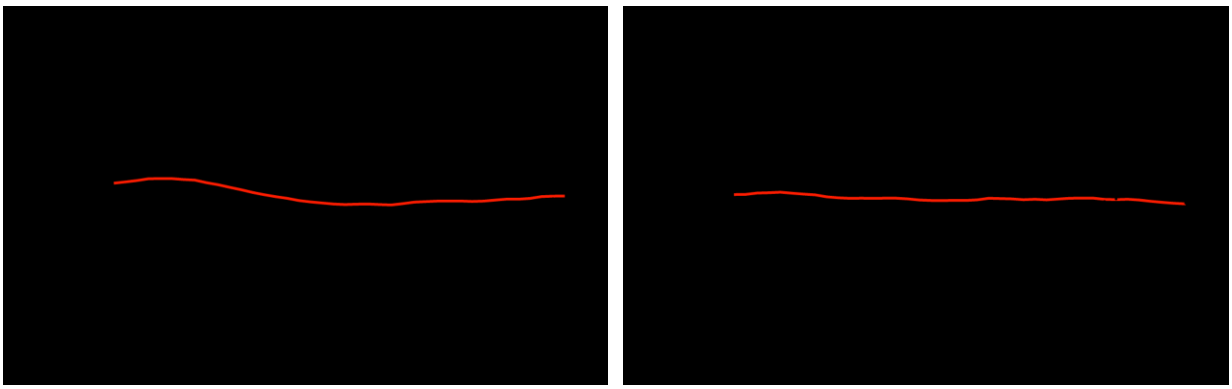

Figure 4.8. Average FeO abundance versus latitude for (a) the North Polar region, and (b) the South Polar region. The red line represents the average FeO abundance measured by the Lunar Prospector Gamma-Ray Spectrometer, the black line represents the average FeO abundance calculated herein using data from the Spectral Profiler, and the dashed lines represent ±2 wt.% FeO. Although we see an increase in FeO abundance with latitude using the Spectral Profiler data, which is absent in the Gamma-Ray Spectrometer data, the discrepancy is within 2 wt.% FeO for latitudes within ±80°. The mineral maps are not affected by this discrepancy within ±80° in latitude as we are analyzing the library spectra that have ±2 wt.% FeO of a given pixel.

4.3.4 Identifying the central peaks and basin rings

To identify and define the region that corresponds to a given central peak or basin ring, we use Lunar Orbiter Laser Altimeter topography data at 128 pixels per degree, USGS geologic maps [*Fortezzo and Hare*, 2013], the diameter of the innermost ring of *Neumann et al.* [2015], and ArcMAP software. We first use the location of the innermost ring of *Neumann et al*. [2015] to identify the ring, and then use the USGS geologic maps to define the area that corresponds to the ring material, termed "circumbasin materials" or "basin materials" in the USGS geologic maps using ArcMAP [*Fortezzo and Hare*, 2013]. There is no identified "circumbasin materials" or "basin materials" at the location of the innermost ring for Coulomb-Sarton, so we digitized the area of the ring based on its difference in topography relative to the basin floor. For Schiller-Zucchius, an area containing "basin materials" is present at the location of the innermost ring but includes portion of the basin floor. We confine the area to the ring only based on topography.

4.3.5 Depth estimates

Previous studies have used different ways to investigating the relationship between the composition of central peaks and basin rings and the depth of origin of the material they expose; some look at the depth of origin of the material relative to the top of the crust, and others look at the depth of origin of the material relative to the crust/mantle boundary, as proposed by *Cahill et al*. [2009]. The lunar basins have greatly redistributed material since the formation of the lunar crust [*Petro and Pieters*, 2008], and using the top of the lunar crust as a reference may obscure depth relationships established at the time of origin of the lunar crust. Therefore, we use the depth of origin of the material relative to the crust/mantle boundary (P) to investigate the composition of the lunar crust in this study. P is calculated from [*Cahill et al*., 2009]:

$$P = T - D_{exc} \tag{4.6}$$

T is the crustal thickness model (Model 1) using data from GRAIL (http://www.ipgp.fr/~wieczor/GRAILCrustalThicknessArchive/GRAILCrustalThicknessArchive.html), and D_o is the depth of origin of the material exposed by the central peak or the basins' innermost ring. For central peaks, we use $D_o = 0.1D$ (where D_{tr} is the transient crater diameter)

from *Melosh* [1989]. For the basins' innermost ring, we use the depth of origin derived in Chapter Three; $D_o = 0.06D_{tr}$ for the shallow component, and $D_o = 0.16D_{tr}$ for the deep component. We also use the percentages of shallow component ($-0.20D_{tr}+140$) and deep component ($0.15D_{tr}-23$) derived in Chapter 3.

4.4. Results

The abundance of olivine, low-calcium pyroxene, high-calcium pyroxene and plagioclase poleward of 50° in latitude is shown in Figures 4.9 to 4.12. Low-calcium pyroxene is more abundant than high-calcium pyroxene, which stands in contrast with the respective abundance of the pyroxenes, as derived using the Multiband Imager data within ±50° in latitude in Chapter Three (Figs. 4.13-4.14). Thus, before we report the composition of the central peaks and basin rings, we compare the mineralogy derived using the Multiband Imager data to the mineralogy derived using the Spectral Profiler data.

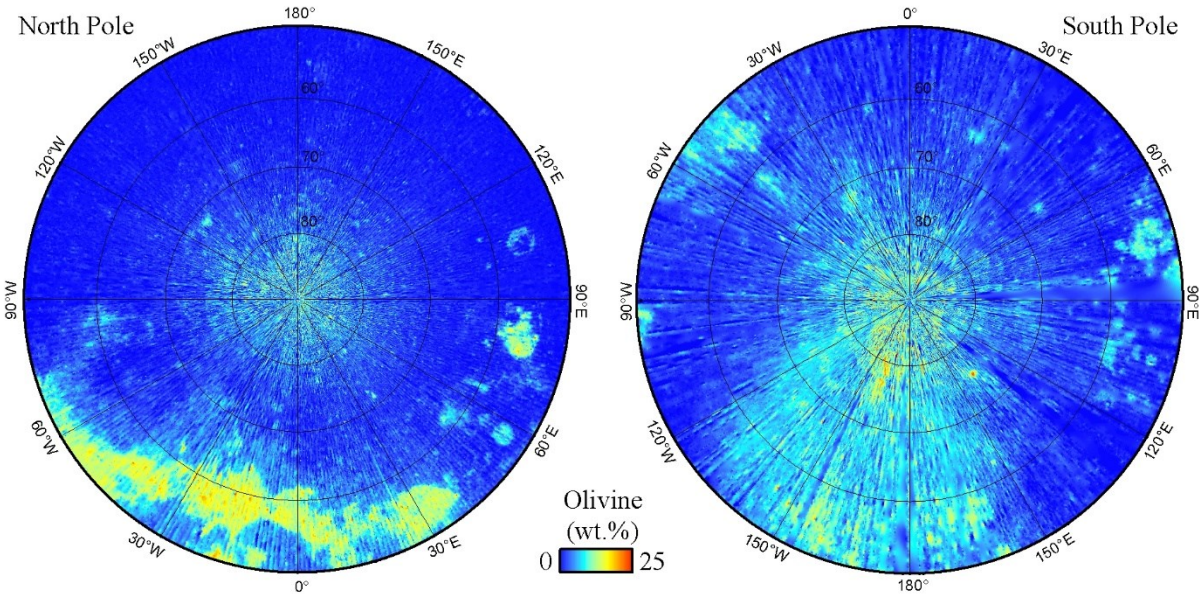

Figure 4.9. Polar maps of olivine derived in this study. The maps are derived for latitudes poleward of ±50° and are shown in polar stereographic projection.

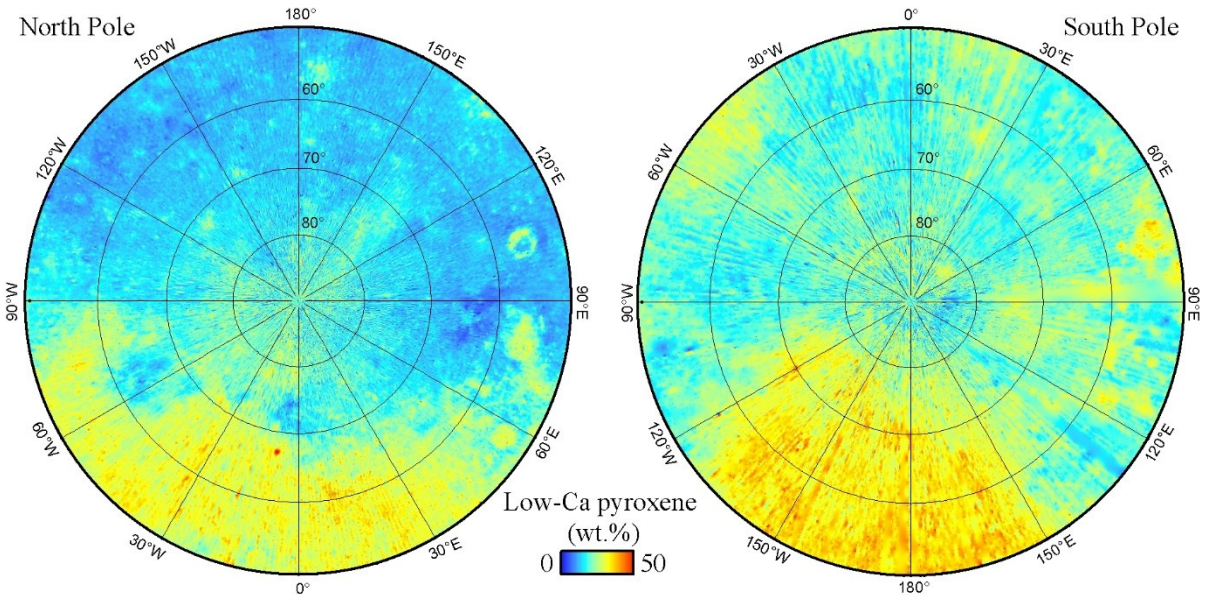

Figure 4.10. Polar maps of low-calcium pyroxene derived in this study. The maps are derived for latitudes poleward of ±50° and are shown in polar stereographic projection.

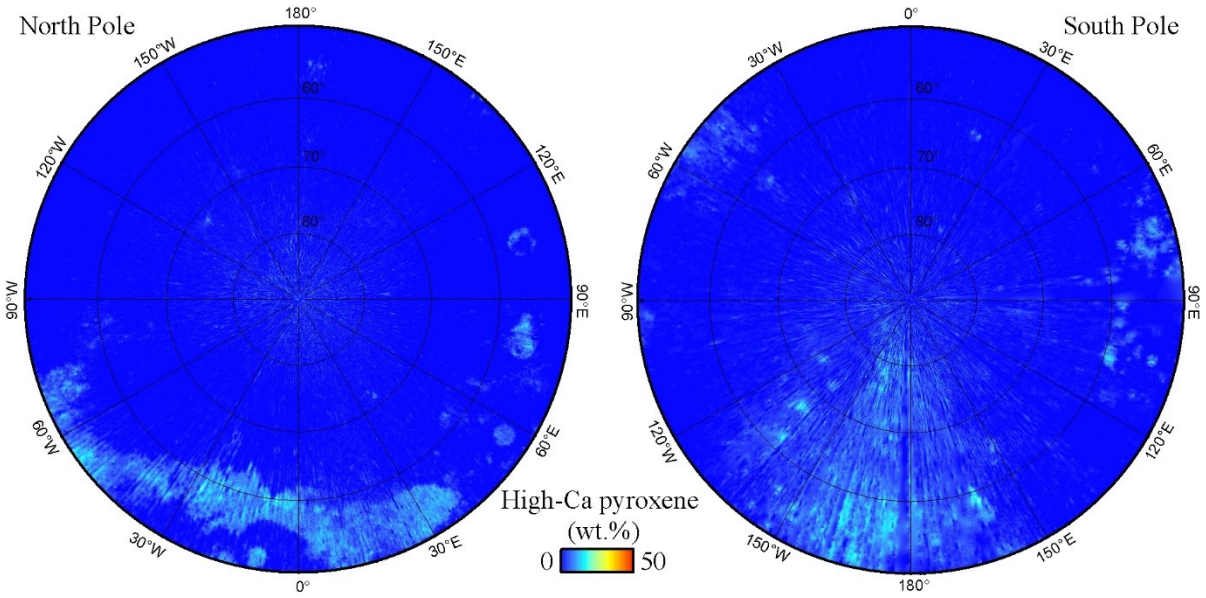

Figure 4.11. Polar maps of high-calcium pyroxene derived in this study. The maps are derived for latitudes poleward of ±50° and are shown in polar stereographic projection.

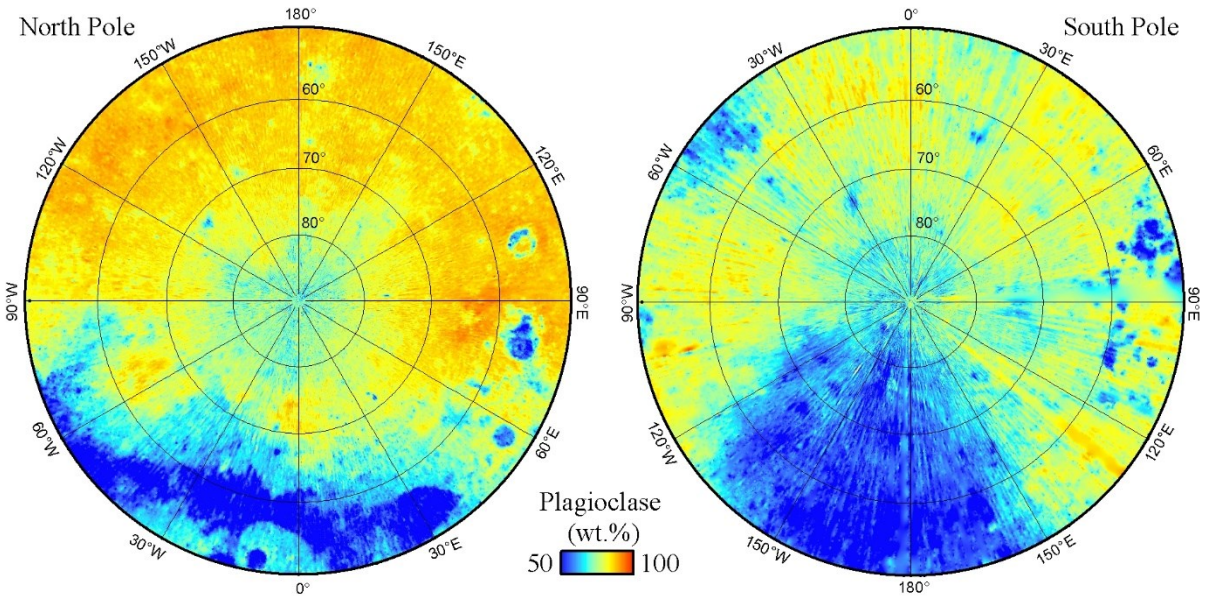

Figure 4.12. Polar maps of plagioclase derived in this study. The maps are derived for latitudes poleward of ±50° and are shown in polar stereographic projection.

4.4.1 Comparative mineralogy: Multiband Imager versus Spectral Profiler data

Figure 4.13 shows the abundance of olivine, low- and high-calcium pyroxene, as well as plagioclase derived using Multiband Imager data (within 50º in latitude, Chapter Two and Three) and using Spectral Profiler data (poleward of 50° in latitude, current Chapter). The abundance of olivine and plagioclase is consistent using either dataset, but the abundance of low- and high-calcium pyroxene is not (Fig. 4.14).The dominance of low-calcium pyroxene is regional within 50° in latitude (in the Multiband Imager data), but ubiquitous poleward of 50° in latitude (in the Spectral Profiler data). The main factor controlling the relative proportion of low-calcium pyroxene and high-calcium pyroxene using radiative transfer modeling in the 750 to 1550 nm wavelengths range is the position of the absorption band near 1000 nm. This absorption band is due to electronic transitions of Fe^{2+} and shifts towards longer wavelengths with increasing iron and calcium content [*Adams*, 1974]. For low-calcium pyroxene, this absorption band occurs near ~900 nm. For high-calcium pyroxene it occurs near ~1000 nm. Thus, potential explanations for the differences in pyroxene abundances as derived from the Multiband Imager or the Spectral Profiler dataset include: (1) the use of optical constants optimized differently for each dataset, or (2) the inherently different reflectance measured by each instrument, we investigate both.

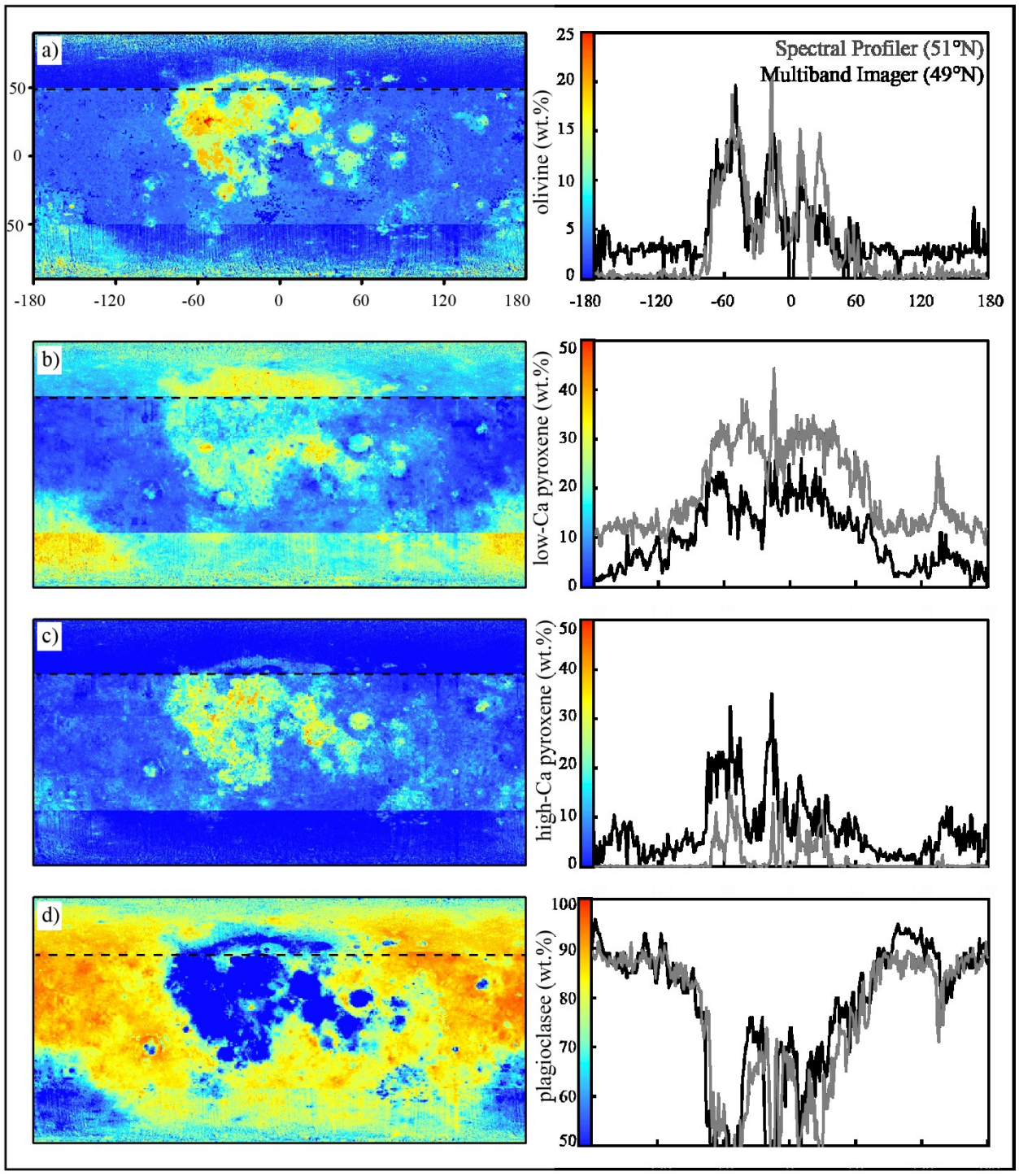

Figure 4.13. Abundance of the major lunar minerals as derived using the Multiband Imager (MI) within ±50° in latitude, and using the Spectral Profiler (SP) poleward of ±50° in latitude. Left: global mineral maps. Right: cross section of the mineral abundance at 49°N from MI data (black line), and mineral abundance at 51°N from the SP data (gray line). The abundance of olivine and plagioclase are in good agreement, but the abundance of pyroxenes are not (Δ > error of 9 wt.%).

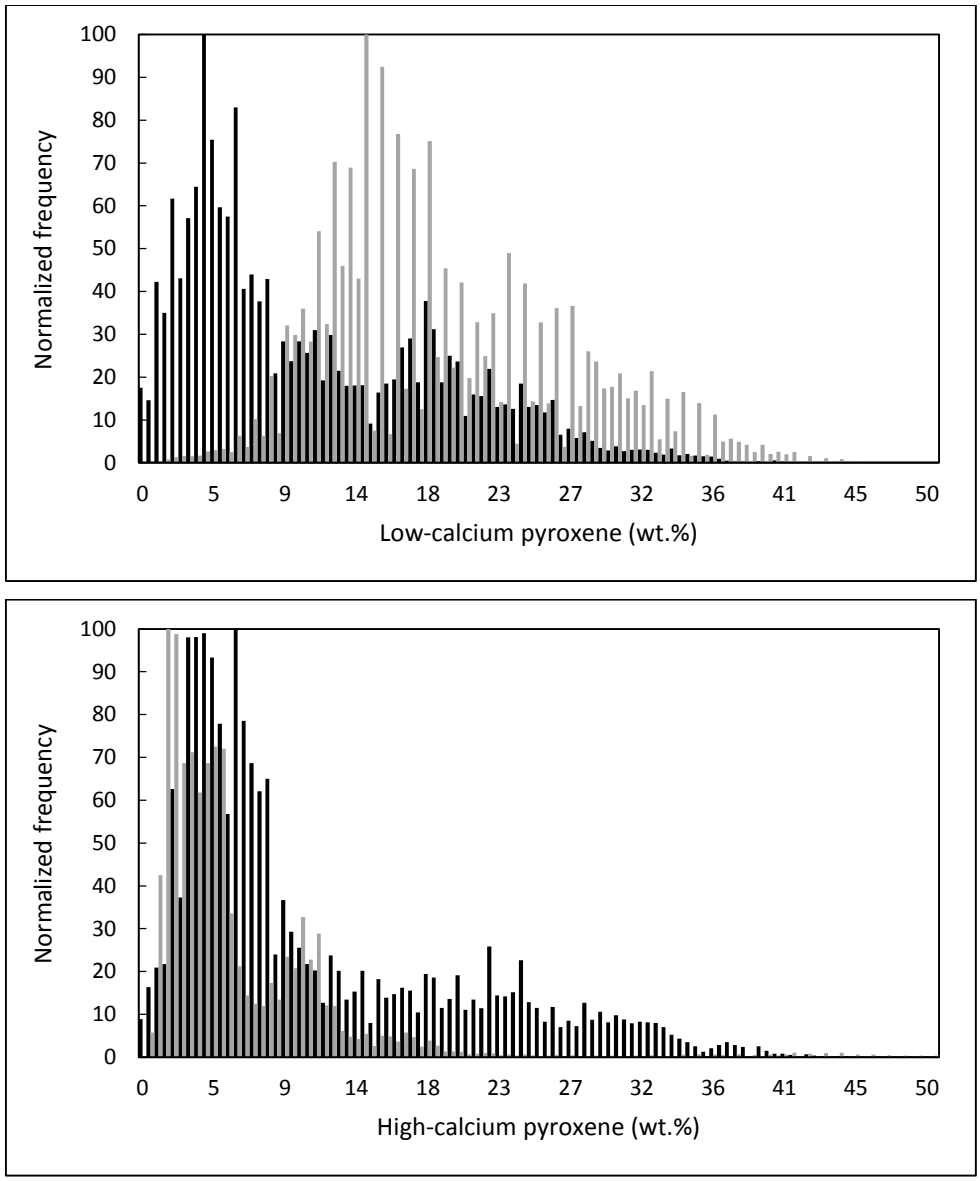

Figure 4.14. Abundance of low-calcium pyroxene and high-calcium pyroxene as derived using the Multiband Imager data within 50° in latitude (black) and the Spectral Profiler poleward of 50° in latitude (gray). While the Multiband Imager data suggests that low and high calcium pyroxene are present in similar abundances in the equatorial region, the Spectral Profiler data suggests that low-calcium pyroxene is much more abundance than high-calcium pyroxene in the polar region.

To derive the spectral libraries in this study, we use the optical constants of *Lucey* [1998] which we validate and optimize using the reflectance spectra of Apollo soil samples of known mineralogical composition. In *Lemelin et al.* [2015] these optical constants were refined at the Multiband Imager wavelengths and yielded an error of ~8 wt.% in mineral abundance estimation. In this Chapter, these optical constants were refined at the Spectral Profiler wavelengths and yield an error of ~9 wt.% in mineral abundance estimation. Figure 4.15 shows the continuum removed spectra of the resulting pure end-members as used by *Lemelin et al*. [2015] (dashed line), and in this Chapter (solid line). The position of the absorption band for low-calcium pyroxene (blue) and for high-calcium pyroxene (red) is not significantly different using either method, and thus we conclude that the different optical constants cannot explain the Multiband Imager and Spectral Profiler pyroxene abundance discrepancy.

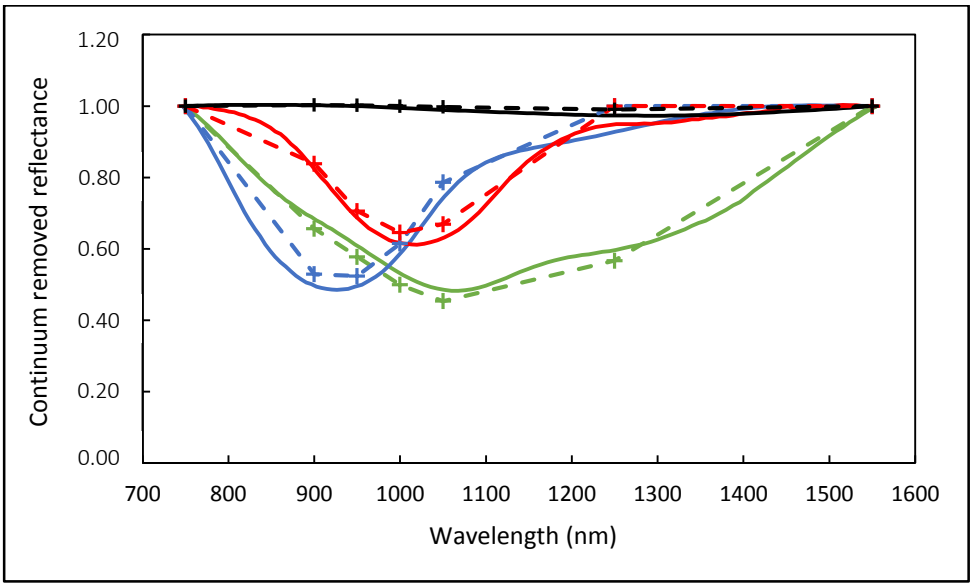

Figure 4.15. Modeled spectra for olivine (green), low-calcium pyroxene (blue), high-calcium pyroxene (red), and plagioclase (black). The solid line represent the modeled spectra in this study at the Spectral Profiler wavelengths. The dashed line represent the modeled spectra in Chapters 2 and 3 using the Multiband Imager wavelengths.

Alternatively, the difference in pyroxene abundances can be due to differences in calibration by each instrument. To investigate this possibility, we identify the position of the band minimum in each of the datasets at similar spatial resolution. We use the reflectance mosaic of the Multiband Imager data at 32 pixel per degrees (~1 km per pixel), within ±50° in latitude, remove the continuum and record the position of the band minimum. For the Spectral Profiler data, we use the reflectance of each data point (~500 m per point) poleward of ±50° in latitude from the 1144 orbits studied herein, remove the continuum and record the position of the band minimum. Figure 4.16 shows the distribution of the band minimum (in the wavelengths range relevant for the pyroxenes) for each dataset. The highest occurrence of band minimum in both datasets occur at 950 nm (which can correspond to a pyroxene of intermediate composition, or equal proportions of low and high-calcium pyroxenes), with respectively 78 % of the Multiband Imager data, versus only ~10 % of the Spectral Profiler data. Approximately 18 % of the Multiband Imager data is characterized with a band minimum at 1000 nm, versus <1 % of the Spectral Profiler data, which is consistent with the low abundance of low-calcium pyroxene derived from the Spectral Profiler data. Thus, the difference in pyroxene abundances is due to the inherently different reflectance measured by each instrument.

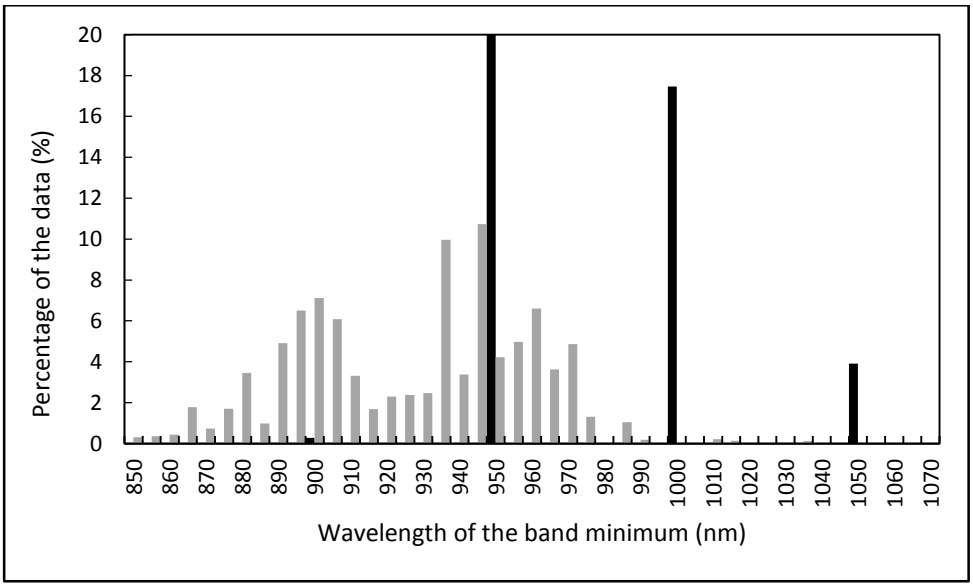

Figure 4.16. Position of the band minimum between 750 and 1550 nm in the Spectral Profiler continuum removed reflectance data poleward of 50° in latitude (gray), and of the Multiband Imager data within 50° in latitude (black). The position of the band minimum is shown here for

the wavelength range representative of the two pyroxene compositions in our spectral library: ~900 nm for low-calcium pyroxene, and near ~1000 nm for high-calcium pyroxene. The band minimum for the Spectral Profiler data was calculated using the reflectance data from the 1144 orbits studied herein, and the band minimum for the Multiband imager data was calculated using the gridded data at 32 pixels per degree. The band minimum occurs almost always at shorter wavelengths than 1 μm in the Spectral Profiler, explaining the dominance of low-calcium pyroxene detected. The band minimum is often near ~950 nm in the Multiband Imager data (78% of the Multiband Imager data) explaining the detection of both pyroxenes in similar proportions.

In a series of review papers, "One Moon, many measurements", *Pieters et al*. [2013], *Besse et al*.[2013], and *Ohtake et al*. [2013] respectively describe the different radiance values, photometric corrections and reflectance values associated with various recent remote sensing instruments in orbit around the Moon, namely the Multiband Imager and the Spectral Profiler. While the radiance values measured by the Multiband Imager and the Spectral Profiler are similar [*Pieters* et al., 2013], their photometric correction have differences. The photometric correction used for the Multiband Imager data removed the contribution of local topography, while the photometric correction used for the Spectral Profiler data does not. Most importantly, the reflectance measured by the Multiband Imager data has undergone ground truth correction; the reflectance measured by the Multiband Imager over the Apollo 16 sampling site has been calibrated to match the laboratory reflectance of the Apollo 62231 in absolute albedo and continuum slope [*Ohtake et a*l., 2010]. The ground truth procedure has also been done for the Spectral Profiler data, but has not been delivered (and has not been done in the processing level 2B1 used herein). As shown in figure 4.17 [from *Ohtake et al.,* 2013], the ground truth procedure also results in a shift of the 1000 nm absorption band to longer wavelength. Thus, since the composition of the pyroxene is so different when derived from each instrument, in the following sections we report the total abundance of both pyroxenes as one.

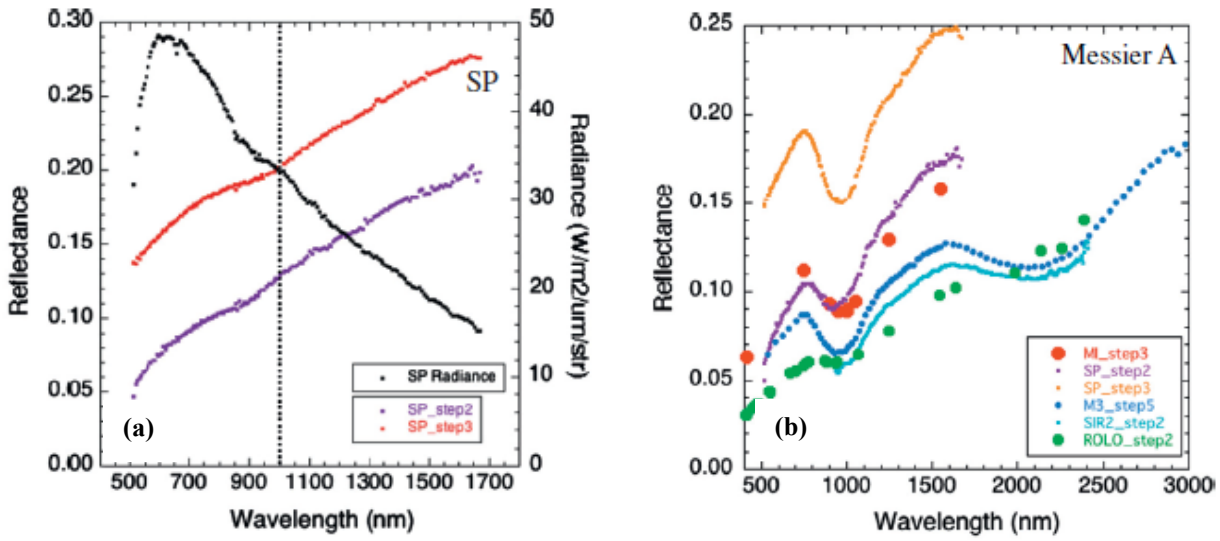

Figure 4.17. Reflectance spectra derived from various instruments and processing levels. Left: Spectra of the Apollo 6 standard site measured by the Spectral Profiler before (SP_step2) and after (SP_step3) the ground truth calibration. This figure shows the shift if the absorption band position near 900 nm before and near 1000 nm after the correction. Right: Reflectance spectra derived by various instruments at Messier A, a fresh mare region. This figure shows the difference in the position of the absorption band between the Multiband Imager data (MI_step3, near 1000 nm) and the Spectral Profiler data (SP_step2, near 900 nm). Both figures are from *Ohtake et al*. [2013].

4.4.2 Mineral abundance of the central peaks and basin rings

We extracted the average abundance of plagioclase, olivine, pyroxenes, and iron for each central peak (Table 4.1) and for each basin ring (Table 4.2), along with the proximity to the crust/mantle boundary (P), the crustal thickness (T) and the depth of origin (D_o) of each impact structure. We find that with few exceptions the central peaks and the basin rings in the Feldspathic Highlands Terrane have anorthositic compositions, whereas the central peaks in the South Pole Aitken Basin have the composition of norite or gabbro. The only new polar central peak we analyze in the Procellarum KREEP terrane also has a composition corresponding to either anorthositic norite/gabbro or norite/gabbro. We observe the same compositions for the basin rings in the respective geochemichal terranes. Consistent with *Lemelin* et al. [2015] and with Chapter Three, we find that pyroxene is always more abundant than olivine on the central peaks and on the basin rings.

Table 4.1. Average abundance of plagioclase (PLG), olivine (OL), pyroxene (PYX), and iron (FeO) of the central peak in the craters analyzed in this study, estimated proximity to the crust/mantle boundary (*P*), crustal thickness (*T*), and depth of origin (D_o).

Crater	Latitude (deg)	Longitude (deg)	PLG (wt.%)	OL (wt.%)	PYX (wt.%)	FeO (wt.%)	*P* (km)	*T* (km)	D_o (km)
Feldspathic Highlands Terrane (FHT)									
Stormer	57.0	146,7	82	1	17	9	27	34	7
Zucchius	-61.4	-50,3	66	11	22	9	26	32	6
Stebbins	64.6	-142,9	87	1	12	5	25	38	13
Carpenter	69.4	-50,9	80	3	17	5	25	31	6
Moretus	-70.7	-6,1	75	8	16	7	24	35	11
Hausen	-65.0	-87,7	77	6	17	7	24	41	17
Lilius	-54.5	6,0	71	2	27	7	23	29	6
Repsold	51.5	-78,3	74	2	24	6	22	33	11
Bettinus	-63.4	-44,8	75	4	21	6	22	29	7
Pythagoras	63.5	-63,0	86	3	12	5	20	34	14
Vlacq	-53.5	38,7	81	0	20	5	18	27	9
Compton	55.3	103,8	78	3	18	6	12	28	16
Clavius	-58.8	-14,1	85	1	14	5	6	30	25
Bel'kovich	61.1	90,2	92	1	7	4	-2	19	21
Minimum			*66*	*0*	*7*	*4*	*-2*	*19*	*6*
Maximum			*92*	*11*	*27*	*9*	*27*	*41*	*25*
Average			*79*	*3*	*17*	*6*	*19*	*32*	*12*
South-Pole-Aitken Basin (SPA)									
Lyman	-64,8	163,6	57	5	38	10	13	22	8
Fizeau	-58,6	-133,9	54	7	38	11	11	18	7
Crommelin C	-66,4	-144,8	63	9	27	9	11	15	4
Lemaitre S	-61,6	-156,3	48	10	42	12	10	13	3
Hopmann	-50,8	160,3	45	9	46	13	10	18	9
Eijkman	-63,1	-141,5	60	7	32	10	10	15	5
Stoney	-55,3	-156,1	44	12	44	15	9	14	5
Crommelin	-68,1	-146,9	54	8	38	11	8	18	9
Boyle	-53,1	178,1	54	9	37	11	8	14	6
Bhabha	-55,1	-164,5	44	9	48	14	7	14	6
Bose	-53,5	-170,0	49	7	45	13	7	16	9
Antoniadi	-69,7	-172,0	47	11	43	12	3	18	14
Minimum			*44*	*5*	*27*	*9*	*3*	*13*	*3*
Maximum			*63*	*12*	*48*	*15*	*13*	*22*	*14*
Average			*52*	*9*	*40*	*12*	*9*	*16*	*7*
Procellarum KREEP Terrane (PKT)									
Aristoteles	50,2	17,4	60	5	35		15	24	9

Table 4.2. The average abundance of plagioclase (PLG), olivine (OL), pyroxene (PYX), and iron (FeO) of the basins' innermost ring, the estimated proximity to the crust/mantle boundary (*P*), crustal thickness (*T*), and the depth of origin of the shallow (D_s) and deep (D_d) component.

Basin	Latitude (deg)	Longitude (deg)	PLG (wt.%)	OL (wt.%)	PYX (wt.%)	FeO (wt.%)	P_s	P_d	T	D_s	D_d
Feldspathic Highlands Terrane (FHT)											
Birkhoff	58.9	-146.6	87	1	11	4	30	12	41	11	29
Schiller-Zucchius	-55.7	-45.2	76	3	21	6	21	1	33	12	32
Coulomb-Sarton	51.2	-122.5	90	1	9	4	19	-15	39	20	54
Humboldtia-num	57.3	82.0	85	1	14	5	11	-18	28	17	46
Minimum			76	1	9	4	11	-18	28	11	29
Maximum			90	3	21	6	30	12	41	20	54
Average			85	2	14	5	20	-5	35	15	40
South-Pole-Aitken Basin (SPA)											
Schrödinger	-74.9	133.5	76	5	20	7	16	-7	30	14	37

Figure 4.18 shows the average plagioclase content of each central peak (triangles) and basin ring (circles) versus their proximity to the crust mantle boundary. On the left (Fig. 4.18a-c), the central peaks and basin rings from this study are shown. On the right, (Fig. 4.18b-d) both the central peaks and basin rings in this study and from the two previous chapters are shown. On the top (Fig. 4.18a-b), the depth of origin of the shallow component of the basin is shown in blue, and the deep component in green. Because we concluded that the shallow component largely dominates the material exposed on the innermost ring of basins, on the bottom figure (Fig. 4.18c-d) we show only the shallow component to represent the basin composition, and color code according to the three geochemical terranes. The top figure (Fig. 4.18a-b) shows that the central peaks and basin rings in the polar region have similar composition to the central peaks and basin rings in the equatorial region, and that the shallow components of the innermost basin rings have similar composition to the central peaks at similar depths, reinforcing the fact that the innermost rings are dominated by its shallow component. The average plagioclase content appears to be decreasing as the material originates from closer to the crust-mantle boundary, as suggested by [*Ryder and Wood*, 1977]. However, *Lemelin et al*. [2015] suggest that this is an artifact due to the fact that the central peaks SPA are inherently more mafic and expose material originating closer to the crust-mantle boundary than the central peaks in the FHT. They argued that the

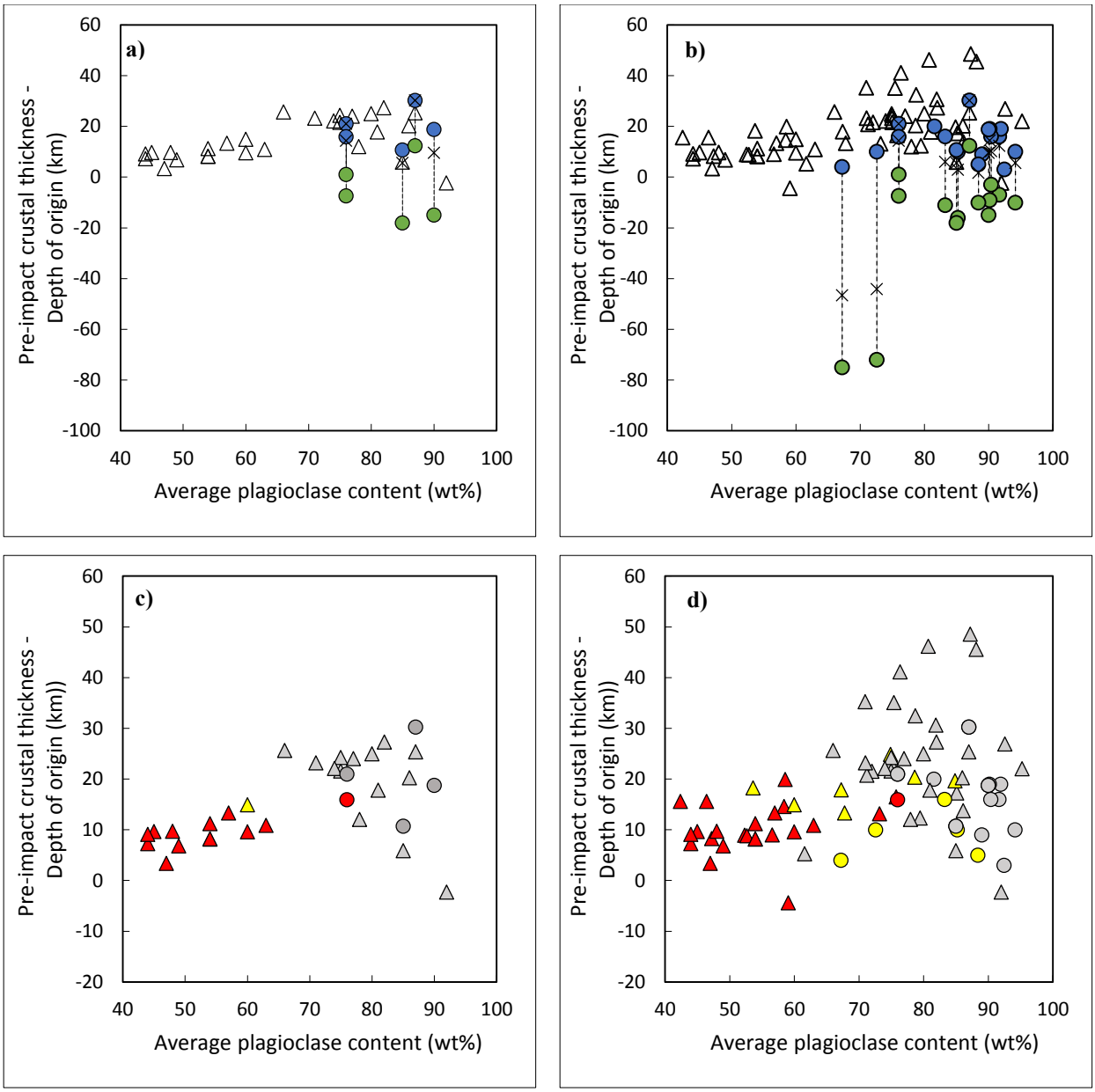

Figure 4.18. Average plagioclase content of the central peaks (triangles) and basin rings (circles) versus their proximity to the crust mantle boundary. Left: central peaks and basin rings in this study (>50° in latitude). Right: central peaks and basin rings at all latitudes, including those studied by *Lemelin et al.* [2015] presented in Chapters Two and Three (50° in latitude) and in this study (>50° in latitude). Top: the shallow component of the basins is shown in blue, the deep component in green. Bottom: the central peaks and basins are color coded according to their geochemical terranes, red: South Pole Aitken basin, yellow: Procellarum KREEP Terrane, gray: Feldspathic Highlands Terrane. The shallow component is shown for the basins.

central peaks in the FHT span through the entire column and are not more mafic with depth when confined to this single terrane. The bottom figure (Fig. 4.18c-d) shows the composition of the central peaks and basin rings according to their respective geochemical terrane. As found by *Lemelin et al.* [2015], the central peaks and basin rings in the polar region span through most of the crustal column and do not become more mafic with depth. However, there might be a decrease in plagioclase content with depth when considering only the central peaks and basin rings in SPA (Fig. 4.18c). When looking at the data from all latitudes (Fig. 4.18d), a weak decrease in plagioclase content with depth might still be present.

4.4.2.1 South Pole-Aitken basin

The South Pole-Aitken basin (SPA) in the oldest and largest impact structure on the Moon (~2000 km in diameter). The impact that led to its formation ejected crustal material, and likely produced a ~50 km thick melt sheet that differentiated [*Morrison,* 1998; *Potter et al*., 2012]. *Hurwitz and Kring* [2014] modeled the differentiation of the potential melt sheet following 9 different scenarios, each one involving a different initial melt composition. They concluded that a ~6 km thick gabbroic norite layer overlying a ~8 km thick noritic gabbro layer (overlying a ~23 km thick gabbro layer) could have formed as the result of impact into a pre-overturn, Fe, Al-enriched, fractionally crystallized Moon, consistent with the magnitude of gravity anomalies in the interior of SPA which suggests a ~12.5 km thick layer of norite [*Wieczorek et al*., 2013]. The central peaks located in SPA, both from this study and form *Lemelin et al.* [2015] have a noritic/gabbroic composition from the top of the SPA down to ~25 km deep, consistent with this theory. There appears to be a weak decrease in plagioclase content with increasing proximity to the crust mantle boundary, although some central peaks do not follow that trend (Fig. 4.19). Inspection of the geological context for those central peaks suggest that they expose either material being previously overturned by other craters and basins, or that they are located towards the outer edges of the crater (*e.g*., Von Karman, Birkeland, White, Dryden). As billion years of impact cratering occurred after the formation of SPA, we hypothesize that a potential decrease in plagioclase abundance with increasing proximity to the crust/mantle boundary might be due to the redistribution of anorthositic material on top of SPA by surrounding impact craters.

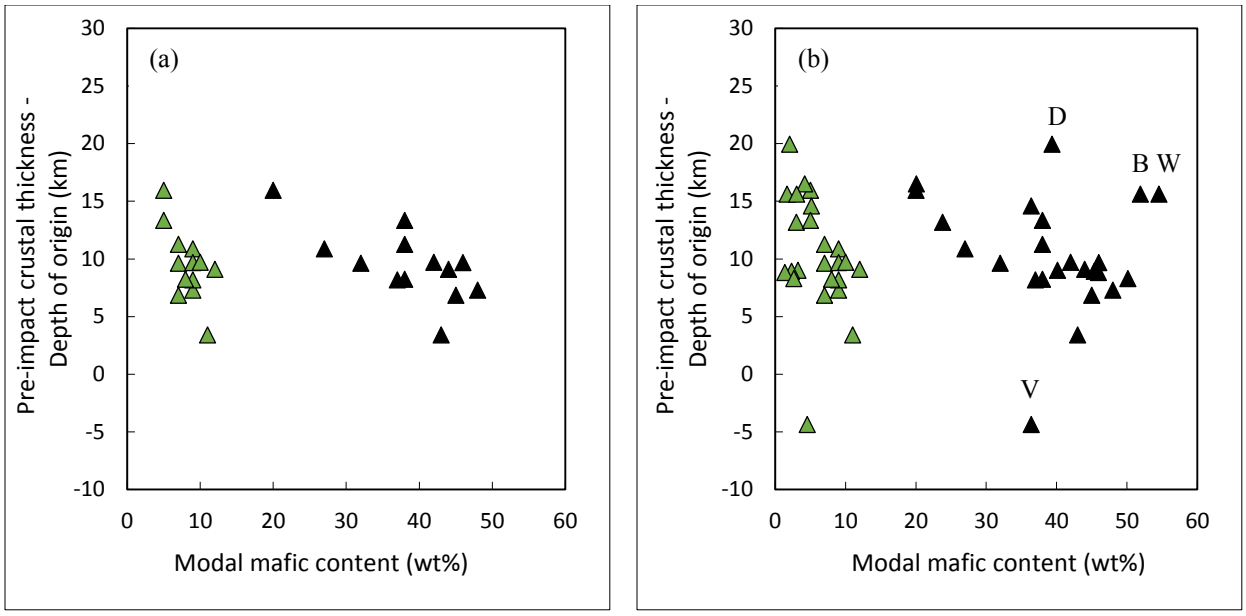

Figure 4.19. Average abundance of olivine (green) and pyroxene (black) content of the central peaks in the South Pole-Aitken basin (including the inner ring of Schrödinger basin) versus their proximity to the crust mantle boundary. (a) central peaks and basin rings in this study (>50° in latitude). (b) central peaks at all latitudes in the South Pole Aitken basin, including those studied by *Lemelin et al.* [2015] presented in Chapters Two and Three, and in this study (>50° in latitude). There appears to be a weak decrease in plagioclase content with increasing proximity to the crust mantle boundary, although some central peaks do not follow that trend: Von Karman (V), Birkeland (B), White (W), Dryden (D).

4.4.2.2 Comparison with previous studies

To compare our results with results from previous studies, we investigate the composition of Schrödinger basin. Studies detected spectra dominated by pure anorthosite [*Ohtake et al*., 2009] and olivine [*Yamamoto et al*., 2010] associated with Schrödinger basin. *Kramer et al.* [2013] confirmed the presence of large areas of anorthite-rich material, low-calcium pyroxene material (a noritic unit), and olivine-rich material (troctolite or dunite), although the precise modal mineralogy was not determined. We find exposures of anorthosite in the same region as detected by *Ohtake et al*. [2009] and *Kramer et al.* [2013] (Fig. 4.20). We also find exposures of norite as detected by *Kramer et al.* [2013] with ~50 wt.% plagioclase and ~50 wt.% low-calcium pyroxene (Fig. 4.20). We also detect regions with high olivine abundances as detected by *Yamamoto et al*. [2010], but our radiative transfer modeling suggests that the highest abundance

of olivine on the ring is ~ 20 wt.% and corresponds to anorthositic troctolite (Fig. 4.20). As *Yamamoto et al*. [2010] searched through nearly 70 million spectra, and we used only ~1000 of these spectra, it is conceivable that we analyzed pixels contiguous to, but not exactly the same as, the ones analyzed by *Yamamoto et al*. [2010].

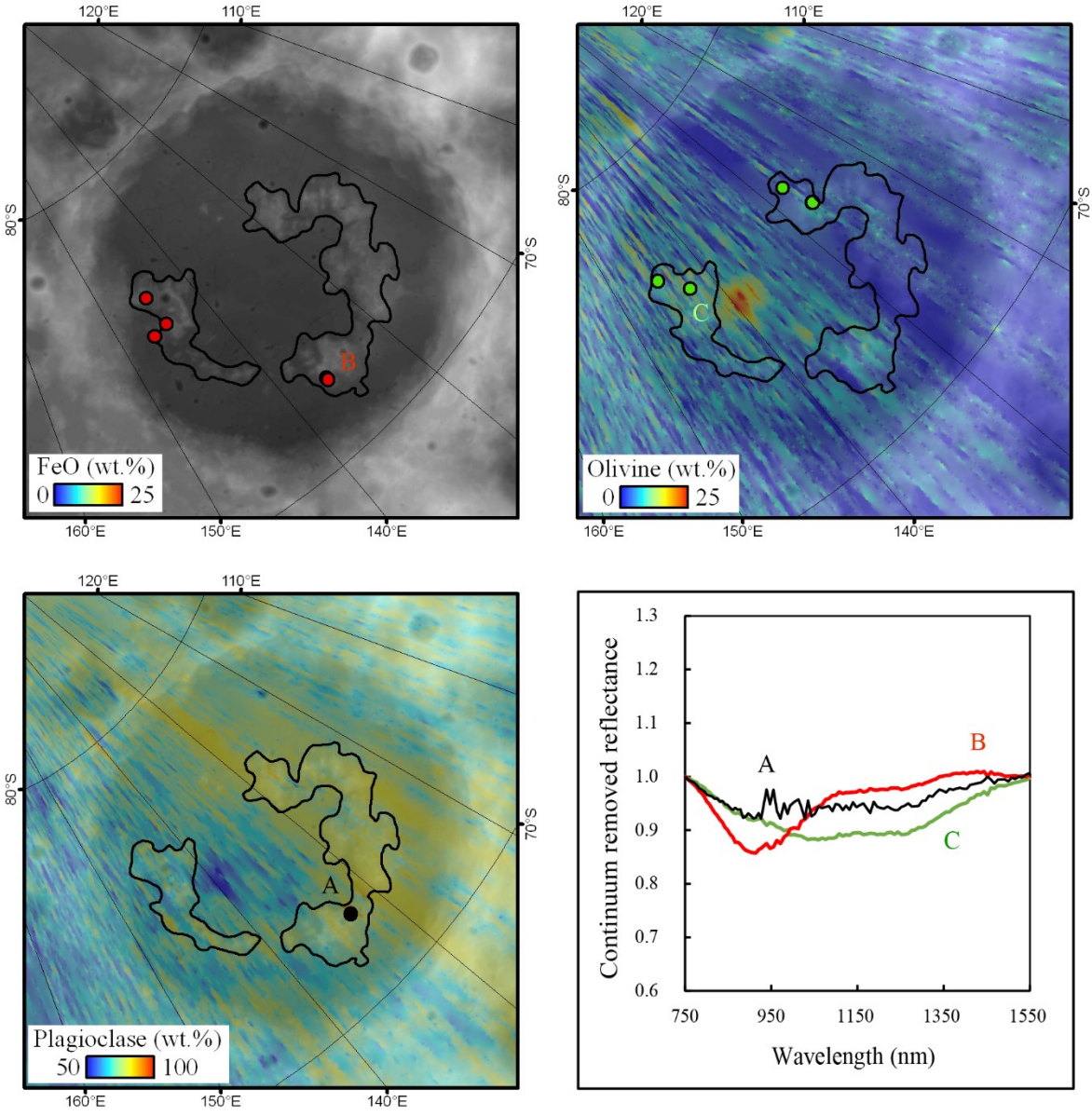

Figure 4.20. Abundance of iron, olivine, and plagioclase in Schrödinger basin over topography from the Lunar Orbiter Laser Altimeter. The black line shows the outline of the ring. Three continuum removed reflectance spectra from the ring material are shown: A-anorthosite with 90 wt.% plagioclase and 10 wt.% low-calcium pyroxene (orbit 4734), B-norite with 50 wt.%

plagioclase and 50 wt.% low-calcium pyroxene (orbit 4731), and C-anorthositic troctolite with 25 wt.% olivine, 11 wt.% low-calcium pyroxene and 64 wt.% plagioclase (orbit 4726).

4.5. Conclusion

In this study, we took a novel approach and used strong signal and well calibrated reflectance data acquired by two different instruments, the Kaguya Spectra Profiler and the Lunar Orbiter Laser Altimeter, in order to derive the first high resolution FeO and mineralogic maps of the polar regions. The polar map of iron derived from these two datasets is in good agreement with the abundance of iron measured by the Lunar Prospector Gamma-Ray Spectrometer, and few remaining artifacts will be investigated and corrected in the future, namely the slow increase in iron with latitude and the presence of noise between 80-90° in latitude. We used the mineral maps to study the composition of 27 central peaks and 5 basin rings in the polar regions, nearly doubling the number of central peaks and basin rings studied in Chapters Two and Three. The mineral abundances derived herein use different datasets than the mineral abundances from the previous Chapters, and consist in an independent dataset to study composition of the lunar crust. Consistent with Chapter Two, we find that the central peaks and basin rings in Feldspathic Highlands Terrane are mostly anorthositic in composition, whereas the central peaks and basin rings in the South Pole-Aikten are mostly noritic and gabbroic. We also measured an intermediate composition for the central peak located in the Procellarum KREEP Terrane. We find that the central peaks in the South Pole-Aitken basin are noritic and gabbroic at all depths (about 27 km away from the crust/mantle down to approximately the crust/mantle boundary), consistent with the presence of a large differentiated melt sheet of such composition [*e.g*., *Potter et al*., 2012; *Hurwitz and Kring,* 2014]. It is possible that there is a weak decrease in plagioclase content with increasing proximity to the crust mantle boundary in the South Pole-Aitken basin, although there is no unambiguous trend. Also, even besides the difference in abundances of the pyroxene composition derived from the Multiband Imager data [*Lemelin et al*., 2015] and from the Spectral Profiler data herein, we find that pyroxene (low-calcium pyroxene) is the most abundant mafic mineral in all the central peaks and basin rings we study. To compare our results with results from other previous studies, we investigate the composition of Schrödinger basin, and confirm the presence of anorthosite, norite and anorthositic troctolite previously identified by *Ohtake et al*. [2009], *Yamamoto et al*. [2010] and *Kramer et al*. [2013].

CHAPTER 5

IMPROVED CALIBRATION OF REFLECTANCE DATA FROM THE LRO LUNAR ORBITER LASER ALTIMETER (LOLA) AND IMPLICATIONS FOR SPACE WEATHERING

Published as: M. Lemelin, P.G. Lucey, G.A. Neumann, E.M. Mazarico, M.K. Barker, A. Kakazu, D. Trang, D.E. Smith, and M.T. Zuber (2016), Improved calibration of reflectance data from the LRO Lunar Orbiter Laser Altimeter (LOLA) and implications for space weathering, Icarus, vol. 273, pp.315-328, doi:10.1016/j.icarus.2016.02.006.

*A*bstract—The Lunar Orbiter Laser Altimeter (LOLA) experiment on Lunar Reconnaissance Orbiter (LRO) is a laser altimeter that also measures the strength of the return pulse from the lunar surface. These data have been used to estimate the reflectance of the lunar surface, including regions lacking direct solar illumination. A new calibration of these data is presented that features lower uncertainties overall and more consistent results in the polar regions. We use these data, along with newly available maps of the distribution of lunar maria, also derived from LRO instrument data, to investigate a newly discovered dependence of the albedo of the lunar maria on latitude (Hemingway et al., 2015). We confirm that there is an increase in albedo with latitude in the lunar maria, and confirm that this variation is not an artifact arising from the distribution of compositions within the lunar maria, using data from the Lunar Prospector Neutron Spectrometer. Radiative transfer modeling of the albedo dependence within the lunar maria is consistent with the very weak to absent dependence of albedo on latitude in the lunar highlands; the lower abundance of the iron source for space weathering products in the lunar highlands weakens the latitude dependence to the extent that it is only weakly detectable in current data. In addition, photometric models and normalization may take into account the fact that the lunar albedo is latitude dependent, but this dependence can cause errors in normalized reflectance of at most 2% for the majority of near-nadir geometries. We also investigate whether the latitude dependent albedo may have obscured detection of small mare deposits at high latitudes. We find that small regions at high latitudes with low roughness similar to the lunar maria are not mare deposits that may have been misclassified owing to high albedos imposed by the latitude dependence. Finally, we suggest that the only modest correlations among space weathering indicators defined for the lunar samples may be due to mixing of soils from distinct latitudes.

5.1. Introduction

The Lunar Orbiter Laser Altimeter (LOLA) reflectance experiment is unique among optical measurements of the Moon in that it measures the reflectance of the Moon at a constant phase angle (the angle between illumination source, target and measurement) of nearly zero degrees independent of latitude or solar illumination from a global nadir viewing perspective [*Smith et al*., 2010]. The quantity reported in the LOLA data set and in this paper is normal albedo, the radiance of the Moon at zero phase angle relative to a Lambert surface illuminated normally. This paper presents and relies upon a new calibration of the LOLA reflectance data based on experience gained since the publication of the initial calibration by *Lucey et al*. [2014], with a more uniform methodology and tighter constraints on data quality.

Using this improved calibration, we investigate a newly discovered latitude dependence of lunar albedo. *Lucey et al*. [2014] reported that no increase in reflectance with latitude was present in laser reflectance data obtained by the LOLA laser altimeter. Yet in a closer look, using Clementine data and LOLA data of *Lucey et al*. [2014], *Hemingway et al*. [2015] found that the reflectance in the lunar maria increases from the equator to ± 70° latitude (they could not study higher latitudes due to the lack of good reflectance measurements from Clementine in the polar regions). Based on that and other evidence, they argued that solar wind sputtering, which is attenuated with increasing latitude by definition, was a controlling agent of this latitude dependent albedo variation. As this latitude dependence of albedo is not present among the assumptions in prior work characterizing the lunar phase and photometric function, we investigate the errors introduced in photometric normalization caused by this phenomenon.

5.2. Improved calibration of LOLA reflectance data

The work discussed here uses reflectance data calculated using measurements archived in the LOLA Reduced Data Record (RDR) products (available on the Planetary Data System Geosciences Node website at http://pds-geosciences.wustl.edu/missions/lro/ lola.htm), version 1.0, for all 13 months of the nominal mission phase ("LRO_NO_01"to "LRO_NO_13"). The nominal mission phase extended from September 2009 to September 2010, and consists of 4657 orbits (orbits 1005-5661). The equation that relates the raw RDR LOLA measurements to apparent reflectance (r), where r = I/F, the reflectance relative to a Lambert surface illuminated

normally (and for monostatic LIDAR systems like LOLA is also equal to the normal albedo) is [rearranged from *Riris and Cavanaugh*, 2010]:

$$I/F = K \frac{(E_{Rx} - r_D)}{E_{Tx}} \frac{\pi d^2}{\varepsilon_{Rx} \delta_{Tx} A_R} \tag{5.1}$$

Of the variables in Eq. (5.1), the following are available from the raw LOLA RDR products: E_{Tx} is the transmitted energy (nJ), E_{Rx} is the received energy (zJ), and d is the range to the surface (mm). Three constants for each of LOLA's five detectors are given in Table 5.1: r_D (zJ) is an electronic offset that corresponds to the response of LOLA's detectors at infinite range, ε_{Rx} is the receiver optical efficiency, and δ_{Tx} is the efficiency of the diffractive optic that divides the LOLA transmitted pulse into five beams. A_R is the LOLA receiver telescope area (0.0154 m^2), and the constant K reconciles the various units provided in LOLA RDR from the Planetary Data System and has a value of 10^7 nJ·m^2 /zJ·mm^2. When using the LOLA software RDR2TAB or RDR2CSV to extract the raw RDR data, *ETx* is given in mJ, *ERx* is given in fJ and *d* is given in km, thus r_D (Table 5.1) has to be converted to fJ ($r_D \cdot 10^7$), and K becomes 10^{-5}.

Table 5.1. Detector Dependent Calibration Constants

Detector	1	2	3	4	5
r_D (zJ)	$0.135 \cdot 10^{-7}$	$0.1159 \cdot 10^{-7}$	$0.1303 \cdot 10^{-7}$	$0.1775 \cdot 10^{-7}$	$0.2164 \cdot 10^{-7}$
ε_{Rx}	84.046	87.438	85.326	90.274	80.809
δ_{Tx}	0.2	0.14	0.14	0.14	0.14

Eq. (5.1) does not capture sources of uncertainty identified in analysis of in-flight data. For clarity we will refer to I/F computed with Eq. (5.1) as "apparent reflectance." The apparent reflectance exhibits several anomalies including a steady decline with time over the course of the nominal mission, a rapid loss of signal when LRO transitions between the day and night sides near the poles or is near the terminator, and days-long periods of anomalous low return at some latitudes early in the mission. The steady decline of apparent reflectance with time and polar behavior was characterized empirically by Lucey et al. (2014). Subsequent work with the LOLA data set has led to improved understanding of the behavior of the instrument, and an improved calibration is presented here.

5.2.1. Correction for the sensitivity drift of the lasers with time

Inevitably, pulsed laser systems will degrade with time as optics accumulate damage from high power densities. Indeed, a slow and relatively steady decrease in apparent reflectance over the course of the first year of data is observed in the LOLA reflectance data; *Lucey et al*. [2014] presented a calibration of this drift. Subsequent work with the LOLA reflectance data set revealed anomalies related to which of LOLA's two lasers was operating. In lunar orbit, LOLA experiences constant thermal variations which change the laser cavity dimension, at wavelength scale, and cause variations in the transmitted energy. These variations are more frequent near certain critical temperatures, which is a function of the LRO orbit position about the moon. Inspection of Eq. (5.1) shows that the energy transmitted by the laser is a key parameter in determining reflectance, and the received energy is normalized to the transmitted energy. However, the transmitted energy is not well characterized when laser 2 is in operation. Fig. 5.1 shows the variation in transmitted energy for a month of data. In the case of laser 1, the transmitted energy image shows bright stripes roughly parallel to lines of latitude indicating brief bursts of higher laser power. These bright stripes can also be discerned in the received energy image. The calibrated reflectance image for laser 1, which has been normalized by the transmitted energy, is free of these artifacts. However, data collected with laser 2 shows clear horizontal stripe artifacts in both the received energy and calibrated reflectance (Fig. 5.1). These stripes are especially apparent at mid southern latitudes and are prominent in South Pole–Aitken Basin. This symptom strongly indicates a problem with the characterization of the transmitted energy when using laser 2. Inspection of the transmitted energy images from the two lasers reveal qualitative differences; laser 1 transmitted energy features zones of relatively constant transmitted energy bounded by the previously mentioned bright stripes, indicating a short lived increase in output power, whereas these bright boundaries are not present in the laser 2 transmitted energy data. However, these power excursions must occur, because they are obvious in the received energy image when using laser 2. Thus, it is clear that the laser 2 energy monitor is not properly characterizing the output of the laser when laser 2 is in operation. Consequently, reflectance data measured by laser 2 has substantially higher uncertainty than reflectance data measured by laser 1. This important difference in behavior led us to separate the calibration of the data set by the laser used. We present calibration for both lasers in this paper, but we use only data obtained using laser 1 in our science analysis.

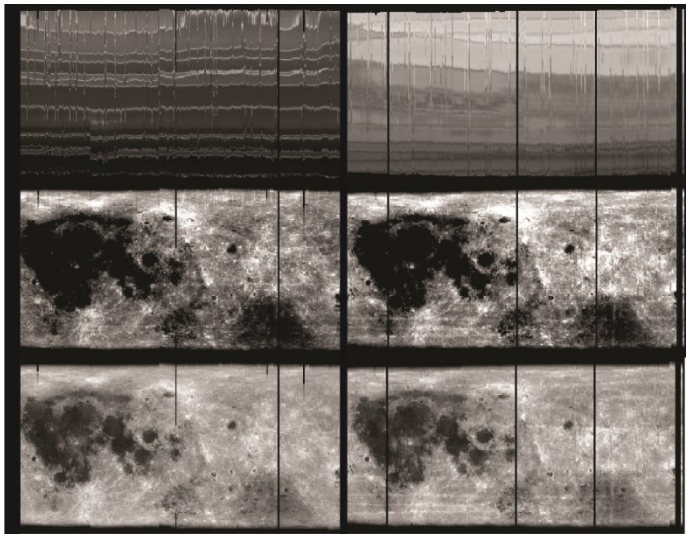

Figure 5.1. The effect of incompletely removed transmitted energy from measurements obtained with laser 2. Left: laser 1, Right: laser 2. Top: transmitted energy recorded by LOLA (scaled from 2.5 to 4.5 mJ). Middle: received energy minus 0.13 times the square of the range, Bottom: Apparent reflectance (scaled from 0.1 to 0.5). The transmitted energy shows the changes in output laser power as thermal variations experienced at different latitudes change the laser cavity dimension. For laser 1 (left) each increase in output power manifest as stripes parallel to lines of latitude. These stripes can also be seen in the received data image, but have been normalized out in the apparent reflectance image at the bottom. Laser 2 transmitted energy shows qualitatively different behavior. While the output laser power also changes, the transmitted energy is not accompanied by positive excursions near the boundaries of the change. However, in the received energy images horizontal stripes indicating increases in laser power are evident, and these stripes are not removed by normalization. This indicates an as yet unexplained inaccuracy in the recorded transmitted energy for laser 2.

The decrease in apparent reflectance over time is most clearly seen when dividing the apparent reflectance by the normal albedo calibrated by *Lucey et al*. [2014] (Fig. 5.2a), which removes albedo features. Two trends are then noticeable in data from each laser; there is a slow decrease in apparent reflectance with time before June 17th 2010, (TDT = $3.3 \cdot 10^8$, where the Terrestrial Dynamical Time (TDT) is the time unit used by LOLA and defined in Neumann et al., 2010), and a faster decrease afterwards (Fig. 5.2a). We fit the trends characterizing the change in apparent reflectance (r) over time for each laser and each of these two TDT segments

(Table 5.2). Data were limited to within ±10° in latitude to avoid the influence of any possible latitude dependent trends. The data was fitted using a second-degree polynomial before TDT = $3.3 \cdot 10^8$ (Eq. 5.2), and a linear fit after TDT = $3.3 \cdot 10^8$ (Eq. 5.3), with the resulting ratios shown in Fig. 5.2b.

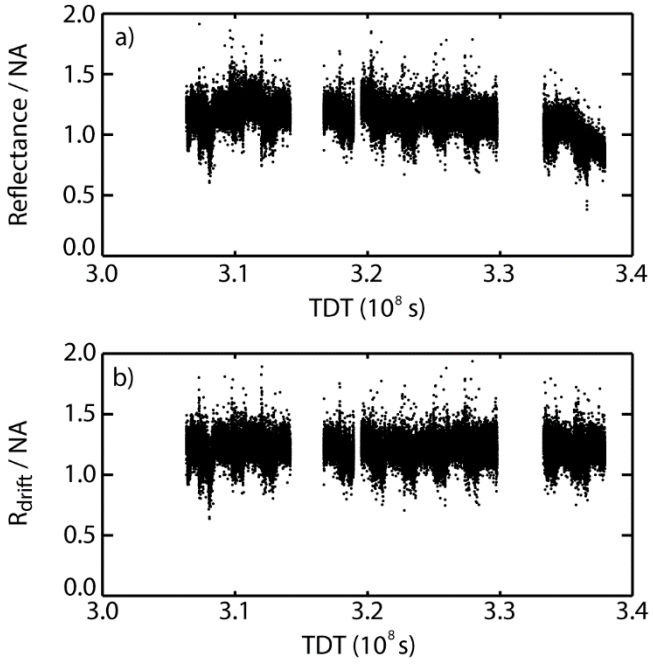

Figure 5.2. Reflectance measured by LOLA's laser 1 and laser 2 during daytime within 10° latitude of the equator, divided by the normal albedo calibrated by *Lucey et al*. [2014]. (a) apparent reflectance and (b) reflectance corrected for the change in reflectance over time (*r corrected*, Eqs. 5.1 and 5.2). The two gaps in data correspond to measurements made when LRO was orbiting the terminator.

Table 5.2. Coefficients used to compute the trend of decrease in reflectance with time.

	Coefficients TDT $<3.3 \cdot 10^8$			Coefficients TDT $\geq 3.3 \cdot 10^8$	
	a	b	c	d	e
Laser 1	$-3.070 \cdot 10^{-16}$	$1.937 \cdot 10^{-7}$	-29.606	$-4.576 \cdot 10^{-8}$	16.168
Laser 2	$-4.675 \cdot 10^{-16}$	$2.941 \cdot 10^{-7}$	-45.252	$3.793e \cdot 10^{-8}$	-11.806

$$r_{corrected} = r / (a \cdot TDT^2 + b \cdot TDT + c) \quad (5.2)$$

$$r_{corrected} = r / (d \cdot TDT + e) \quad (5.3)$$

5.2.2. Exclusion of anomalous data

In the calibration process we noticed portions of the data with anomalous apparent reflectance. Anomalies included measurements made when the received energy was very low, when the instrument was pointing off-nadir or at very small off-nadir angles, when the range was atypically large, and when the spacecraft was orbiting the night side. We excluded data acquired when the received energy was lower than 0.14 fJ, when the spacecraft was pointing "off-nadir", which in this case corresponds to off-nadir angles <0.2° or >0.4° (LOLA usually operated at a "nadir" angle of ~0.27° during the nominal mission months), and when the range was greater than 70 km (which mostly occurred when the instrument was pointing off-nadir).

We also found portions of the data that show anomalously low apparent reflectance (Fig. 5.3a) values in the beginning of the mission (between orbits 1016 and 1311 inclusively), especially when we divided the apparent reflectance by the normal albedo of *Lucey et al*. [2014] (Fig. 5.3b). However, none of the parameters we monitored (received energy, transmitted energy, range, beta angle, off-nadir angle) appeared anomalous in the same ranges of orbit number and latitude so this artifact remains unexplained. Lacking an explanation and mitigation, we masked these areas and excluded them from our analysis. Portions of those orbits with non- anomalous reflectance measurements were retained.

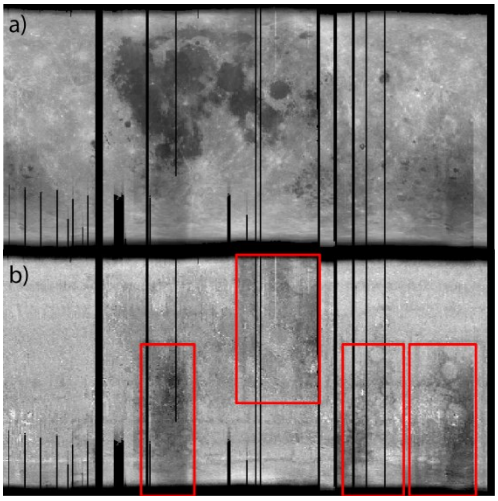

Figure 5.3. Anomalously low reflectance values are measured in the beginning of the nominal mission, in orbits 1005–1400 shown here. (a) LOLA reflectance and (b) LOLA reflectance divided by the normal albedo of *Lucey et al*. [2014]. Four regions with anomalously low

reflectance values occur between orbits 1016–1311, and have been removed from our analysis by defining bounding boxes around them (red).

5.2.3. Conversion to normal albedo

The equations above (Eqs. 5.1–5.3) provide only a relative calibration of the reflectance measured by LOLA. Lacking an absolute reference to derive normal albedo, we scaled our data to the normal albedo from *Lucey et al*. [2014] who calibrated LOLA's reflectance measurements to observations of the Moon at zero phase angle by the Kaguya Multiband Imager at a wavelength (1050 nm) close to that of LOLA (1064 nm). In turn, the calibration of the Kaguya Multiband Imager radiance, upon which the LOLA calibration of *Lucey et al*. [2014] relies, is described in *Kodama et al*. [2010] and *Ohtake et al.* [2010]. We computed the linear regression between a 4 pixel per degree map of our newly calibrated reflectance data, and the 4 pixel per degree map of the normal albedo presented by *Lucey et al*. [2014]. The regression coefficients (Table 5.3) are then used to convert LOLA reflectance ($r_{\text{corrected}}$) to normal albedo (NA) (Eq. 5.4):

$$NA = (r_{\text{corrected}} * a) + b \quad (5.4)$$

Table 5.3. Coefficients used to convert apparent reflectance to normal albedo

	Coefficients	
	a	b
Laser 1	0.6904	0.0424
Laser 2	0.6904	0.0427

Mosaics produced from the above calibration contained orbit-orbit stripe artifacts indicating some residual calibration issues. Once the normal albedo had been computed for all 4657 orbits of the 13 months that constituted the nominal mission phase (LRO_NO_01 to LRO_NO_13), we produced 1 pixel per degree maps for each 360° rotation of the Moon under the LRO orbit. We then compared each of these rotation maps to the average normal albedo value and derived a small correction ratio to be applied to the normal albedo data for each rotation map in order to form a seamless map when using all the data together (Table 5.4). For rotations 5 and 12, LRO was orbiting near the terminator, which resulted in lower signal to noise ratios. We excluded these orbits from our analysis.

Table 5.4. Correction ratio applied to the normal albedo data for each rotation measured by LOLA.

Rotation	Minimum orbit	Maximum orbit	Correction ratio
1	1006	1231	1.001090
2	1232	1579	0.999902
3	1580	1927	1.005750
4	1928	2274	0.998078
5	2275	2247	N/A
6	2448	2795	0.999426
7	2796	3142	1.001280
8	3143	3490	0.999307
9	3491	3837	1.000650
10	3838	4185	1.000290
11	4186	4533	1.002550
12	4534	4708	N/A
13	4850	5055	0.993231
14	5056	5403	1.006010
15	5404	5661	0.999202

5.2.4. Correction for loss of signal from temperature dependent loss of alignment

Early analysis of the LOLA data revealed a strong drop in apparent reflectance as the spacecraft approached the poles or when the LRO orbit was near the terminator. It was determined that this was due to temporary misalignment of the LOLA laser transmitter telescope dependent on the thermal load from the Moon. When viewing low temperature surfaces near the lunar terminator (including the poles), the insulating blankets surrounding the instrument cool and contract. This contraction pulls the LOLA transmit telescope out of alignment, causing the images of the laser spots on the lunar surface to temporarily drift off their detectors (in other words, each laser spot on the lunar surface is pulled outside the field of view of its intended detector, this is also called the "thermal blanket anomaly" in *Smith et al.*, 2010). The thermal contraction and misalignment occur when the spacecraft enters and exits lunar shadow during an orbit (*i.e.*, near the poles) and also when the LRO orbit is close to the terminator (*i.e.*, beta angle close to 90°). The effect causes a temporary, but complete, loss of received laser signal. There is a brief period, between the onset of the thermal contraction and the complete loss of signal, when reflectance data are still received; *Lucey et al*. [2014] applied an empirical correction to those

data that averaged the signal drop-off with time over several orbits in order to extend the LOLA reflectance data closer to the pole. We refined this method by using a physical model of the signal loss.

The spatial pattern of the laser signal at the focal plane of the LOLA receiver telescope is approximately Gaussian. When the laser spots drift off their detector (*i.e.*, the spacecraft enters the night side), the received signal (D) can be approximated by the sigmoidal logistic function (Eq. 5.5), where a equals 1 (the vertical axis goes from 0 to 1, or 0 to 100% of the signal strength), S is the slope (positive when the laser spots drift off their detector), T is the observation time (TDT) , and T_0 corresponds to the time in an orbit where the signal strength has dropped by 50%. When the laser spots drift back on their detectors (*i.e.*, the spacecraft views warm surfaces on the day side causing the thermal blankets to heat and relax), the re-appearance of the received signal can be approximated by the same function with a negative slope. We manually estimated T_0 for each orbit, and iteratively refined T_0 and the slope by finding the drop-off curve (D) that best fits the albedo signal within two minutes of the manually identified T_0. To find the drop-off curve that best fits the albedo for a given orbit, we made the drop-off curve run through the data points by temporarily setting a to the average albedo value of that orbit.

$$D = a/(1+\exp[S \cdot (T - T_0)]) \tag{5.5}$$

Consistent with the contraction of the thermal blankets, we found that the time when the signal is lost is dependent on the beta angle (the angle between the plane of the LRO orbit and the Sun–Moon line) at the time of the observation (Fig. 5.4). At low beta angles, LOLA rapidly encounters warm surfaces as it transitions to the daylit side of the Moon so the drop-off occurs at high latitudes; as the beta angle increases and the LRO orbit approaches the terminator, surfaces that are warm enough to allow the thermal blankets to relax occur at increasingly low latitudes and so does the drop-off. At beta angles above 60°, the range of latitude with correctable data rapidly declines. At beta angles above 80°, the lunar surface below the spacecraft at all latitudes is too cold to allow the thermal blankets to relax and no usable signal is present.

After finding the drop-off curve that best fits the loss or re-appearance of signal for a given orbit, we divided the normal albedo (*NA*) of that orbit by the drop-off curve (*D* , Eq. 5.5), where *a* equals 1). Fig. 5.5 shows drop-off curve that best fits the albedo for orbit 1090 using Eq. (5.5) (where $a = 0.4$). Because the signal to noise ratio falls with the signal, we only retained the corrected normal albedo measured before the signal dropped by 50%. We found that for the orbits measured close to the terminator (beta angle ≥60°), in the low albedo South Pole-Aitken Basin region (95°E–110°W), the normal albedo was noisy even before the signal dropped by 50%. Therefore, we only retained the normal albedo measured before the signal dropped by 25% in this region.

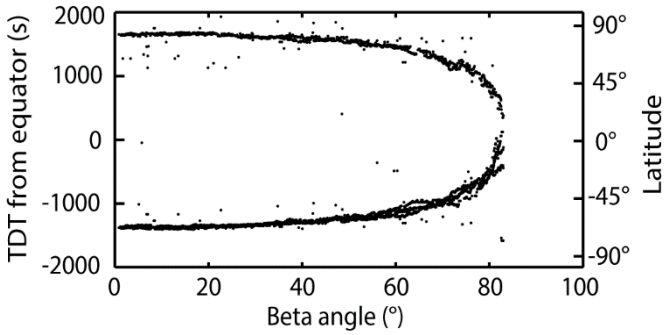

Figure 5.4. Terrestrial Dynamical Time (TDT) during each orbit at which LOLA's apparent reflectance passes through 50% of the local maximum value, normalized to when LRO passed over the equator in that orbit (TDT from equator = 0). Negative values represent the appearance of signal when LRO emerges from the night side; positive values represent the disappearance of signal when LRO passes into shadow. Data from all orbits of the nominal mission months (orbits 1005–5561, LRO_NO_01 to LRO_NO_13). Latitude is shown on the right axis for context.

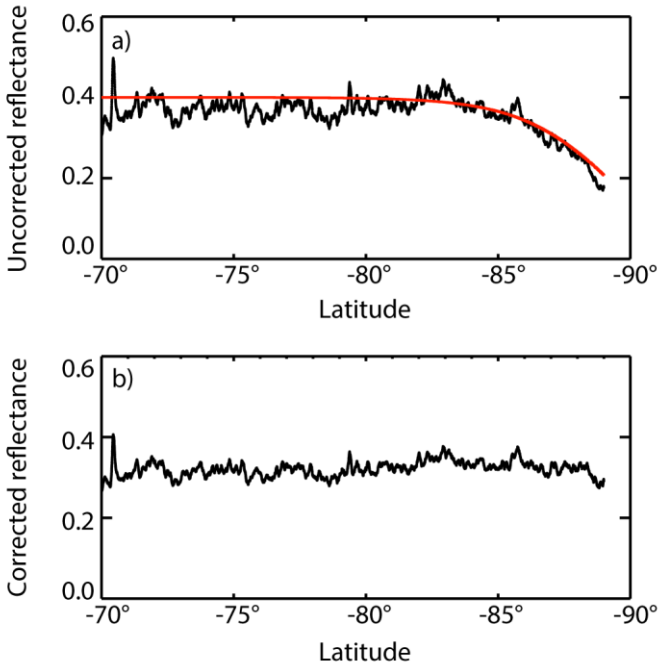

Figure 5.5. Example of the sigmoidal logistic function fit to the drop-off in signal caused by the contraction of LOLA thermal blankets. (a) The uncorrected reflectance and smoothed reflectance are shown for orbit 1090 in the south polar region, along with the drop off fit (red). (b) The corrected reflectance. This correction recovers much of the lost data above 85 S. Orbit 1090 has an average longitude of 143 °E between 70–85 °S, and covers the eastern portion of Schrödinger basin.

5.2.5. On the dark side

After the loss of signal near the poles, as the spacecraft moves over low temperature surfaces, thermal contraction of the insulating blankets continues until two of the five laser spot images move partially onto detectors 3 and 4, re-establishing ranging, and also receiving enough energy to make a reflectance measurement. However, signal is low relative to dayside (warm Moon), indicating that the laser spot images may not move completely onto the detectors. Applying the corrections described above, that assume a fully illuminated detector, yield low relative reflectance and normal albedo values relative to data obtained on the dayside. Furthermore, the corrections provided above are applied to the combination of a specific laser and detector, and the data on the night side use different combinations. Despite these caveats, the

data obtained on the portions of the lunar night side, or more properly, the lunar cold side, appears stable and contains usable signal that we exploit in the next section.

5.2.6. Filling polar data gaps

A gap in coverage remains near both poles when the constraints listed in sections above are applied to the warm Moon (dayside) data. However, during lunar winter, the poles are poorly illuminated and are cold enough that LOLA produces polar data in its cold Moon (night side) mode. A portion of these data were used by *Zuber et al*. [2012] in their analysis of the albedo of Shackleton crater. For the south polar region, we included cold Moon data from orbits 4014-4264 (used in *Zuber et al.*, 2012) between 85–90°S. For the north polar region, we included cold Moon data from orbits 4920–4971 and orbits 5318–5360, between 87–90°N. We calibrated the data for both polar regions using Equations 5.1–5.3, and scaled the cold Moon data in the region of overlap to the warm Moon data calibrated above. Correction factors to normal albedo for the polar night side data are in Table 5.5.

Table 5.5. Correction factors to produce normal albedo from polar night side data

Pole	Orbit Range	Correction Factor
SP	4010-4264	0.812014
NP	4850-4971	0.814133
NP	5318-5370	0.816358

5.2.7. Calibration result

Using the data from laser 1, we produced new equatorial and polar mosaics of LOLA's normal albedo, at a spatial resolution of respectively 3 km and 1 km per pixel. We first smoothed the normal albedo data using a 50 point boxcar mean filter along the orbit tracks, gridded the data, and averaged overlapping data points to produce the maps using the GMT software (version 5.1.1). We then used the GMT function "surface", an adjustable tension continuous curvature spline function, to interpolate over data gaps within the map. The parameters that we inputted into the surface function include a tension of 0.1 and a search radius of 5°. The new equatorial mosaic (Fig. 5.6) and the new polar mosaics (Fig. 5.7) can be accessed online via the

PDS Geosciences Node website at http://pds-geosciences.wustl.edu/missions/lro/lola.htm (LRO Release 24, Gridded Data Records, or GDR), along with the calibrated normal albedo for each individual orbit (Radiometry Data Records, or RADR). Note that the normal albedo archived online has not been smoothed to preserve the original signal.

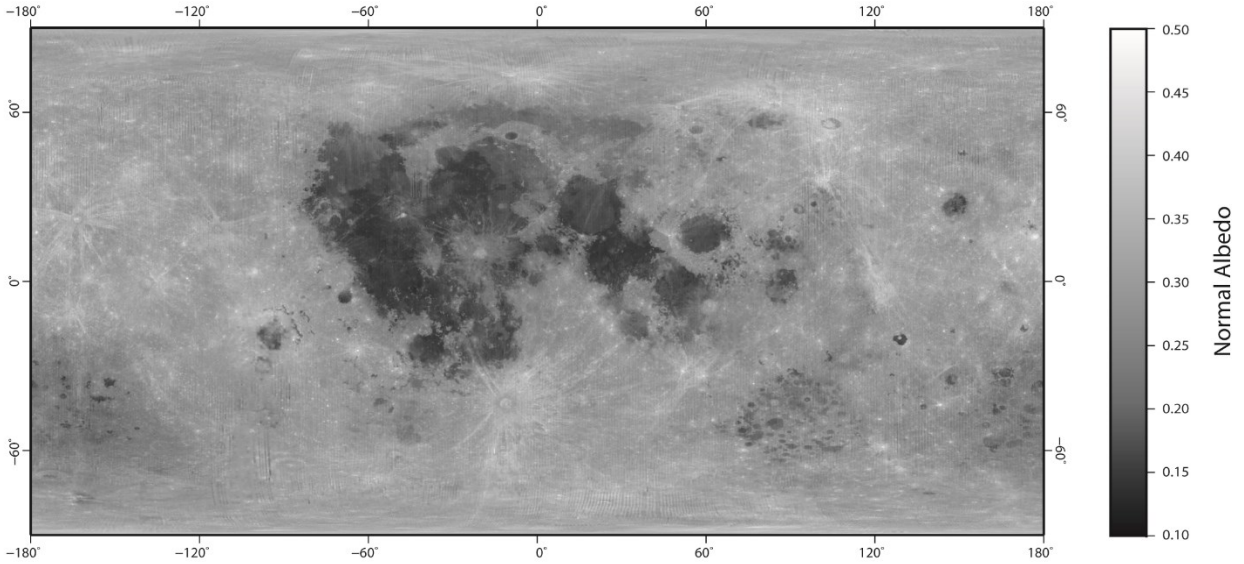

Figure 5.6. Global equatorial mosaic of the calibrated normal albedo from LOLA, in simple cylindrical projection.

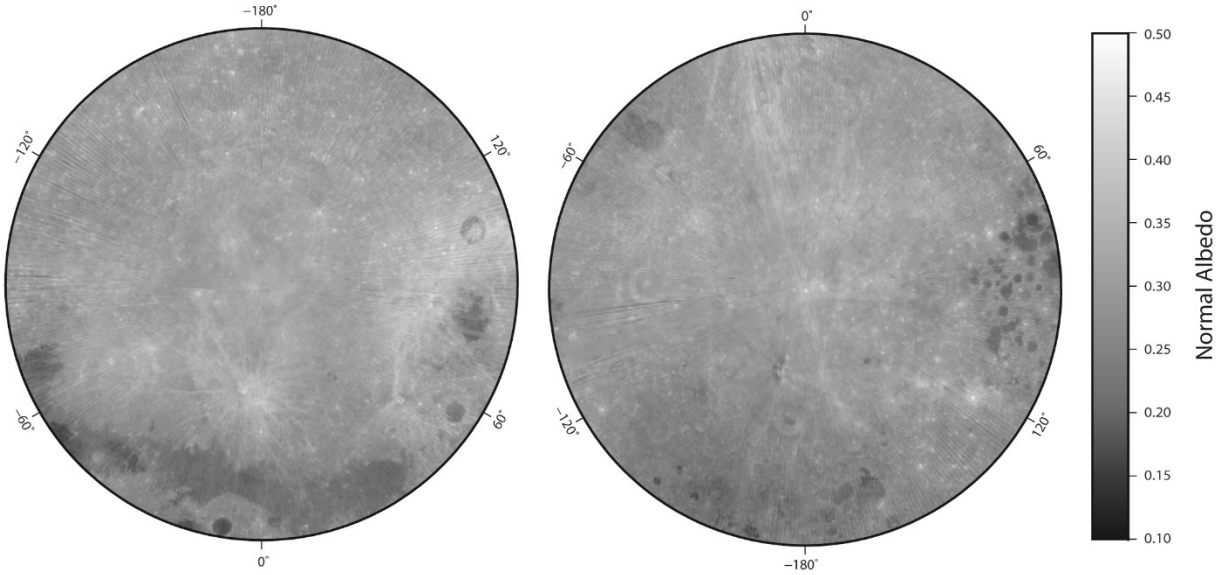

Figure 5.7. Polar mosaics of the calibrated normal albedo from LOLA. Left: north polar region and Right: south polar region. The data is shown poleward of 50° in latitude, in polar stereographic projection.

5.3. Confirming and investigating the increase in normal albedo with latitude

Hemingway et al. [2015] suggested that their discovery of the dependence of albedo on latitude appears to follow a cosine function leading to the conclusion that the albedo was affected by a quantity related to the average solar flux, in their case the solar wind flux. To verify this assumption, we compare the normal albedo presented herein to solar wind flux derived from two techniques, one for latitudes within ±55°, and one for latitudes poleward of 55°.

At low latitudes, we estimate the average solar exposure from the cosine of the latitude, where a unit of 100 would be a surface element illuminated normally by the Sun for 1/2 a lunar day. Because of the cosine dependence of solar illumination, the maximum value observed at the equator is ~63.6. Fig. 5.8 shows a two-dimensional histogram of the normal albedo plotted against the average solar flux estimated from latitude (temporarily for all latitudes). For each bin of average solar flux, the histogram has been normalized to its maximum to better reveal patterns (the area at a given average flux decreases toward the pole, so the histogram without normalization has a strong gradient that obscures patterns). The histogram is strongly bimodal (corresponding to the lunar maria and highlands) at high average fluxes near the equator (flux values above 50). Note that the maria mode steadily increases in normal albedo with decreasing solar flux (increasing latitude); this was the discovery of *Hemingway et al*. [2015].

While the cosine of the latitude is a good approximation of solar-related fluxes at low latitudes and at low spatial resolution, local topography strongly affects the average flux at any individual location near the poles. This can be seen in Fig. 5.8, where two large excursions in normal albedo are observed at very low (0–10) average solar flux values (*i.e*., high latitude). Therefore, for subsequent analysis in the regions poleward of ~55° latitude, we use a spatially-resolved estimate of the average solar flux at 250-m resolution computed over several lunar precession cycles, following the methods of *Mazarico et al*. [2011]. Fig. 5.9 shows the variation in average solar flux with latitude for the data poleward of ~55° latitude [*Mazarico et al*., 2011]. At any given latitude a large range of average fluxes are present; these represent the effect of equator facing and pole facing slopes that increase or decrease the average flux relative to a flat surface. Data for regions in permanent shadow are apparent as points that hug the zero-flux axis. Fig. 5.10 shows two-dimensional histograms of south polar normal albedo against latitude and average solar flux. A sharp increase in normal albedo with latitude is seen in Fig. 5.10a (as in Fig. 5.8), but this is an artifact of abundant permanent shadow near the pole. In Fig. 5.10b, data

are plotted versus average solar flux and a steady increase in normal albedo is observed as average fluxes decline. There is a sudden increase at zero average flux: those are regions of permanent shadow, noted by *Lucey et al*. [2014] to be anomalously bright relative to areas that receive some illumination. The north polar region shows somewhat different behavior, with a much flatter change in albedo with declining flux (Fig. 5.11). Fig. 12 summarizes the results for each hemisphere. The modes of the histograms of normal albedo for each bin of average solar flux are shown. Because highland points are so much more abundant than maria, these curves are the loci of the behavior of the lunar highlands. The southern hemisphere shows a weak increase in mode with decreasing flux, whereas variation of normal albedo with the average solar flux of the northern hemisphere is arguably flat.

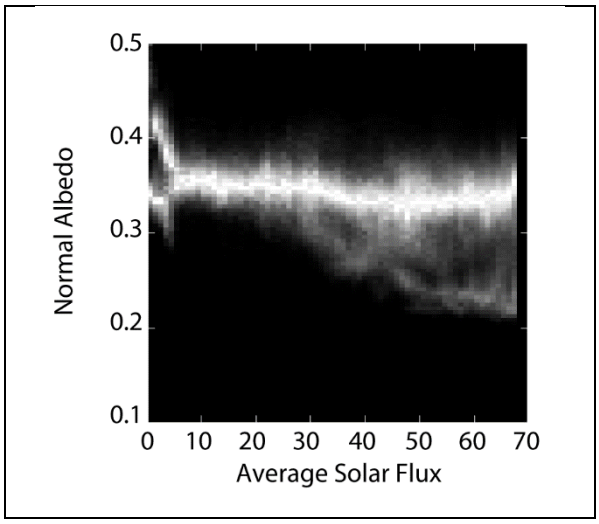

Figure 5.8. Global normal albedo versus average solar flux estimated from latitude. Each bin of average flux has been normalized to its maximum value. At high values of average flux, above 50, the distribution is bimodal reflecting the inherent difference in albedo between maria and highlands. The strong excursions at low flux are artifacts of the breakdown of the assumption that average flux can be estimated from latitude.

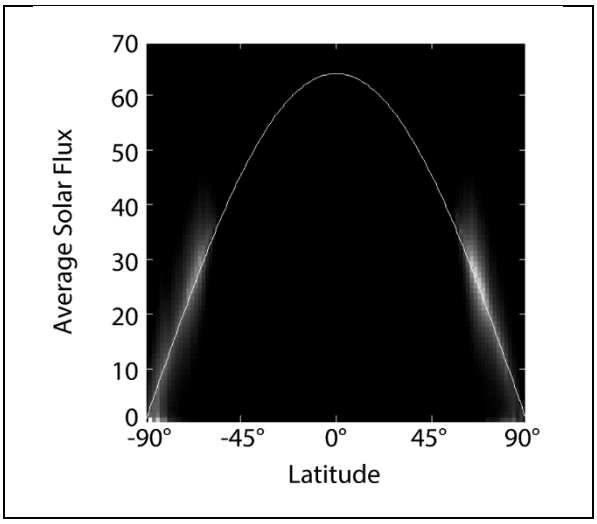

Figure 5.9. Distribution of average solar flux for the polar data used in this paper. The solid curve is the average flux for a flat surface, the diffuse points are the computed average fluxes including the effect of topography. Data above the "flat surface" curve are equator-facing slopes, while data below the curve are pole-facing slopes. The cluster at along the axis at zero flux are regions of permanent shadow.

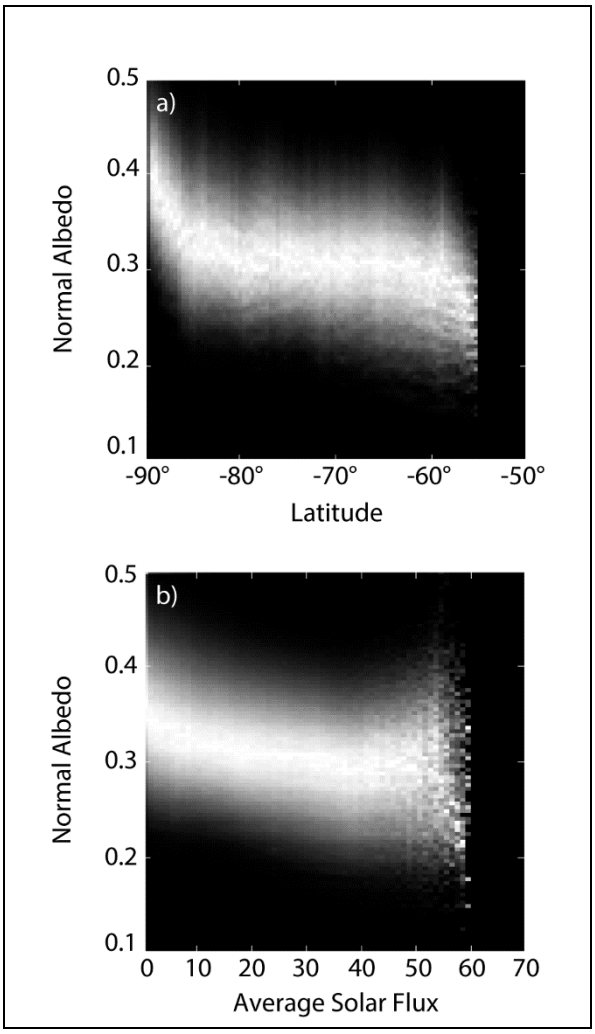

Figure 5.10. Distribution of normal albedo for versus (a) latitude, and (b) average solar flux for the south polar region. The former case (a) shows a sharp upturn of normal albedo at high latitudes: this is due to the presence of increasing amounts of permanent shade as the pole is approached. In the latter case (b), the normal albedo increase is present, but smooth, with a step increase in reflectance at zero flux (permanent shadow).

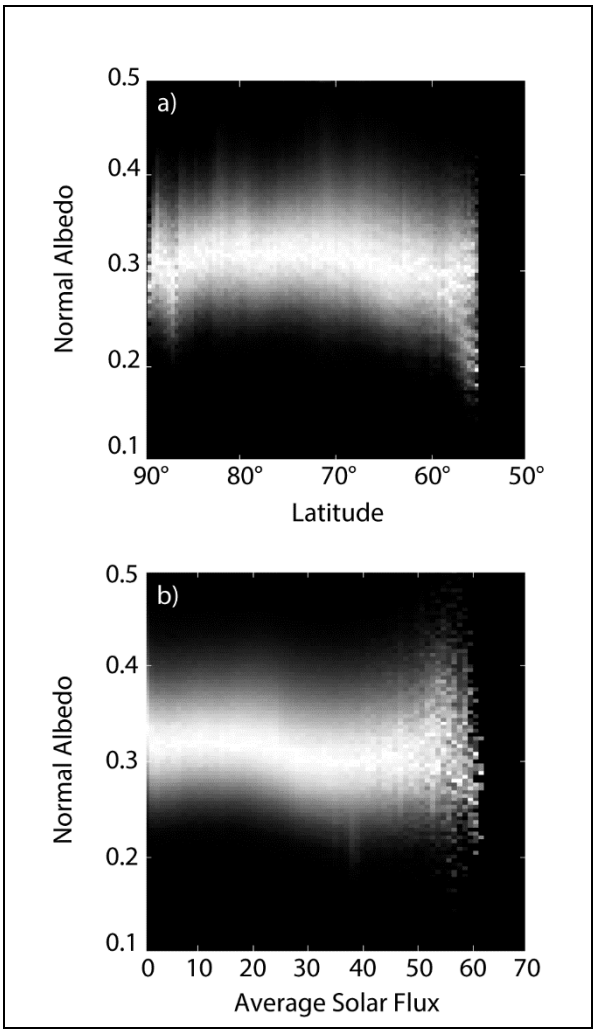

Figure 5.11. Distribution of normal albedos versus (a) latitude and (b) and average solar flux for the north polar region. There is only a weak increase in normal albedo with decreasing solar flux, except in regions of permanent shadow (0 average solar flux). At average flux values below about 20, the distribution is flat unlike the south pole (Fig. 5.10b).

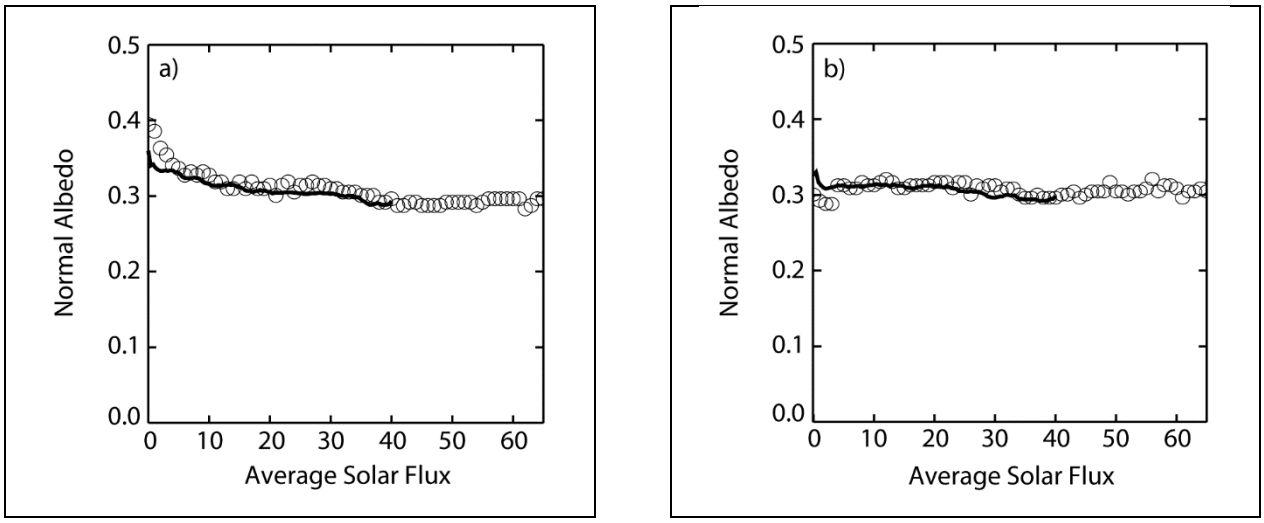

Figure 5.12. Variation in mode of the normal albedo histogram with average solar flux for (a) the southern hemisphere, and (b) the northern hemisphere. Open circles are modes from data shown in Fig. 5.8, the solid line is the locus of the modes from Figs. 5.10b and 5.11b. The curves diverge near the poles because the low resolution global data estimates average solar flux from latitude. At values below about 10 units of average solar flux the solid line representing the polar data better represents the relationship.

5.3.1. Confirming the trend in the maria

As shown in Fig. 5.8, the histogram of normal albedo versus average solar flux is strongly bimodal, suggesting that the higher mode corresponds to the lunar highlands and the lower mode corresponds to the lunar maria. Here we will isolate the normal albedo data of the maria from the normal albedo data of the highlands in an attempt to confirm the dependence of albedo on latitude for the maria.

One of the innovations of *Hemingway et al*. [2015] was to use the roughness metric of *Kreslavsky et al*. [2013] as an independent indicator of the presence of mare deposits. However, the roughness criterion may admit high albedo smooth plains into this analysis that could potentially corrupt the observed trends. Therefore, we will revisit the roughness approach to isolate maria and highlands (in Section 5.4.1), but we first turn to a new data set of classically mapped mare deposits from *Nelson et al*. [2014] (Fig. 5.13). *Nelson et al*. [2014] digitized mare boundaries by zooming in to the resolution of the three basemaps where features could be

distinguished within a few pixels: (1) a 100 m/pixel LROC Wide Angle Camera 643 nm reflectance mosaic, (2) a 400 m/pixel LROC Wide Angle Camera 321 nm/415 nm mosaic, and (3) a 1 km/pixel Clementine UVVIS color ratio). The mare boundaries shapefile they generated (available at http://wms.lroc.asu.edu/lroc/view_ rdr/ SHAPEFILE _ LUNAR _ MARE) covers the Moon from 64.7°N to 66.5°S. With the *Nelson et al*. [2014] mare mask applied, we see the trend of Hemingway et al. (2015) clearly (Fig. 5.14). The normal albedo of the maria is a strong and crudely linear function of the average solar flux. In contrast, the highland mode shown in Fig. 5.8 shows only a modest increase in reflectance, if at all.

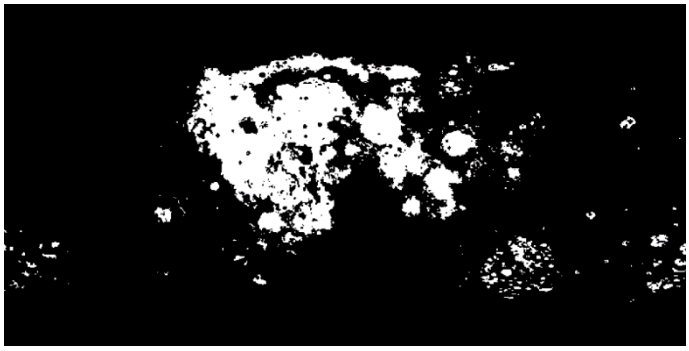

Figure 5.13. Mapped mare deposits of *Nelson et al*. [2014] sampled at two pixels per degree. These deposits have been classically mapped and explicitly exclude light plains that may be present in data based on roughness alone.

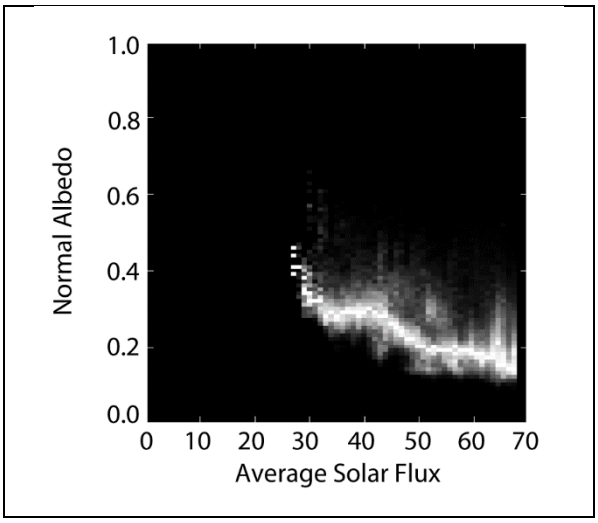

Figure 5.14. Dependence of normal albedo on average solar flux for mare units mapped by *Nelson et al*. [2014]. Each bin of average flux has been normalized to its maximum value. The strong general inverse correlation is the phenomenon discovered by *Hemingway et al*. [2015]. Values extending above the modal value are immature surfaces including craters that occur within the mapped maria.

5.3.2. Potential causes

The hypothesis posed by *Hemingway et al.* [2015] was that the observed increase in reflectance with latitude within the lunar maria is independent of mare composition, and so could be attributed to solar wind flux, which depends on latitude, as a known agent of space weathering. Therefore, we first investigate if the increase in reflectance with latitude within the maria is independent of mare composition by using the newly calibrated LOLA data presented herein and fast neutron counts from Lunar Prospector's Neutron Spectrometer. Then, we investigate if the increase in reflectance with latitude in the maria is related to the abundance of nanophase and/or microphase iron, which are solar wind related space weathering products, using the radiative transfer model of *Lucey and Riner* [2011] and Kaguya Multiband Imager reflectance data.

5.3.2.1. Composition

Hemingway et al. [2015] used data from Lunar Prospector's Gamma Ray Spectrometer (GRS) to attempt to isolate the effects of composition from the observed latitude dependent reflectance within the maria. Some of both the darkest and most Ti-rich maria are located near the equator so this segregation is important to distinguish coincidental latitude dependent compositional variations from a reflectance variation that is independent of the underlying composition. In their study, *Hemingway et al*. [2015] used over 30 combinations of GRS derived Fe and Ti bins and observed latitude dependent albedo variations within each bin.

To independently isolate the effects of composition from the observed latitude dependent reflectance, we use a different measure of composition: the rate of arrival of fast neutrons measured by the Lunar Prospector's Neutron Spectrometer, at 60 km of spatial resolution (*Feldman et al*., 1998; available at http://pds-geosciences.wustl.edu/lunar/lp-l-grs-3-rdr-v1/lp_2xxx/ns/). The flux of these neutrons is proportional to the average atomic mass of the lunar surface at the point of measurement, and this mass is in turn dominated by the abundance of Ti and Fe, owing to their high atomic masses [*Gasnault et al*., 2001]. These elements also dominate the reflectance of lunar rock and soil: the effect of Ti is imposed by its presence in low albedo ilmenite, and that of Fe in its control on the reflectance of silicates. Fig. 5.15 a shows the distribution of fast neutron counts versus average solar flux for the entire lunar surface. The strong mode at 400 counts is the lunar highlands showing little dependence on average solar flux. Values above 400 counts largely represent the lunar maria. Fig. 5.15b shows the distribution of fast neutron counts versus average solar flux for the maria only, using the mapped-mare mask of *Nelson et al.* [2014].

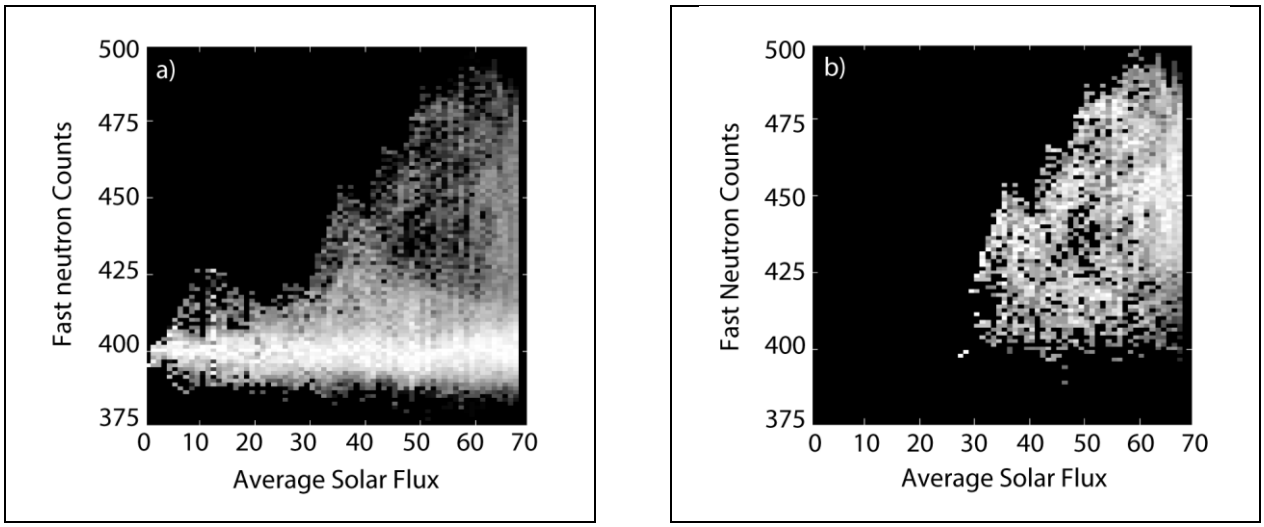

Figure 5.15. Two dimensional histograms of Lunar Prospector fast neutron counts per 32 seconds versus average solar flux. In (a) the histogram represents the entire Moon, highlands and maria, and in (b) the histogram is limited to the mapped maria of *Nelson et al.* [2014]. In (a) the major mode near 400 fast neutron counts across all fluxes corresponds to the relatively compositionally constant lunar highlands. In (b), low values extending to 400 fast neutron counts are pixels highly contaminated by highland signal owing to the small area of those mare deposits and the low resolution of the neutron data. Above about 450 counts, mare deposits are concentrated at low latitudes.

Mixing is an important issue in the relationships shown in Fig. 5.15 owing to the low spatial resolution of the neutron data. Small mare patches, mapped at very high resolution, will have their Lunar Prospector's Neutron Spectrometer fast neutron count rate values reduced by the presence of the surrounding highlands in the spectrometer field of view, while large expanses of mare will preserve their inherent fast neutron count rate values. It is evident that large patches of mare showing high atomic masses tend to be concentrated at low latitudes (high average solar flux), so there is only a small variation in average solar flux at these high atomic masses available to define a trend. To mitigate this issue, we present in Fig. 5.16 the distribution of reflectance for mare surfaces with fast neutron counts greater than 425 and less than 450, a range of values where there is also a wide range of average solar flux. This approach is analogous to the binning of Fe and Ti GRS data done by *Hemingway et al*. [2015]. Within these bounds, there is a wide range of average solar flux values, and while there is contamination from highland

material (Fig. 5.17), the composition is uniform in terms of average abundance of absorbing elements Fe and Ti. With the application of these compositional constraints, the reflectance continues to show an increase with decreasing solar flux, as shown by *Hemingway et al*. [2015] using Lunar Prospector gamma-ray data. Thus, we also find that the surface composition is not the direct cause of the observed latitude dependent reflectance within the maria.

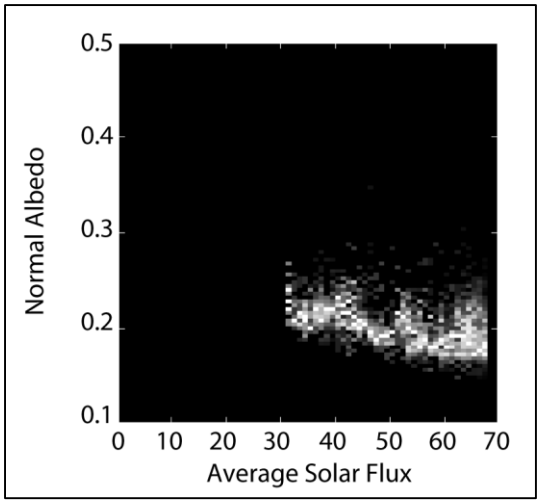

Figure 5.16. Distribution of normal albedo for mare deposits with fast neutron counts between 425 and 450 counts per 32 second. These data include a narrow range of compositions and show that the dependence of normal albedo on average solar flux still persists.

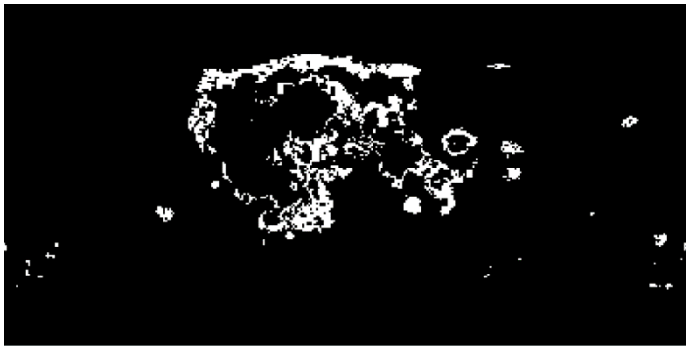

Figure 5.17. Spatial distribution of points shown in Fig. 5.16. These locations are dominated by mixed locations near the boundaries of the maria

5.3.2.2. Nanophase and microphase iron

The contrasting difference in behavior between the very strong trend exhibited by the lunar maria and the very weak trend in the lunar highlands (Fig. 5.8) invites explanation. *Morris* [1978] showed that, to first order, the abundance of nanophase iron in a lunar soil sample is both a function of exposure to space, and of the total iron abundance of the soil. This would suggest that color and albedo trends dominated by nanophase iron would be amplified in the lunar maria (15–16 wt% FeO), and attenuated in the low iron lunar highlands (3–5 wt% FeO). On the other hand, the highly transparent lunar highlands soil is more susceptible to the darkening effect of contaminants and this might act to counter the underlying iron effect. Here we test these narratives using radiative transfer modeling; first we estimate the global abundance of nanophase iron and its variation implied by the mare trend, then we scale the abundance of nanophase iron to the lunar highlands iron content, and finally compute the change in reflectance expected for this abundance of nanophase iron.

We use the radiative transfer model of *Lucey and Riner* [2011], validated using lunar soils, to estimate the variation in abundance of nanophase iron in the mare trend of Fig. 5.14. In that model, nanophase iron is accounted for in two forms: classical nanophase iron with sizes less than 33 nm that is a strong darkening and reddening agent [*Hapke*, 2001], and "microphase iron" or "Britt Pieters particles" [*Lucey and Riner*, 2011], with sizes larger than the nanophase iron but still submicroscopic that is a darkening (but not reddening) agent. The microphase iron is necessary to account for lunar albedo and color trends, and is concentrated in lunar agglutinate glass. Here we apply the radiative transfer model to global data from the Kaguya Multiband Imager [*Ohtake et al*., 2008] at 1 km spatial resolution in four spectral bands (750, 1050, 1250 and 1500 nm) outside the major iron absorption band (1000 nm). We derived the global reflectance mosaic using the Kaguya Multiband Imager data. We fit each four-point spectrum with a mixture of nanophase and microphase iron in a spectrally neutral host. Fig. 5.18 shows the resulting global maps of the distribution of nanophase iron and microphase iron in the lunar maria. The prominent dark maria, especially Mare Tranquilitatis and Oceanus Procellarum, show high abundances of microphase iron. The nanophase iron map is more uniform, with the classic dark maria less emphasized. As the radiative transfer model of *Lucey and Riner* [2011] is currently formulated, the microphase component is ambiguous with respect to the presence of spectrally neutral opaque minerals (*i.e*., the detected microphase iron could in fact be an opaque

mineral). Therefore, we believe that the microphase map (Fig. 5.18b) is likely influenced by the presence of opaque ilmenite. However, the sensitivity of the model to nanophase iron is not compromised by the presence of opaque minerals and more accurately reflects the abundance of this space weathering derived iron.

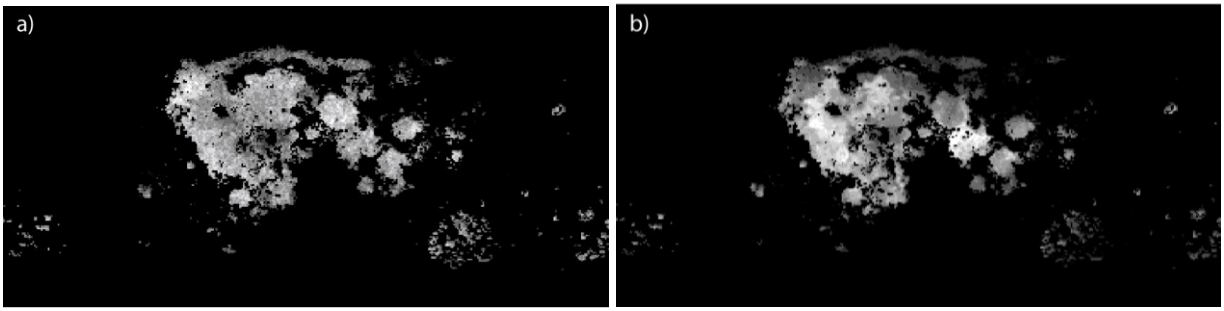

Figure 5.18. Maps of nanophase (a) and microphase iron (b) within the mapped maria from radiative transfer modeling of Kaguya Multiband Imager data. The microphase iron map (b) includes the effects of opaque minerals, seen in Mare Tranquilitatis, and presumably in the unsampled Oceanus Procellarum. In contrast, the nanophase iron map (a) is more uniform, reflecting only the presence of the space weathering coloring agent.

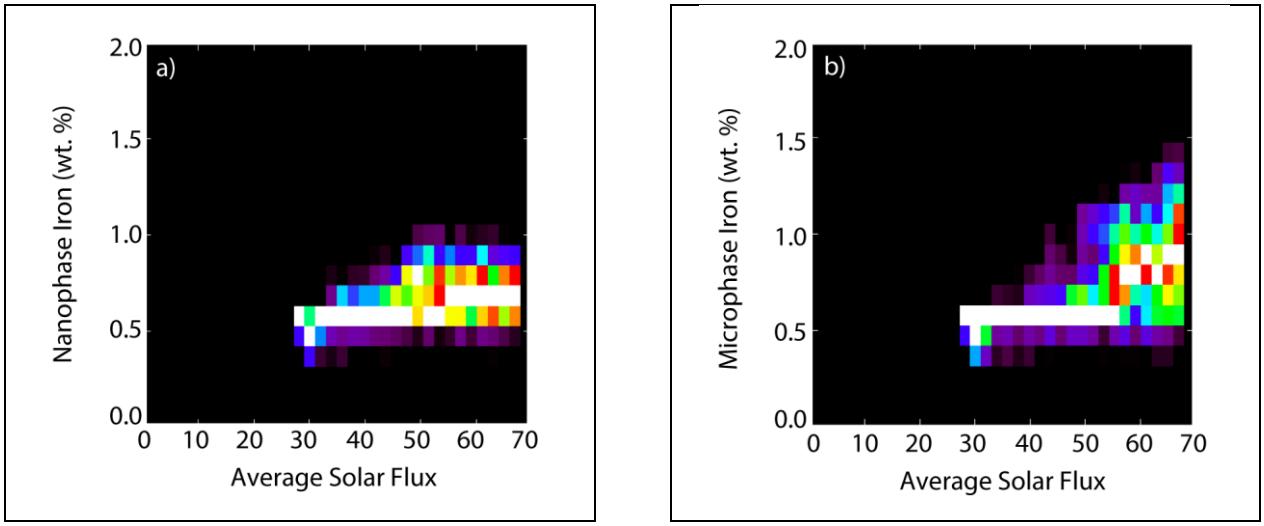

Figure 5.19. Two dimensional histograms of the distribution of nanophase iron (a) and microphase iron (b) versus the average solar flux within the mapped maria. Each solar flux bin has been normalized to its maximum value, so the white points track the position of the mode of the histogram as a function of average solar flux. The data is scaled between 0 and 1, from black,

through the rainbow, to white. In both cases the amount of modeled space weathering produced decreases with decreasing average solar flux, following the albedo variations.

Fig. 5.19 shows the abundance of nanophase and microphase iron within the maria as a function of average solar flux with the expected decline with decreasing flux. We find that the abundance of nanophase iron in the mare (A_{nm}) is dependent on the average solar flux, as shown in Eq. (5.6). The constant (0.37) represents the value of nanophase iron for a mare deposit at zero average illumination, which is close to the average value for the lunar highlands. Accounting for the fact that the lunar highlands has about four times less iron than the mare surfaces [*Feldman et al.*, 2002], the highland nanophase iron (A_{nh}) dependence can be approximated with Eq. (5.7).

$$A_{nm}\ (\text{wt. \%}) = (0.004 \cdot \text{average solar flux}) + 0.37 \quad (5.6)$$

$$A_{nh}\ (\text{wt. \%}) = (0.001 \cdot \text{average solar flux}) + 0.37 \quad (5.7)$$

Using Eq. (5.7) to establish the nanophase iron content variation in the highlands, the model change in reflectance over the full range of average solar flux (and latitude) is ∼15%. Inspection of Fig. 5.12 shows approximately this level of decrease in reflectance with increasing average solar flux in the southern hemisphere, and less in the northern hemisphere. The weaker variation with solar flux observed in the northern highlands could be due to a weak latitude dependence in intrinsic iron content that counters the increase in space weathering with decreasing latitude. Thus, the weak variation of albedo with latitude exhibited by the lunar highlands is consistent with the magnitude of the observed effect in the lunar maria when adjusted for the lower iron content of the highlands.

5.3.3. Implications of the observation

5.3.3.1. Stealthy Maria?

The conclusion that the lunar maria show increasing albedo with latitude holds up to the tests that have been presented herein. This allows for the possibility that mare deposits at high latitudes may have gone unrecognized, escaping classical mapping methods [*e.g.*, *Nelson et al.*, 2014], due to their albedos being less contrasting from the surrounding highlands terrain than is typical at low latitudes. Large, tens of kilometer-sized, polar mare deposits are clearly absent

because instruments with similar spatial resolution (~15 to 60 km per pixel) such as the Neutron Spectrometer and the Gamma-Ray Spectrometer onboard Lunar Prospector [*e.g*., *Lawrence et al*., 2002; *Prettyman et al*., 2006] and the Lunar Exploration Neutron Detector (LEND) onboard LRO [*Litvak et al*., 2012] would have detected these deposits. However, smaller un-detected mare deposits might be present. Here we try to identify small, kilometer-sized, unrecognized high latitude mare deposits based on roughness and establish if their albedo matches mare-like albedo values expected at high latitudes.

Krevlavsky et al. [2013] showed that the lunar maria at kilometer baselines are less rough than the lunar highlands, and *Hemingway et al*. [2015] used that method to isolate mare deposits independent of albedo and color. We use that same method to identify candidate small high latitude mare deposits. We compute the RMS of the topography derived from LOLA at a resolution of 500 m over a 2.5 km baseline moon wide, and use it as a roughness indicator. Qualitatively, we find that the lunar maria are distinctly smooth units (Fig. 5.20), similar to the result of *Kreslavsky et al*. [2013]. We create a mask to isolate units with mare-like roughness by including all data with RMS roughness less than 100 m. The map of surfaces meeting this roughness definition is shown in Fig. 5.21. Note that, in addition to the mapped maria, this definition includes many small areas at high latitudes that are potential candidates for stealthy mare deposits.

If small mare deposits were present at high latitudes, they would be expected to fall on the trend of normal albedo versus average solar flux defined by data at lower latitudes such as shown in Fig. 5.14. However, this is not observed. Instead, the normal albedo of these smooth units jumps suddenly up to highland-like values as the average solar flux falls below 30 (Fig. 5.22), also the limit of the mapped maria (Fig. 5.14). While these smooth high albedo plains may be cryptomaria (*i.e*., mare deposits obscured by thin basin ejecta of highland origin) they are not conventional mare deposits that were misclassified owing to high albedo. Overall, we do not find any small high latitude mare deposits that have been unrecognized or misclassified.

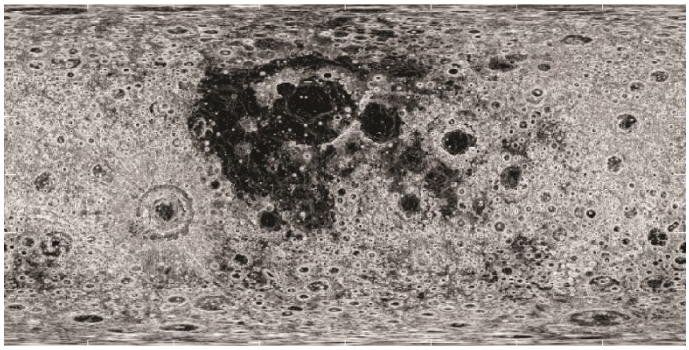

Figure 5.20. Map of roughness at a 2.5 km baseline derived from LOLA topography. Note the maria are extremely smooth. Possible mare surfaces at high latitudes should show similar low values.

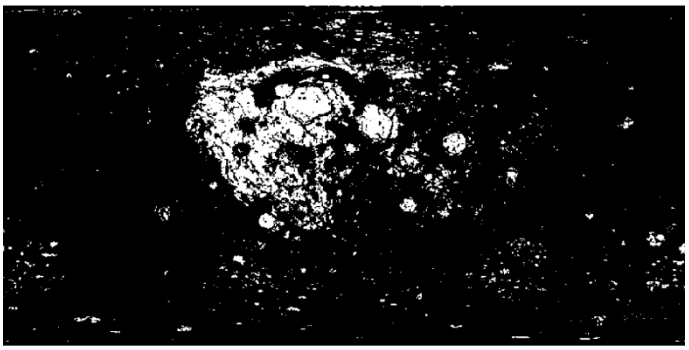

Figure 5.21. Map of surfaces with RMS roughness less than 100 m over the 2.5 km baseline. The image is similar to the classically mapped mare map, but exhibits many more surfaces at high latitudes that are potential mare surfaces obscured by high albedo.

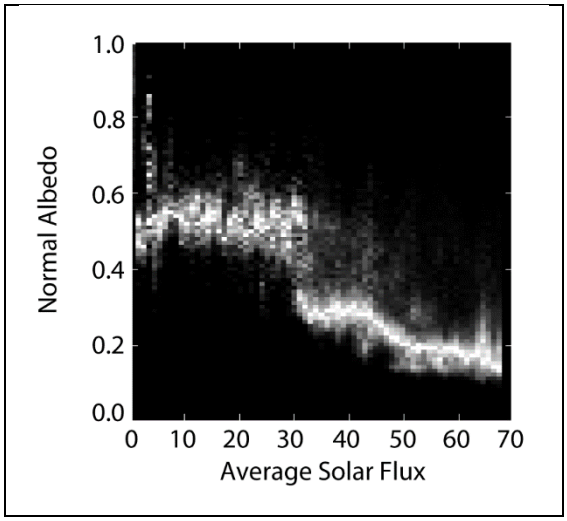

Figure 5.22. Plot of normal albedo versus average solar flux for all surfaces with RMS roughness <100 m. The mare trend is clear down to average solar flux values of about 30, but the trend does not extend to lower values.

5.3.3.2. Lunar soil space weathering indicators

The latitude dependence of space weathering may explain the puzzling relatively poor correlations among space weathering indicators in lunar soils. In the study of lunar soils, many parameters have been suggested to indicate the duration of space weathering exposure (in that literature the *maturity* of the lunar soil), including abundances of solar wind gas (*e.g.*, Ar), the amount of nanophase iron normalized to the total iron content (Is/FeO), and the abundance of petrographic agglutinates [*Morris*, 1976]. The relative abundance of these indicators in lunar soil samples does correlate, but is not highly correlated (Fig. 5.23). If we ignore the potential for experimental errors in the indicator values, the poor correlation may indicate significant differences in how these indicators accumulate in time and space, and the effect of mixing of different soils. One potential explanation is that soils at different latitudes may accumulate solar wind related indicators (nanophase iron and solar wind gas) at different rates than meteorite related indicators (petrographic agglutinates). Sampled lunar soils may then be the result of impact mixing that transported soils from different latitudes to the sample site, for example by crater rays extending hundreds of kilometers away from their source region.

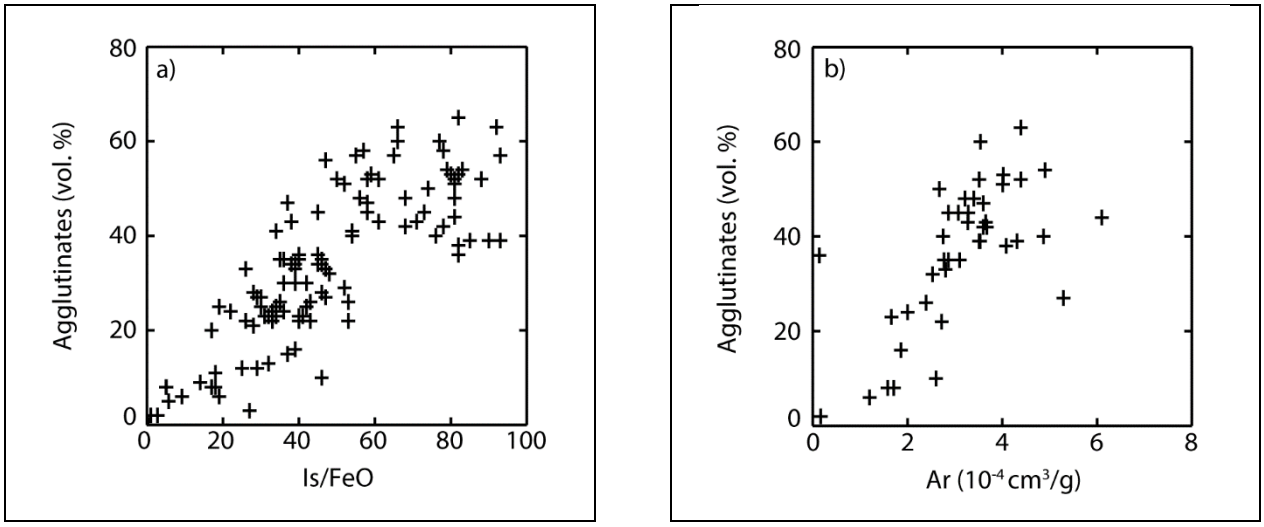

Figure 5.23. Correlation of space weathering indicators based on *Morris* [1976]. The abundance of agglutinates is a function of micrometeorite flux, which does not have the same distribution with latitude as the solar wind flux, whereas the abundance of nanophase iron (Is/FeO) and argon (Ar) are functions of solar wind fluxes. The abundance of Is/FeO can be derived both from solar

wind sputtering and micro meteorite impact vaporization, and the abundance of argon (Ar) is a direct result of interaction of the solar wind.

5.3.3.3. Planetary photometry

The presence of a latitude-dependent albedo phenomenon unaffected by illumination or viewing angles may impact photometric normalization of imaging and spectral data. At the very least, it means there is an additional variable besides viewing and illumination geometry that should be considered to achieve the most accurate results. Also, it underscores the fact that photometric functions derived from isolated locations are not necessarily representative of the whole surface [*e.g.*, *Buratti et al*., 2011], and vice versa. In particular, this effect may explain some of the differences in photometric behavior between mare and highland units that has hindered photometric normalization. A hypothetical hyper-immature mare surface could have a photometric behavior more similar to that of the highlands, and evolve to the typical mature mare surface. In addition, global albedo-binning in the derivation of the phase curve, as in *Yokota et al*. [2011], can mix different proportions of maria and highlands at different latitudes, and, thus, be susceptible to different amounts of space weathering. This may contribute, in part, to the increased scatter in the data for maria and intermediate albedo terrains reported by *Yokota et al*. [2011]. This effect may also help explain some of the differences in reflectances reported by different instruments [*Ohtake et al*., 2013] for the same locations, which are often normalized to a standard viewing geometry using an empirically-derived analytic photometric function.

To determine the magnitude of the effect this could have on photometric normalization, we conduct an experiment in which we start with a known photometric function for the maria, and see what magnitude error arises from assuming an incorrect albedo. To that end, we adopt the 1064 nm maria *Hapke* [1963] model of *Barker et al*. [2016] derived from LOLA passive radiometry. The normal albedo in this model is $A_n \approx 0.18$, which is indicative of maria at $\leq 30°$ latitude. In contrast, maria at 60° latitude have $A_n \approx 0.22$, or ~20 % larger (Fig. 5.16). We assume that this change in normal albedo is entirely due to a change in single-scattering albedo by the same proportion. In this experiment, the scientist does not know the albedo-latitude trend exists, and so uses $A_n \approx 0.18$ for the photometric correction instead of the true $A_n \approx 0.22$.

The normalized reflectance is calculated as:

$$r(30,0,30) = r_{tr}(i,e,g) \cdot \frac{r_b(30,0,30)}{r_b(i,e,g)} \quad (5.8)$$

where $r_{tr}(i, e, g)$ is the reflectance using the true albedo at incidence, emission, and phase angles of, respectively, i, e, and g, and $r_b(i, e, g)$ is the reflectance with the incorrect albedo at the same geometry. The percentage error in normalized reflectance is then:

$$\Delta r(30,0,30) = \frac{r(30,0,30) - r_{tr}(30,0,30)}{r_{tr}(30,0,30)} \cdot 100 \quad (5.9)$$

Fig. 5.24 shows Δr (30, 0, 30) as a function of phase angle for three different emission angles: 0°, 45°, and 85°. At nadir geometry, the farther from g = 30°, the larger the absolute error. The absolute error is <2% at all geometries except at small phase angles ($g \leq$5–10°) or when both phase and emission angles are very large ($g \geq$140° and $e \geq$60°). The absolute error reaches its largest values of 3–4% at the most extreme geometries with $g \geq$160° and $e \geq$85°. Theoretically, the magnitude of the error is controlled primarily by the treatment of multiple scattering and surface roughness in the *Hapke* model. Our understanding of the effects of multiple scattering and roughness on planetary photometry are still evolving, so these curves have some associated uncertainty. Also, the maria photometric function may change to some extent going from low to high latitudes. Small, physically reasonable variations in the parameters of the *Hapke* model, however, do not significantly affect these results. We conclude that the increase in albedo with latitude can cause errors in normalized reflectance of at most 2 % for the majority of near-nadir geometries. However, data obtained at unusual geometries may have higher errors. Extra caution should therefore be exercised when comparing normalized reflectances of mare locations at different latitudes.

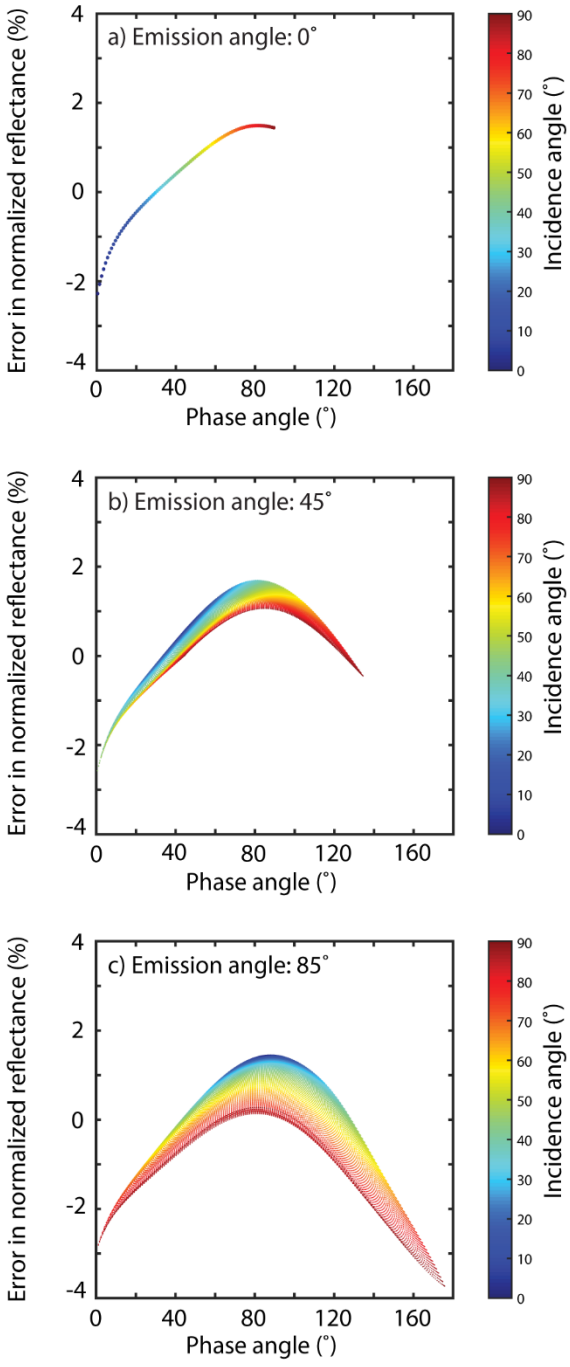

Figure 5.24. Percentage error in normalized reflectance caused by using a photometric correction appropriate for low-latitude maria at high latitudes. The photometric correction to a standard geometry of (i, e, *g*) = (30°, 0°, 30°) incorrectly uses a normal albedo, An ≈0.18, whereas the true value is 20% higher. Three cases are shown: (a) *e* = 0°, (b) *e* = 45°, and (c) *e* = 85°. The points are color-coded by incidence angle. The absolute error is < 2% for the majority of geometries.

5.4. Conclusions

We presented a new calibration of LOLA normal albedo data and documented several types of artifacts in the data set. With independent methods, we have confirmed the observation by *Hemingway et al*. [2015] that the lunar maria exhibit latitude dependent albedo, and that this appears not to be due to latitude dependent compositional variations. The very weak variation of albedo with latitude exhibited by the lunar highlands is found to be consistent with the magnitude of the observed effect in the lunar maria when adjusted for the lower iron content of the highlands, based on radiative transfer modeling. Possible high latitude mare deposits that could have been mis-mapped based on anomalous high albedo are not found; smooth high latitude deposits have albedos consistent with other highland units. The latitude effect may confirm the decoupling of space weathering rates due to solar wind and micrometeorites and explain low correlations of space weathering indicators in the lunar samples. Finally, the presence of a latitude-dependent albedo phenomenon has implications for photometric normalization, as it can cause errors in normalized reflectance of at most 2 % for the majority of near-nadir geometries, and higher errors for unusual geometries. Extra caution should therefore be used when comparing normalized reflectances of mare locations at different latitudes.

CHAPTER 6

CONCLUSION

The Moon represents an ideal laboratory to study a variety of processes occurring in our solar system. In this dissertation, we are specifically interested in learning about the composition of its crust, via the study of central peaks and basin rings, as they expose material originating from various depths. Here we present a summary of the results from each Chapter.

In Chapter Two, we used central peaks in complex craters as probes into the lunar crust to re-examine the hypothesis that the crust becomes more mafic with depth suggested by *Ryder and Wood* [1977]. They found that the impact melts associated with the large Imbrium and Serenitatis basins are more mafic than the surface composition of the Moon. We analyzed the composition of the central peak of 34 complex craters located within 50° in latitude with examples in the three major lunar terranes, the Feldspathic Highlands Terrane (FHT), the Procellarum KREEP terrane (PKT) and the South Pole-Aitken basin terrane (SPAT), using recent remote sensing data and combining the best practices of previous studies. We computed the mineralogy for these 34 central peaks using: (1) nine-band visible and near-infrared topographically corrected and high-resolution reflectance data from the Kaguya mission's Multiband Imager, (2) an improved version of Hapke's radiative transfer model validated with spectra of lunar soils with well-known modal mineralogy, and (3) new crustal thickness models from the Gravity Recovery and Interior Laboratory data to examine the variation in composition with depth [*Wieczorek et al*., 2013]. We found that there is no statistically significant increase in mafic mineral abundances with proximity to the crust-mantle boundary, or with depth from the current lunar surface, and therefore that the crust does not become more mafic with depth. What little correlation exists is due to the systematically closer crust-mantle boundary location and more mafic character of the central peaks in SPAT and in the PKT compared to the central peaks in the FHT. Indeed, craters from the FHT span the entire crustal column and do not become more mafic with depth. We found exposures of purest anorthosites (PAN) largely consistent with the analysis of *Ohtake et al*. [2009], but also found that PAN is a minority constituent and there is no clear evidence of a distinct PAN-rich layer. We also find that the average composition of most of the central peaks we analyze is more mafic than classically defined anorthosites (≥90 wt.%

plagioclase), with an average composition of noritic anorthosite. Low-calcium pyroxene is the dominant mafic component throughout the entire crustal column, followed by lesser amount of clinopyroxene, and olivine. Olivine is the dominant mafic component only in the central peak of Copernicus (PKT). Because of the scarcity of extremely anorthositic lithologies, we suggest that the FHT is a remnant of a primary crust that was a relatively mafic anorthosite, as suggested by *Warren* [1985]. The variability of the mafic assemblage in the FHT relative to the other terranes suggests that at least some of the central peaks in the FHT may be sampling subsequent intrusion of mafic material into that crust, though no ultramafic material was detected that might suggest fully differentiated plutons. The PKT and SPAT impact events probably incorporated an orthopyroxene-rich and olivine-poor mantle component in their melts. Central peaks in SPAT and in some regions of the PKT might also expose material derived from the differentiation of large-scale melt sheets associated with basin formation events.

In Chapter Three, we used the innermost ring of impact basins as probes into the lunar crust to enhance our understanding of the composition of the crust with depth. We conducted a quantitative and thorough analysis of the mineralogical composition of the innermost ring of 13 impact basins, and used a hydrocode model to place constraints on the depth of origin of the material exposed by the innermost ring, producing the first rule of thumb for the depth of origin of basin rings from such models. We found that the average composition of the innermost rings is consistent with the average composition of the central peaks studied in Chapter Two at similar depths. The basin rings and central peaks in the FHT are generally the most anorthositic, and central peaks in SPA the least. We found that the most abundant rock type is anorthosite (≥90 wt.% plagioclase) on the innermost ring of most basins. Orientale has the most abundant proportion of nearly pure anorthosite (with >98 wt.% plagioclase), slightly more than Hertzsprung and Freundlich-Sharonov. We do not find ultramafic lithologies such as pyroxenite, peridotites, or dunites, hence we do not detect exposures of pure mantle material at the scale of the resolution of the Multiband Imager data (~60 m). We detect olivine on the innermost ring of basins where *Yamamoto et al*. [2010] also detected olivine. The lithology in which the olivine is situated is olivine norite or gabbro and troctolitic anorthosite, which can correspond to mixture of crustal anorthositic material and mantle dunite, or originate from magnesium-rich plutons in the Moon's lower crust [*Hess*, 1994]. The hydrocode modeling suggests that basins expose material originating from various depths, a shallow component originates on average from

$0.06\pm0.01D_{tr}$ and a deep component originates on average from $0.16\pm0.01D_{tr}$. The deep component originates from the mantle in 10 of the basins we studied. However, we found that the shallow component largely dominates the ring material, which might explain why we do not detect ultramafic exposures in the Multiband Imager data. We compared the relative proportions of mafic minerals to the proportions of shallow and deep components present on the innermost rings, and found that the average abundance of olivine over the total abundance of mafic minerals generally decreases with increasing proportion of mantle component, suggesting that it originates from the crust. The average abundance of high-calcium pyroxene over the total abundance of mafic minerals generally increases with the proportion of crustal material exposed, also suggesting a crustal origin. The average abundance of low-calcium pyroxene over the total abundance of mafic minerals generally increases with the proportion of mantle material exposed which supports a mantle origin. This is also consistent with the detection of noritic anorthosite in small craters (< 1 km in diameter) in the FHT by *Lucey et al.* [2014]. These small craters sample megaregolith and require an orthopyroxenite mantle to explain their composition.

In Chapter Four, we took a novel approach to study the composition of central peaks and basin rings in the polar regions. The extreme lighting near the poles has not permitted quantitative mineral analysis previously; we combined spectra from the Kaguya Spectral Profiler data, and calibrated reflectance data from the Lunar Orbiter Laser Altimeter (we described the calibration in Chapter Five), in order to derive the first high resolution FeO and mineralogic maps of the polar regions. We used the mineral maps to study the composition of 27 central peaks and 5 basin rings in the polar regions, nearly doubling the number of central peaks and basin rings studied in Chapters Two and Three. As the mineral abundance derived herein use different datasets than the mineral abundances from the previous Chapters, they consist in an independent dataset to study composition of the lunar crust. Consistent with Chapter Two, we found that the central peaks and basin rings in FHT are mostly anorthositic in composition, whereas the central peaks and basin rings in SPA are mostly noritic and gabbroic. We also measured an intermediate composition for the central peak located in the PKT. We found that the central peaks in SPA are noritic and gabbroic at all depths (about 27 km away from the crust/mantle down to approximately the crust-mantle boundary), consistent with the presence of a large differentiated melt sheet of such composition [*e.g.*, *Potter et al*., 2012; *Hurwitz and Kring,* 2014]. It is possible that there is a weak decrease in plagioclase content with increasing

proximity to the crust mantle boundary in the South Pole-Aitken basin, although there is no unambiguous trend. We noted significant difference in abundances of the pyroxene composition derived from the Multiband Imager data and from the Spectral Profiler data, but we found that low-calcium pyroxene is the most abundant mafic mineral in all the central peaks and basin rings in the polar regions. To compare our results with results from other previous studies, we investigated the composition of Schrödinger basin, and confirmed the presence of anorthosite, norite and anorthositic troctolite previously identified by *Ohtake et al*. [2009], *Yamamoto et al*. [2010] and *Kramer et al*. [2013].

In Chapter Five, we calibrated the reflectance data acquired by the Lunar Orbiter Laser Altimeter experiment on Lunar Reconnaissance Orbiter, and produced equatorial and polar mosaics that are now available to the public. We used these datasets to investigate a newly discovered increase in albedo with latitude in the lunar maria [*Hemingway et al*., 2015].We confirmed the increase, and confirmed that it is not an artifact arising from the distribution of compositions within the lunar maria, using data from the Lunar Prospector Neutron Spectrometer. Radiative transfer modeling of the albedo dependence within the lunar maria is consistent with the very weak to absent dependence of albedo on latitude in the lunar highlands; the lower abundance of the iron source for space weathering products in the lunar highlands weakens the latitude dependence to the extent that it is only weakly detectable in current data. We also investigated whether the latitude dependent albedo may have obscured detection of small mare deposits at high latitudes, and found that small regions at high latitudes with low roughness similar to the lunar maria are not mare deposits that may have been misclassified owing to high albedos. Finally, we suggested that the only modest correlations among space weathering indicators defined for the lunar samples may be due to mixing of soils from distinct latitudes.

Overall, we found that the basin rings and central peaks in the FHT have modal plagioclase content ranging between ~60-95 wt.%, with no apparent relationship between the modal compositions and their depth in the crust. As these basin rings and central peaks span through the entire crustal column and likely represent primary crustal material, this suggests that the primary crust is dominantly anorthositic and heterogeneous, including intrusions of more mafic material as suggested by *Cahill et al*. [2009]. Our results are consistent with the model for the solidification of the magma ocean proposed by *Elkins-Tanton et al*. [2011], according to

which magnesium-rich olivine would have crystallized first and sank, followed by low-calcium pyroxene which would have crystallized on top of the olivine cumulates to form the lunar mantle. Ilmenite-rich cumulates containing high concentrations of incompatible radioactive elements would have crystallized between the top of that mantle and the bottom of the anorthositic crust. This would have led to a gravitationally unstable pile of low density magnesium-rich minerals at the bottom grading to high density iron-rich minerals and even denser ilmenite and radioactive elements on top of the mantle. The ilmenite-rich layer and the underlying iron-rich cumulates would have sunk towards the mantle, while the magnesium-rich early cumulates would have buoyantly rose to form the more mafic intrusions in the lunar crust [*Hess and Parmentier*, 1994; 1995].

Overall, our results are not consistent with models that suggest that the lunar crust consists of relatively homogeneous layers, such as a massive layer of nearly pure anorthosite, overlain by a high-calcium pyroxene layer [*e.g*., *Ohtake et al*., 2009; *Yamamoto et al*., 2015]. We identified nearly pure anorthosite in only tens of pixels on a few basin rings and central peaks, which does not support the presence of a massive layer of nearly pure anorthosite. We do not measure a decrease in the high-calcium pyroxene content with depth, and thus do not find evidence of a layer of high-calcium pyroxene over the potential layer of nearly pure anorthosite as suggested by *Yamamoto et al*. [2015].

As we showed in this dissertation, central peaks and basin rings provide important clues regarding the composition of the lunar crust with depth, given that the depth of origin of the material they expose is well constrained. While we provided better constraints on the depth of origin of the material exposed by the innermost ring of basins using hydrocode modeling, obtaining samples from the innermost ring of basins would be invaluable to foster our understanding of impact basin formation, and the composition of the lunar crust. As the hydrocode modeling suggests that the innermost ring expose material originating from the lunar mantle at the subpixel scale (<62 meters per pixel), obtaining samples from the innermost ring of basins would also help us understand the composition of the lunar mantle.

APPENDIX A

Supporting Information for: Lunar Central Peak Mineralogy and Iron Content using the Kaguya Multiband Imager: Reassessment of the Compositional Structure of the Lunar Crust

A.1 Introduction

This supporting information file contains information about the latitude quality dependency in the Multiband Imager data, as well as a detailed explanation of the iron mapping algorithm developed in this study to be used with the Multiband Imager data. It also contains a table with the mineral abundances and other information for each central peak analyzed in this study.

A.2 UVVIS and NIR sensor discrepancy and latitude quality dependency

The Multiband Imager acquired data in five UVVIS spectral bands (415, 750, 900, 950, 1001 nm) and four NIR spectral bands (1000, 1050, 1250, 1550 nm). Color ratio images constructed using the UVVIS sensor (Fig. A.1a) or the NIR sensor (Fig. A.1b) separately produce high quality ratio images at the global scale consistent with prior data sets. However, when forming spectral ratios that use NIR and UVVIS data together, we find abundant artifacts that form rectangular regions, and considerable orbit to orbit striping (Fig. A.2). The artifacts are most clearly displayed in ratios of the two bands near 1000 nm (UVVIS 1001 nm, NIR 1000 nm) where spectral differences should be minimal (Fig. A.2b). This indicates a systematic difference between the two cameras. To correct for this effect, we use the ratio between the two bands near 1000 nm, which is dominated by the artifact, to remove this artifact. Based on the maturity of the Si detector technology used by the UVVIS sensor, we assume that the UVVIS data are reliable, and that the IR data need correction, although this does not have an effect on our mineral mapping algorithm because we use continuum removed reflectance spectra. Based on this assumption, and the artifact characterized by the two ~1000 nm bands, the corrected NIR data are defined by Eq. A.1.

$$NIR_{x\ nm}\ \text{corrected} = (NIR_{1001\ nm}/UVVIS_{1000\ nm}) \cdot NIR_{x\ nm}\ \text{uncorrected} \quad (A.1)$$

Furthermore, the data becomes very noisy poleward of ±50º latitude. Therefore, we choose to restrict our study to central peaks located within ±50º latitude, and to correct the offset in reflectance between the two sensors (Eq. A.1) for each pixel individually in a given central peak.

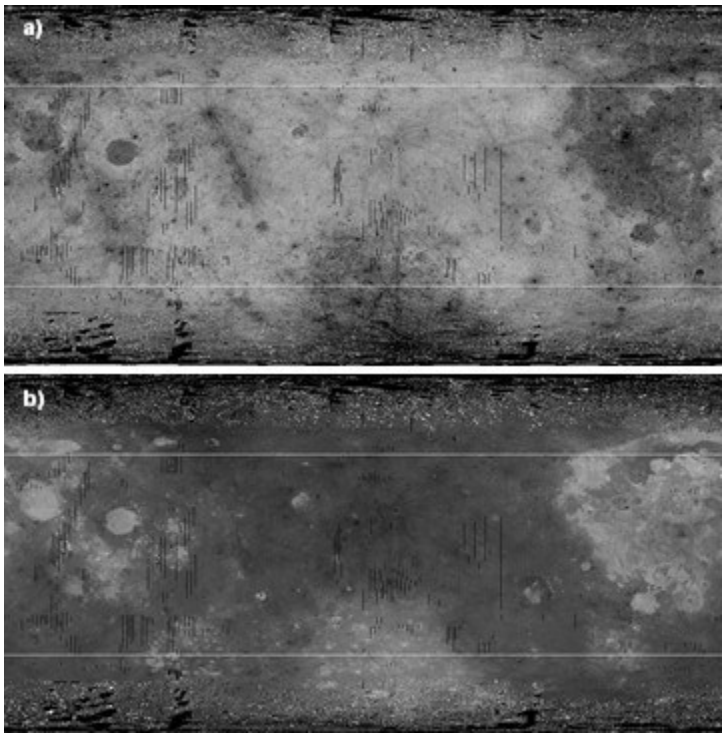

Figure A.1. Color ratio images constructed using reflectance data from separate sensors of the Multiband Imager, at 32 ppd spatial resolution (±90º latitude, white lines denote ±50º latitude). (a) UVVIS color ratio using 950 nm reflectance divided by the 750 nm reflectance. In this image, the maria are evident because of their 1000 nm absorption band generally stronger than in the highlands, and the few large craters apparent at this scale show anomalies due to their shallow continuum slopes due to less nanophase iron. (b) NIR color ratio using 1250 nm reflectance divided by the 1000 nm reflectance. At high latitudes in both images very high and low values are present due to shadowing whereas a few gaps are present in equatorial data. In this image, the maria show high values both because of their 1000 nm absorption band generally stronger than in the highlands, and because of an inherently redder continuum absorption. Space weathering effects in this image are weak, but not absent.

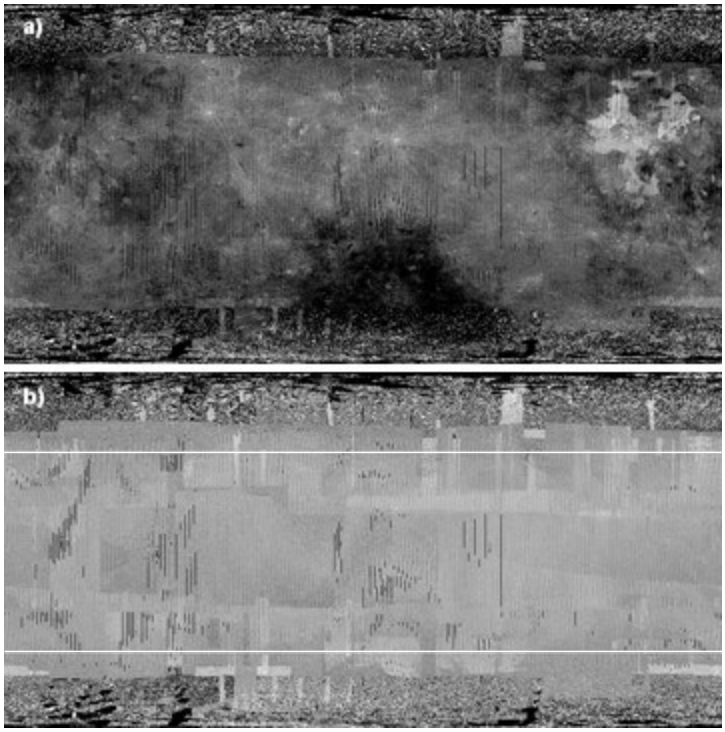

Figure A.2. Color ratio images constructed using reflectance data from both sensors of the Multiband Imager, at 32 pixels per degree of spatial resolution (±90º latitude, white lines denote ±50º latitude). a) UVVIS/NIR color ratio using 950 nm reflectance divided by the 1050 nm reflectance. b) UVVIS/NIR color ratio using 1001 nm reflectance divided by the 1000 nm reflectance. We find abundant artifacts that form rectangular regions, and considerable orbit to orbit striping, which are most clearly displayed in ratios of the UVVIS 1001 nm and NIR 1000 nm reflectance data.

A.3. Iron algorithm for the Multiband Imager data

Because reflectance spectra can have similar shapes (especially when using few spectral bands), but very different chemical composition (Fig. A.3), we use iron as a constraint in our modeling. We compute the iron abundance of each modeled spectra, compute the iron abundance of a given each pixel and make sure that the closest spectral match is within 2 wt.% iron of the iron estimated for that pixel from the reflectance data.

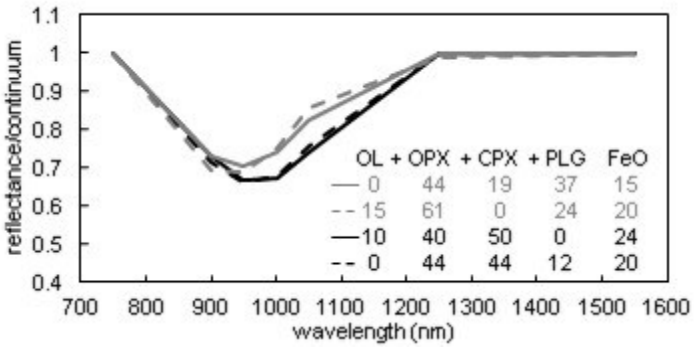

Figure A.3. Examples of continuum removed modeled reflectance spectra that have similar shape at the Multiband Imager spectral sampling, but very distinct mineralogical composition and distinct FeO abundances. The solid and dashed line of each shade show similar spectral shape, but distinct composition. These similar spectra can be distinguished with their distinct FeO content.

An iron algorithm that can be used with the Multiband Imager reflectance data has been presented by *Otake et al.* [2012] where they modified the algorithm of *Lucey et al*. [2000]. *Lucey et al*. [2000] used calibration constants specific to Clementine UVVIS data, to produce a global map of iron. On a global scale, the iron contents derived from Kaguya Multiband Imager data [*Otake et al*., 2012] and from Clementine UVVIS data [*Lucey et al*., 2000] have similar distributions [*Otake et al*., 2012]. However, we find that the algorithm of *Otake et al*. [2012] produces negative iron values in areas where purest anorthosites have been reported, when used with high spatial resolution the Multiband Imager data (~20m and ~60m per pixel), for example in Jackson Crater (Fig. A.7). Since we use iron as a constraint in our radiative transfer model, obtaining non-negative iron value is imperative. Therefore we recalibrate the iron algorithm that can be used with the Multiband Imager reflectance data, including exposures of purest anorthosite (>98 wt% plagioclase), and assuming very low iron contents.

We use the method of *Lucey et al*. [2000] to recalibrate the iron algorithm, and include reflectance data where we detect purest anorthosites as a constraint. First, we downsample Multiband Imager reflectance data to the same spatial resolution as the Lunar Prospector data (0.5 degree per pixel, ~15 km per pixel) and then plot the reflectance ratio 950/750nm versus the reflectance at 750 nm for a subset of the Multiband Imager reflectance data (blue points, Fig. A.4a). The data used comes from a few degrees of latitude and from all longitudes (*i.e.*,

representative of both highlands and maria). We over plot Multiband Imager data from Jackson crater where purest anorthosite have been reported [*Ohtake et al*., 2009] (orange points, Fig. A.4a), and Multiband Imager data from the Apollo landing sites (black points, Fig. A.4a). In the reflectance ratio versus reflectance space, the optimized origin corresponds to the most mature value a pixel can theoretically be [*Lucey et al*., 2000]. In order for all datasets to agree, we find the new optimized origin to be x_{0Fe}=0.04 and y_{0Fe}=1.39 (orange triangle, Fig. A.4a). As a comparison, we show the optimized origin defined for Clementine data [*Lucey et al*., 2000] in figure A.4a (black "X"). We then calculate the iron parameter (θ_{Fe1}) of *Lucey et al*. [2000] for the Multiband imager data, versus their iron content (FeO wt%) in Lunar Prospector data (Fig. A.4b). The black points in figure A.4b correspond to Multiband Imager reflectance data at the Apollo landing sites. Taken alone, the relationship for Apollo data seems to follow a linear trend, as suggested by *Lucey et al*. [2000]. However, we overplot the purest anorthosite pixels from the Multiband Imager data (orange points in Fig. A.4b), assuming they have an iron content of 0.5 wt%, and find that the linear trend does not hold. An exponential trend yields the best results (r = 0.92), which gives the formula for the second iron parameter (θ_{Fe2}). The second iron parameter (θ_{Fe2}) plotted versus iron from Lunar Prospector data, including the purest anorthosite pixels (orange), now show a strong linear agreement (r = 0.93) with the calculated iron abundances (Fig. A.4c). However, there is still an offset between the iron derived from the algorithm and the iron calculated in the Apollo samples. A final correction to this offset is required and is shown in figure A.4d, which now yields a correlation (r) of 0.97 between the iron in Apollo samples, versus the iron calculated with our algorithm using Multiband Imager data. The recalibrated iron algorithm for MI reflectance data is:

$$\theta_{Fe1} = -arctan\left\{\frac{[(r_{950}/r_{750})-y_{0Fe}]}{(r_{750}-x_{0Fe})}\right\} \quad \text{(A.2)}$$

$$\theta_{Fe2} = 0.0656e^{(3.6681\cdot\theta_{Fe1})} \quad \text{(A.3)}$$

$$FeO\ (wt.\%) = (1.0708\cdot\theta_{Fe2}) - 0.3986 \quad \text{(A.4)}$$

Figure A.5 shows a map of the global distribution of FeO calculated using the algorithm herein, where the white lines correspond to ±50º latitude. Figure A.6 shows the histogram distribution of FeO from Lunar Prospector data [*Lawrence et al*., 2002] in white, and from this study in green, between ±50º latitude. Data from the Lunar Prospector at 0.5 degree per pixel has

been used, and MI data has been downsampled to the same resolution. The global distribution of both datasets at 0.5 degree per pixel is strikingly similar.

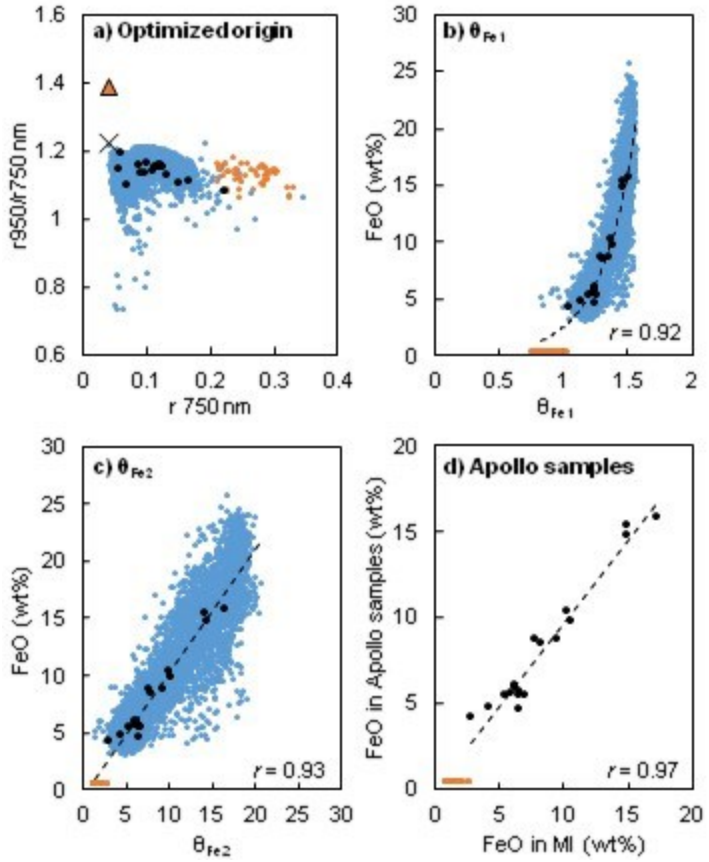

Figure A.4. Calibration of iron mapping algorithm for the Multiband Imager data (blue) using pixels at Apollo sampling sites (black), and pixels where purest anorthosites have been reported by *Ohtake et al*. [2009] in Jackson crater (orange). a) definition of a new optimized origin (triangle). The "X" represents the optimized origin from Clementine data as defined by *Lucey et al*. [2000]. b) regression between the θ_{Fe1} [*Lucey et al*., 2000] of Multiband Imager data and Lunar prospector FeO. c) regression between the θ_{Fe2} of Multiband Imager data and Lunar prospector FeO. d) correlation between the FeO in multiband Imager pixels at the Apollo Landing sites and the laboratory measured FeO of these samples.

Figure A.7 shows the improvement in iron measurement on a local scale, for example on and around the central peak of Jackson crater. Figure A.7a shows the iron abundances (0-10 wt%) using the algorithm of *Otake et al*. [2012], and figure A.7b shows the iron abundances (0-

10 wt%) using the algorithm herein (Eq. A.2-A.4). Figures A.7c shows that the negative iron abundances in figure A.7a are absent in figure A.7b.

Figure A.5. Global FeO map using the algorithm in this study and MI reflectance data at 750 and 950 nm. The image shows ±90º latitude, and the white lines correspond to ±50º latitude.

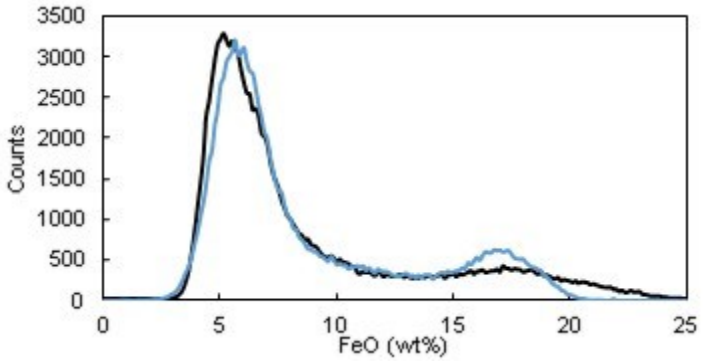

Figure A.6. Global distribution of FeO at 0.5 pixel/degree between ±50º latitude from Lunar Prospector data [black, *Lawrence et al*., 2002], and from theMultiband Imager data (blue, this study).

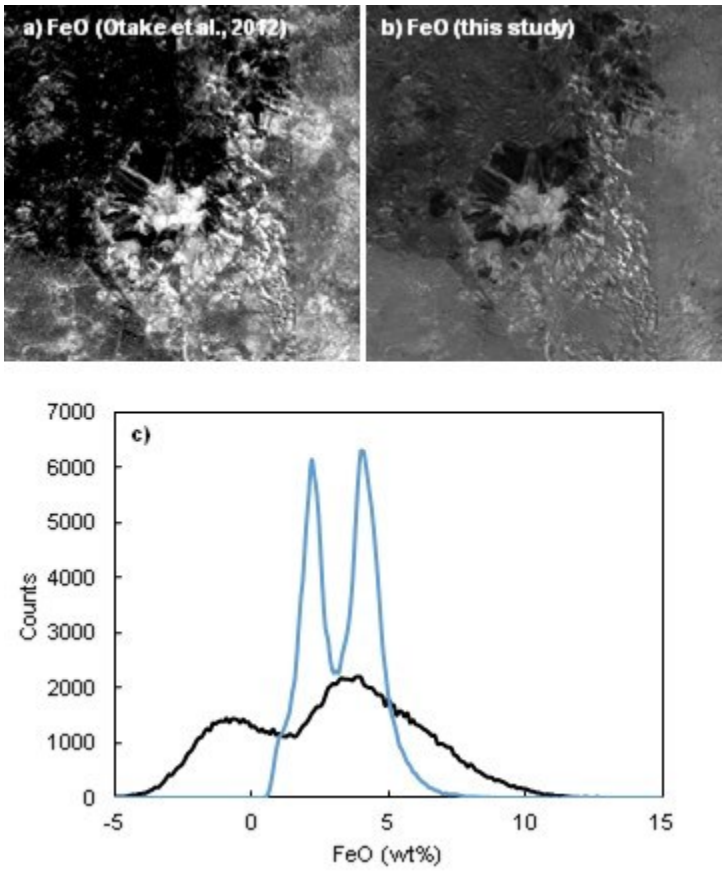

Figure A.7. Distribution of iron (FeO wt.%) on and around the central peak of Jackson Crater. a) FeO abundances (wt.%) using the algorithm of *Otake et al*. [2012] (0-10wt% stretch). b) FeO abundances (wt.%) using the algorithm presented in this study (0-10wt% stretch). c) Histogram of FeO (wt.%) values from both images, *Otake et al*. [2012] (black), and this study (blue).

APPENDIX B

Mineral maps in the equatorial region

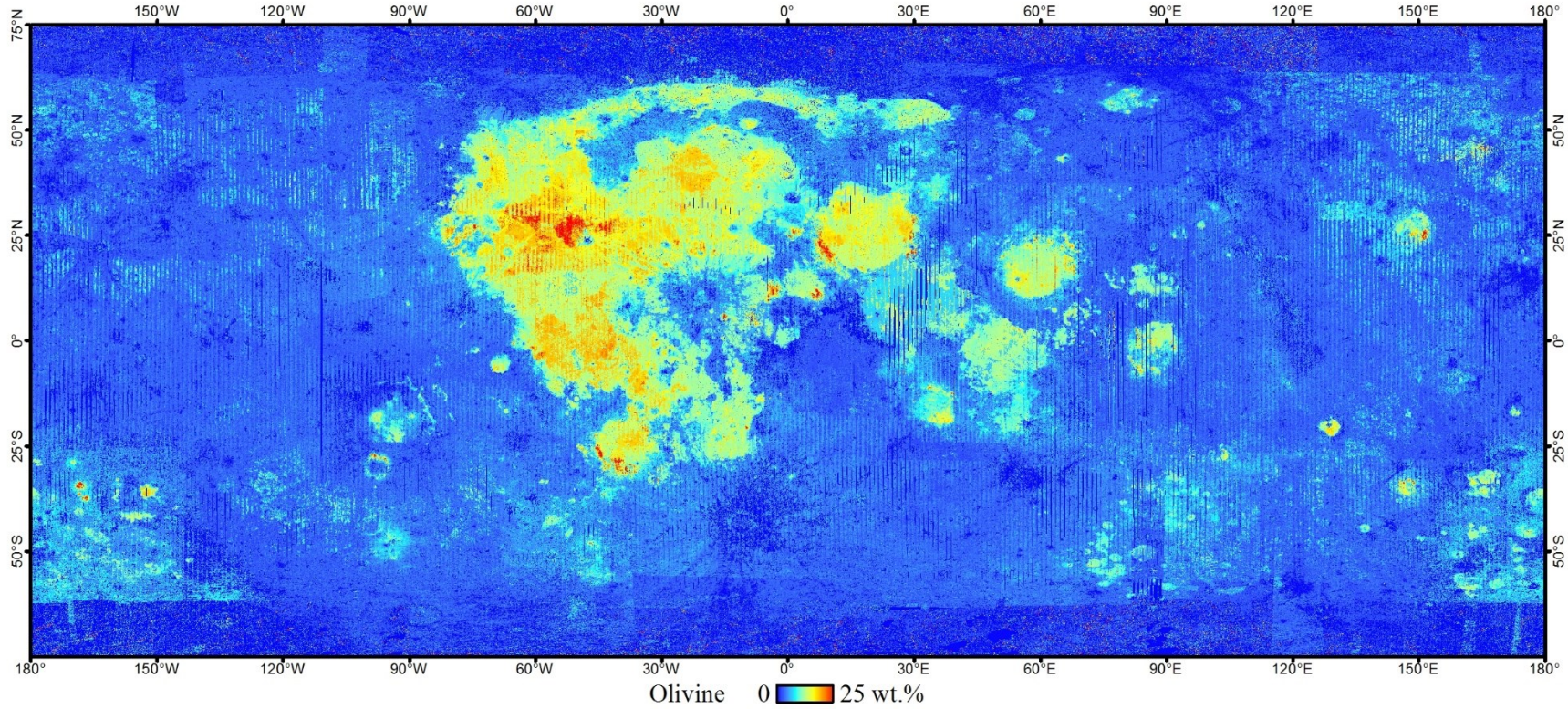

Figure B.1. Global abundance of olivine as derived from the method described in Chapter Three shown here at 32 pixel per degree (~1 km per pixel).

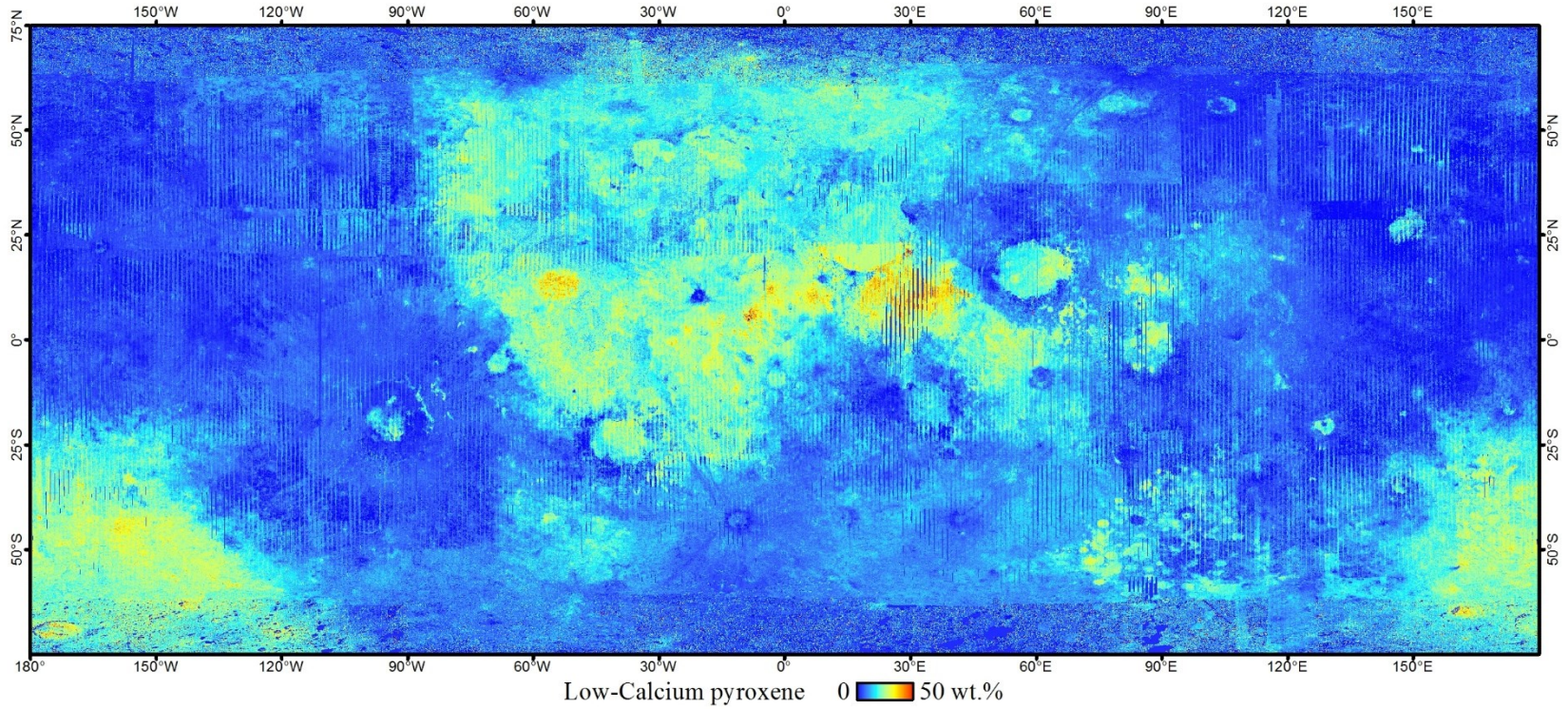

Figure B.2. Global abundance of low-calcium pyroxene as derived from the method described in Chapter Three shown here at 32 pixel per degree (~1 km per pixel).

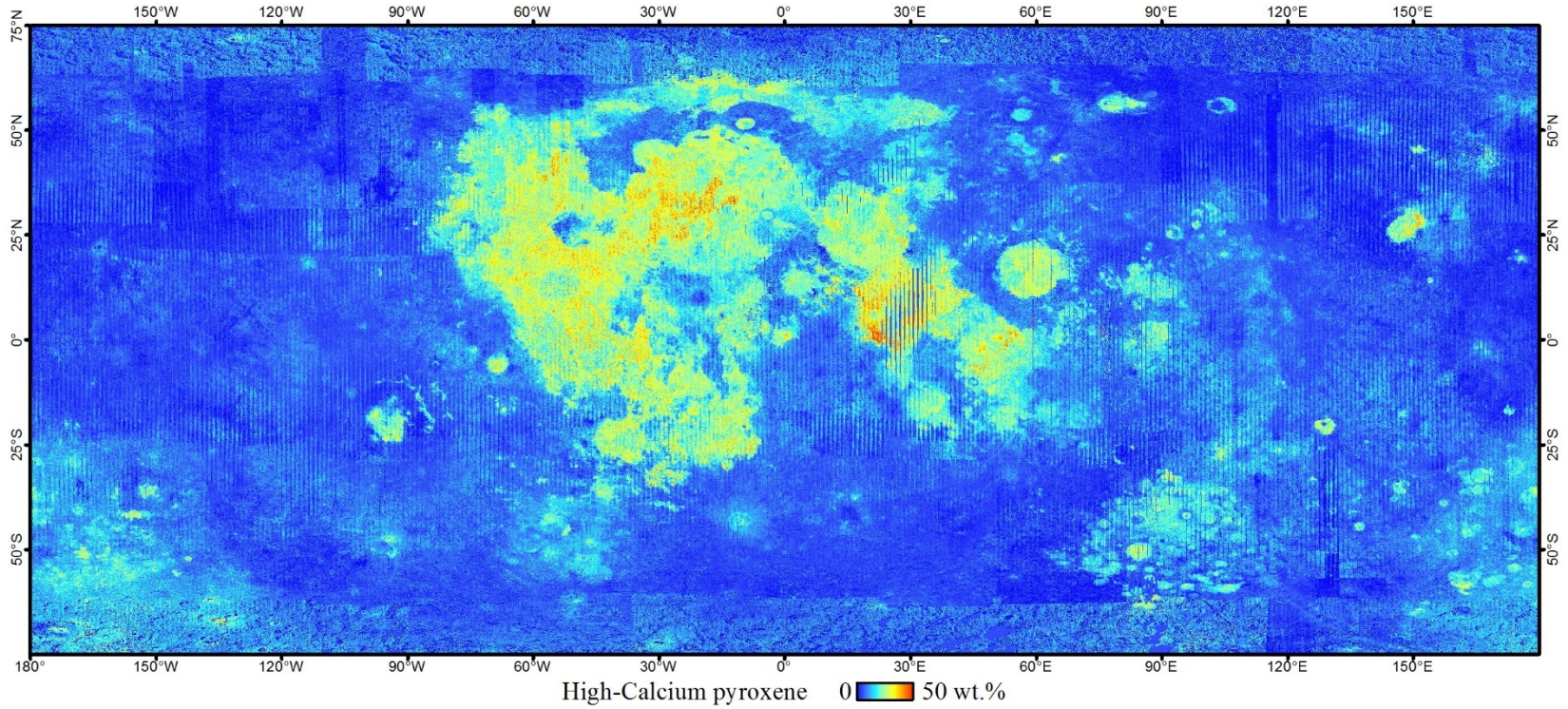

Figure B.3. Global abundance of high-calcium as derived from the method described in Chapter Three shown here at 32 pixel per degree (~1 km per pixel).

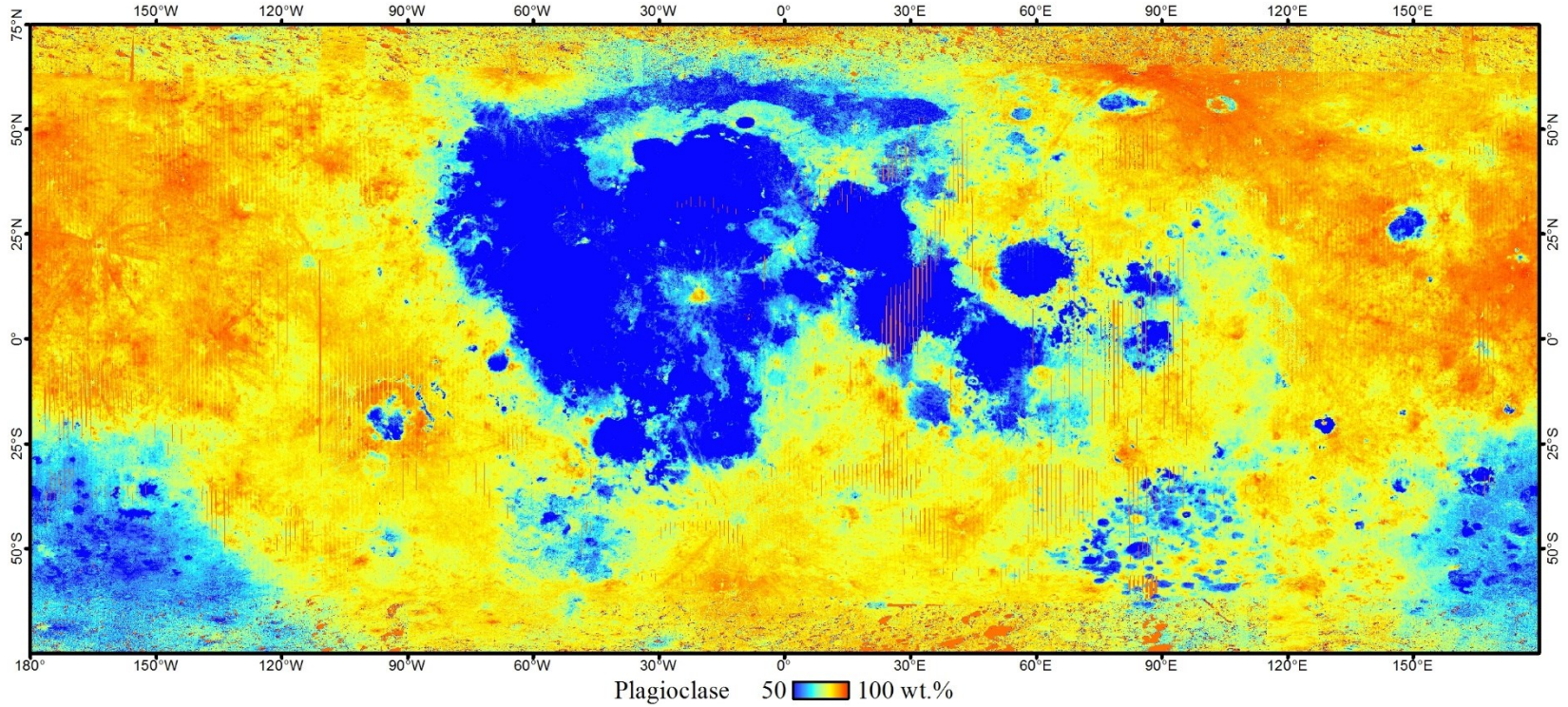

Figure B.4. Global abundance of plagioclase as derived from the method described in Chapter Three shown here at 32 pixel per degree (~1 km per pixel).

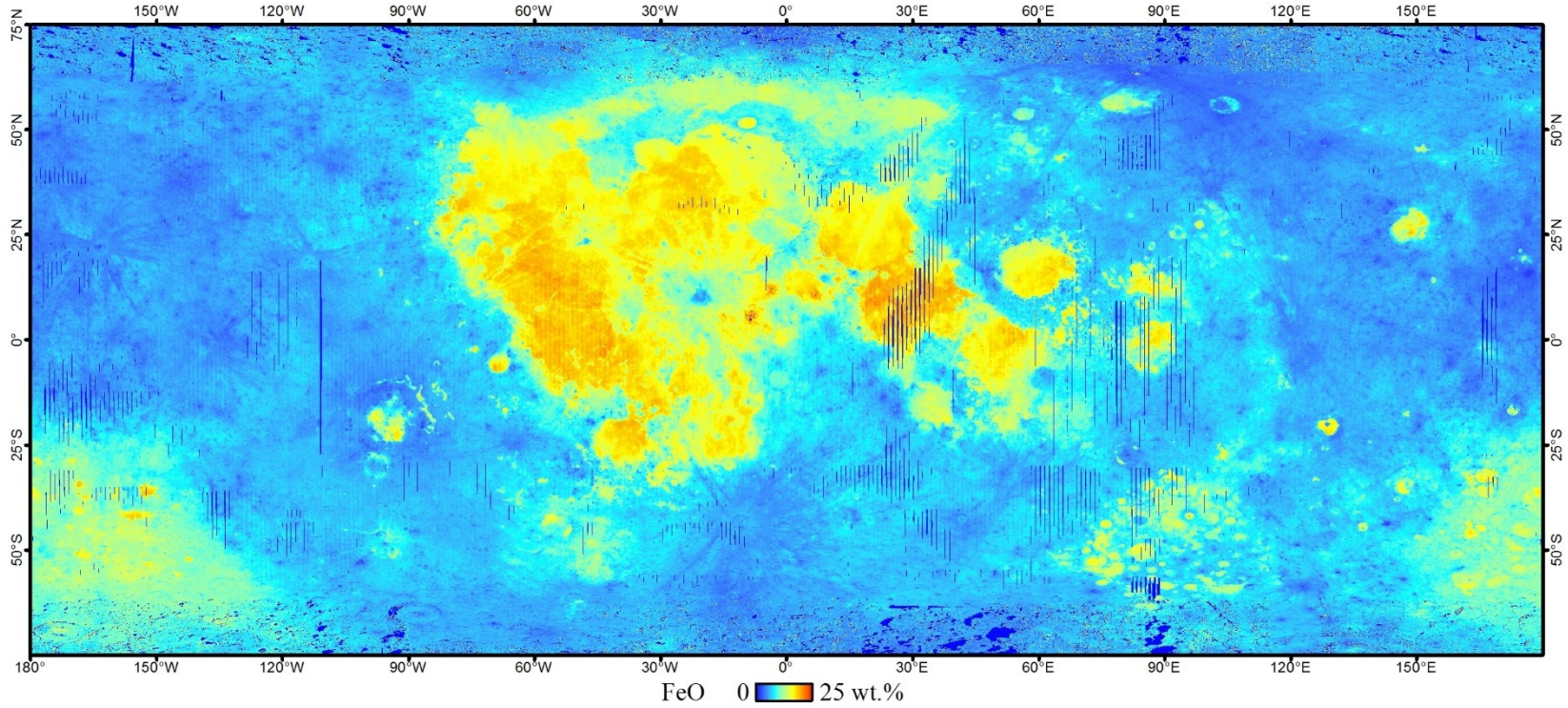

Figure B.5. Global abundance of iron as derived from the method described in Chapter Three shown here at 32 pixel per degree (~1 km per pixel).

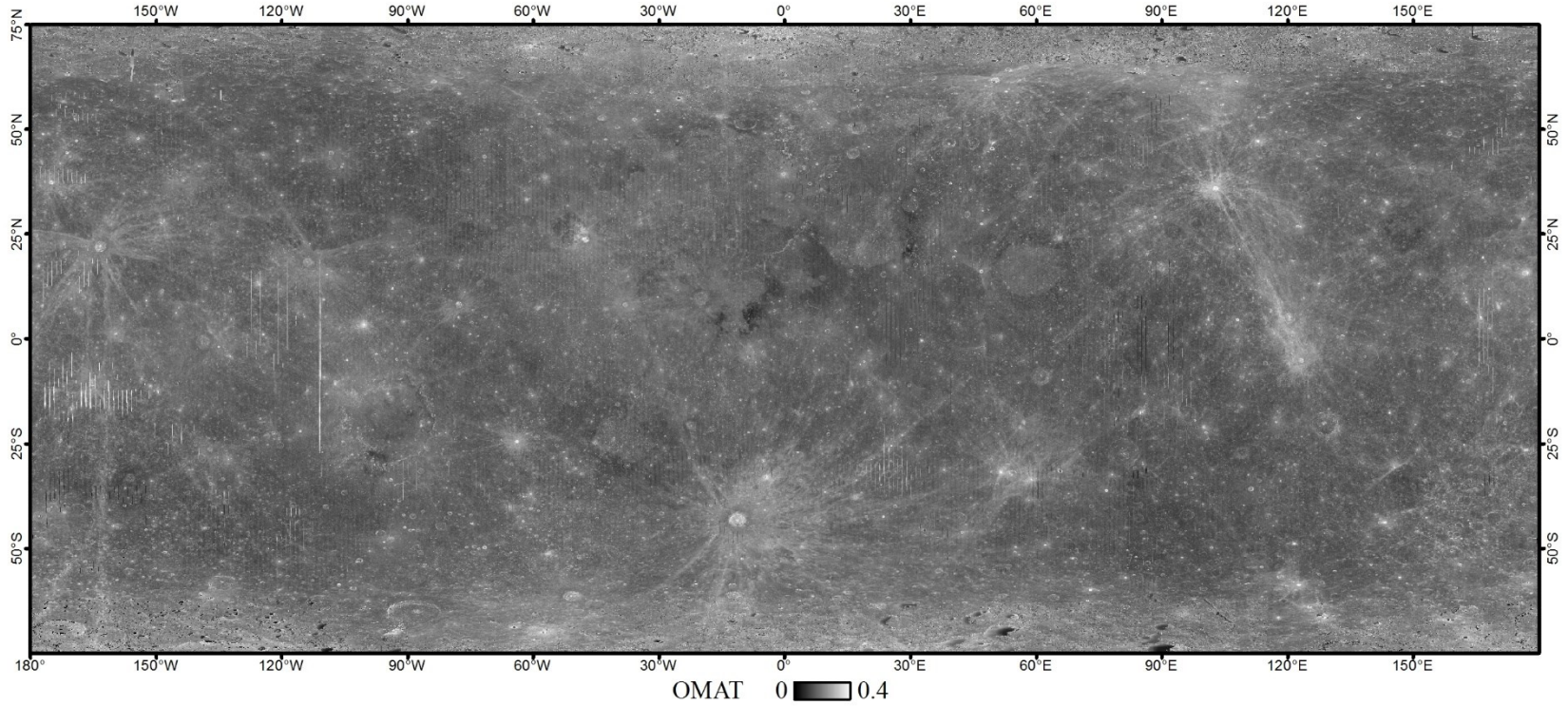

Figure B.6. Global abundance of OMAT (optical maturity parameter) as derived from the method described in Chapter Three shown here at 32 pixel per degree (~1 km per pixel).

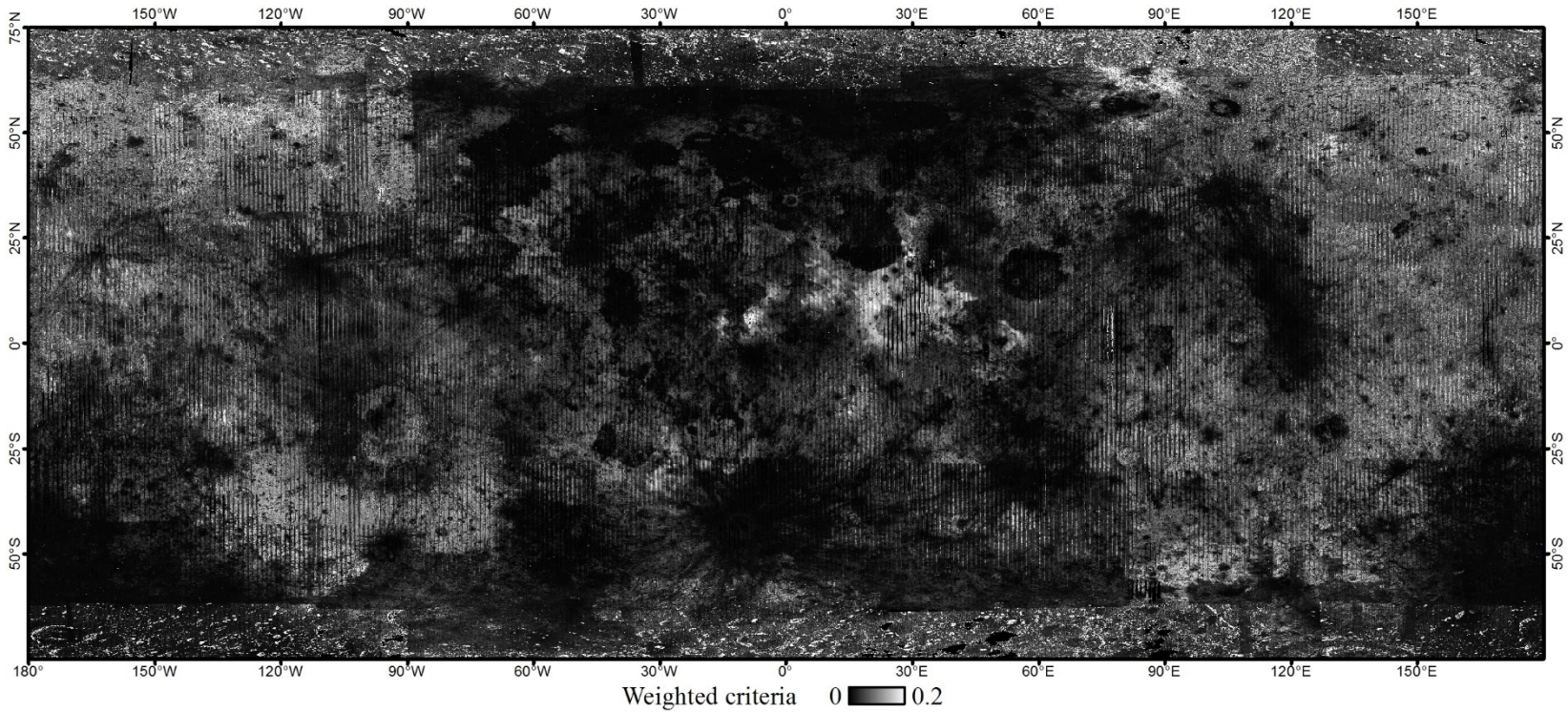

Figure B.7. Global abundance of the weighted criteria associated with the mineral abundances derived from the method described in Chapter Three shown here at 32 pixel per degree (~1 km per pixel). The weighted criteria consist of:

$$\text{weighted criteria} = (0.5 \cdot (1 - \text{correlation}) + (0.5 \cdot$$

absolute difference in continuum removed reflectance between the winning library spectrum and the pixel spectrum)

The lowest the weighted criteria represents the best agreement.

APPENDIX C

Ternary Diagrams for Each Basin Ring Studied in the Equatorial Region

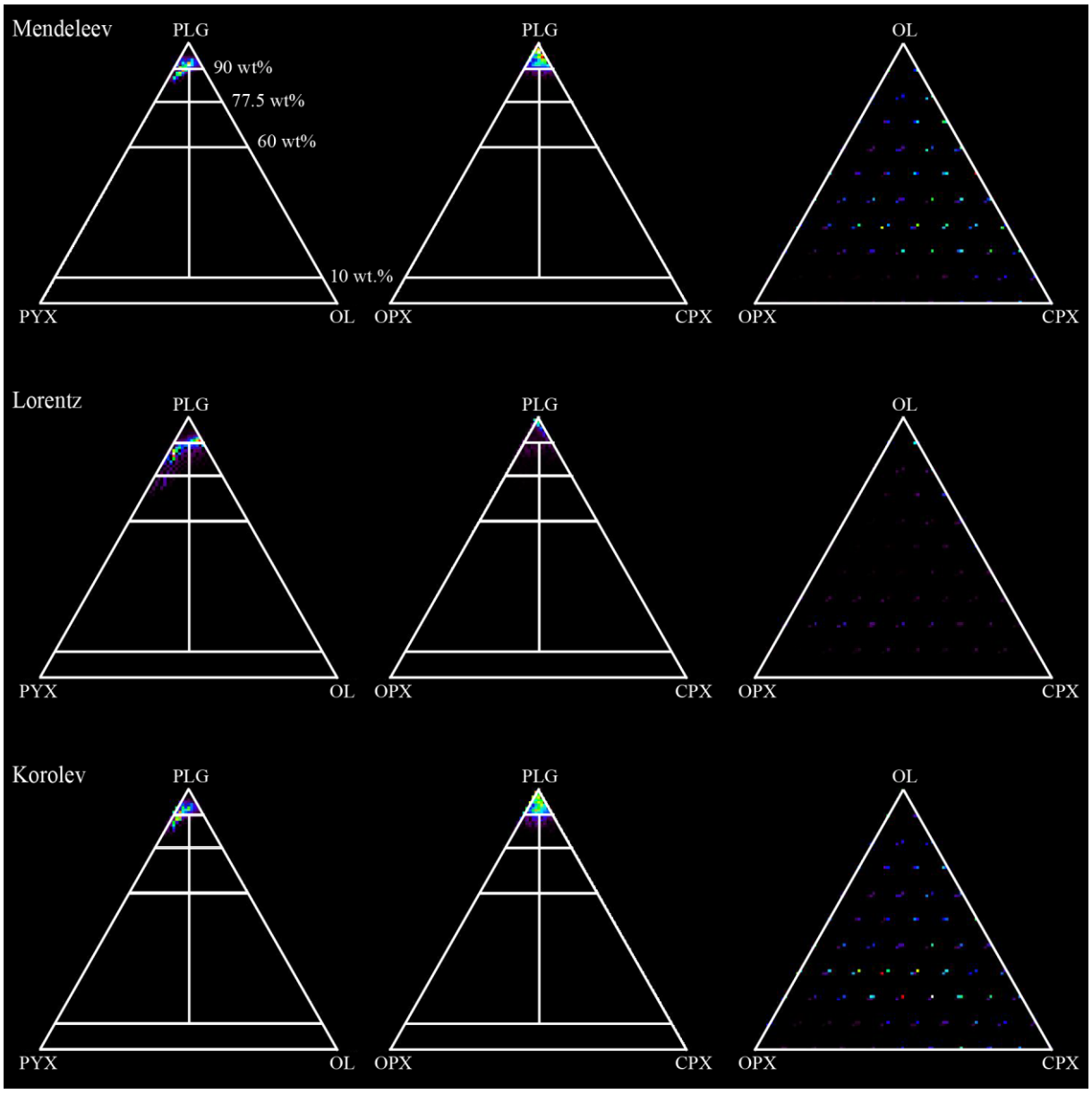

Figure C.1. Ternary diagrams showing the composition of each immature pixel (OMAT >0.2) on the innermost ring of Mendeleev, Lorentz, and Korolev.

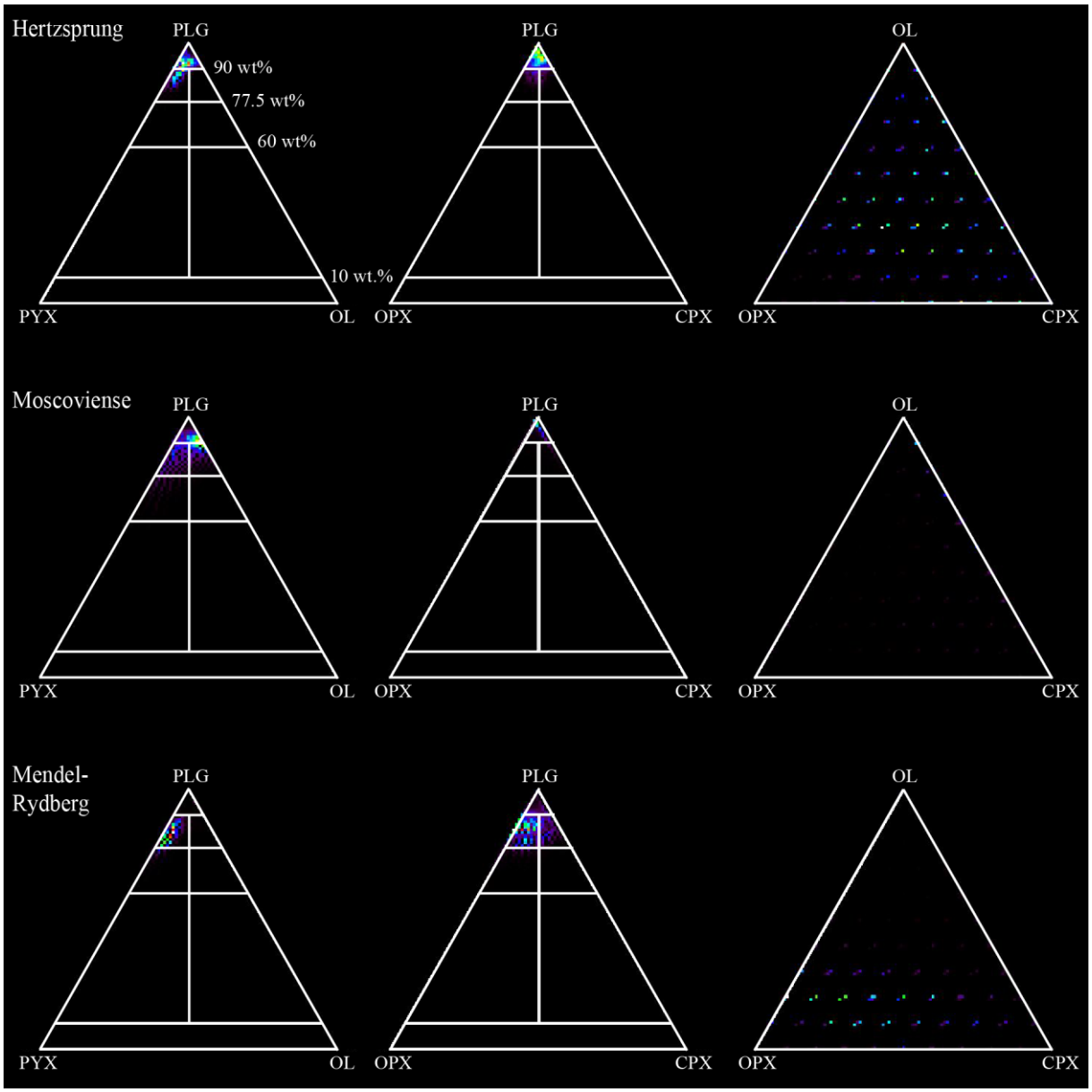

Figure C.2. Ternary diagrams showing the composition of each immature pixel (OMAT >0.2) on the innermost ring of Hertzsprung, Moscoviense, and Mendel-Rydberg.

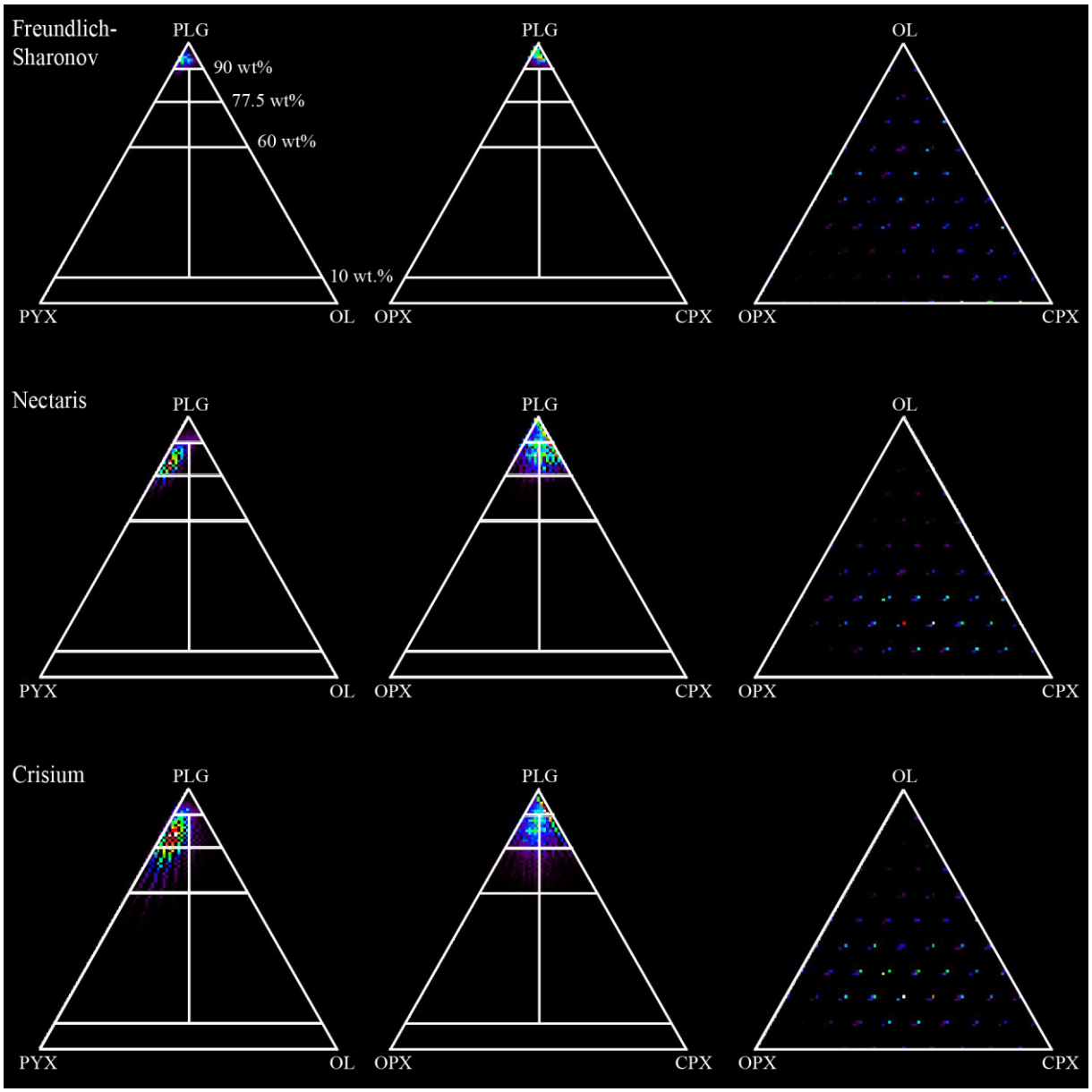

Figure C.3. Ternary diagrams showing the composition of each immature pixel (OMAT >0.2) on the innermost ring of Freundlich-Sharonov, Nectaris, and Crisium.

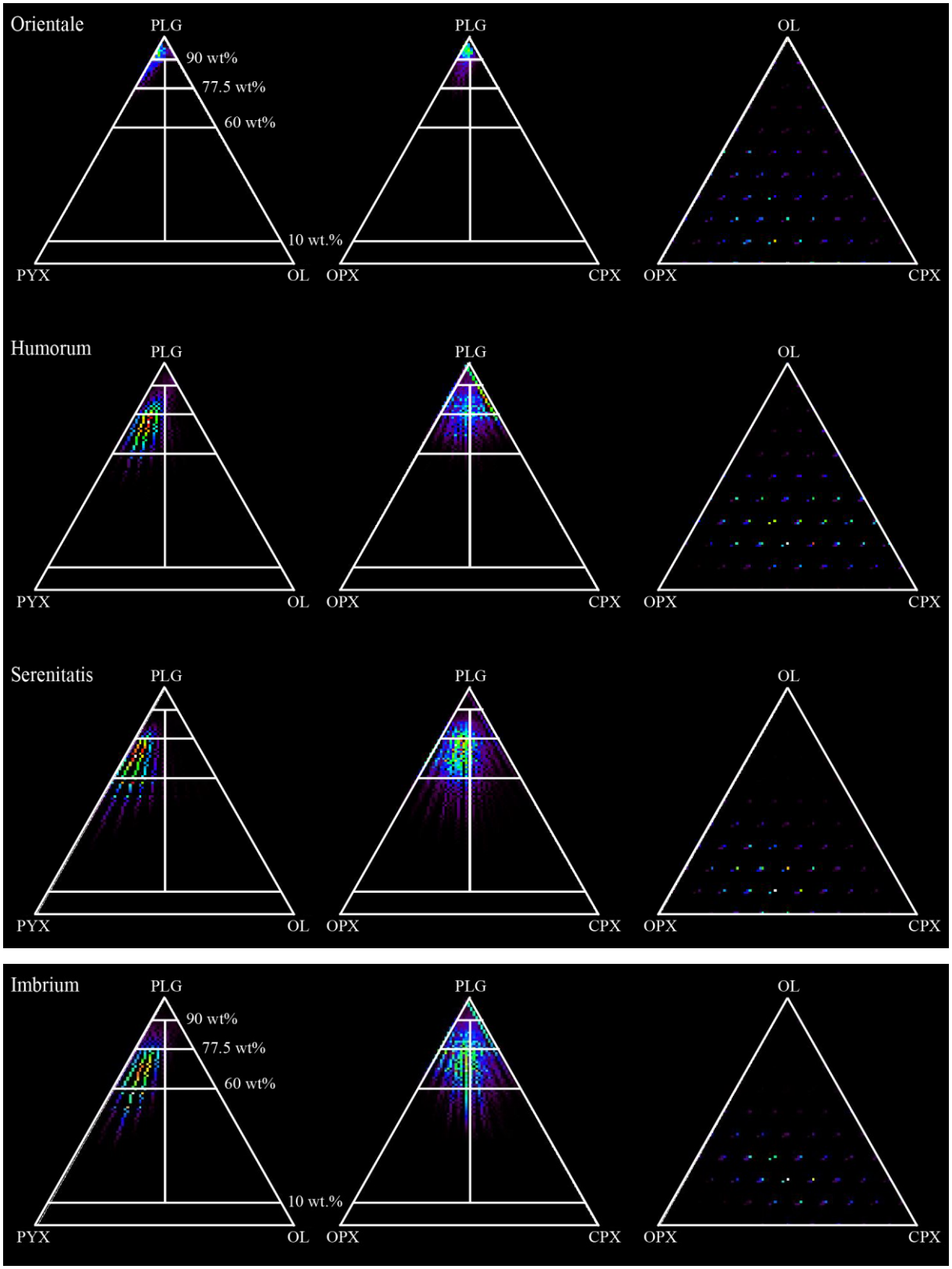

Figure C.4. Ternary diagrams showing the composition of each immature pixel (OMAT >0.2) on the innermost ring of Orientale, Humorum, Serenitatis, and Imbrium.

APPENDIX D

Output of iSALE-2D modeling for each basin studied in the equatorial region

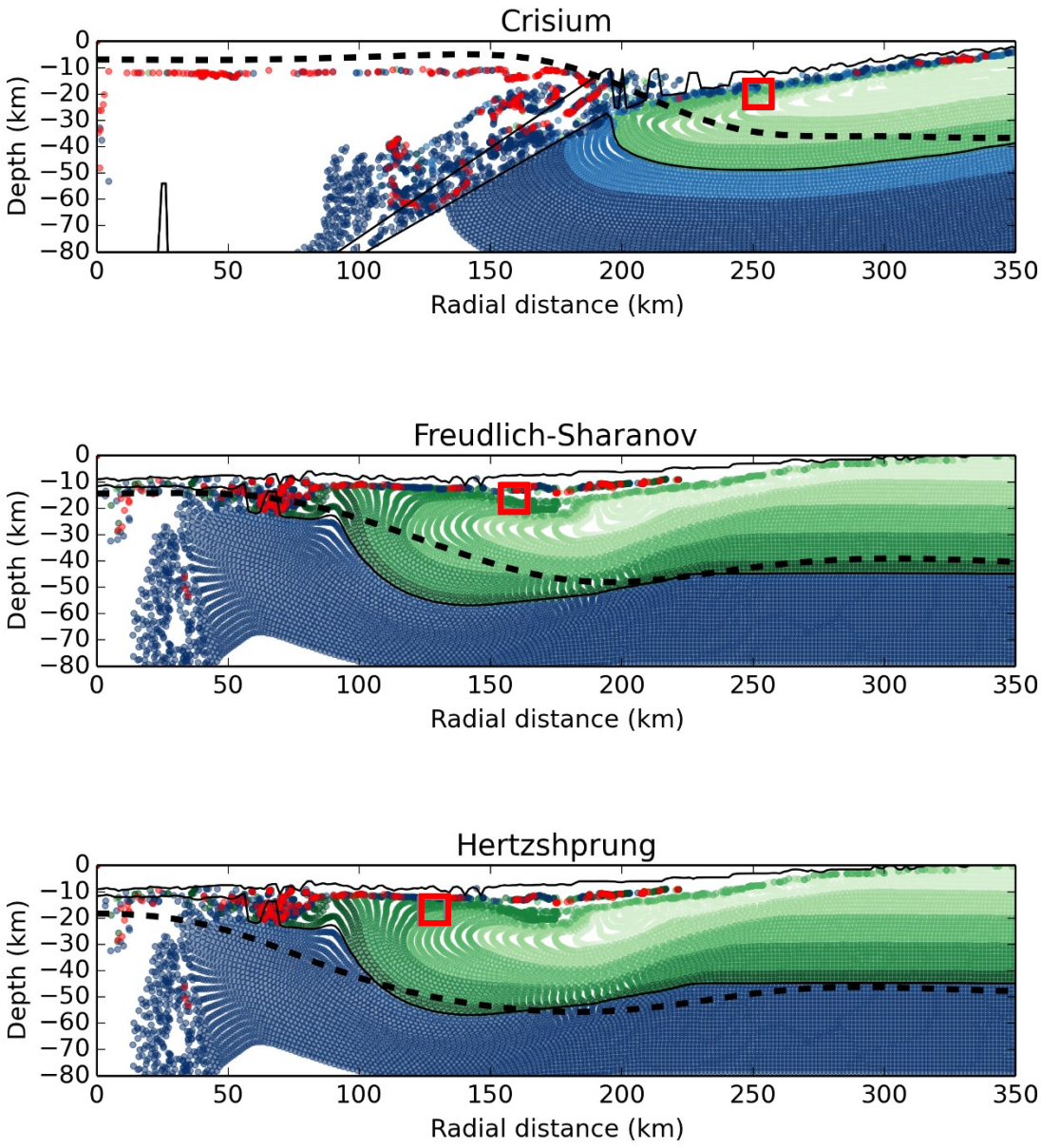

Figure D.1. Configuration of Crisium, Freundlich-Sharonov, and Hertzsprung basins two hours after the impact, as seen by iSALE-2D. Green: crustal tracer particles, blue: mantle tracer particles, red: impactor tracer particles. The dashed black line represents the crust/mantle boundary measured by GRAIL, and the solid black line represents the modeled crust/mantle boundary. The red square is a 10 by 10 km box centered on the diameter of the innermost ring.

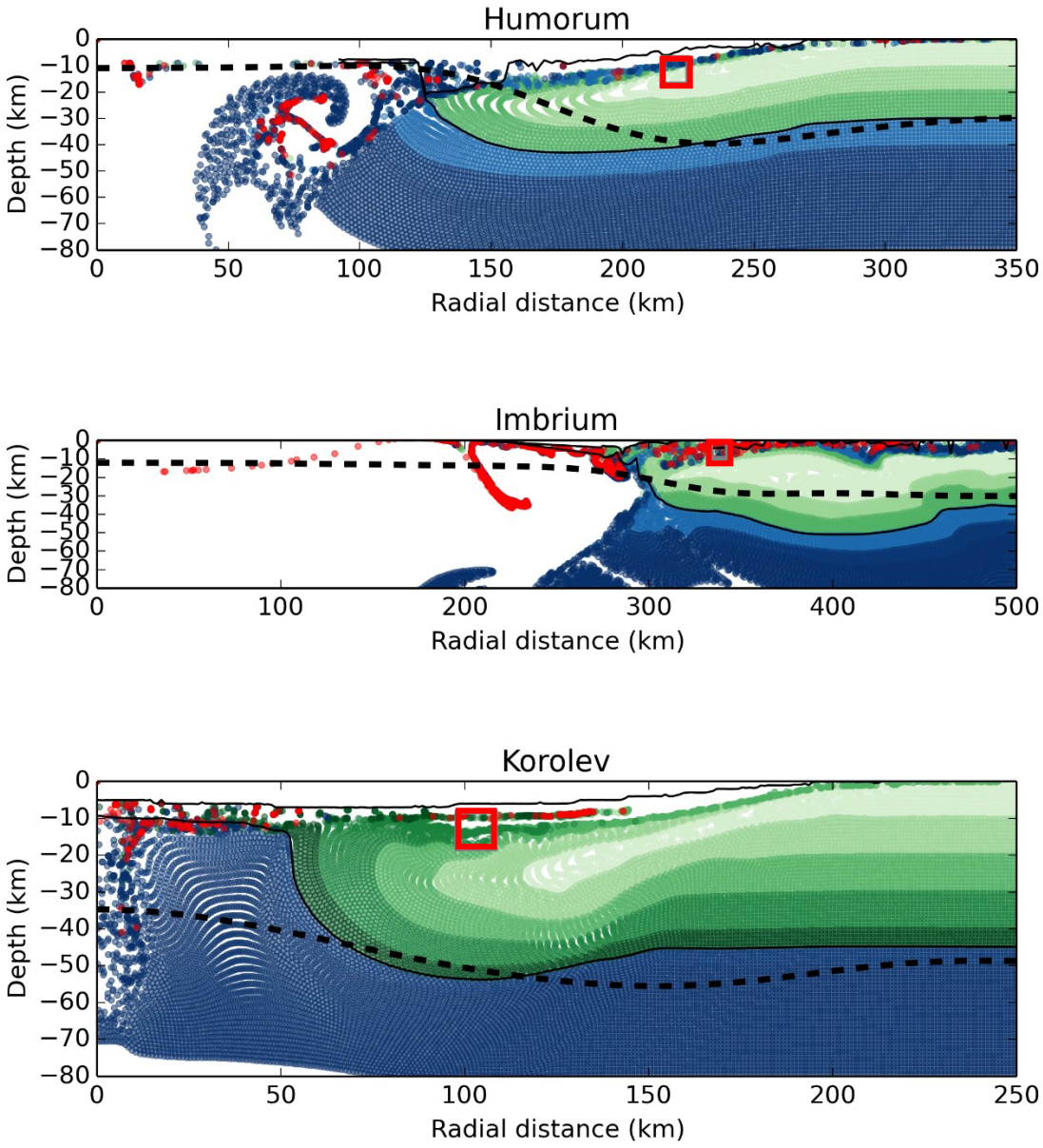

Figure D.2. Configuration of Humorum, Imbrium, and Korolev basins two hours after the impact, as seen by iSALE-2D. Green: crustal tracer particles, blue: mantle tracer particles, red: impactor tracer particles. The dashed black line represents the crust/mantle boundary measured by GRAIL, and the solid black line represents the modeled crust/mantle boundary. The red square is a 10 by 10 km box centered on the diameter of the innermost ring.

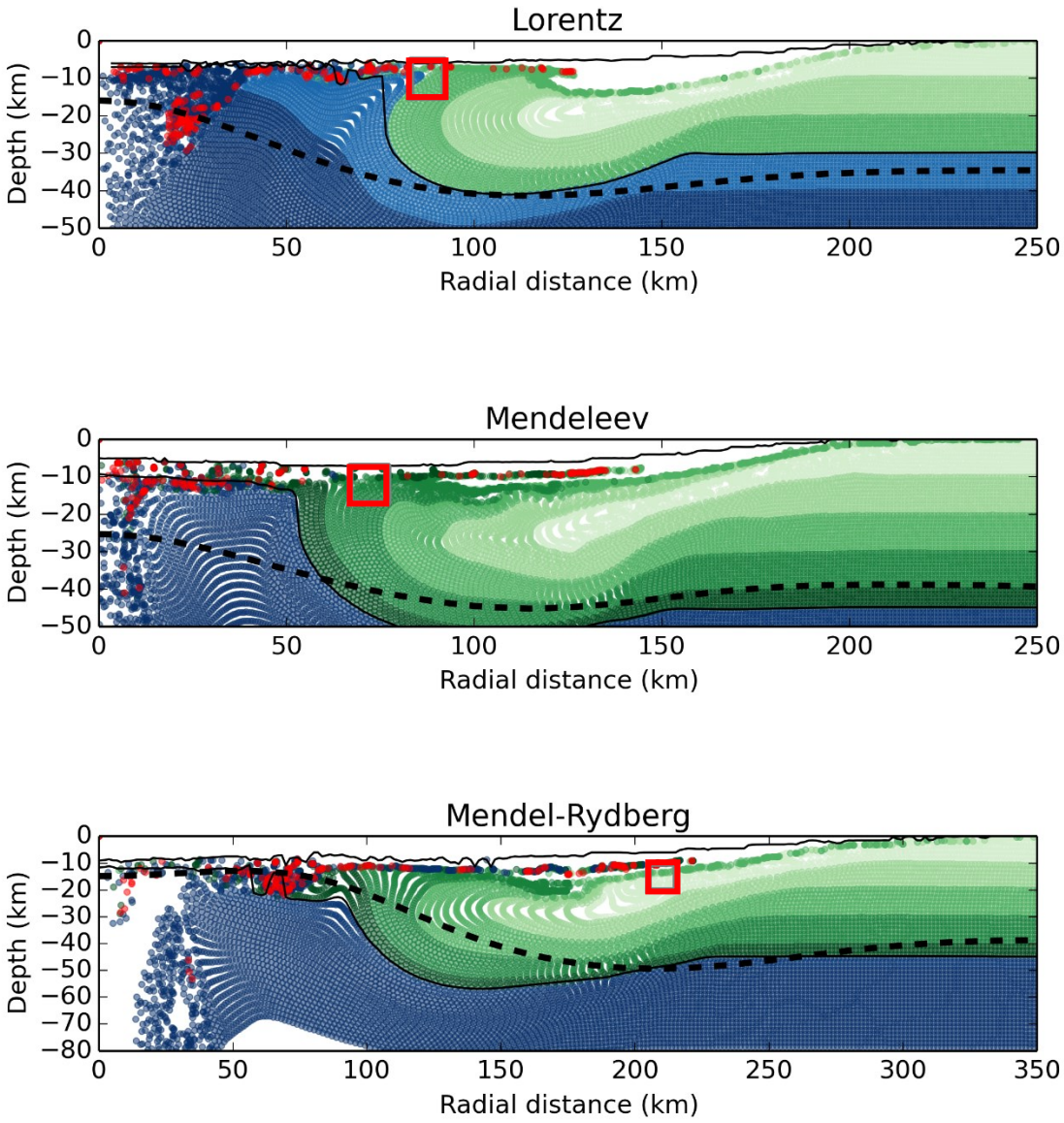

Figure D.3. Configuration of Lorentz, Mendeleev, and Mendel-Rydberg basins two hours after the impact, as seen by iSALE-2D. Green: crustal tracer particles, blue: mantle tracer particles, red: impactor tracer particles. The dashed black line represents the crust/mantle boundary measured by GRAIL, and the solid black line represents the modeled crust/mantle boundary. The red square is a 10 by 10 km box centered on the diameter of the innermost ring.

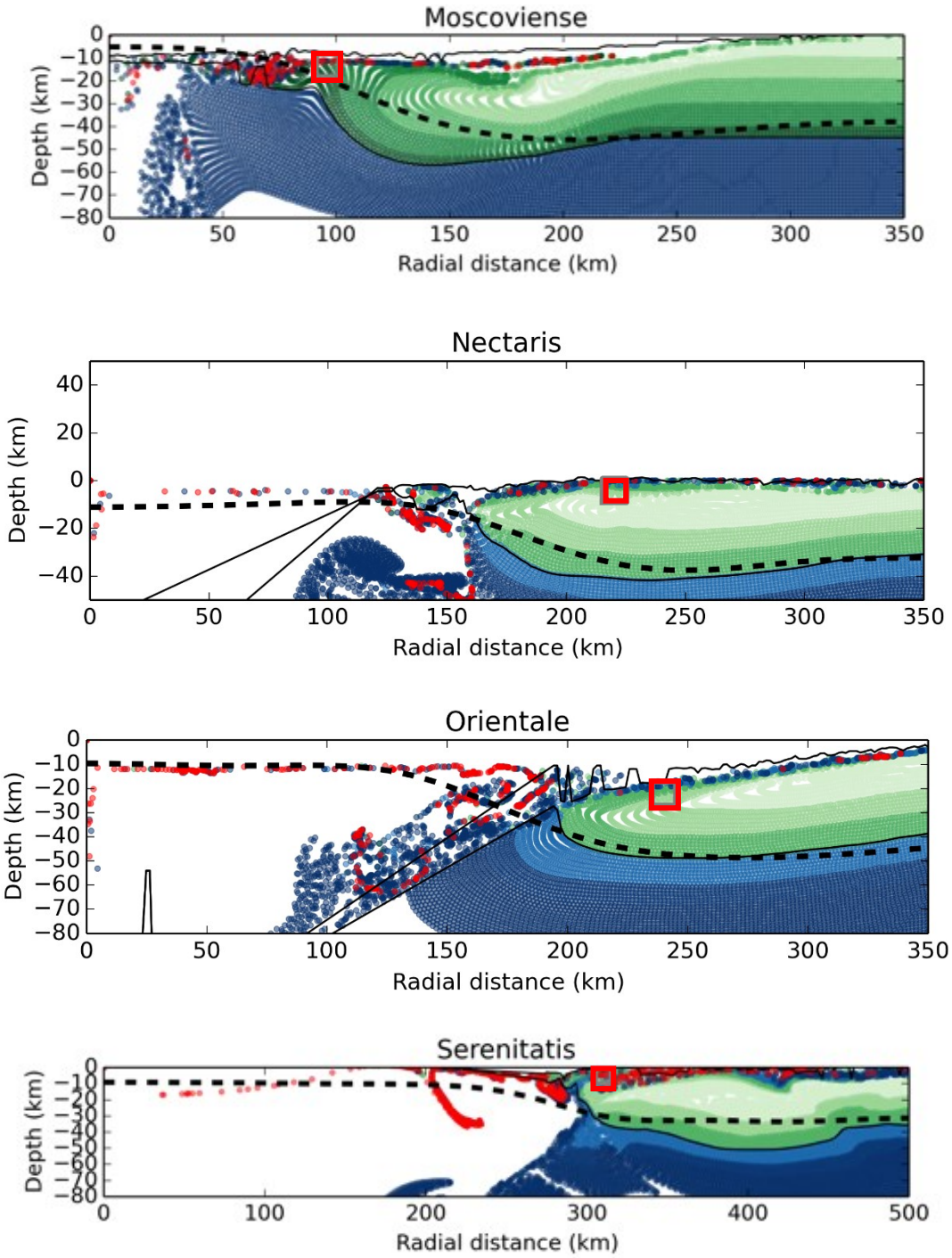

Figure D.4. Configuration of Moscoviense, Nectaris, Orientale, and Nectaris basins two hours after the impact, as seen by iSALE-2D. Green: crustal tracer particles, blue: mantle tracer particles, red: impactor tracer particles. The dashed black line represents the crust/mantle boundary measured by GRAIL, and the solid black line represents the modeled crust/mantle boundary. The red square is a 10 by 10 km box centered on the diameter of the innermost ring.

REFERENCES

Adams, J.B. (1974) Visible and Near-Infrared Diffuse Reflectance Spectra of Pyroxenes as Applied to Remote Sensing of Solid Objects in the Solar System, J. Geophys. Res., 79(32), 4829-4836.

Amsden, A.A., Ruppel, H.M., and Hirt, C.W. (1980) SALE: A Simplified ALE Computer Program for Fluid Flow at all Speeds: Los Alamos National Laboratory Report LA-8095, 101 p.

Baker, D.M.H., and Head, J.W. (2015) Constraints on the depths of origin of peak rings on the Moon from Moon Mineralogy Mapper data, Icarus, 258, 164-180, http://dx.doi.org/10.1016/j.icarus.2015.06.013.

Baldwin, R.B. (1972) The tsunami model for the origin of ring structures concentric with large lunar craters. Physics of the Earth and Planetary Interiors, 6, 327–339.

Barker, M.K., Sun, X., Mazarico, E., Neumann, G.A., Zuber, M., and Smith, D.E. (2016) Lunar Phase Function at 1064 nm From Lunar Orbiter Laser Altimeter Passive and Active Radiometry, Icarus, 273, 96-113, doi:10.1016/j.icarus.2016.02.008.

Besse, S., Yokota, Y., Boardman, J., Green, R., Haruyama, J., Isaacson, P., Mall, U., Matsunaga, T., Ohtake, M., Pieters, C., Staid, M., Sunshine, J., and Yamamoto, S. (2013) One Moon, Many Measurements 2: Photometric corrections, Icarus, 226, 127–139.

Britt D.T., and Pieters, C.M. (1994) Darkening in black and gas-rich ordinary chondrite meteorites: The spectral effects of opaque morphology and distribution. Geochemica et Cosmochimica Acta 58, 3905-3919.

Buratti, B.J., Hicks, M.D., Nettles, J., Staid, M., Pieters, C.M., Sunshine, J., Boardman, J., and Stone T.C. (2011). A wavelength-dependant visible and infrared spectrophotometric function for the Moon based on ROLO data, J. Geophys. Res., 116(E00G03), doi:10.1029/2010JE003724.

Cahill, J.T.S., Lucey, P.G., and Wieczorek, M.A. (2009) Compositional variations of the lunar crust: Results from radiative transfer modeling of central peak spectra, J. Geophys. Res., 114(E09001), doi: 10.1029/2008JE003282.

Cheek, L.C., Donaldson Hanna, K.L., Pieters, C.M., Head, J.W., and Whitten, J.L. (2013) The distribution and purity of anorthosite across the Orientale basin: New perspectives from

Moon Mineralogy Mapper data, J. Geophys. Res., 118, 1805-1820, doi: 10.1002/jgre.20126.

Collins, G.S., Melosh, H.J., Morgan, J.V., and Warner, M.R. (2002) Hydrocode Simulations of Chicxulub Crater Collapse and Peak-Ring Formation, Icarus, 157, 24-33, doi:10.1006/icar.2002.6822.

Crites, S.T., and Lucey, P.G. (2015) Revised mineral and Mg# maps of the Moon from integrating results from the Lunar Prospector neutron and gamma-ray spectrometers with Clementine spectroscopy, American Mineralogist, 100, 973-982.

Dhingra, D., Pieters, C.M., and Head, J.W. (2014) Impact melt mineralogy at lunar complex craters: systematics of melt emplacement and evolution, Lunar and Planetary Sci. Conf., 45th, abstract #2138.

Dhingra, R.D., Dhingra, D., and Carlson, L. (2014) Evaluating the extent of impact melt on central peaks of lunar complex impact craters, Lunar and Planetary Sci. Conf., 45th, abstract #1754.

Dhingra, D., and Pieters, C.M. (2012) Spectroscopy of impact melts – Results from lunar crater Tycho, Lunar and Planetary Sci. Conf., 43rd, abstract #1836.

Donaldson Hanna, K.L., Cheek, L.C., Pieters, C.M., Mustard, J.F., Greenhagen, B.T., Thomas, L.R., and Bowles, N.E., (2014) Global assessment of pure crystalline plagioclase across the Moon and implications for the evolution of the primary crust, J. Geophys. Res. Planets, 119, 1516–1545, doi:10.1002/2013JE004476.

Feldman, W.C., Maurice, S., Binder, A.B., Barraclough, B.L., Elphic, R.C., and Lawrence, D.J. (1998) Neutrons from the Lunar Prospector: Evidence for Water Ice at the Lunar Poles, Science, 281(5382), 1496-1500.

Feldman, W.C, Gasnault O., Maurice S., Lawrence, D.J., Elphic, R.C., Lucey, P.G., Binder, A.B. (2002) Global distribution of lunar composition: New results from Lunar Prospector, J. Geophys. Res., vol. 107(E3), doi:10.1029/2001JE001506.

Fortezzo, C.M., and Hare, T.M. (2013) Completed digital renovation of the 1:5,000,000 lunar geologic map series, Lunar and Planetary Sci. Conf., 44th, abstract #2114.

Gasnault, O., Feldman, W.C., Maurice, S., Genetay, I., d'Uston, C., Prettyman, T.H., and Moore, K.R., (2001). Composition from fast neutrons: application to the Moon. Geophysical Research Letters, 28, 19, 3797-3800.

Grieve, R.A.F., Robertson, P.B., and Dence, M.R. (1981) Constraints on the formation of ring impact structures, based on terrestrial data, Proc. Lunar Planet Sci., 12A, 37-57.

Gross, J., Treiman, A.H., and Mercer, C.N. (2014) Lunar feldspathic meteorites: Constraints on the geology of the lunar highlands, and origin of the lunar crust, Earth and Planetary Science Letters, 388, 318-328.

Hapke, B. (1963). A theoretical photometric function for the lunar surface, J. Geophys. Res, 68(15), 4571–4586.

Hapke, B. (1981), Bidirectional Reflectance Spectroscopy, 1. Theory, J. Geophys. Res., 86(B4), 3039-3054.

Hapke, B. (1993), Theory of Reflectance and Emittance Spectroscopy, Cambridge University Press, New York, Topics in Remote Sensing (No. 3).

Hapke, B. (2001), Space weathering from Mercury to the asteroid belt, J. Geophys. Res., 106(E5), 10,039-10,073.

Haruyama, J., Matsunaga, T., Ohtake, M., Morota, T., Honda, C., Yokota, Y., Torii, M., Ogawa, Y., and the LISM Working Group (2008) Global lunar-surface mapping experiment using the Lunar Imager/Spectrometer on SELENE, Earth Planets Space, 60, 243-255.

Haruyama, J., Yamamoto, S., Yokota, Y., Ohtake, M., and Matsunaga, T. (2013) An explanation for bright areas inside Shackleton Crater at the Lunar South Pole other than water-ice deposits, Geophys. Res. Let, 40, 3,814-3,818.

Hawke, B.R., Lucey, P.G., Taylor, G.J., Bell, J.F., Peterson, C.A., Blewett, D.T., Horton, K., Smith, G.A., and Spudis, P.D. (1991) Remote sensing studies of the Orientale region of the Moon: A pre-Galileo view, Geophys. Res. Let., 18, 11, 2141-2144.

Hawke, B.R., Peterson, C.A., Blewett, D.T., Bussey, D.B.J., Lucey, P.G., Taylor, G.J., and Spudis, P.D. (2003) Distribution and modes of occurrence of lunar anorthosite, J. Geophys. Res., 108, E6, 4,1-4,16, doi:10.1029/2002JE001890.

Head, J.W. (2010) Transition from complex craters to multi-ringed basins on terrestrial planetary bodies: Scale-dependent role of the expanding melt cavity and progressive interaction with the displaced zone, Geophys. Res. Let., 37, 1-5, doi:10.1029/2009GL041790.

Hemingway, D.J., Garrick-Bethell, I., Kreslavsky, M.A. (2015). Latitudinal Variation in Spectral Properties of the Lunar Maria and Implications for Space Weathering, Icarus, doi: http://dx.doi.org/10.1016/j.icarus.2015.08.004.

Hess, P.C. (1994) Petrogenesis of lunar troctolites, J. Geophys. Res., 99, E9, 19,083-19,093.

Hess, P.C., and Parmentier, E.M. (1994) Overturn of magma ocean cumulate layer: implications for lunar magmatic evolution and formation of the lunar core, Lunar and Planetary Sci. Conf., XXIV, 651-652.

Hess, P.C., and Parmentier, E.M. (1995) A model for the thermal and chemical evolution of the Moon's interior: implications for the onset of mare volcanism, Earth and Planetary Science Letters, 134(3-4), 501-514.

Hodges, C.A., and Wilhelms, D.E. (1978) Formation of lunar basin rings, Icarus, 34(2), 294-323.

Hurwitz, D.M., and Kring, D.A. (2014) Differentiation of the South Pole–Aitken basin impact melt sheet: Implications for lunar exploration, J. Geophys. Res. Planets, 119, 1110–1133, doi:10.1002/2013JE004530.

Ivanov, B.A., Deniem, D., and Neukem, G. (1997) Implementation of dynamic strength models into 2D hydrocodes: Applications for atmospheric breakup and impact cratering, Int. J. Impact Engng, 20, 411-430.

Jolliff, B.L., Gillis, J.J., Haskin, L.A., Korotev, R.L., and Wieczorek, M.A. (2000) Major lunar crustal terranes: Surface expressions and crust-mantle origins, J. Geophys. Res., 105(E2), 4197–4216, doi:10.1029/1999JE001103.

Johnson, B.C., Andrews-Hanna, J.C., Collins, G.S., Melosh, H.J., Head, J.W., Blair, D.M., Freed, A.M., Miljković, K., Soderblom, J.M., and Zuber, M.T. (2015) The formation of lunar multi-ring basins, Lunar and Planetary Sci. Conf., 46th, abstract #1362.

Kodama, S., Ohtake, M., Yokota, Y., Iwasaki, A., Haruyama, J., Matsunaga, T., Nakamura, R., Demura, H., Hirata, N., Sugihara, T., and Yamamoto, Y. (2010) Characterization of multiband imager aboard SELENE, Space Sci. Rev., 154, 79-102, doi:10.1007/s11214-010-9661-z.

Kramer, G.Y., Kring, D.A., Nahm, A.L., and Pieters, C.M. (2013) Spectral and photogeologic mapping of Schrödinger Basin and implications for post-South Pole-Aitken impact deep subsurface stratigraphy, Icarus, 223, 131-148.

Kreslavsky, M.A., Head, J.W., Neumann, G.A., Rosenburg, M.A., Aharonson, O., Smith, D.E., and Zuber, M.T. (2013). Lunar topographic roughness maps from Lunar Orbiter Laser Altimeter (LOLA) data: Scale dependence and correlation with geologic features and units, Icarus, 226(1), 52–66, doi:10.1016/j.icarus.2013.04.027.

Kuriyama, Y., Ohtake, M., Haruyama, J., and Iwata, T. (2012) Distributions of impact melts within lunar complex craters Jackson and Tycho, Lunar and Planetary Sci. Conf., 43rd, abstract #1395.

Laneuville, M., Wieczorek, M.A., Breuer, D., and Tosi, N. (2013) Asymmetric thermal evolution of the Moon. J. Geophys. Res., Planets118, 1435–1452.

Lawrence, D.J., Feldman, W.C., Elphic, R.C., Little, R.C., Prettyman, T.H., Maurice, S., Lucey, P.G., and Binder, A.B. (2002) Iron abundances on the lunar surface as measured by the Lunar Prospector Gamma-Ray and Neutron Spectrometers, J. Geophys. Res., 107(E12), 1-26.

Lemelin, M., Lucey, P.G., Song, E., and Taylor, J. (2015) Lunar central peak mineralogy and iron content using the Kaguya Multiband Imager: Reassessment of the compositional structure of the lunar crust, J. Geophys. Res. Planets, 120, 869–887, doi:10.1002/2014JE004778.

Lemelin, M., Lucey, P.G., Neumann, G.A., Mazarico, E.M., Barker, M.K., Kakazu, A., Trang, D., Smith, D.E., and Zuber, M.T. (2016) Improved calibration of reflectance data from the LRO Lunar Orbiter Laser Altimeter (LOLA) and implications for space weathering, Icarus, 273, 315-328.

Litvak, M.L., Mitrofanov, I.G., Sanin, A., Malakhov, A., Boynton, W.V., Chin, G., Droege, G., Evans, L.G., Garvin, J., Golovin, D.V., Harshman, K., McClanahan, T.P., Mokrousov, M.I., Mazarico, E., Milikh, G., Neumann, G., Sagdeev, R., Smith, D.E., Starr, R., and Zuber, M.T. (2012) Global maps of lunar neutron fluxes from the LEND instrument, J. Geophys. Res. Planets, 117, E00H22, doi:10.1029/2011JE003949.

Lucey, P.G. (1998) Model near-infrared optical constants of olivine and pyroxene as a function of iron content, J. Geophys. Res., 103(El), 1703-1713.

Lucey, P.G. (2004) Mineral maps of the Moon, Geophys. Res. Letters, 31(L08701), doi:10.1029/2003GL019406.

Lucey, P.G. (2006) Radiative transfer modeling of the effect of mineralogy on some empirical methods for estimating iron concentration from multispectral imaging of the Moon, J. Geophys. Res., 111(E08003), doi:10.1029/2005JE002661.

Lucey, P.G., and Noble, S.K. (2008) Experimental test of a radiative transfer model of the optical effects of space weathering, Icarus, 197(1), 348-353.

Lucey, P.G., and Riner, M.A. (2011) The optical effects of small iron particles that darken but do not redden: Evidence of intense space weathering on Mercury, Icarus, 212, 451-462.

Lucey, P.G., Blewett, D.T., and Jolliff, B.L. (2000) Lunar iron and titanium abundance algorithms based on final processing of Clementine ultraviolet-visible images, J. Geophys. Res., 105(E8), 20,297-20,305.

Lucey, P.G., Blewett, D.T., Taylor, G.J., Hawke, B.R. (2000) Imaging of lunar surface maturity, J. Geophys. Res., 105(E8), 20,377-20,386.

Lucey, P.G., Norman, J.A., Crites, S.T., Taylor, G.J., Hawke, B.R., and Lemelin, M. (2014) A large spectral survey of small lunar craters: Implications for the composition of the lunar mantle, The American Mineralogist, 99, 2251-2257.

Lucey, P.G., Neumann, G.A., Riner, M.A., Mazarico, E., Smith. D.E., Zuber, M.T., Paige, D.A., Bussey, D.B., Cahill, J.T., McGovern, A., Isaacson, P., Corley, L.M., Torrence, M.H., Melosh, H.J., Head, J.W., and Song, E. (2014). The global albedo of the Moon at 1064 nm from LOLA, J. Geophys. Res. Planets, 119, 1665–1679, doi:10.1002/2013JE004592.

Matsunaga, T., Ohtake, M., Hirahara, Y., and Haruyama, J. (2001) Development of a visible and near infrared spectrometer for Selenological and Engineering Explorer (SELENE), Proceedings of SPIE, 4151, 32-39.

Mazarico E., Neumann, G.A., Smith, D.E., Zuber, M.T., and Torrence, M.H. (2011). Illumination condition of the lunar polar regions using LOLA topography, Icarus. 211, 1066–1081, doi:10.1016/j.icarus.2010.10.030.

McCormick, K.A., Taylor, G.J., and Keil. K. (1989) Sources of clasts in terrestrial impact melts: Clues to the origin of the LKFM, Proceedings of the 19th Lunar and Planetary Science Conference, pp.691-696.

Melosh, H.J. (1989) Impact Cratering, A Geologic Process, Oxford monographs on Geology and Geophysics no. 11, Oxford University Press, N.Y.

Melosh, H.J., and McKinnon, W.B. (1978) The mechanics of ringed basin formation, Geophys. Res. Letters, 5(11), 985-988.

Melosh, H.J., Ryan, E.V., and Asphaug, E. (1992) Dynamic Fragmentation in Impacts: Hydrocode Simulation of Laboratory Impacts, J. Geophys. Res., 97, E9, 14,735-14,759.

Melosh, H.J., Freed, A.M., Johnson, B.C., Blair, D.M., Andrews-Hanna, J.C., Neumann, G.A., Phillips, R.J., Smith, D.E., Solomon, S.C., Wieczorek, M.A., and Zuber, M.T. (2013) The origin of lunar mascon basins, Science, 340, 1552-1555.

Miljković, K., Wieczorek, M.A., Colins, G.S., Laneuville, M., Neumann, G.A., Melosh, H.J., Solomon, S.C., Phillips, R.J., Smith, D.E., Zuber, M.T. (2013) Asymmetric Distribution of Lunar Impact Basins Caused by Variations in Target Properties, Science, 342, 724, 1-18, doi:10.1126/science.1243224

Miljković, K., Wieczorek, M.A., Collins, G.S., Solomon, S.C., Smith, D.E., and Zuber, M.T. (2014) Excavation of the mantle in basin-forming events on the Moon, Lunar and Planetary Sci. Conf., 45th, abstract #1828.

Miljković, K., Wieczorek, M.A., Colins, G.S., Solomon, S.C., Smith, D.E., Zuber, M.T. (2015) Excavation of the lunar mantle by basin-forming impact events on the Moon, Earth Planet Sci. Lett., 409, 243-251.

Morris R.V. (1976) Surface exposure indices of lunar soils: A comparative FMR study. 7th Lunar and Planetary Science Conference, 315-335.

Morris, R.V. (1978). The surface exposure (maturity) of lunar soils: Some concepts and Is/FeO compilation. Proc. Lunar Sci. Conf. IX, 2278–2297.

Morrison, D.A. (1998) Did a thick South Pole-Aitken basin melt sheet differentiate to form cumulates? Lunar and Planetary Sci. Conf., 29th, abstract #1657.

Nagaoka, H., Takeda, H., Karouji, Y., Ohtake, M., Yamaguchi, A., Yoneda, S., and Hasebe, N. (2014) Implications for the origins of purest anorthosites found in the feldspathic lunar meteorites, Dhofar 489 group, Earth, Planets and Space, 66(115).

Nakamura, R., Yamamoto, S., Matsunaga, T., Ishihara, Y., Morota, T., Hiroi, T., Takeda, H., Ogawa, Y., Yokota, Y., Hirata, N., Ohtake, M., and Saiki, K. (2012) Compositional evidence for an impact origin of the Moon's Procellarum basin, Nature Geoscience Letters, 5, 775-778, doi:10.1038/NGEO1614.

National Research Council (2007) The Scientific Context for Exploration of the Moon, National Academy Press, Washington, 107p.

National Research Council (2011) Vision and Voyages for Planetary Science in the Decade 2013–2022, National Academy Press, Washington, 400p.

Nelson, D.M., Koeber, S.D., Daud, K., Robinson, M.S., Watters, T.R., Banks, M.E., Williams, N.R. (2014). Mapping Lunar Maria Extents and Lobate Scarps Using LROC Image Products, 45th Lunar and Planetary Science Conference, Abstract #2861.

Neumann, G.A., Smith, D.A., Scott., S.R., Slavney, S., and Grayzek, E. (2010), Lunar Reconnaissance Orbiter - Lunar Orbiter Laser Altimeter - Reduced Data Record and Derived Products - Software Interface Specification, version 2.53, http://pds-geosciences.wustl.edu/lro/lro-l-lola-3-rdr-v1/lrolol_1xxx/document/rdrsis.pdf

Neumann, G.A., Zuber, M.T., Wieczorek, M.A., Head, .W., Baker, D.M.H., Solomon, S.C., Smith, D.E., Lemoine, F.G., Mazarico, E., Sabaka, T.J., Goossens, S.J., Melosh, H.J., Phillips, R.J., Asmar, S.W., Konopliv, A.S., Williams, J.G., Sori, M.M., Soderblom, J.M., Miljkovic, K., Anderews-Hanna, J.C., Nimmo, F., and Kiefer, W.S. (2015) Lunar impact basins revealed by Gravity Recovery and Interior Laboratory measurements, Sci. Adv., 1-10.

Noble, S.K., Pieters, C.M., and Keller, L.P. (2007) An experimental approach to understanding the optical effects of space weathering, Icarus, 192(2), 629-642.

Ohtake, M., Haruyama, J., Matsunaga, T., Yokota, Y., Morota, T., Honda, C., and the LISM team (2008) Performance and scientific objectives of the SELENE (KAGUYA) Multiband Imager, Earth Planets Space, 60, 257-264.

Ohtake, M., Matsunaga, T., Haruyama, J., Yokoya, Y., Morota, T., Honda, C., Ogawa, Y., Torii, M., Miyamoto, H., Arai, T., Hirata, N., Iwasaki, A., Nakamura, R., Hiroi, T., Sugihara, T., Takeda, H., Otake, H., Pieters, C.M., Saiki, K., Kitazato, K., Abe, M., Asada, N., Demura, H., Yamaguchi, Y., Sasaki, S., Kodama, S., Terazono, J., Shirao, M., Yamaji, A., Minami, S., Akiyama, H., and Josset, J.-L. (2009) The global distribution of pure anorthosite on the Moon, Nature, 461, 236-241.

Ohtake, M., Matsunaga, T., Yokoya, Y., Yamamoto, M., Ogawa, Y., Morota, T., Honda, C., Haruyama, J., Kitazato, K., Takeda, H., Iwasaki, A., Nakamura, R., Hiroi, T., Kodama, S., and Otake, H. (2010) Deriving the absolute reflectance of lunar surface using SELENE (Kaguya) multiband imager data, Space Sci. Rev., 154, 57-77, doi:10.1007/s11214-010-9689-0.

Ohtake, M., Pieters, C.M., Isaacson, P., Besse, S., Yokota, Y., Matsunanga, T., Boardman, J., Yamamoto, S., Haruyama, J., Staid, M., Mall, U., and Green, R.O. (2013) One Moon, Many Measurements 3: Spectral reflectance, Icarus, 226, 364-374.

Otake, H., Ohtake, M., and Hirata, N. (2012) Lunar iron and titanium abundance algorithms based on selene (kaguya) multiband imager data, Lunar and Planetary Sci. Conf., 43rd, abstract #1905.

Papike, J., Taylor, L., and Simon, S. (1991) Lunar Minerals, in Lunar Sourcebook a user's guide to the Moon, edited by Grant H. Heiken et al., pp. 121-181, Cambridge University Press, New York.

Petro, N.E., and Pieters, C.M. (2008) The lunar-wide effects of basin ejecta distribution on the early megaregolith, Meteoritics and Planetary Science, 43, 1517-1529.

Pieters, C.M. (1982) Copernicus Crater Central Peak: Lunar Mountain of Unique Composition, Science, 215(4528), 59-61.

Pieters, C.M. (1986) Composition of the Lunar Highland Crust from Near-Infrared Spectroscopy, Reviews of Geophysics, 24(3), 557-578.

Pieters, C.M., Fisher, E.M., Rode, O., and Basu, A. (1993) Optical Effects of Space Weathering: The Role of the Finest Fraction, J. Geophys. Res., 98(E11), 20,817-20,824.

Potter, R.W. K., Collins, G.S., Kiefer, W.S., McGovern, P.J., and Kring, D.A. (2012) Constraining the size of the South Pole–Aitken basin impact, Icarus, 220, 730–743.

Prettyman, T.H., Hagerty, J.J., Elphic, R.C., Feldman, W.C., Lawrence, D.J., McKinney, G.W., and Vaniman, D.T. (2006) Elemental composition of the lunar surface: Analysis of gamma ray spectroscopy data from Lunar prospector, J. Geophys. Res. Planets, 111, E12007, doi:10.1029/2005JE002656.

Reid. A.M., Warner, J., Ridley, W.I., and Brown R.W. (1972) Major element composition of glasses in three Apollo 15 soils, Meteoritics, 7(3), 395-415.

Riris, H. and Cavanaugh, J. (2010) Lunar Reconnaissance Orbiter Project – Calibration Documents for the Lunar Orbiter Laser Altimeter (LOLA) Instrument, Revision 2, http://pds-geosciences.wustl.edu/lro/lro-l-lola-3-rdr-v1/lrolol_1xxx/calib/calibrpt.pdf

Robinson, M.S., and Jolliff, B.L. (2002) Apollo 17 landing site: Topography, photometric corrections, and heterogeneity of the surrounding highland massifs, J. Geophys. Res., 107 (E11), 5110, doi: 10.1029/2001JE001614.

Ryder, G., and Wood, J.A. (1977) Serenitatis and Imbrium impact melts: Implications for large-scale layering in the lunar crust, Proc. Lunar Sci. Conf. 8th, 655-668.

Sharpton, V.L. (2014), Outcrops on lunar crater rims: Implications for rim construction mechanisms, ejecta volumes and excavation depths, J. Geophys. Res. Planets, 119, 154–168, doi:10.1002/2013JE004523.

Smith, D. E., and the LOLA team. (2010), The Lunar Orbiter Laser Altimeter Investigation on the Lunar Reconnaissance Orbiter Mission, Space Sci. Rev., 150(1-4), 209–241, doi:10.1007/s11214-009-9512-y.

Song, E., Bandfield, J.L., Lucey, P.G., Greenhagen, B.T., and Paige, D.A. (2013) Bulk mineralogy of lunar crater central peaks via thermal infrared spectra from the Diviner Lunar Radiometer: A study of the Moon's crustal composition at depth, J. Geophys. Res., 118, 689-707, doi: 10.1002/jgre.20065.

Spudis, P.D., Hawke, B.R., and Lucey, P.G. (1984) Composition of Orientale Basin deposits and implications for the lunar basin-forming process, J. Geophys. Res., 89(S01), C197–C210.

Spudis, P.D. (1993) The geology of multi-ring impact basins: The Moon and other planets, Cambridge University Press, 263p.

Spudis, P.D., Martin, D.J.P., and Kramer, G. (2014) Geology and composition of the Orientale Basin impact melt sheet, J. Geophys. Res. Planets, 119, 19-29.

Stöffler D., Knöll H.-D., Marvin U.B., Simonds C.H., and Warren P.H. (1980) Recommended classification and nomenclature of lunar highland rocks, Proc. Conf. Lunar Highland Crust (Papike J.J. and Merrill R.B., eds.), Pergamon Press, New York, 51-70.

Taylor, L.A., Pieters, C.M., Keller, L.P., Morris, R.V., and McKay, D.S. (2001) Lunar Mare Soils: Space weathering and the major effects of surface-correlated nanophase Fe, J. Geophys. Res., 106(E11), 27985-27999, doi: 10.1029/2000JE001402.

Taylor, L.A., Pieters, C.M., Patchen, A., Taylor, D.H.S., Morris, R.V., Keller, L.P., and McKay, D.S. (2010) Mineralogical and chemical characterization of lunar highland soils: Insights into the space weathering of soils on airless bodies, J. Geophys. Res., 115(E02002), doi: 10.1029/2009JE003427.

Tompkins, S., and Pieters, C.M. (1999) Mineralogy of the lunar crust: Results from Clementine, Meteoritics & Planet. Sc., 34, 25-41.

Vaughan, W.M., Head, J.W., Wilson, L., and Hess, P.C. (2013) Geology and petrology of enormous volumes of impact melt on the Moon: A case study of the Orientale basin impact melt sea, Icarus, 223, 749-765.

Warren, P.H. (1985) The magma ocean concept and lunar evolution, Ann. Rev. Earth Planet Sci. 13, 201-240.

Wieczorek, M.A., and Zuber, M.T. (2001) The composition and origin of the lunar crust: Constraints from central peaks and crustal thickness modeling, Geophys. Res. Letters, 28(21), 4023-4026.

Wieczorek, M.A., Neumann, G.A., Nimmo, F., Kiefer, W.S., Taylor, J.G., Melosh, J.H., Phillips, R.J., Solomon, S.C., Andrews-Hanna, J.C., Asmar, S.W., Konopliv, A.S., Lemoine, F.G., Smith, D.E., Watkins, M.W., Williams, J.G., and Zuber, M.T. (2013) The crust of the moon as seen by GRAIL, Science, 339, 671-675.

Wilhelms, E., (1987) The geologic history of the Moon, U.S. Geological Survey Professional Paper, 1348, 302p.

Wood, J.A., Dickey, J.S., Marvin, U.B., and Powell, B.N. (1970) Lunar anorthosites and a geophysical model of the moon, Proc. of the Apollo 11 Lunar Sc. Conf., 1, 965-988.

Yamamoto S., Nakamura, R., Matsunaga, T., Ogawa, Y., Ishihara, Y., Morota, T., Hirata, N., Ohtake, M., Hiroi, T., Yokota, Y., and Haruyama, J. (2010) Possible mantle origin of olivine around lunar impact basins detected by SELENE, Nature Geoscience Letters, 3, 533-536.

Yamamoto, S., Nakamura, R., Matsunaga, T., Ogawa, Y., Ishihara, Y., Morota, T., Hirata, N., Ohtake, M., Hiroi, T., Yokota, Y., and Haruyama, J. (2012) Massive layer of pure anorthosite on the Moon, Geophys. Res. Letter, 39(L13201), doi:10.1029/2012GL052098.

Yamamoto, S., Nakamura, R., Matsunaga, T., Ogawa, Y., Ishihara, Y., Morota, T., Hirata, N., Ohtake, M., Hiroi, T., Yokota, Y., and Haruyama, J. (2015) Global occurrence trend of high-Ca pyroxene on lunar highlands and its implications, J. Geophys. Res. Planets, 120, doi:10.1002/2014JE004740.

Yokota, Y. et al. (2011), Lunar photometric properties at wavelengths 0.5–1.6μm acquired by SELENE Spectral Profiler and their dependency on local albedo and latitudinal zones, Icarus, 215(2), 639–660, doi:10.1016/j.icarus.2011.07.028.

Zuber, M.T., Head, J.W., Smith, D.E., Neumann, G.A., Mazarico, E., Torrence, M.H., Aharonson, O., Tye, A.R., Fassett, C.I., Rosenburg, M.A., and Melosh, H.J. (2012) Constraints on the volatile distribution within Shackleton crater at the lunar south pole, Nature, 486, 378-382, doi:10.1038/nature11216.

0